

HYDROGEOLOGICAL STUDIES AROUND WADI MAGHAMEISH, EASTERN SIDE OF MATRUH AREA, NORTHWESTERN STRIP OF EGYPT

Kh.S. Gemail, * , Sh.A. Ibrahim*, A. Samir, *, Chr.Oelsner, **, S.A. Mousa ***

* *Geology Dept. Faculty of Science, Zagazig University.*

** *Institute of Geophysics, Freiberg University of mining and technology, Germany*

*** *Geophysics Dept. Faculty of Science, Ain Shams University.*

دراسات هيدروجيوفيزيائية حول وادي ماغاميش ، في الجانب الشرقي من مدينة مطروح، الساحل الشمالي الغربي لمصر

الخلاصة: يقع وادي ماغاميش إلى الشرق من مدينة مطروح التي تتميز بوجود مجموعة من حواجز الحجر الجيري تحصر بينها مجموعة من المنخفضات. يمتد وادي ماغاميش من الهضبة الجنوبية إلى الشريط الساحلي شمالاً، وهو يستقبل كمية كبيرة من مياه الأمطار في خط الصرف الرئيسي وروافده. تمت الدراسة الهيدروجيوفيزيائية باستخدام طريقة الجس الكهربي الرأسي حيث تم توزيع ٥٣ جسة (أو نقطة قياس) كهربية على طول الوادي الرئيس وروافده والأماكن المحيطة بالوادي وذلك وباستخدام نظام شلمبرجير لتوزيع الأقطاب، لغرض دراسة نوعية وتتابع توزيع الطبقات تحت السطحية وكذا ابعاد خزان المياه الجوفية بمنطقة الدراسة. بالإضافة إلى استخدام طريقة المسح الكهربي ثنائي وثلاثي الأبعاد متكامل مع المسح السيزمي الإنكساري، وذلك لتحديد تفاصيل وضع المياه الجوفية ورسم الحد الفاصل بين المياه العذبة والمالحة في دلتا وادي ماغاميش.

تم تفسير منحنيات الجسات الكهربية المقاسة وصفيًا وكيميًا باستخدام عدة طرق لعمل نموذج لكل الجسات على عدة قطاعات. تحليل هذه النماذج والقطاعات الجيوكهربية أوضح وجود تغير سريع في قيمة المقاومة الكهربية في كلا من الإتجاهين الأفقي والرأسي. بالإضافة إلى وجود نطاقان صالحان لخزن المياه الجوفية وهما: الطبقة الأولى السطحية وهي مكونة من رواسب الوديان ذات إمتداد وسمك محدود وتتبع عمر الهولوسين. أما الطبقة الثانية عبارة عن حجر جيري حبيبي وهي تمثل الخزان الرئيسي لمنطقة شرق مطروح. وتمثل دلتا الوادي حوض مياه جوفية ضحل ومحدود ويظهر فيه مستوى المياه الجوفية العذبة على عمق ٨ متر ، أما نطاق المياه المالحة يبدأ من عمق ١٧ متر.

ABSTRACT: The area east of Matruh, where Wadi Maghameish is located, is dominated by limestone ridges alternated with shallow depression. Wadi Maghameish extends from the southern tableland to near the sea-coast and receives a great amount of floods through its tributaries. Hydrogeophysical investigations were executed using 53 points of 1D Schlumberger soundings distributed along the wadi and its surroundings to outline the subsurface layer distributions and aquifer boundaries. 2D and 3D resistivity imaging surveys integrated with seismic refraction profiling were applied for determination of the detailed groundwater conditions and mapping the boundary between the fresh and saltwater in the delta of the wadi.

The inversion models indicate that, there are rapid changes of the subsurface resistivities in horizontal and vertical sections. The limited inhomogeneous aeolian and alluvial deposits of Holocene age (93 to 1016 Ωm) represent the surface water-bearing horizon. The oolitic limestone layer of Pleistocene age (10 to 167 Ωm) represents the second and main aquifer in east Matruh area. The delta of Wadi Maghameish is considered as a shallow and local hydrographic basin, the freshwater appears at the depth of 8 m (10 to 21 Ωm), while saltwater layer starts at the depth of 17 m (less than 2 Ωm).

INTRODUCTION

The northwestern coastal strip of Egypt is characterized by semiarid climatic conditions of low and infrequent rainfall, large variations between maximum and minimum temperatures, high evaporation, and medium to low relative humidity. The average annual runoff inflow at Matruh area is about 14.0 Million m^3 , while the average rainfall is about 143.0 mm (Sewidan, 1978 and El Ramly and Abdel Fattah, 1991).

The considered area is located between Latitudes 31° 08' to 31° 17' N and Longitudes 27° 17' to 27° 26' E (Fig. 1). It includes three main drainage lines of Wadi El-

Kheir, Wadi Maghameish, and Wadi El-Garawla, which are dendritic in pattern. In the eastern side of Matruh, the width of the coastal plain is varied and controlled by the boundaries of the southern tableland. This plain has different morphologic features due to the influence of local structures, lithologic and physiographic conditions. It exhibits the landforms of foreshore dunes, several elongated coastal ridges and coastal depressions (El Shamy et al., 1969 and Hassanein and El Senussi, 1984).

The exposed rocks range in age from Early Miocene to Holocene. (CONCCO, 1986). Loose and aeolian

deposits along the shore zone and alluvial deposits, which filled the depressions between the ridges and the channels of drainage lines, represent the Holocene deposits. The Pleistocene deposits are represented by oolitic limestone, which formed the elongated ridges sub-parallel to the coastal plain (Fig. 2). It has been encountered in numerous boreholes resting over the Miocene rocks, Marmarica Limestone (El Shazly, 1964 and Said, 1990).

The geophysical measurements started with the execution of 1D resistivity sounding along the coastal area and the main wadis and their tributaries. According to the results of 1D resistivity model, the deltaic plain of Wadi Maghameish is selected for applying the 2D and 3D resistivity surveys using the pole-dipole, dipole-dipole and pole-pole arrays. In addition the seismic refraction method which is well suited for small scale mapping of near-surface layers and location of the water table (Milson, 1989 and Telford et al., 1990). The data are measured and interpreted to provide information about the velocities and thicknesses of the layers.

Integration between seismic refraction and resistivity imaging increases the reliability of identification of layers, determination of their thickness and building a good hydrogeological model (Van Overmeeren, 1981; Frasheri et al., 1998 and Scott et al., 2000).

DATA ACQUISITION

According to the available geological information, 53 Schlumberger 1D resistivity sounding points were measured. The maximum current electrode spacing ranged from 200 m at the coast to 800 m near the tableland (Fig. 1). Some of these soundings were conducted nearby boreholes and dug wells to correlate the sounding results with their lithological and hydrogeological information.

2D survey was carried out in the delta of Wadi Maghameish, using dipole-dipole array, with maximum length of 240 m and 10 m spacing. Along the same profile, forward and reverse pole-dipole profiles were executed using 22 electrodes with spacing of 10 m and 8 fixed datum level to produce 132 measured points. The second current electrode is placed at a distance more than 700 m from the profile. The lateral resolution of this array is reduced by the double sides measurements (Loke, 2001). The pseudosections were plotted in the field for quality control during data acquisition.

3D-resistivity survey was executed using 25 electrodes arranged in pole-pole array over a square grid with 10 m spacing. The two far electrodes were placed at more than 500 m from the grid. The potential is measured at the cross points to produce 172 measured points for each grid.

Along the measured 2D resistivity profiles, the seismic refraction survey was applied to measure the P-wave velocity (Fig. 1). Three seismic layouts were measured using 6 shot points as reciprocal shooting. The in-line profiling system (the shot points and the geophones are on the same line) was applied with a uniform spacing of 10 m and a geophone-spread cable of 110 total lengths. The shot point was placed at 10 m from the first geophone position. The reciprocal survey is used to map the dipping interfaces (Sjögren, 2000). The measurement was carried out using a twelve-channel signal seismograph model ES-1225. The wave is generated by a cone-shaped steel plate with a 14 kg sledgehammer. The instrument has a power to enhance the signals from several strikes added together to increase the total signal and produce hard copies as seismic record.

DATA PROCESSING AND INVERSIONS

The obtained multi-layer model of the 1D sounding curves, using the automatic technique of Zohdy (1989), was used as preliminary model for IPI2win program (Bobachev et al., 2003). This program is based on linear filtering and Newton algorithm of the least number of layers. It treats the data for a profile as a unity representing the geological structure of the survey area as a whole.

The 2D and 3D inversion procedures for resistivity tomography (resistivity imaging) aims to construct an image of the true resistivity distribution and map the saltwater intrusion within the deltaic plain in form of horizontal and vertical slices. The data were inverted using RES2DINV and RES3DINV programs vers., 3.54 and 2.15 (GEOTOMO, 2004 a and b), respectively. The inversion procedures is based on the smoothness-constrained least-squares algorithm (deGroot-Hedlin and Constable, 1990). The subsurface is divided into layers, which subdivided into rectangular blocks of the same size (Loke and Barker, 1996) and the resistivities of the blocks is calculated by the finite element method using iterative manner (Sasaki, 1994 and Loke and Dahlin, 2002). The obtained models are controlled by the available geological and hydrogeological data of drilled boreholes and results of 1D sounding. These data include lithology, depth to water table and salinity of groundwater.

The measured seismic layouts were picketed up and the first arrivals of reciprocal records were corrected for elevation and used to construct the time-distance curves, which were interpreted using the intercept time and crossover distance methods to obtain the velocities and thicknesses of the layers (Lankston, 1990 and Sjögren, 2000). The subsurface irregularities of refractors were mapped, from the forward and reverse travel times, using the delay time (ABC) method (Wyrobek, 1956).

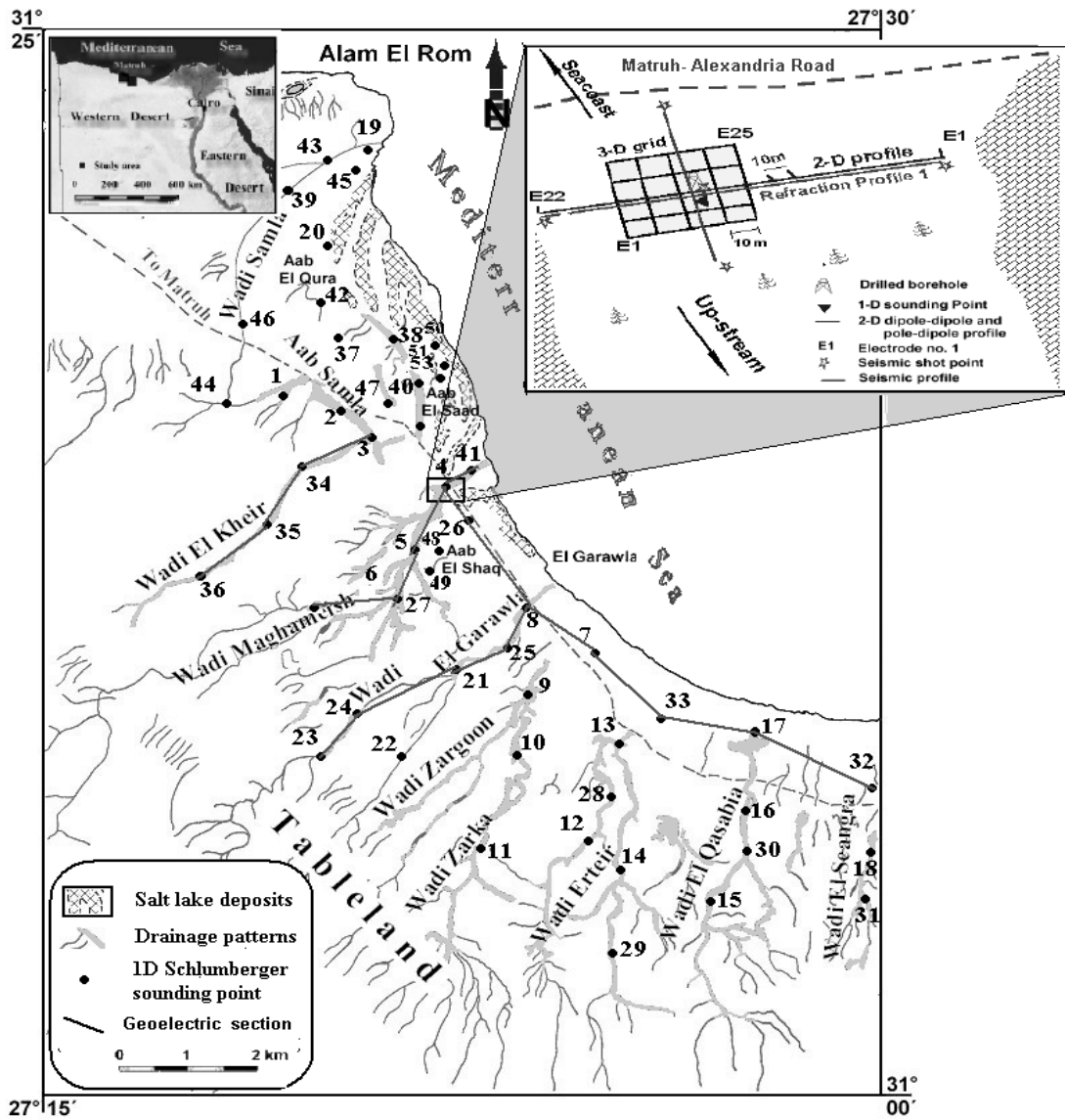


Fig. (1): Location map of the geophysical field measurements.

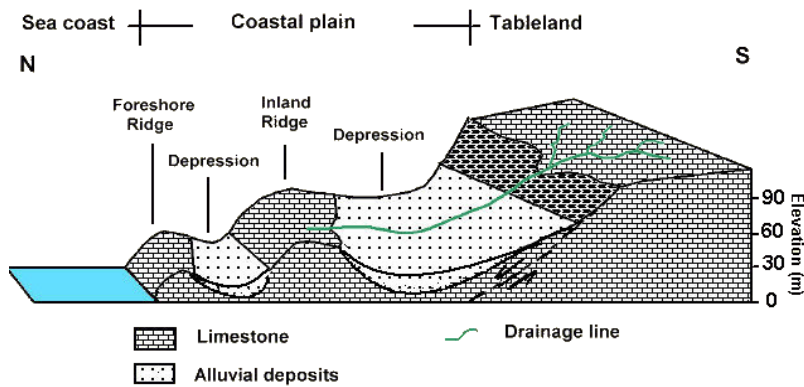


Fig. (2): Generalized block diagram shows the most geomorphologic features in the area.

The delay time values and depths below the geophones were obtained using WinSism 10 software (Jenny et al., 2004). The limitations of the resistivity and seismic methods can be overcome by combination of the obtained results with the drilling boreholes referencing.

RESULTS AND DISCUSSIONS OF THE RESISTIVITY SPECTRUM

The results of 1D sounding interpretation have been inspected to determine the litho-stratigraphic boundaries of subsurface layers and to define the possible water-bearing layers. The deduced geoelectric horizons were correlated with the surface geological exposures and subsurface lithology from drilled boreholes and previous hydrogeological and geophysical investigations such as Hassan and El Ramly (1966), Shata et al. (1978), Atwa (1979), Rizk (1982), Hussein (1994) and El Fiky (1996). These allow to establish a spectrum of resistivity for the subsurface layers distribution (Table, 1), that was used as a guide for construction the geoelectric cross-sections.

A) Geoelectric Cross-Sections

To define the parameters of the subsurface layers and outline the extension of the groundwater aquifers and their related possible structures, four geoelectric cross-sections were constructed along the main wadis and the coastal plain.

1- Wadi Maghameish section

The geoelectric section along the wadi, in NE-SW direction, (Fig. 3) can be differentiated into four layers. The first one corresponds to alluvium loam, with resistivity range from 93 Ω m to 1016 Ω m.

This high resistivity may be due to change of the constituents from sands with limestone boulders near the tableland to silt and fine materials near the coast. The second layer is the oolitic and marly limestone aquifer as indicated from shallow drilled boreholes near sounding no. 4. The groundwater in this aquifer occurs as perched lenses in the limestone overlying clayey layer. Its resistivity varies between 10 to 167 Ω m and its thickness ranges from 7m (sounding no. 41) to about 20 m (sounding no. 6).

The third geoelectric horizon has very low resistivity ranging between 1 Ω m (soundings no. 4 and 41) to 4 Ω m (sounding no. 27), which may indicate shale and marl intercalations. This layer has a thickness of about 70 m at the coastal plain and decreases towards the tableland. The last layer has a resistivity ranging between 26 and 42 Ω m. It may correspond to Miocene limestone layer.

2- Wadi El-Kheir section

Along this section (Fig. 4), five geoelectric horizons could be distinguished. The top one has resistivities ranging from 76 to 630 Ω m, that reflects the inhomogeneity of the alluvium loam constituents (sands, silts, with limestone boulders). The thickness increases toward the deltatic plain of the wadi. At sounding no. 34, the resistivity decreases to 30 Ω m at about depth of 2 m, indicating limited water-bearing zone. The second corresponds to shale layer (2 to 8 Ω m), which is exposed at the surface near sounding no. 36 to form the walls of wadi with underlying oolitic and marly limestone.

The third horizon displays resistivities between 17 and 25 Ω m, correlated with some drilled boreholes as saturated oolitic and marly limestone aquifer. The maximum thickness is about 27 m recorded at sounding no. (34).

Table (1): Resistivity spectrum and lithology of the obtained subsurface layers in the area.

Formation	Lithologic description	Resistivity (Ω m)	Average thickness (m)
Holocene deposits	Wadi filling, loam, sands, silts with limestone boulders.	50 – 1400	1.6
	Saturated sand and gravel	5 – 50	3.5
	Hard limestone intercalated with loam.	100 – 500	7
Upper shale layer	Shale, sandy in parts, with silt.	2 – 6	14
Upper limestone aquifer (Pleistocene)	Oolitic, marly limestone, friable to moderately hard.	10 – 150	25.5
Lower clay layer	Clay with marls intercalations, sandy, gypsiferous.	1- 8	54.3
Lower limestone aquifer (Miocene)	Cavernous and fissured limestone intercalated with clay and marl.	9 – 55	--

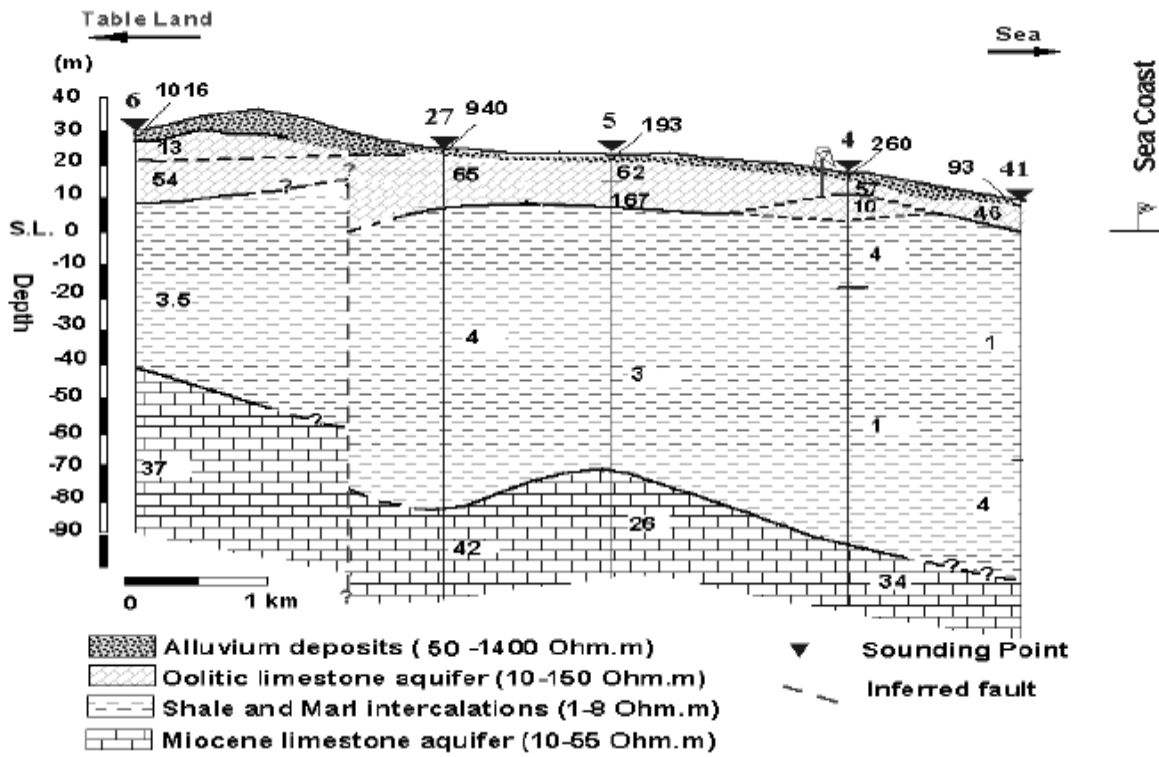


Fig. (3): Goelectric cross-section along Wadi Maghameish.

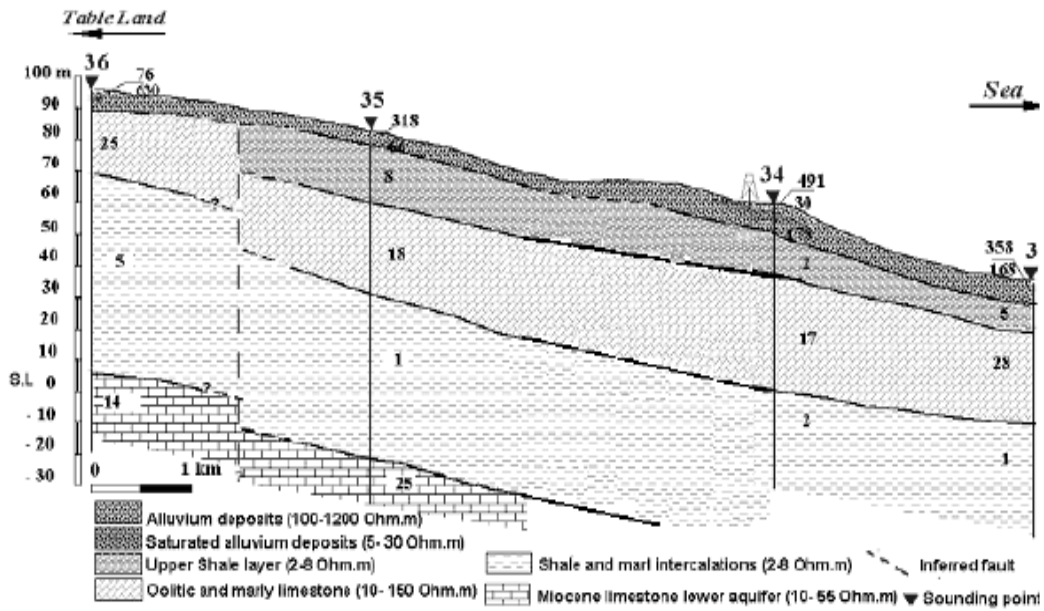


Fig. (4): Goelectric cross-section along Wadi El khair.

The fourth geoelectric layer has very low resistivity (1 to 5 Ωm) corresponding to shale and marl intercalations. The base of this layer is recorded only at soundings no. 36 and 35, where the last geoelectric horizon is outlined with a resistivity ranging from 14 to 25 Ωm . It may correspond to Miocene limestone.

3- Wadi El-Garawla section

This section shows four geoelectric layers (Fig. 5). The first one is the alluvium with resistivity ranging between 1471 and 126 Ωm . The second layer is the expected aquifer of oolitic and marly limestone with resistivities range between 10 to 87 Ωm . Increasing value at sounding no. 24 may indicates the variation in the saturation and fractures along this layer. It has nearly uniform thickness of about 18 m. The third layer with very low resistivity (2 to 6 Ωm), may indicates clay and marl. The last layer may correspond to deeper limestone with resistivity range from 17 to 44 Ωm . 4- Coastal plain section

The section passing through the inlets of Wadi Maghameish and Wadi El-Garawla (fig. 6) indicates that, the holocene deposits displays two resistivity zones. The first (260 Ωm) corresponds to the surface alluvium loam with 1 to 2 m thick, while the second zone has 6 m thick and resistivities of 6 and 37 Ωm at soundings no. 7 and 33 respectively. This may reflect saturation zone with fresh and brackish water.

The resistivity of the oolitic and marly limestone aquifer reduces from west to east. The maximum thickness (about 35 m) recorded at sounding no. 33 is represented by structurally low area. The variation in depth, thickness and topographic uplift between soundings no. 4 and no. 26 could be explained as due to vertical structural dislocations. Lower limestone is recorded at soundings no. 4, 8 and 7, with resistivities of 31 to 44 Ωm , which may point to a higher content of clay or high groundwater salinity.

The variations in the thicknesses and depths of the suggested aquifers are controlled by the tableland faults, which could be suggested along the constructed four sections and others inferred from the geological studies. These faults play an important role in the groundwater movements and conditions within the eastern part of Matruh area, where they control the locations and orientation of the drainage lines, as well as the groundwater has been detected in the northern downthrown sides.

B) Delta Wadi Maghameish

In the deltaic plain (Fig. 1), the groundwater is found at a depth of 7.5 m with salinity of 2400 ppm, as indicated from the borehole near sounding no. 4 (Fig. 7).

The 2D inverted sections of double sides pole-dipole array (Fig. 8a and b) indicates that a low resistivity zone in the form of lens-shaped body appears at a depth of 8 m in the area between spacing of 80 and 160 m and extends to depth of 15 m. Its resistivity varies between 10 and 21 Ωm and corresponds to the freshwater aquifer, which occurs over the saltwater zone with a resistivity of less than 2 Ωm . A transition zone with a resistivity of 4 Ωm is encountered between the fresh and salt water. The high resistivities (46 to 202 Ωm) in the upper parts of the inverted sections indicate dry alluvium deposits together with the upper parts of the dry limestone. The dipole-dipole inverted section (Fig. 8c) explains, the depth to freshwater body at 130 m spacing is about 8 m with resistivity range between 10 and 21 Ωm and extends to maximum depth of 17 m.

The image of the 3D model from pole-pole inversion in horizontal slices and vertical sections (Fig. 9a and b) is similar to that of 2D inversion. The horizontal slices (Fig. 9a) displays a high resistivity values between 45 and 202 Ωm for the dry top layers, which corresponds to alluvium loam combined with oolitic limestone and extends to a depth of about 8 m. At 8 m depth, the freshwater aquifer appears with resistivity values between 10 and 21 Ωm and 9 m thickness. The saltwater layer starts at the depth of 17 m with a resistivity of less than 2 Ωm . The transition zone of brackish and saltwater could be noticed with a resistivity of 5 Ωm over the saltwater. The vertical sections (Fig. 9b) reflect the lens-shape of the freshwater body with maximum thickness at the first section, and decreases towards section no. 4.

The comparison between these sections shows that the dipole-dipole array has a greater horizontal resolution but lower signal quality in deeper parts of the section. The pole-dipole array has less horizontal resolution but better signal quality in deeper parts. While, the pole-pole array has greatest investigation depth compared with other arrays.

The seismic refraction survey was executed to delineate the lateral velocity variations, measure the depth to water table, thickness of aquifers and confirm the results of the resistivity surveys. The level of groundwater table can be revealed by a sudden velocity increase (Goodman, 1976), may be up to 150 % as indicated by Haeni, 1988 and Berger et al., 2001.

The first time-distance curves and seismic section (Fig. 10) runs along the same line of the 2D resistivity and shows three subsurface layers. The thickness of the first layer varies from 6.8 m (shot point 1) to 8 m (shot points 2 and 3) and velocity varies from 468 to 727 m/sec., which correspond to dry alluvium loams combined with the upper part oolitic limestone.

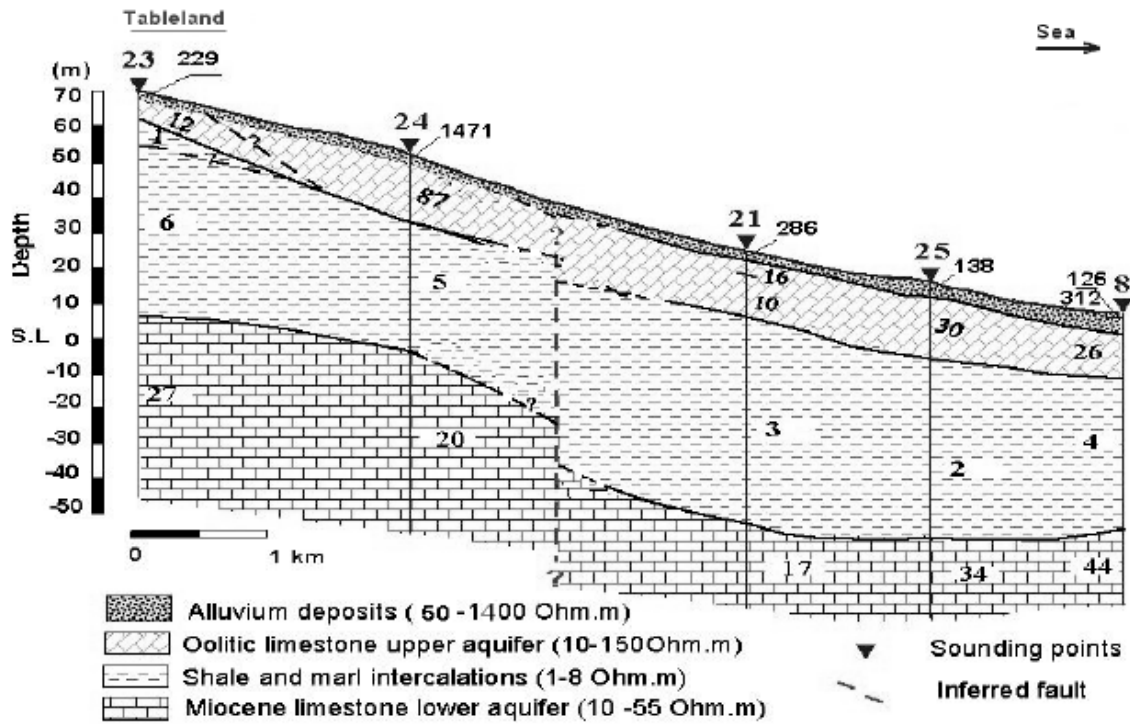


Fig. (5): Goelectric cross-section along Wadi El-Garawla.

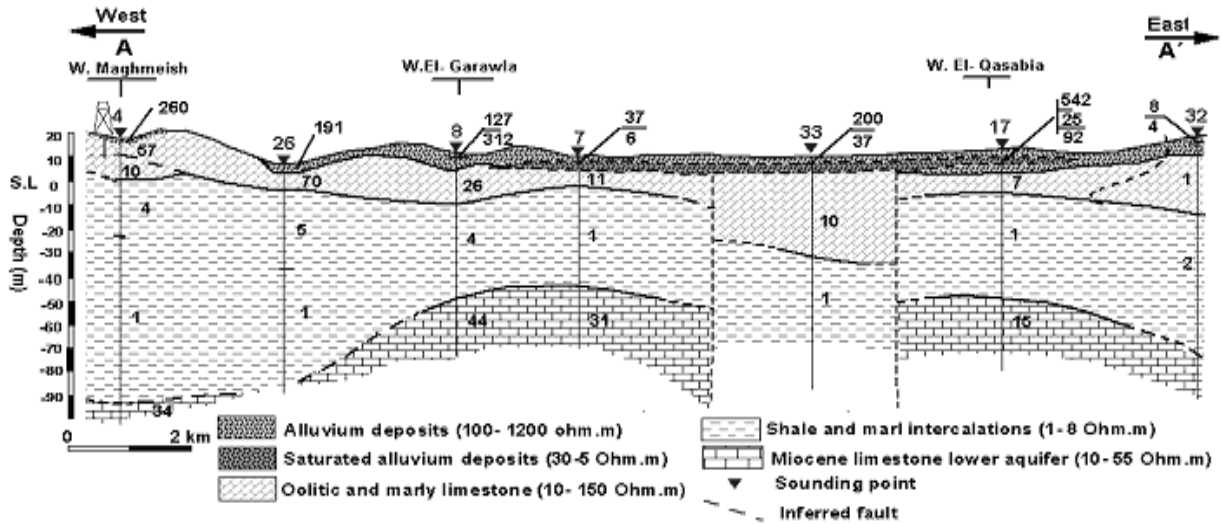


Fig. (6): goelectric cross-section along the coastal plain.

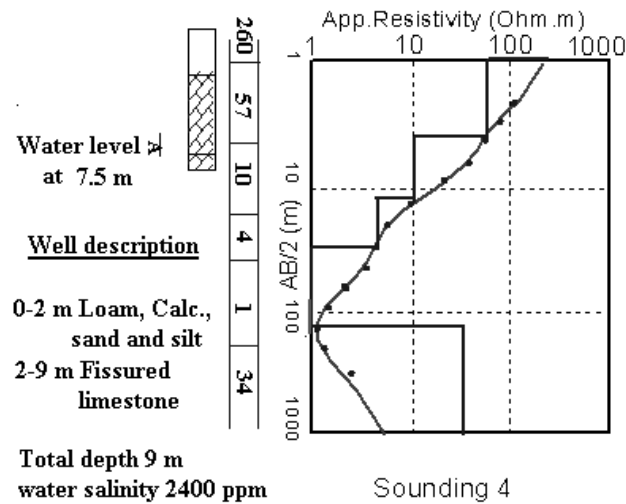


Fig. (7): 1D model and borehole data at the site of sounding no. 4.

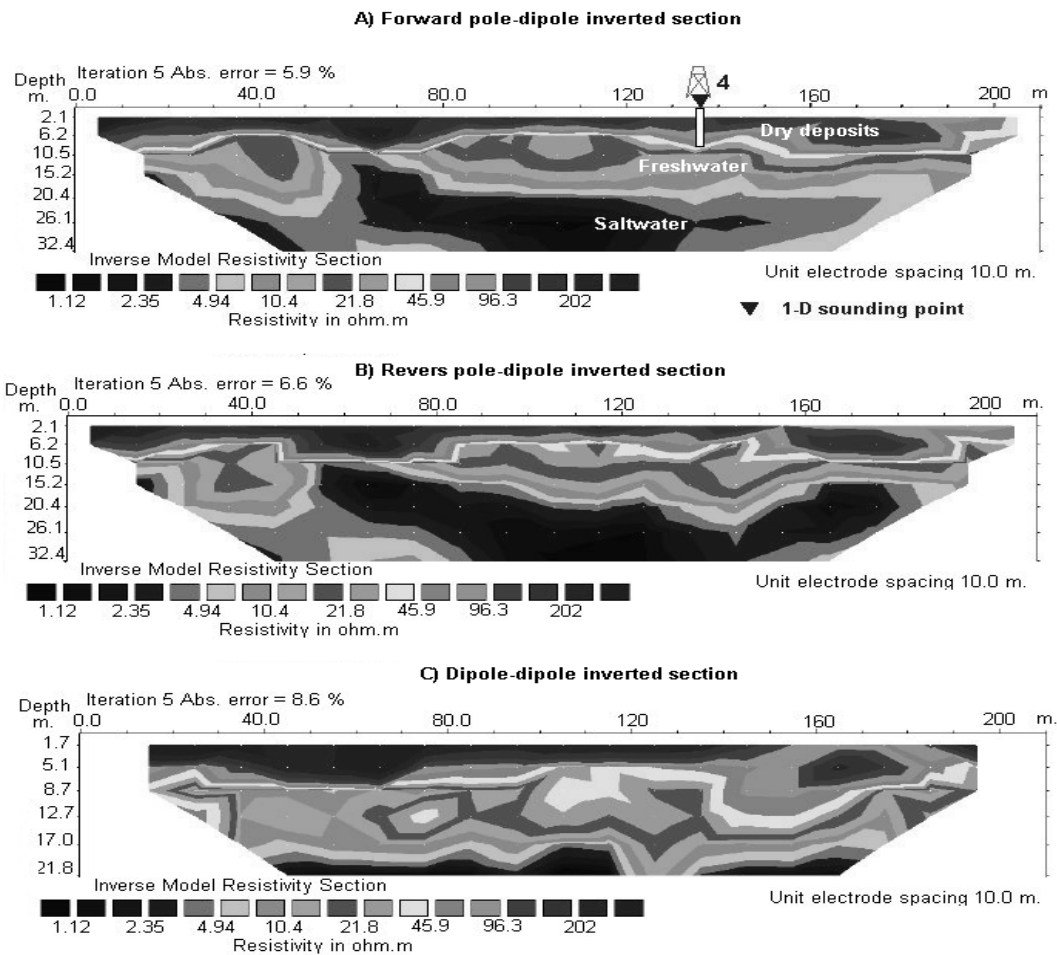


Fig. (8): 2D inverted sections at the delta of Wadi Maghameish obtained from a) forward pole- dipole, b) reverse pole-dipole and c) dipole-dipole data.

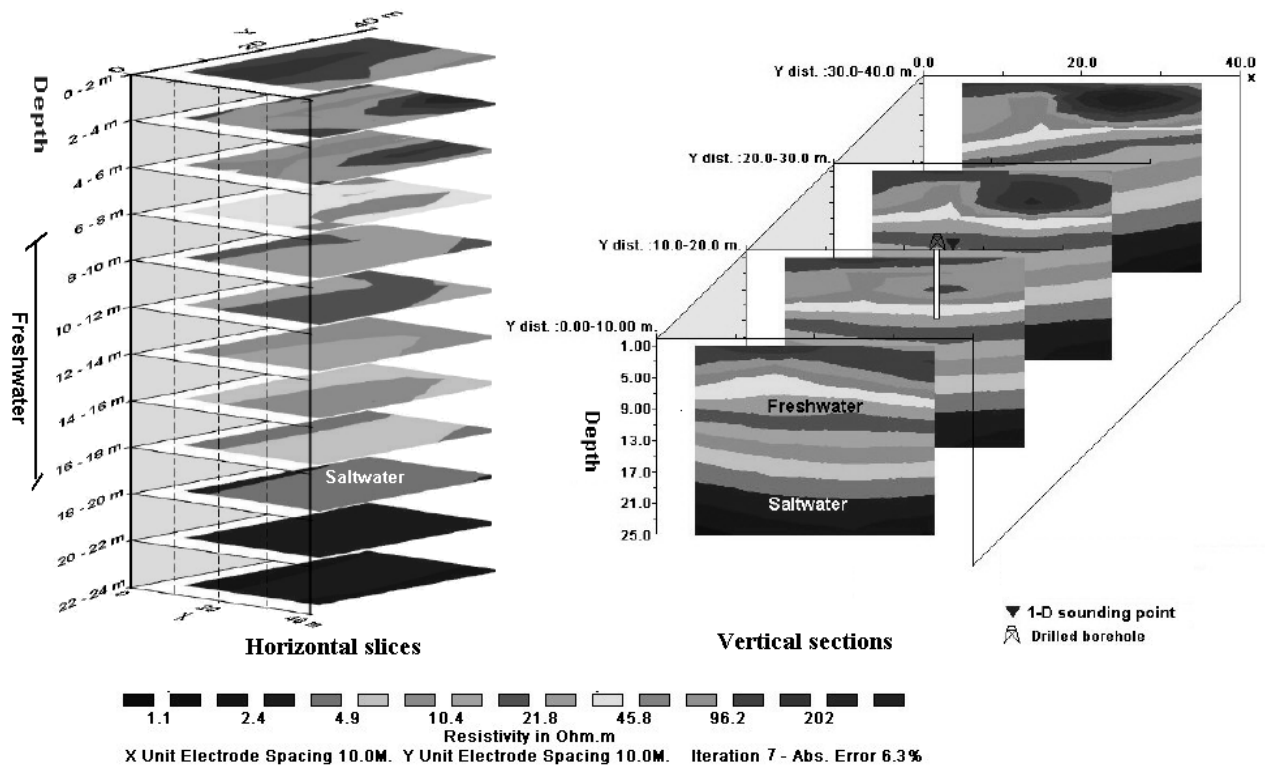


Fig. (9): 3D obtained model from the inversion of pole-pole survey at the delta of Wadi Maghmeish.

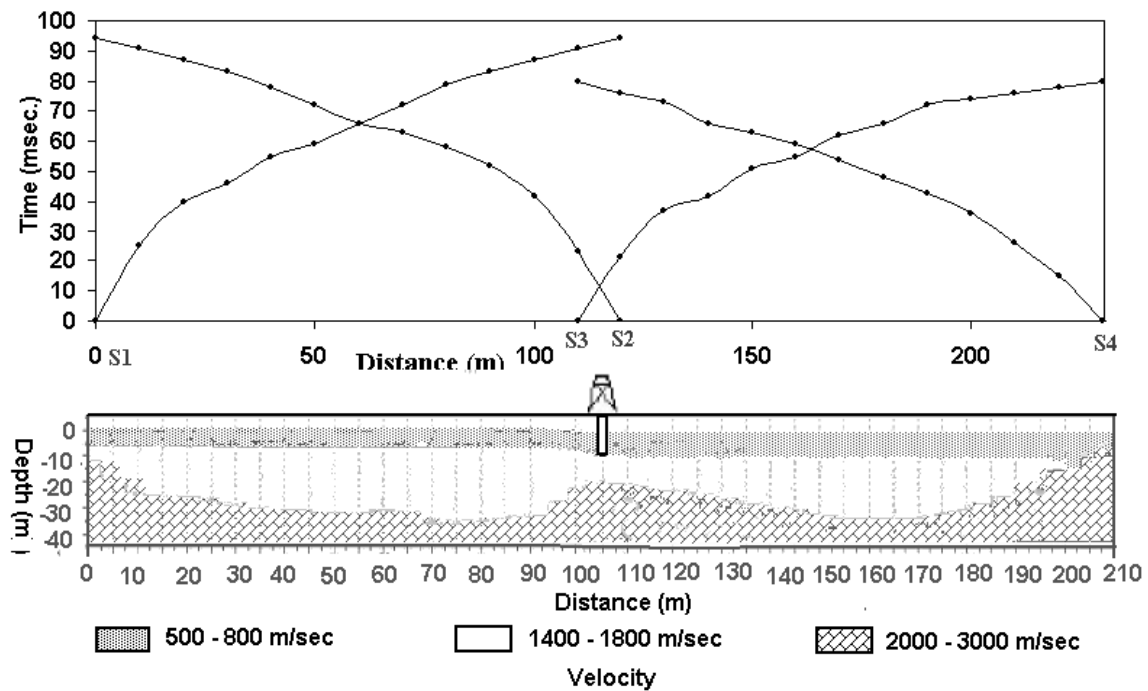


Fig. (10): Time-distance curve and the interpreted seismic section using ABC method, a cross of Wadi Maghmeish.

The second layer, which may refer to saturate fissured oolitic limestone, has a velocity of 1699 to 1795 m/sec and thickness of 9 to 18 m. It could be noticed that the freshwater and saltwater layers in the resistivity surveys appear as one seismic layer. The third seismic layer exhibits velocities between 2500 and 2858 m/sec, which corresponds most probably to the lower shale layer with marly limestone as interpreted from the 1D resistivity surveys.

The second seismic profile of figure (11) displays the same three layers with variations in the depth and thickness of some layers. Under the second shot point the thickness of the second layer is diminished towards the limestone walls of the wadi. The distortion of velocities under the first shot point is resulted from the traffic noise along the road.

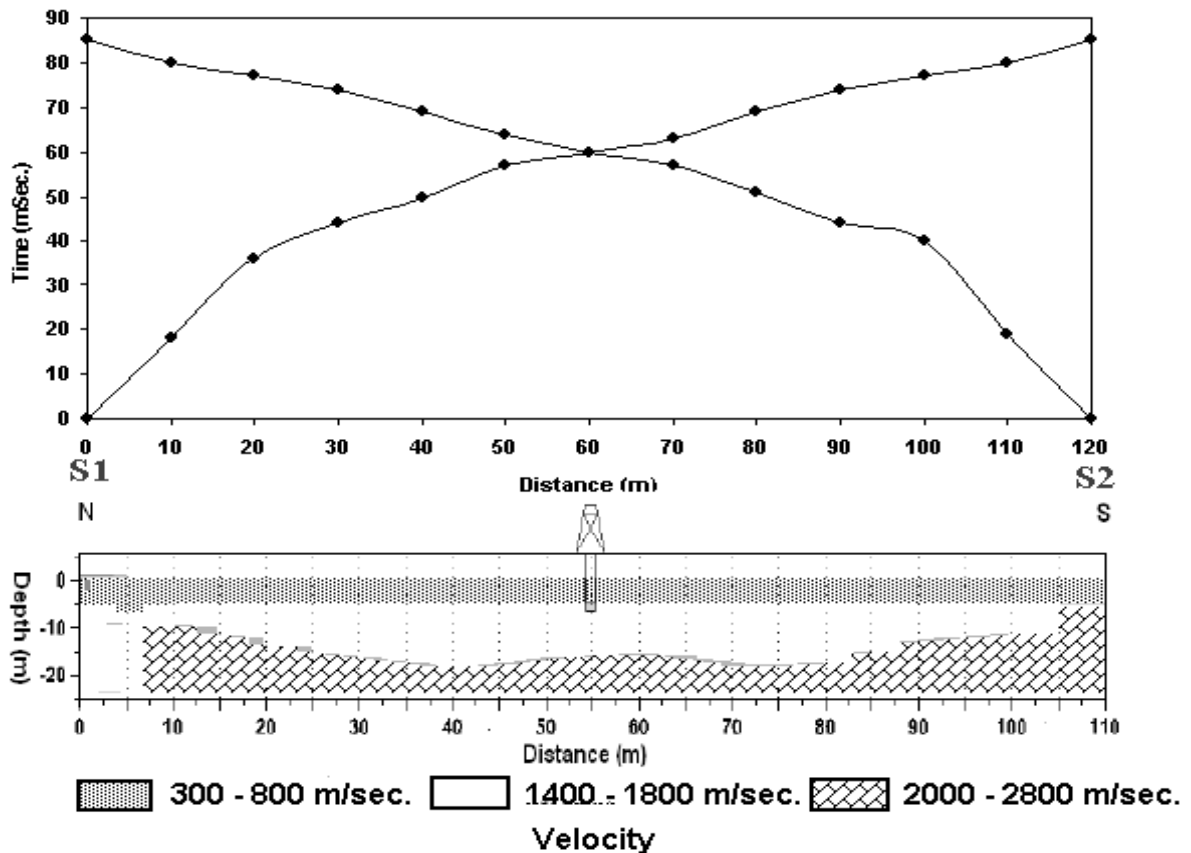


Fig. (11): Time-distance curve and the interpreted seismic section using ABC method, along the axis of Wadi Maghameish.

Table (2): Spectrum of the resistivity value and seismic velocity at delta Wadi Maghameish.

Formation	Resistivity (Ωm)	Velocity (m/sec.)
Alluvium cover and dry limestone	46 – 202	486 – 727
Saturated oolitic limestone	10 – 21	1699 – 1795
Saturated limestone with saltwater	2 – 5	---
Lower shale and marl layer with saltwater	< 2	2500 – 2858

The hidden layer or blind zone could be seen along the two measured profiles where, freshwater zone with saltwater layer and alluvium with oolitic limestone zone are combined with others due to its limited thickness and small velocity contrast. Thus, the integration of resistivity and seismic results (Table, 2) is useful for mapping the subsurface conditions.

CONCLUSIONS

The 2D and 3D resistivity imaging survey give a clear picture of the investigated subsurface layers and the boundary between the fresh and saltwater that would have been, most probably, not sufficiently accurate in case of 1D survey, where the geology changes within short distance. The combination of seismic refraction and 2D resistivity imaging can be considered as good geophysical mapping tools for explaining the hydrogeological model of the shallow fissured limestone aquifer in the area.

The surface water-bearing layer is represented by the aeolian and alluvial deposits of Holocene age which fill the main drainage lines. The groundwater occur as small freshwater lenses overlying upper shale layer or compacted limestone with thickness varying between 2 to 6 m. The freshwater accumulated due to the recharge of rainwater and the height of aquifer above sea level.

The second aquifer is the oolitic and marly limestone of Pleistocene age that represents the main aquifer in the area. It has well defined boundaries and underlined by a thick low permeable clay and marl layer that, act as confining bed saturated with saltwater. The near-shore ridge and its cover of foreshore dunes and alluvium act as collecting basins for watershed, while the southern ridges, hard limestone, act as water dividing areas.

In the northwestern part of the area, at Wadi El-Kheir and the western wall of Wadi Maghameish, the oolitic limestone aquifer is underlined by clay layer which is favorable for the perched groundwater of good quality. The delta of wadi Maghameish is considered as a shallow and local hydrographic basin and its alluvial aquifer increase to the downstream portion, therefore the delta represents the most favorable site for freshwater accumulations.

RECOMMENDATIONS

For planning and increasing the development of agricultural and industrial policy in Matruh area, detailed investigations of the groundwater and management of its uses are recommended, because the rainy seasons are short and fluctuating according to the climatic conditions.

REFERENCES

- Atwa, S.M.M., 1979.** Hydrogeology and hydrogeochemistry of the northwestern coast of Egypt. Ph.D. Thesis, Fac. Sci., Alexandria Univ., Egypt.172 p.
- Berger, D.L.; Ponce, A.D. and Ross, W.C., 2001.** Hydrogeologic framework of Antelope Valley and Bedell Flat, Washoe County, West-Central Nevada. U.S.G.S., Open Report File 01- 4220, 11 p.
- Bobachev, A.A.; Modin I.N. and Shevnin V.A., 2003.** IPI2Win v. 4.0 :User's Guide. Moscow State Uni., Geological Faculty, Dept.of Geophysics, 35 p.
- CONOCO Coral, 1986.** Geological map of Egypt scale 1:500 000, NH-35 NE Alexandria. The Egyptian General Petroleum Co., EGPC.
- deGroot-Hedlin, C. and Constable, S.C., 1990.** Occam's inversion to generate smooth-dimensional models from magnetotelluric data. Geophysics ,vol. **55**, pp. 1613-1624.
- El Fiky, A.A., 1996.** Geophysical and hydrogeological investigations on some groundwater problems at the area between Fuka and Ras Umm El-Rakham, Mediterranean coastal zone, Egypt. Ph.D.Thesis, Fac.Sc.,Alex.,Uni., Egypt, 271 p.
- El Ramly, I.M. and Abdel Fattah, A., 1991.** Rainfall-soil conservation as an important tool for rangeland management along the Western Desert coastal region, Egypt. First workshop on Rahabil., and Develop., Siwa Oasis and Western Desert, 27 p.
- El Shamy, I.Z.; El Shazly, M.M. and Shata, A.A. 1969.** Contribution to the geology of El Dabaa area (Western Mediterranean Littoral Zone) Part 1: Geomorphology. Bull. Inst. Desert Egypt, vol., **19** (1), pp. 63-96.
- El Shazly, M.M. 1964.** Geology, pedology and hydrogeology of Mersa Matruh area (Western Mediterr., Littoral, U.A.R.), Ph.D. Thesis, Fac. Sci., Cairo Univ., 164 p.
- Fraseri, A.; Kapliani, L. and Dhima, F., 1998.** Geophysical landslide investigation and prediction in the hydrotechnical works. J., Balkan Geophys., Soc.,vol. **1**, pp. 38-43.
- GEOTOMO Software, 2004a.** RES2DINV ver. 3.54 manual. www.geoelectrical.com.
- GEOTOMO Software, 2004b.** RES3DINV ver. 2.15 manual. www.geoelectrical.com.

- Goodman, R.E., 1976.** Methods of geological engineering in discontinuous rocks. West Publ., Co., New York, 356 p.
- Haeni, F.P., 1988.** Application of Seismic refraction techniques to hydrologic studies. U.S.G.S., Techn., Water-Resources Invest., Ch D2, Book 2, 86 p.
- Hassan, A.A. and El Ramly, I.M., 1966.** Preliminary groundwater investigation in Ras El Hekma area, western Mediterranean Littoral, U.A.R.Desert Inst., Cairo.18 p.
- Hassanein, A.M. and El Senussi, M.Y, 1984.** Geomorphology aspects of the area between longitudes 26 30- 27 30E along the Mediterranean Coast Zone, Egypt. Bull. Fac. Sci., Zag. Univ., vol., 6 (6), pp. 136-155.
- Hussein, G.H.G., 1994.** Geophysical studies to delineate the geological and hydrogeological conditions in the area between Ras Alam El-Rum Ras Abu Laho, northwestern coast, Egypt. Ph.D. Thesis, Geoph. Dep., Fac. Sci. Ain Shams Uni., 165 p.
- Jenny, J.; Borreguero, M. and Burgisser, A., 2004.** WinSism ver.10, seismic refraction processing software for windows: Instruction manual. www.geosoft.ch , 47 p.
- Koefoed, O., 1979.** Geosounding principles, 1D resistivity sounding measurements. Elsevier Scientific Publishing Co., Amsterdam, 276 p.
- Lankston, R.W., 1990.** High-resolution refraction seismic data acquisition and interpretation. In investigations in geophysics no. 5, review and tut., 1, pp. 45-73.
- Loke, M. H., 2001.** Tutorial: 2-D and 3-D electrical imaging surveys. Penang, Malaysia, Universiti Sains Malaysia, Unpublished course notes, 129 p.
- Loke, M.H., and Barker, R.D., 1996.** Rapid least-squares inversion of apparent resistivity pseudosections by a quasi-Newton method. Geophys. Prosp., vol., 44, pp. 131-152.
- Loke M.H. and Dahlin T., 2002.** A comparison of the Gauss-Newton and quasi-Newton methods in resistivity imaging inversion. J. Applied Geophysics, vol., 49 (3), pp. 149-162.
- Milsom, J., 1989.** Field Geophysics. New York, Open University Press, Milton Keynes, Geological Society of London, Handbook, 182 p.
- Muiuane, E.A. and Pedersen, L. B., 1999.** Automatic 1D interpretation of DC resistivity sounding data. J. Applied Geophysics, vol., 42 (1), pp. 35-45.
- Rizk, Z.S., 1982** Geological and hydrogeological studies on some localities along the northwestern coast of Egypt. M. Sc. Thesis, Geol. Dept., Fac. Sci., Menoufia Univ., Egypt. 163 p.
- Said, R., 1990.** The geology of Egypt. Balkema, Netherlands, 733 p.
- Sasaki, Y.,1994.** 3-D resistivity inversion using the finite-element method Geophysics, vol., 59, pp. 1839-1848.
- Scott, J.B.T.; Barker, R.D. and Peacock S., 2000.** Combined seismic refraction and electrical imaging. 6th meeting of Env., and Eng.,Geophy., Germany, EL05.
- Sewidan, A.S., 1978.** Water budget analysis for the northwestern coastal zone of the Arab Republic of Egypt. Ph.D. Thesis, Fac. Sci., Cairo Univ., Egypt. 188 p.
- Shata, A.; Hammad, F.A.; Atia, S.H.; El Shamy, I.Z.; Abdel Mogheeth, S.M. and El Sayed, M.A., 1978.** The groundwater resources in the northwestern coastal zone, Egypt. Preliminary report, Water Resources Dept., Desert Institute, Cairo. 26 p.
- Sjögren, B., 2000.** A brief study of applications of the generalized reciprocal method and of some limitations of the method. Geophys., Prosp., vol., 48, pp. 815-834.
- Telford, W.M.; Geldart, L.P. and Sheriff, R.E., 1990.** Applied geophysics, 2nd ed. Cambridge University Press, Cambridge.
- Van Overmeeren, R.A., 1981.** A combination of electrical resistivity, seismic refraction and gravity measurements for groundwater exploration in Sudan. Geophysics, vol., 46, pp. 1304-1313.
- Wyrobek, S.M., 1956.** Application of delay and intercept times in the interpreta-tion of multiplayer refraction time distance curves. Geophys. Prosp., vol., 4, pp. 112-130.
- Zohdy, A.A.R., 1989.** A new method for automatic interpretation of Schlumberger and Wenner sounding curves. Geophysics, vol., 54, pp. 245-253.

SEISMIC HAZARD ASSESSMENT FOR THE SOUTHWESTERN ARABIAN PENINSULA AND RED SEA REGION

M.A. AL-MALKI* and A.M.S. AL-AMRI**

* Seismic Analysis Center, King Abdulaziz City for Science and Technology, P.O. Box 6086, Riyadh 11442, Saudi Arabia.

** Department of Geology, King Saud University, P.O. Box 2455, Riyadh 11451, Saudi Arabia.

تقييم الأضرار السيزمية للجزء الجنوبي الغربي لشبه الجزيرة العربية ومنطقة البحر الأحمر

الخلاصة: تعرض الجزء الجنوبي الغربي لشبه الجزيرة العربية وجنوب البحر الأحمر لعدد كبير من الزلازل التاريخية والحديثة في المدة من سنة ٢٠٠٠ إلى سنة ٢٠٠٥ وبدرجات مختلفة تتراوح بين أكبر من اثنين وأقل من ثمانية على مقياس ريختر. وقد أظهر التوزيع المكاني لمراكز هذه الزلازل توافق عام مع الجيولوجية الإقليمية والأوضاع التكتونية المميزة للمنطقة، وبناءً على النشاط الزلزالي وتحليل ميكانيكية البؤرة والتراكيب الجيولوجية والتكتونية يمكن تقسيم المنطقة إلى أربعة نطاقات للمصادر الزلزالية هي جنوب الدرع العربي - جنوب البحر الأحمر - شمال اليمن - منتصف البحر الأحمر، حيث تم حساب القيمة العظمى للدرجة المتوقعة،

وقد وجد أن القيمة (b) تتطابق جيداً مع الحالة التكتونية حيث تزداد تدريجياً في اتجاه الجنوب مع انفتاح البحر الأحمر، وهذا يعكس بدوره عدم تجانس القشرة الأرضية وكذلك مجالات الاجهادات الإقليمية. وقد تم تطبيق الطرق الإحصائية لتقييم الأضرار الزلزالية باستخدام برامج الحاسب المتقدمة لمحاكاة الحركة القوية، حيث أظهرت النتائج أن القيمة العظمى للعجلة الأرضية القصوى على صخر الأساس لهذه الفترة التاريخية هي ٤١,١ جال للمدصر جنوب البحر الأحمر بينما تبلغ العجلة الأرضية القصوى ٧٢,١٥ جال على سطح الأرض لنفس المصدر.

ABSTRACT : There are a great number of historical and recent earthquakes have occurred in the southern Red Sea and southwestern Saudi Arabia between Latitudes 14°-19°N and Longitudes 39°-45°E in the period of 200-2005 A.D. with magnitudes ranges from $2 \leq M \leq 8.0$. The area of interest has a complicated geological structures and tectonics. The epicentral distribution of both historical and instrumental earthquakes shows a general correlation with the regional geology and tectonics. Concentration of activity are seen where the spreading zone is intersected by NE transform faults. Most of the seismicity of this area is of swarm type and volcanic-related. Based on the seismic activity, focal mechanism solutions, geological structures and tectonics, four seismic source zones were defined; Southern Arabian Shield, Southern Red Sea, Northern Yemen and Middle of the Red Sea. The maximum expected magnitude for each seismic source zone was estimated. The b values correlate well with the tectonic environment and seem to increase gradually southwards with the opening of the Red Sea where it has 0.57 for the middle Red Sea and attains 1.06 for the southern Arabian Shield. This may reflects the heterogeneity of the crust and regional stress field. The stochastic method is applied for the seismic hazard assessment using more recent and advanced FORTRAN program for Strong Motion SIMulation (SMSIM). The area was divided into small grid of point each 0.5 degree for both of latitude and longitude. The source parameters and the maximum expected magnitude for each seismic source were implemented into the method as input data also the path and site effect taken into consideration for the assessment of seismic hazard potentialities within the area in terms of Peak Ground Acceleration (PGA) and the response spectra for different rock units at the populated cities. The results of this method show that the maximum simulated time history of PGA on the bed-rock is 41.1 cm/sec^2 resulted from the southern Red Sea source, while the maximum PGA on the ground surface is 72.15 cm/sec^2 resulted also from the southern Red Sea source. The response spectra were calculated for different rock units at selected sites for 1%, 3%, 5% and 10% from the critical damping.

INTRODUCTION

The study area located between Lat. 14°-19° N and Long. 39° - 45° E including southwestern part of Saudi Arabia, Northern Yemen and the southern part of the Red Sea (Fig. 1). It is characterized by a various topographic features as plateaux of Hejaz and Asir (1300 -2000 m above Sea level) extends along the western coast of Saudi Arabia. The Northern Yemen has a complicated topographic regions as; 1) coastal plain region, extends along the coast of Yemen; 2) mountain highs region extends from the northern to southern

Yemen borders; 3) mountain basins region that includes the main basins and plains within the mountain highs (e.g. Yarim, Dhamar, Sadah) and finally plateaux belt which present in the east and north of mountain highs region. The Red Sea can be divided into three physiographic regions; the narrow continental margins, the main trough and the deep axial trough (Drake and Girdler, 1964). South of Latitude 24° N, a deep axial trough appears in the main trough.

The importance of conducting this study is related primarily to the study area as follows; 1) The area has a new urban communities and big cities with heavy populations, 2) The area is promising with many strategic and developmental projects, 3) its buildings don't follow the seismic design regulations although it is affected by many destructive earthquakes (e.g. 1982 Yeman earthquake), 4) its complicated structural and tectonic setting. So, it is necessary to assess its seismic hazard potentialities in terms of Peak Ground Acceleration (PGA) and the site response characteristics at big cities lie within this area to mitigate the direct impact of earthquakes on the human life and buildings within the area.

The previous studies showed that the Arabian plate subjected to the tectonic movements since Pliocene age, where great lateral movements started to move the continental blocks toward the north (40km) of the Arabian plate with relative to the African plate and formed narrow strait of Bab El-Mandeb (Abdel-Gawad, 1969). These movements continued to the northeastern direction along the Gulf of Aqaba (150 km) (Freund et al., 1970) in the Middle Miocene age. Left-Lateral movement (40 – 45 km) for the Miocene rocks in Sinai area and led to the formation of the axial trough of the Red Sea. The spreading rate was asymmetric during these movements along the Red Sea as indicated from the change in the width of the axial trough. As a result of these movements a more complicated structures were formed including major faults in the south of Saudi Arabia and causing many earthquakes. Depending on the geological, geophysical studies as well as the distribution of recent earthquakes in the Red Sea and comparison with the location of earthquakes in Tahoma and Arabian Shield, it is noticed that there is a possibility for the extension of some faults from offshore into the land especially between 16.3° – 17.4°N to the northeastern of Abha and it is considered that these faults are responsible for the western Abha earthquake 1408 H (5.2 magnitude). The northeastern faults were formed due the separation of Arabian plate from African plate in the northeastern direction. Based on the Heat Flow Density (HFD) studies (Makris, 1986 & 1989), the type of crust can be differentiated.

From the historical and instrumental earthquake studies (Al-Amri, 1994) it is noticed that most of earthquakes have occurred along the axial trough of the Red Sea. But there are four earthquakes in 1941 (mb=6.25), 1955 (mb=5.7), 1962 (ms=4.7) and 1982 (mb= 6, North Yemen) have occurred away from the axial trough of Red Sea (Langer et al., 1987). Some seismic hazard studies (Barazangi, 1981 and Thenhaus et al., 1986) carried out for the southern Red Sea based on

the probabilistic approach. Al-Amri (1995) divided the southern Red Sea into two main seismic source zones.

GEOLOGICAL SETTING OF THE AREA

The structural pattern of the eastern Arabian region (Powers et al., 1966) was set in Precambrian time with stabilization of the Arabo-Nubian shield. The igneous and metamorphic rocks constitute the main part of the Arabian Shield. The age of Arabian Shield ranges from 1000 to 450 my. This shield covers a vast surface area of the study area including southern Saudi Arabia and Yemen. The Arabian Shield rocks represent communities of many Arc Islands with some residuals of oceanic crust (Ophiolite) that gathered due to collision for 900 to 650 my. The thickness of crust is increased by magmatic activity (Brown et al., 1963). This shield is divided into intraoceanic island-Arc terrains (hijaz and Asir). These terrains are separated by suture zones of two types, island Arc-island Arc collisional sutures and island Arc – continental collisional sutures. Nabitah orogenic belt is of second type and is the longest and most prominent, dividing the exposed shield in the middle. The western sutures are NE trending while the eastern ones are N-S trending. These Arabian Shield rocks are overlaid by sedimentary rocks of Cambrian to recent (Fig. 2).

In Late Tertiary the great rift-fault systems of Africa and Red Sea also began to take on their present form, although movement on these faults may have started somewhat earlier. The Red Sea was developed by three tectonic movements led to formation of the southern part, northern part and Red Sea itself. The southern part the Red Sea is connected to the Gulf of Aden, which trends ENE-WSW, in Afar area where injected magma upward from the upper mantle and led to the formation of the regional joints in this part within 20 to 30 my.

SEISMIC HAZARD ASSESSMENT

Seismicity of the Area

The study area is affected by about 441 earthquakes with magnitude ranges from 2.4 to 8 during the period from 200 to 2005 A.D. This earthquake activity can be divided into two types;

Historical Seismicity (200 - 1964):

According to the research in the published compilations of historical earthquakes for the Middle East (Poirier & Taher, 1980; ElSinawi, 1983 & 1986; Ambraseys & Mellville, 1983; Ambraseys et al., 1994), the historical seismicity is of the swarm-type and mainly related to the volcanic eruptions along the western Arabia. There are about 78 earthquakes have occurred in the area of study in the period from 200 till 1900 (Fig.3).

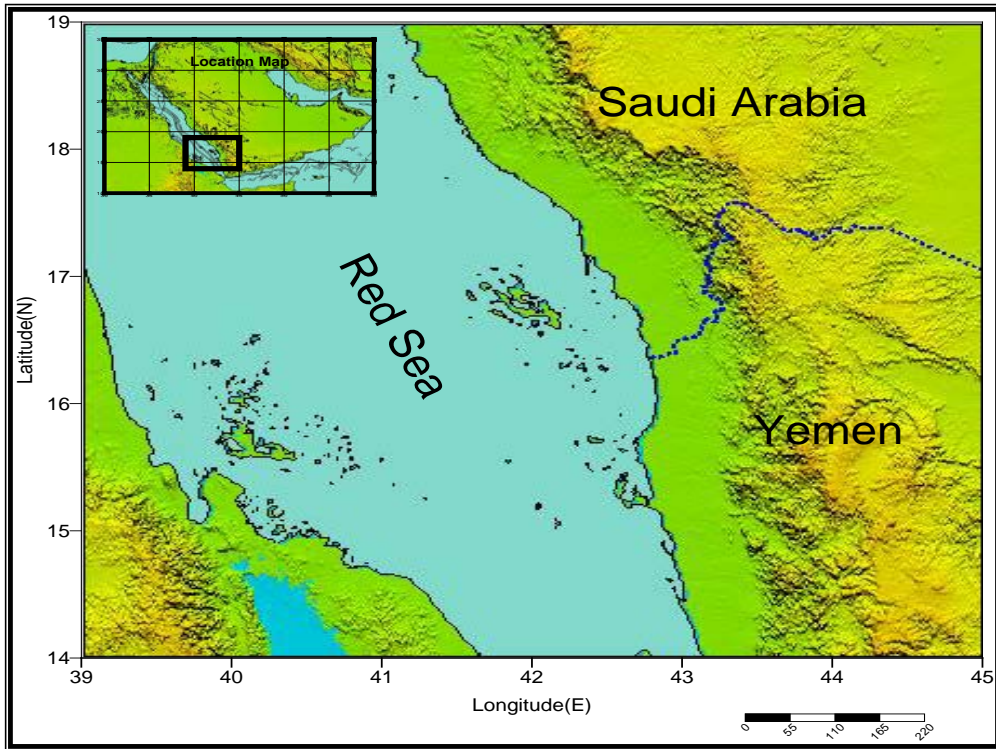


Fig. (1): Location and topographical features of the study area.

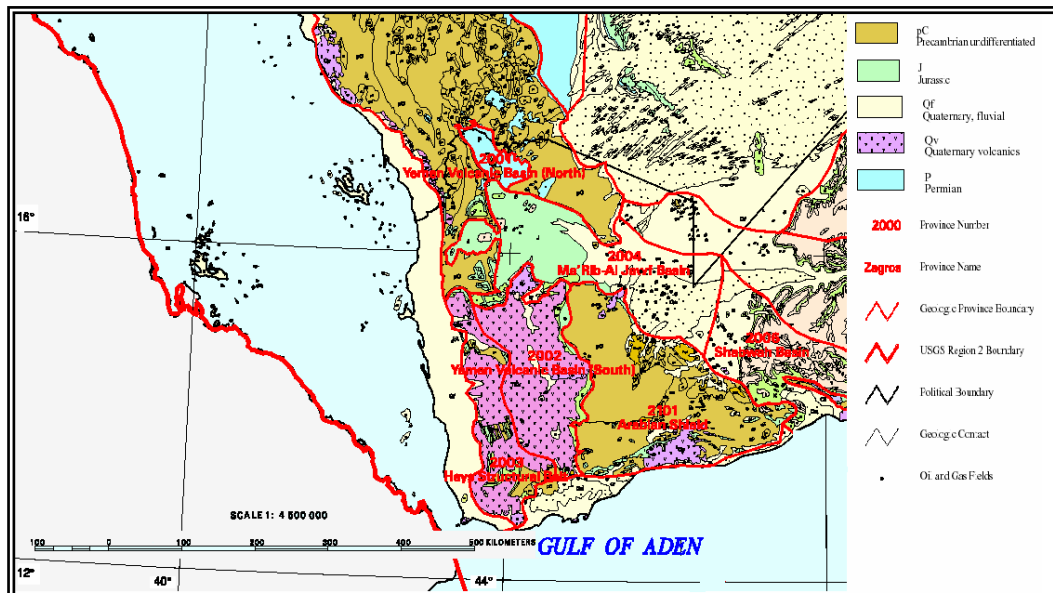


Fig. (2): Surface geological units of study area.

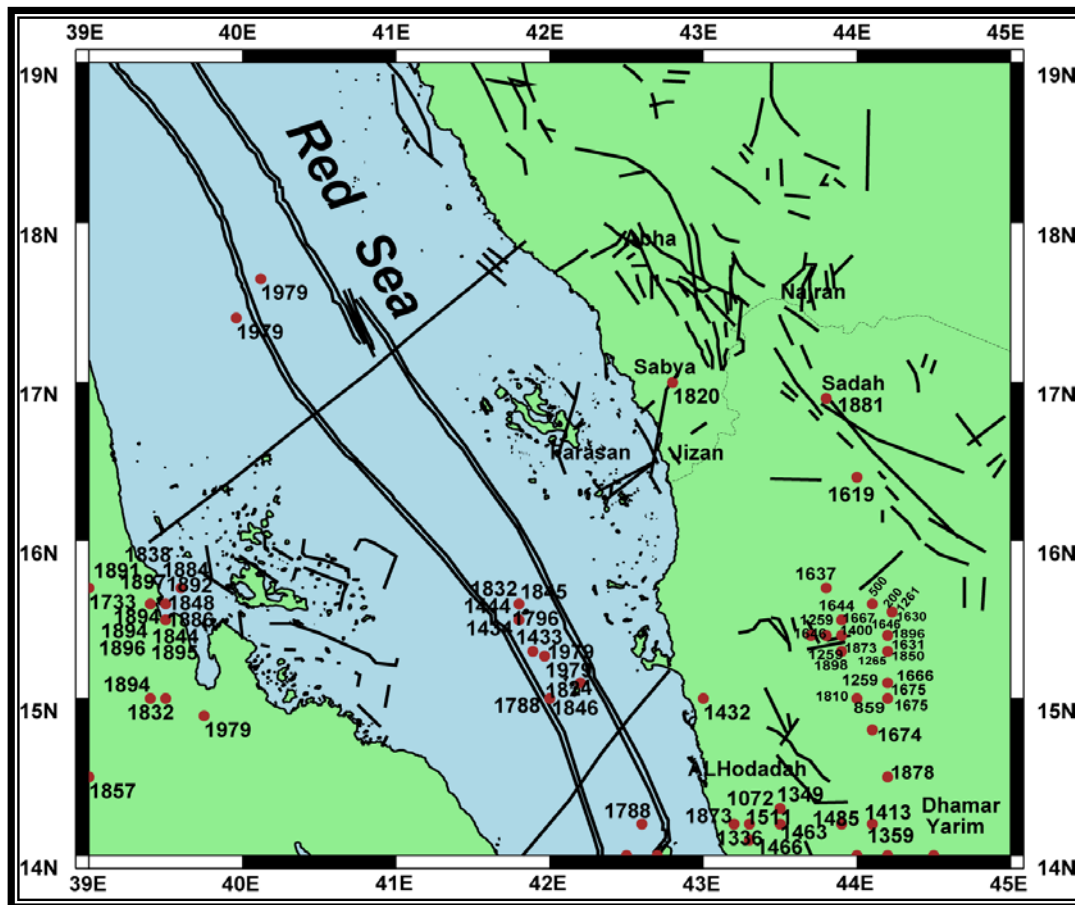


Fig. (3) Historical Seismicity within the area of study.

From this figure it is noticed that; 1) most of earthquakes are concentrated around Sanaa – Aden along the Red Sea and this due to the past distribution of population density in Arabia. 2) Some of the historical earthquakes have occurred on offshore and these earthquakes were felt on the land which reflects the continuation of marine tectonics into the land. There are about 22 earthquakes have occurred in the period from 1900 till 1964 with magnitude ranges between 4 and 6.3. 3) Most of historical earthquakes seem to correlate with the general tectonics of the region (El-Isa & Al-Shanti, 1989). A major characteristic of the epicenters is a NW alignment, parallel to the axis of the Red Sea where some instrumental earthquakes occur as well. A perpendicular alignment is also observed.

Instrumental Seismicity (1964 - 2005):

The instrumental earthquakes are collected from a number of seismological catalogues and bulletins including those of the International Seismological Centre (ISC) and the National Earthquake Information Service (NIES) and related publications of El-Isa and Al-Shanti, (1989), Al-Amri, (1994). It is found that about 438 earthquakes are occurred study area within the period 1964 – 2005 with magnitudes in the range $2 \leq m_b \leq 6.9$.

One hundred Forty-eight of these had a magnitude $M \geq 4$. While the rest these have a magnitude lower than 4 and are considered also in this study. The epicentral distribution of the instrumental seismicity of the study area (Fig. 4) shows the following characteristics; 1). The general distribution of earthquakes seems to correlate well with the major structures of the area. Many earthquakes are distributed within the spreading zone of the Red Sea. South of Sanaa a concentration of epicenters correlates well with a regional Tertiary and Quaternary volcanic plateau. 2). The instrumental earthquakes show a noticeable higher activity in the southern Red Sea and Middle of Red Sea compared with other areas. 3) The seismicity of this region is characterized by both mainshock- aftershock and swarm types of activity (El-Isa & Ah-Shanti, 1989). The swarm type may occur on strike-slip and normal faults and may or not may be of volcanic origin.

Seismic Source Zones

The definition of a seismic source zone is based - to large extent- on the interpretation of the geological, geophysical and seismological data. Thenhaus (1983) noted that the procedures used in delineating the seismic source zones are ill defined. Seismic zones delineation

is important not only for theoretical reasons (improvement of understanding the geodynamics of a region, etc.) but also for practical reasons.

The definition of seismic zones carried out in the present work depends on both of historical and instrumental earthquakes as well as the results of the previous geophysical and geological studies including the kind of seismic faulting (Papazachos et al., 1984), seismicity rate (a-value) (Papazachos, 1980), b values (Hatzidimitriou et al., 1985), major trends of geological zones (Mountrakis et al., 1983), and the fault plane solutions of the major earthquakes (i.e. strike, dip and stress axes). A seismic zone is a configuration within which it is assumed that an earthquake recurrence process is considered to be spatially and temporally homogeneous. The delineation of the seismotectonic sources is usually represents the major part of any seismic hazard analysis.

According to this study the seismic activities are concentrated in four narrow belts (Fig. 5) and these belts are: -

- 1- Sana'a – Dhamar (southern Arabian Shield) zone.
- 2- Southern Red Sea zone.
- 3- Northern Yemen zone.
- 4- Middle of Red Sea zone.

1- Sana'a-Dhamar (southern Arabian Shield) zone.

This zone includes the Sadah active fault which characterized by its higher seismic activity. The strongest earthquake that occurred in this zone is December 12, 1982 earthquake ($M_s = 6.1$). The fault plane solution of this earthquake indicates normal fault. There are many destructive earthquakes and swarms have occurred in this zone (Ambraseys, 1988 and Al-Amri 1998).

2- Southern Red Sea zone.

This zone includes many earthquakes occurred in the southern Red Sea and north of Gulf of Aden. This zone characterized by high rate of seismic slip and this due to presence of this zone near to the triple junction point between east African Rift system, Gulf of Aden and the Red Sea. The Heat Flow studies also indicate that there is a high rate of Heat Flow Density (HFD) due to igneous magmatic intrusions in this seismic zone. From the fault plane solution of earthquakes in this zone indicate that about 75% of earthquakes were occurred along the normal faults (Dhamar area) while, 25 % were strike-slip fault (Zabid area).

3- Northern Yemen zone.

This zone includes the earthquakes located in the axial trough and the main trough of the Red Sea. It is noticed that there are two types of faults prominent in the Red Sea; the Red Sea Axial Rift Spreading System of faults and the other is the transform faults. It is

concluded that the seismic activity in this zone is related to the transform faults accompanied with the tensional movements. But the seismic activity of this zone in the mainland is related to isolated (not connected) tectonic structures where the strongest earthquake in this zone was in January 11, 1941 ($M_s = 6.2$).

4- Middle of Red Sea zone.

This zone includes the seismic activity extends along the axial trough of the Red Sea which is characterized by high rate of Heat Flow Density and Bouguer anomalies. The seismic activity in this zone is related to the opening mechanism of the Red Sea (Al-Amri 1994 and 1998). From the earthquakes that occurred in this zone, the 1967 earthquake ($M_b = 6.7$) with strike-slip fault (Fairhead, 1968; Mckenzie et al., 1970; Fairhead and Girdler 1970 and 1972).

Determination of a- & b-values

The seismicity of an area can be defined as a function of the size of the earthquakes (magnitude, seismic moment, etc.) and of the frequency of the occurrence of these earthquakes. The basic law, which is applied for determination of the seismicity of an area, is the well-known frequency-magnitude statistical relation (Gutenberg and Richter, 1965). But there are some conditions to apply this relation for the determination of the seismicity in an area; the area must be seismotectonically homogeneous (constant value of the b parameter of the frequency-magnitude relation, etc.). For this reason, it is necessary to separate the whole study region into seismic zones, which should be as much as possible seismotectonically homogeneous.

For each seismic source, the magnitude distribution was taken to be exponential and of the form given by the Richter relation of occurrence frequencies:

$$\log N = a - bM \quad (1)$$

Where N: is the number of earthquakes of magnitude $\geq M$, a & b are constants, and the logarithms are taken to the base 10. The value of "a" depends on the period of observation, the size of the region considered and the level of seismic activity. Whereas "b" depends on the ratio of the number of earthquakes in low – to high magnitude groups. The values of "b" have been reported to differ from 0.5 to 1.5 approximately and mostly between 0.7 and 1.0 (Isacks and Oliver, 1964). Nevertheless, many researchers believe that "b" varies from region to region and also varies with the focal depth. Besides, its value depends on the stress conditions and on the heterogeneity of the rock volume generating the earthquakes (Mogi, 1962, and Karnik, 1969).

In the study area it is found that, some of the seismic source zones have a small number of earthquakes and also preclude direct assessment of a-values for individual zones. Hence, a regional rate of earthquake activity was calculated for whole area of

study by summing all the activity in all the seismic source zones. This regional rate of activity was then apportioned among the individual source zones so that the amount of activity applied to any one zone is in rough proportion to the number of earthquake events occurring in that zone.

The magnitude–Frequency relations for different tectonic units (and sometimes subunits) are calculated (Fig. 6 and table 1) assuming a linear relation between $\log N$ and M .

Table (1): Parameters of defined seismic source zones.

Seismic zone	N	a-value	b-value
1	48	4.233	1.061
2	87	4.238	0.887
3	51	3.4	0.591
4	77	3.2	0.572

These cumulative recurrence curves confirm the existence of differing values of "b". They also demonstrate that:

- The zones of moderate seismic activity (zones 1 and 2) are characterized by moderate slopes (0.88 -1.06) which correlate with tensional forces under these zones. While the lowest slopes (lowest "b" ranging from 0.57 to 0.59) correspond to the zones of lesser seismic activity (zones 3 and 4) and this may also indicate the scarcity of strong earthquakes in this tectonic unit.
- It is possible to correlate between the slopes "b" and the stage of tectonic development for the tectonic province of southern Red Sea, that the "b" values increase in the direction of the opening.

Determination of the Maximum Expected Magnitude ($M_{w \max}$.)

This step requires a determination of the maximum earthquake for each of the identified seismotectonic sources. In the deterministic analyses, it is more common to define the maximum earthquake as a maximum credible earthquake. This earthquake is based upon an evaluation of those processes, which are reasonably expected to be associated with an earthquake source. Therefore, the maximum expectable or maximum probable earthquake is sometimes used in place of maximum credible (Reiter, 1991). Another kind of maximum earthquake is the maximum historic earthquake. The maximum historic earthquake often defines the lower bounds of maximum credible events. If an earthquake struck in the past, then it is certainly credible that it may strike in the future. The instrumental and historical records of earthquake activity, which are often too short to reflect the full potential of faults, may be extended back thousands of years or more to obtain estimates of maximum earthquake occurrence during the past and present tectonic regimes.

Some of the regression relationships are reviewed regarding certain issues on their use as follows;

- 1- Source ruptures length. It is the most frequently employed relationship. Papazachos et al., (2004) defined an empirical relationship between the seismic moment and the rupture length of the fault as:

$$\log(L) = 0.50M_w - 1.86 \quad (2)$$

Where M_w is the moment magnitude and L is the rupture length. To determine the maximum earthquake size that could be generated from the fault, the length of the fault or fault zone is measured and assume that some fixed maximum fraction would rupture in a single earthquake. Along San Andreas this fraction is one-third to two-fifth of the fault total length. Here, this portion is taken to be two-fifth of the total fault length to ensure the conservatism of the results.

Another approach has been adopted to use the historical record by increasing the maximum historical earthquake by arbitrary certain amount and assumes that this value is the appropriate maximum earthquake. This increasing increment is usually taken to be 0.5. This technique is used for some zones for which the fault information is absent. The source rupture length and the maximum historic earthquake on the fault with some increment above it are used to determine the maximum earthquake at each zone within the area of study (table 2).

Table (2): Maximum expected magnitude for each zone.

Zone	M_{\max}	Lat (N)	Lon (E)
Z1	7.5	15.00	44.00
Z2	7.2	14.2	42.6
Z3	8.5	15.2	40.5
Z4	6.1	17.2	40.58

SIMULATION OF GROUND MOTION USING STOCHASTIC METHOD

The stochastic simulation method (Boore, 2003) is applied in the area under study in order to predict the ground motion of earthquakes and for the assessment of seismic hazard in terms of Peak Ground Acceleration (PGA) and site response spectra.

Outlines of the method

The ground motion prediction is based upon the stochastic model, in which ground motion is modeled as band-limited Gaussian noise; the method assumes evenly distributed radiated energy over a specified duration. The method begins with the specification of the Fourier amplitude spectrum of ground acceleration as a function of seismic moment and distance, $Y(M_o, R, f)$, represented by:

$$Y(M_o, R, f) = E(M_o, f) P(R, f) G(f) I(f) \quad (3)$$

where $E(M_o, f)$ is the earthquake source spectrum for a specific seismic moment (i.e., Fourier spectrum of the ground acceleration at a distance of 1 km) and $P(R, f)$ is the path effect that models the geometric spreading

and the anelastic attenuation of the spectrum as a function of hypocentral distance (R) and frequency (f), G(f) is the site effect and I(f) is a filter used to shape the spectrum to correspond to the particular ground motion measure of interest. The time domain implementation of the stochastic method used in this study begins with the generation of a windowed acceleration time series comprised of random Gaussian noise with zero mean amplitude and variance chosen to give unit spectral amplitude on the average. The duration of the window is chosen as a function of magnitude and distance. The spectrum of the windowed time series is multiplied by the desired spectrum [Y(Mo, R, f) from equation (3)]. The filtered spectrum is then transformed back into the time domain to yield a simulated record for that magnitude and distance.

Input Parameters

These include all the terms of equation (3) and the duration of motion. The simulations will apply to the random horizontal component of the shear phase of ground motion.

i. The source parameters [E (Mo, f)]

The earthquake source spectrum E (Mo, f) for the horizontal component of ground motion is given by the following:

$$E(Mo, f) = C(2\pi f)^2 Mo S(Mo, f) \tag{4}$$

where S(Mo, f) is the displacement source spectrum and C is a constant. $C = R_s VF / (4\pi \rho \beta^3 R)$, with R = 1km, R_s = average shear wave radiation pattern (= 0.55), F = free surface effect (= 2.0), V = partition onto two horizontal components (= 0.71), ρ = the density at the source and β is the shear wave velocity at the source. In this study the value of stress drop ($\Delta\sigma$) was taken as 30 bar (the average value) (table 3).

Table (3): Source parameters of the effective earthquakes in each zone.

ZONE	$\Delta\sigma$	M_b (MAX)	Depth (km)	Density (ρ)	V_P	Shear wave (β)
Z1	30	7.5	9.7	2.85	6.8	3.95
Z2	30	7.2	45	3.2	7.9	4.59
Z3	30	8.5	41	3.2	7.9	4.59
Z4	30	6.1	32.1	3.2	7.9	4.59

Where, $\Delta\sigma$ is the stress drop (in bar) and β calculated using Al-Amri and Al-Khalifa, (2004) relation.

ii. The path (attenuation) effect (P(R,f), duration)

The path effect or the attenuation parameters that affect the spectrum of motion at a particular site are classified into the geometrical spreading and the anelastic attenuation as represented by the quality factor Q (f).

In this study, the three segments geometrical spreading operator of Atkinson and Boore (1995) is used. R^{-1} geometrical spreading is assumed for distance less than 70 km and $R^{0.0}$ for distances from 70 km to 130 km and $R^{0.5}$ for greater distances. Although the Fourier spectrum of ground motion is not dependent on the duration, it is a very important parameter for peak motions decrease with increasing duration. The duration is a function of the path, as well as the source:

$$T = T_o + bR \tag{5}$$

where, T_o is the source duration and bR represents the path dependent term that accounts for dispersion. Following Hanks and McGuire (1981), the source duration is related to the corner frequency by:

$$T_o = f_c^{-1} \tag{6}$$

Empirical observations and theoretical simulations suggest that the path-dependent part of the duration can be represented by a connected series of straight-line segments with different slopes. The function of Atkinson and Boore (1995) is used where the path duration is modeled as trilinear, using the transition distances 70 and 130 km for consistency with the attenuation model. The slope is 0.16 for the distance ranges between 10 and 70 km, -0.03 for the distance ranges between 70 and 130 km and 0.04 for the distance ranges from 130 to 1000 km. The slope is assumed to zero for distances less than 10 km.

It is difficult to study the attenuation effect in the western Arabia and this due to the absence of strong motion records and its complicated crustal structure. The propagation of seismic waves from the Arabian Shield into coastal areas is accompanied with low attenuation like Shield zones allover the world (Thenhaus et al., 1986). Hence one of the empirical attenuation relations for other regions can be selected but these regions should be similar in both of crustal structure and seismotectonic environment with the study area. So, the attenuation relations of the eastern coast of the United States (Nuttli and Herrmann, 1984) were used due to the similarity of its geological characteristics with the western coast of the Arabian Peninsula and these relations are as follows;

$$\begin{aligned} \text{Log } A_h = & 0.57 + 0.50 m_b - 0.83 \log (R^2 + h^2)^{1/2} \\ & - 0.00069R \end{aligned} \tag{7}$$

$$\begin{aligned} \text{Log } V_h = & -3.60 + 1.00 m_b - 0.83 \log (R^2 + h^2)^{1/2} \\ & - 0.00033R \end{aligned} \tag{8}$$

Where R is the hypocetral distance, h is the focal depth of earthquakes in the area of study, A_h is the horizontal Peak ground Acceleration and V_h is horizontal peak ground velocity. These equations were used to study the behavior of waves in the upper crust and to get the attenuation curves of PGA within the study area (Fig. 7). It is concluded that the Arabian Shield has a low attenuation values for selected magnitudes when compared with other side of the Red Sea.

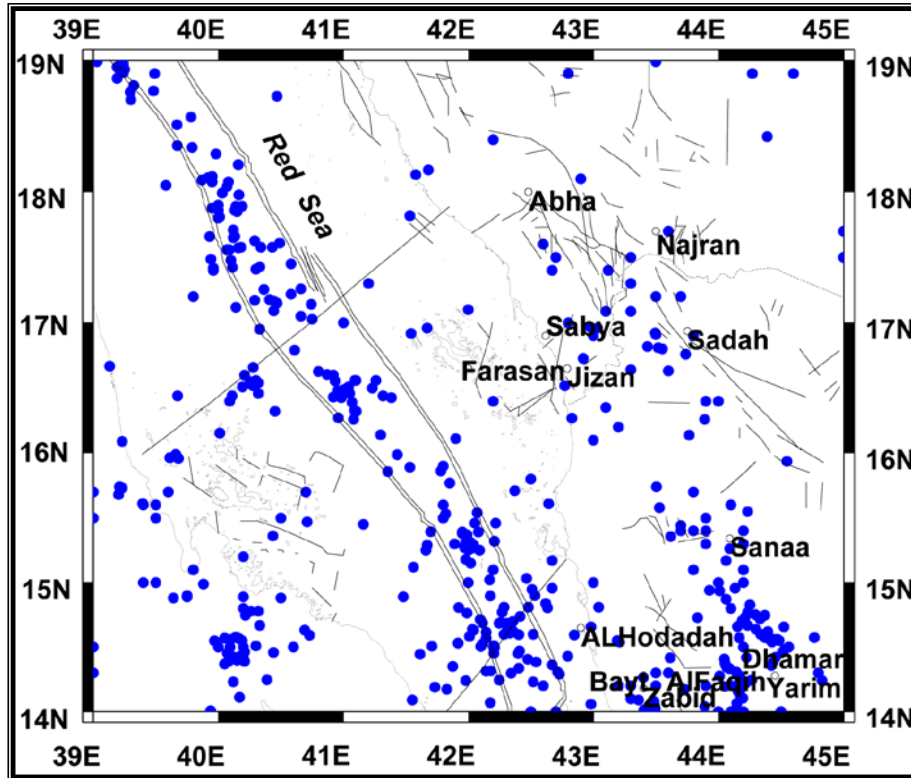


Fig. (4): Distribution of instrumental earthquakes within the area.

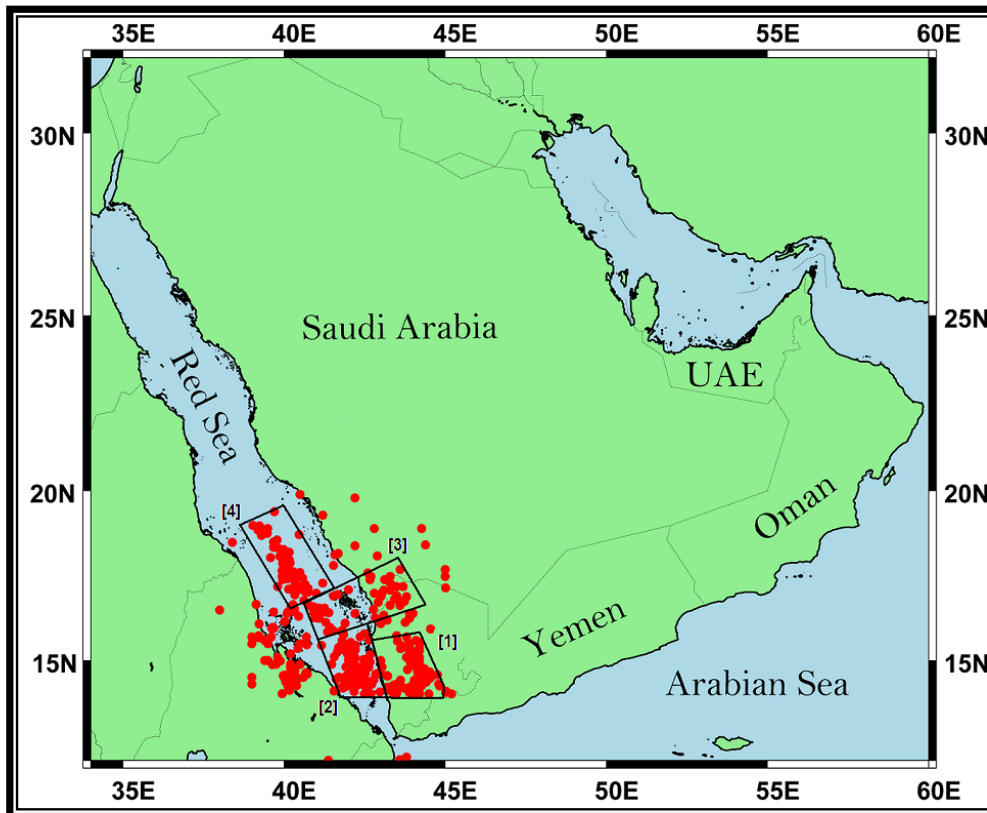


Fig. (5): Delineated seismic source zones.

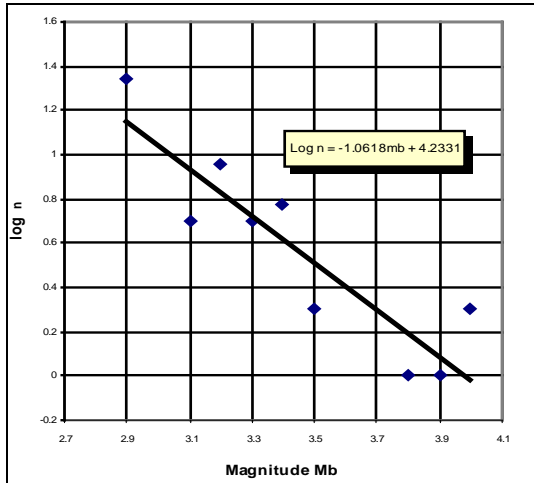


Fig. (6a): Gutenberg-Richter relation for zone 1.

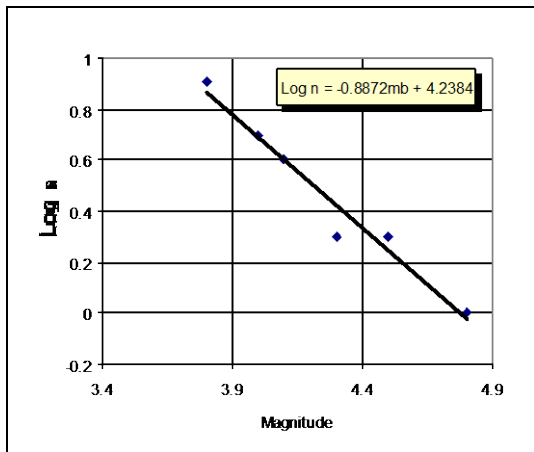
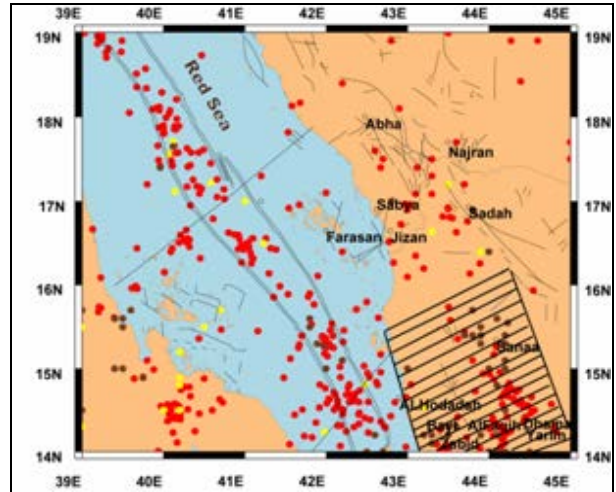


Fig. (6b): Gutenberg-Richter relation for zone 2.

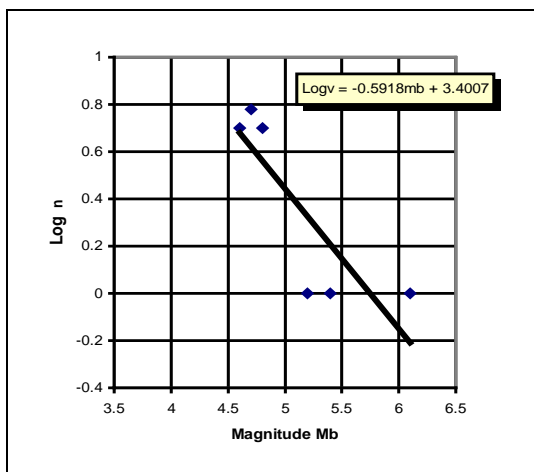
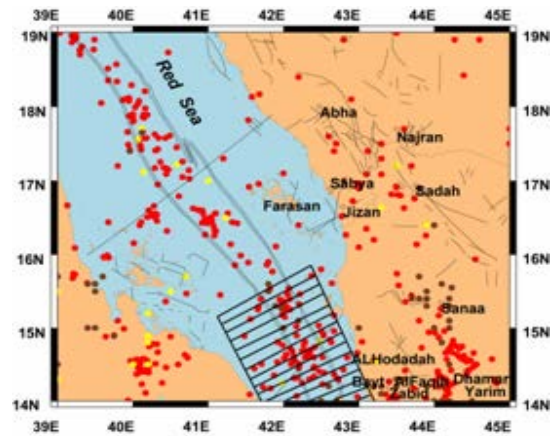
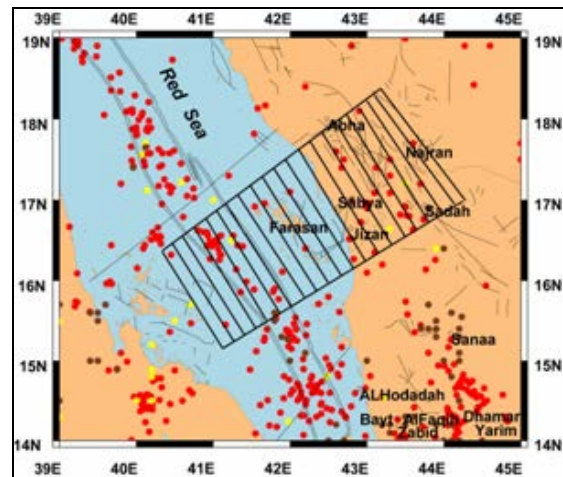


Fig. (6c): Gutenberg-Richter relation for zone 3.



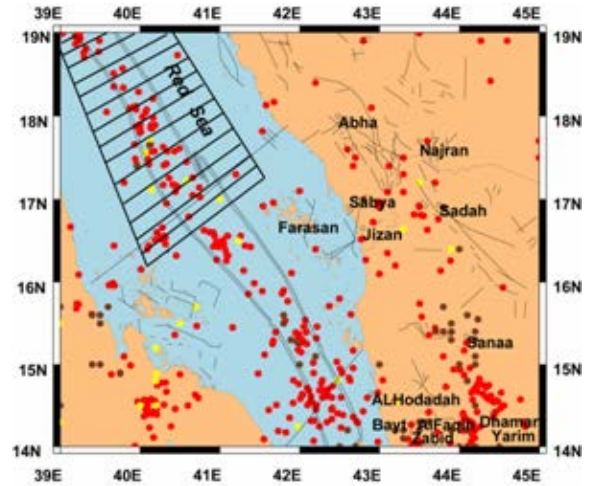
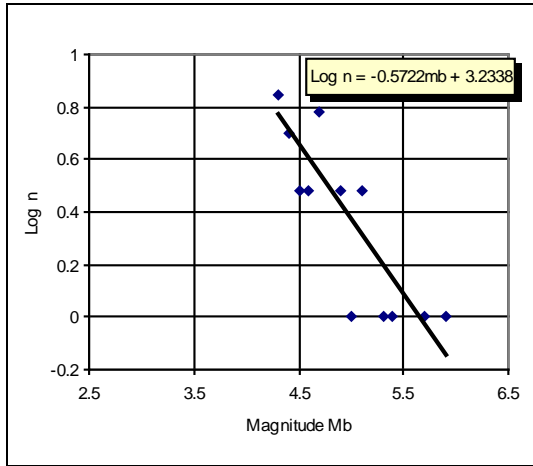


Fig. (6d): Gutenberg-Richter relation for zone 4.

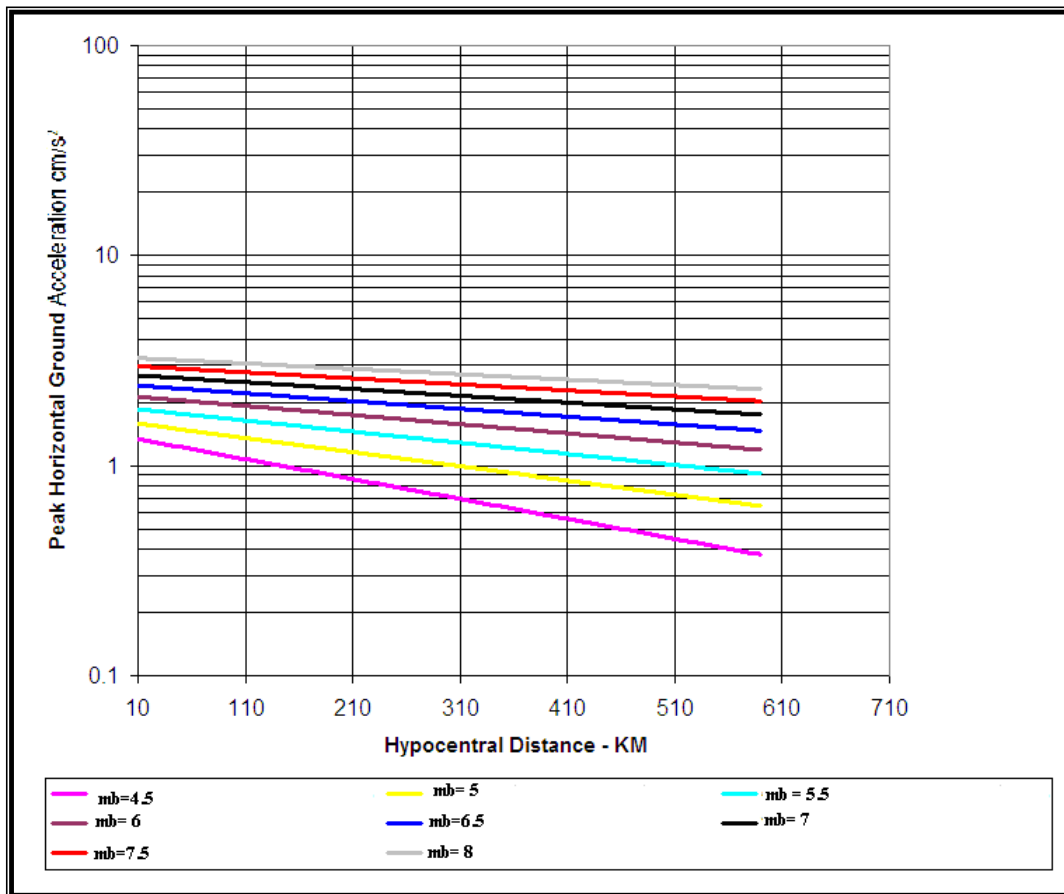


Fig. (7): Attenuation curves for Peak Ground Acceleration within the area.

iii. Local site effect (G(f))

The site properties (effect) that control the change of the seismic ground motion amplitudes at the earth's surface are amplification and diminution (Boore, 2002 & 2003) as follows:

$$G(f) = A(f) + D(f) \tag{9}$$

Velocity and density model is converted into site amplification A(f), using the square root of the impedance ratio between the source and the surface. For polarized shear waves, the impedance is defined as the product of the shear wave velocity, density and the cosine of the angle of incidence. The amplification is relative to the surface motion that would exist if the material were replaced with uniform material whose velocity and density equals those at the source. Several relationships between surface geology and local site amplification have deduced (Table 4).

Table (4) Relation between relative amplification and local geology

Reference	Amplification	Geological unit
El-Difrawy,1996	6.5	Quaternary and fluvial
Midorikawa, 1987	1.0	Pre-Cambrian undifferentiated
Midorikawa, 1987	1.0	Cretaceous Volcanic Rocks
Midorikawa, 1987	1.0	Jurassic

The diminution operator D(f) of equation (9) accounts for the path independent loss of high frequency in the ground motion. For this high-cut filter, (Boore, 1983 and 1996) was used:

$$D(f) = [1 + (f/f_{max})^8]^{-0.5} \tag{10}$$

Where f_{max} is the high-frequency cutoff proposed by Hanks (1982), for a limited data set, a value of $f_{max} = 20$ Hz is assumed, due to the absence of strong motion records in Egypt suitable for such determination and to avoid the vital frequencies from engineering sense (up to 10 Hz).

Data Treatment and Results

The area of interest was divided into grid of points every 0.5 degree in latitudes and longitudes. The SMSIM-Program was running at each point of this grid for each one of the seismic source zone. So, there are different values of PGA at each point of the grid. The maximum expected magnitude of seismic sources that affect the area was used to estimate the ground motion resulted from each zone. Then the maximum PGA value at each point was taken as the representative value at that point and then these values are contoured into maps of PGA at the bedrock and ground surface (Figs. 8&9).

The maximum peak ground acceleration value at bedrock is resulted also from southern Red Sea seismic

source and is found to be 41.1 cm/sec². While the lowest value of PGA locates in the northeastern part of the area which may relate to the scarcity of earthquake data in this part. The results of this study are compared with the previous studies (Table 5). These studies were based on the probabilistic approach for seismic hazard assessment but the present study depends on the stochastic approach which takes all the contribution parameters of the seismic source, attenuation relation due to path and the local site effects into consideration for hazard assessment so, some results are quite different from the previous studies (Thenhaus et al., 1986; Al-Haddad et al., 1994 and Al-Amri, 1995).

While the maximum PGA value at the ground surface reflects the amplification effect of the sedimentary soils at Zabid (32cm/sec²), Al-Hodadah (29cm/sec²), Farasan (14 cm/sec²) and Jizan (11.07 cm/sec²) cities but there is no amplification at other cities. This figure shows that the values of PGA along the Red Sea coast zone are higher than that on the land which reflects the amplification effect of the soft soil along the coast on the PGA values. It is found that the maximum PGA value at the surface is 72.15 cm/sec² and resulted also from the southern Red Sea source zone. This indicates that the southern Red Sea area has a great effect on the whole study area.

RESPONSE SPECTRA

Response spectra are defined on the basis of the response of single degree of freedom damped oscillator to the earthquake acceleration. The response spectra of an accelerogram serve the dual function characterizing the ground motion as a function of frequency and provide a tool for determining earthquake resistant design criteria. The response spectra are calculated for four selected damping values at 1%, 3%, 5% and 10 % of the critical damping for different rock units (Figs. 10 to 12). From figure (10), it is noticed that the predominant period is 0.1 sec. at Quaternary rocks of Sanaa city. The spectral acceleration values are 120 cm/sec², 76 cm/sec², 62 cm/sec² and 46 cm/sec² at damping ratios 1%, 3%, 5% and 10% of critical damping respectively. Also, it is noticed that the spectral curves are attenuated rapidly which reflects the rapidly changes in the behavior of Quaternary sediments under the horizontal forces of earthquakes. Figure (11) shows the maximum spectral acceleration value for Permian rocks (Mesozoic time) at Dhamar city is 34 cm/sec² at damping ratio 1%, 22 cm/sec² at damping ratio 3 %, 18 cm/sec² at damping ratio 5 % and 14 cm/sec² at damping ratio 10 % of critical damping. The natural period at this site is 0.15 sec. Figure (12) reflects that the predominant period for Pre-Cambrian rocks at Abha city is 0.25 sec. While the spectral acceleration values for damping ratios 1%, 3%, 5% and 10% are 1.25 cm/sec², 0.89 cm/sec², 0.75 cm/sec² and 0.55 cm/sec² respectively. Also, it is noticed that the spectral curves are broad and attenuated slowly.

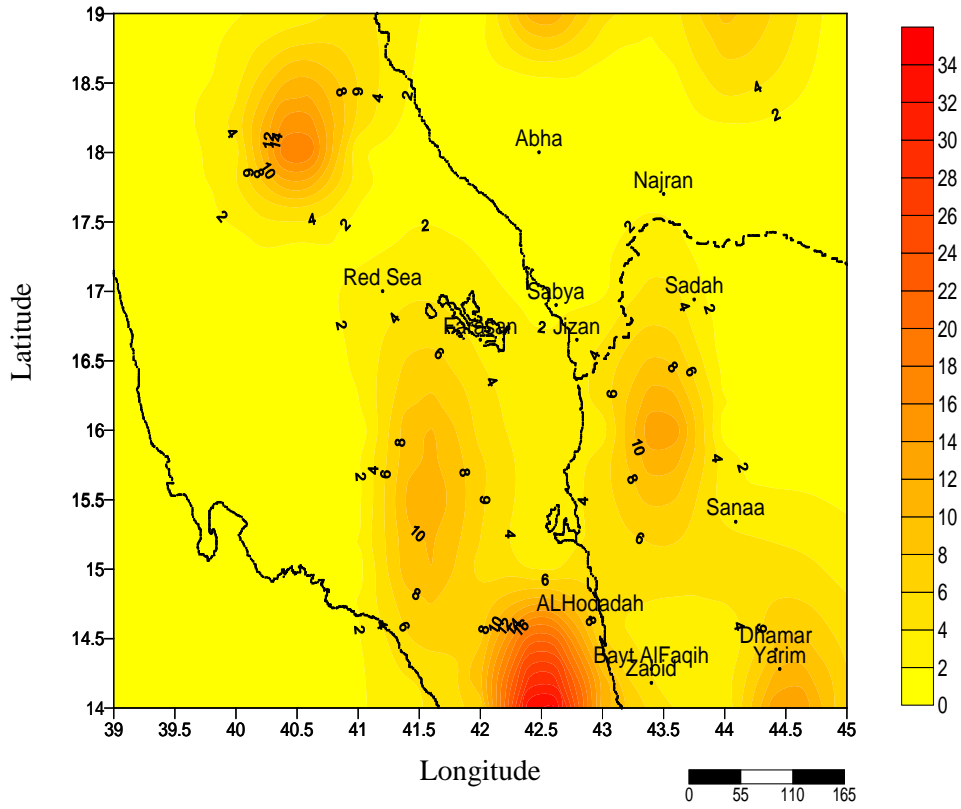


Fig. (8): Contour map for values PGA (cm/sec^2) on the bedrock.

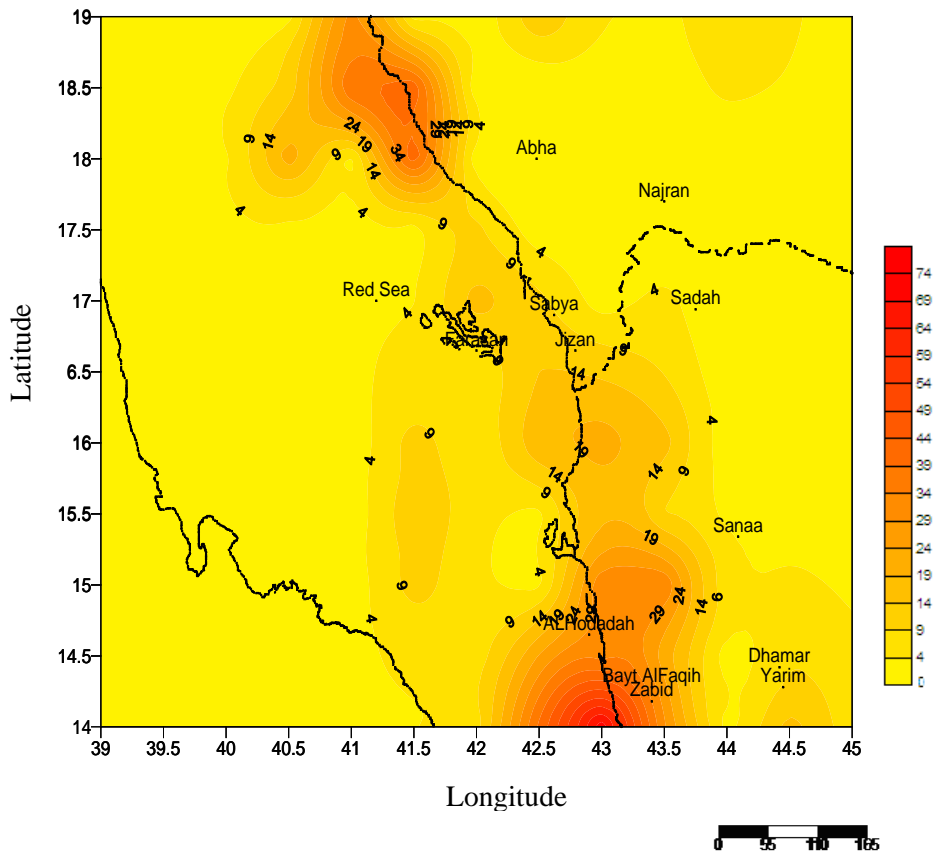


Fig. (9): Contour map for values PGA (cm/sec^2) on the ground surface.

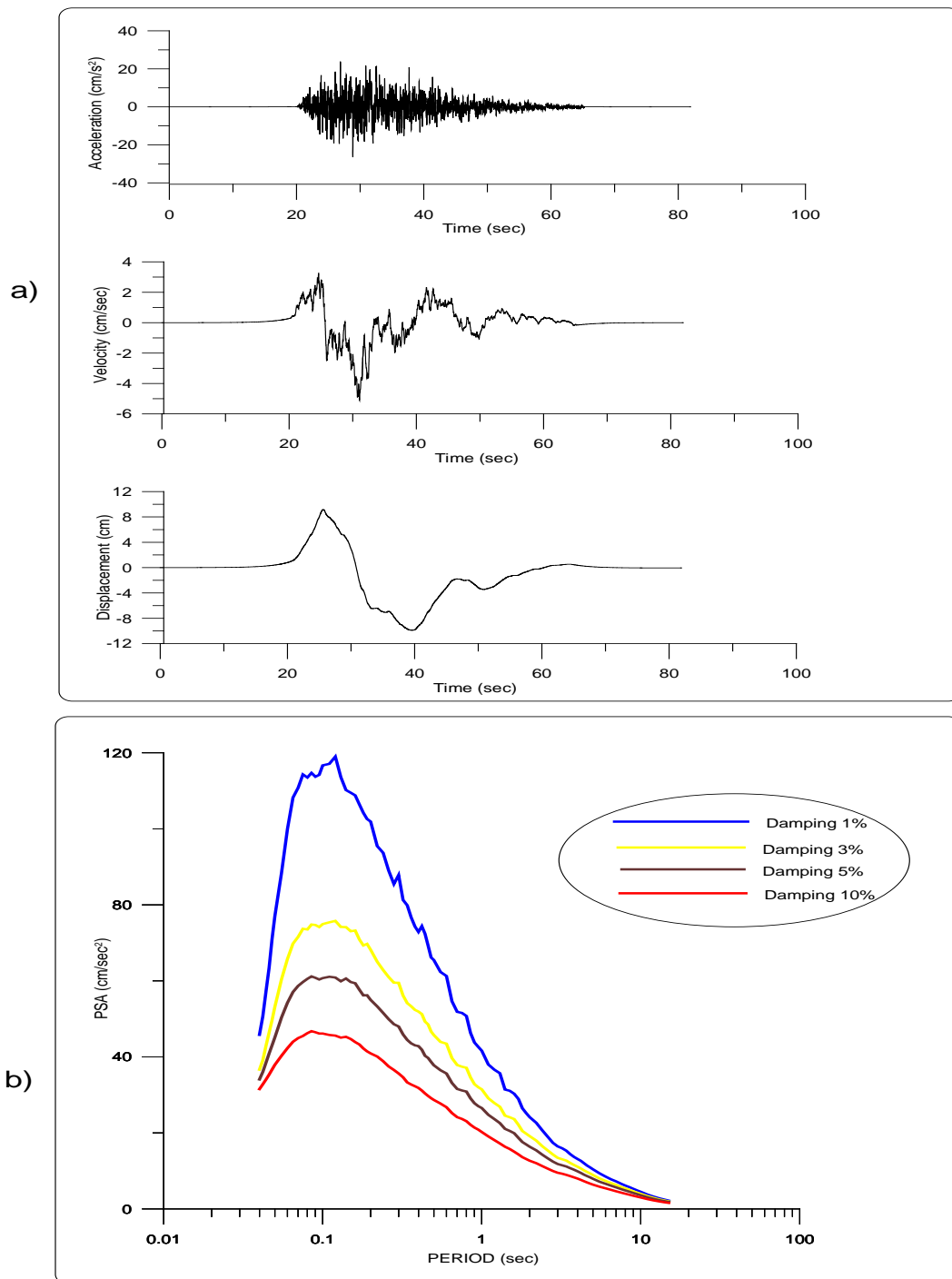


Fig. (10): a) Simulated time history of PGA, velocity and displacement at Sanaa area in Quaternary rocks and b) the response spectra at Sanaa with maximum PGA resulted in zone 1.

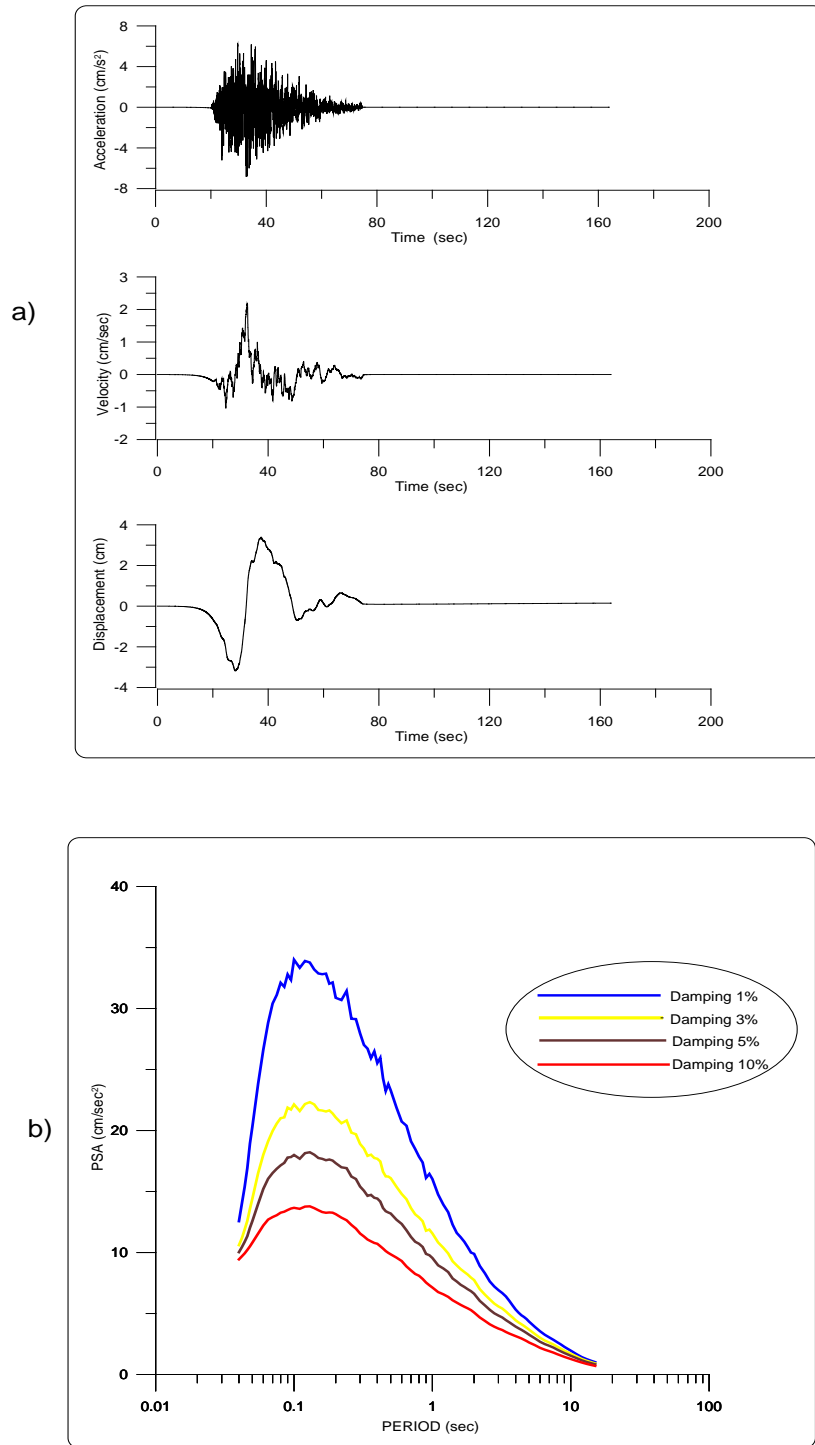


Fig. (11): a) Simulated time history of PGA, velocity and displacement at Dhamar area in Permian rocks and b) the response spectra at Dhamar with maximum PGA resulted in zone 1.

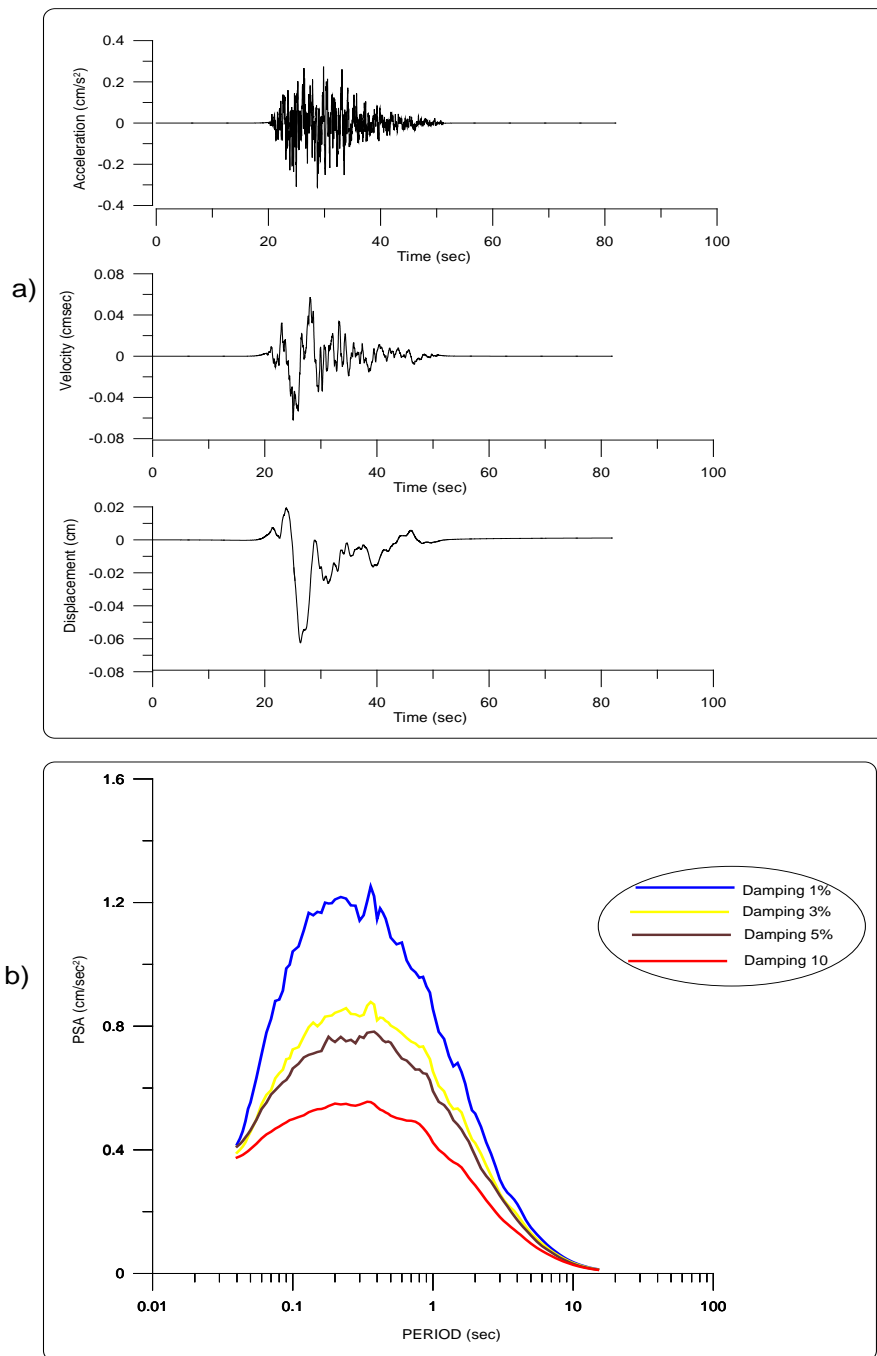


Fig. (12): a) Simulated time history of PGA, velocity and displacement at Abha area in Pre-Cambrian rocks and b) the response spectra at Abha with maximum PGA resulted in zone 4.

Table (5): The PGA values from the present study and previous studies.

City	Thenhaus et al., 1986 cm/sec ²	Al-Haddad et al., 1994 cm/sec ²	Al-Amri 1995 cm/sec ²	Current study cm/sec ²	
				Bed-rock	Ground surface
Abha	10	15	17	10	10
Jizan	20	20	20	2.16	11.07
Sadah	21	10	12	8	9
Southern Red Sea	40	20	20	41.1	72.12
Najran	10	10	12	1.5	3
Sanaa	23	17	20	10	20
AlHodadah	20	**	**	6	29
Dhamar	22	20	**	12	12
Farasan	15	20	20	3.9	14
Zabid	21.5	**	**	5	32

Where "**" this city not included in the previous study.

From these figures it is concluded that the values of the predominant period are varies greatly from one city to another depending on the type of underlying rocks or sediments. Also the maximum values of spectral acceleration are quite different for the area of study depending on many factors concerning with the seismic sources, path and local site characteristics. So, it is recommended that the detailed studies for the spectral accelerations and site response are necessary needed at each city and the results should take into consideration in the design of strategic buildings and developmental projects at each site.

CONCLUSIONS

The presence of the economic and heavy populated cities close to the earthquake belts of the Red Sea and southern Arabian Shield and due to the scarcity of strong earthquakes lead to increasing the seismic hazard potentialities for strategic buildings (e.g. dams, power plants) within these cities. So, this study depends on the available geological, geophysical and seismological data to assess the seismic hazard for the area. The area characterized by complicated geological structures due to the tectonic movements and volcanic eruptions accompanied with the Red Sea and later. This is indicated in the presence of various topographic features in Saudi Arabia and the Northern Yemen. From the distribution of both historical (200–1964) and instrumental (1964-2005) earthquakes, it is noticed that there are more than five hundreds of earthquakes have occurred in the area. Their magnitudes range from $2 \leq M \leq 8.0$. Most of earthquakes are epicentred along the transform faults of the southern Red Sea and southern Arabian Shield. The seismological catalogue is completed for earthquakes with magnitude less than 3 from 2001. About 218 earthquakes have relocated using more recent crustal structure models to enhance their

location. Depending on these data there are four seismic source zones have defined for the area and these are; Sanaa-Dhamar zone; Southern Red Sea zone; Northern Yemen and Middle of Red Sea source zone.

From the recurrence study of earthquakes, it is found that the b value for the southern part of Arabian Shield is relatively high (1.06) compared with b values in the southern Red Sea ($b= 0.57-0.88$) which reflects the heterogeneity of the crust. Due to the separation of Arabian plate from the African one in the northeastern direction, the earthquakes that occurred along the Red Sea are of normal fault type from the location of their epicenters on the axial trough. On the other hand, the presence of transform faults bisected the Red Sea with NE-SW directions confirm the presence of some earthquakes with transform focal mechanism. The focal mechanisms of the recent earthquakes confirm that most of earthquakes in the southern Red Sea represent the strike-slip movements trending NE-SW. While the earthquakes on the land in the southern Arabian Shield occurred as a result of the vertical movement trending NW parallel to the axis of the Red Sea.

The seismic hazard assessment for the area in terms of Peak Ground Acceleration (PGA) time history and the calculation of response spectra was done using stochastic method. The results show that the value of PGA is different from one city to another one. PGA value for the bedrock at Yarim and Dhamar cities is about 12 cm/sec^2 , 6 cm/sec^2 at Al-Hodadah, 5 cm/sec^2 at Zabid, 3.9 cm/sec^2 at Farasan, 1.5 cm/sec^2 at Najran, 8 cm/sec^2 at Sadah, 2.16 cm/sec^2 at Jizan and 0.67 cm/sec^2 at Abha city. The values of PGA is affected by the local soil sediments on the ground surface where PGA value is 32 cm/sec^2 , 29 cm/sec^2 , 14 cm/sec^2 , 11.7 cm/sec^2 at Zabid, Al-Hodadah, Farasan, and Jizan respectively. There is no effect at the other cities due to their location on the basement rocks. While Abha city

can be affected the coastal plain of the Red Sea where the value of PGA is about 39 cm/ sec² due to the amplification effect of soft sediments of soil.

The seismic hazard potentialities increase in the southwest of Arabian Shield close to Zabid area due to the amplification of soft soil sediments. Also the hazard potentialities for the southern Red Sea are relatively high but the presence of the oceanic crust and salt structures may attenuate the seismic waves.

Response spectra for different rock units at the big cities within the area were calculated with 1%, 3%, 5% and 10 % of critical damping. The results show that the highest value of PGA simulated at Sanaa and Al-Hodadah is 120 cm/ sec² with 1% of critical damping. It is noticed that the amplification of Quaternary rocks should be taken into consideration in the design of strategic projects and buildings.

ACKNOLEDGMENTS

The authors would like to express their thanks and deep gratitude to all staff members of the earthquake Research Center, King Saud University, and especially Dr. Naser Al-Arifi for their kind helps and supporting with the earthquake data and scientific reports about the area. Also, the authors are indebted too much for all colleagues in the Research Institute of Astronomy & Geophysics, King AbdulAziz City for Science & Technology, represented by Prof. Dr. Tarek Alkhalifah, the general supervisor of the Institute, for their valuable support with data, suggestions and useful discussions during preparing this study.

REFERENCES

- Abdel-Gawad, M., 1969.** New evidence of transcurrent movements in the Red Sea area and Petroleum implications, *Am. Assoc. Petrol. Geol. Bull.*, 53, 7, 1466-1479.
- AL-Amri A. M., 1994.** Seismicity of the south-western region of the Arabian Shield and southern Red Sea, Department of Geology, King Saud University, *Journal of African Earth Sciences*, Vol. 19, No 1, pp. 17-25.
- Al-Amri, A. M., 1995.** Preliminary seismic hazard assessment of the southern Red Sea region, *European Earthquake Engineering*, pp. 33-38.
- Al-Amri, A. M., 1998.** The crustal structure of the Western Arabian platform from the spectral analysis of long-period P-wave amplitude ratios, *Tectonophysics*, 290, pp.271-283.
- Al-Amri, A. M., Punsalan B. T. And Uy E. A., 1998.** Spatial distribution of the seismicity parameter in the Red Sea regions. *Journal of Earth Sciences*, Vol. 16, Nos. 5-6, pp. 557-563.
- Al-Amri A. and Alkhalifah T., 2004.** Improving the level of seismic hazard parameters in Saudi Arabia using earthquake location and magnitude calibration. Project no. 20-68, King Abdul Aziz City for Science & Technology, Riyadh.
- AL-Haddad M., Siddiqi G. H., AL-Zaid R., Arafah A., Necioglu A., and Turkelli N., 1994.** A Basis for Evaluation of Seismic Hazard and Design for Saudia Arabia, *Earthquake Spectra*, Volume 10, number 2, pp.231-258.
- Alsinawi, S. A., 1983.** Dhamar Earthquake of 13/12/82 A report Submitted to the Yemeni Government, 34p. (Arabic text).
- Alsinawi, S. A., 1986.** Historical Seismicity of the Arab Region. *Proceedings of the Third Arab Seismological Seminar*, Riyadh Saudi Arabia, pp. 11-33.
- Ambraseys N. N., 1988.** The seismicity of Saudi Arabia and adjacent area, Report Prepared for the Kingdom of Saudi Arabia. ESEE, Imperial Col. Sci. Tech., London, U.K. Report 88/11. 294p
- Ambraseys, N. N. and Melville, C.P., 1983.** Seismicity of Yemen. *Nature*, Vol. 303, pp. 321-323.
- Ambraseys, N. N.; Melville, C.P. and Adams, R. D., 1994.** The Seismicity of Egypt, Arabia and the Red Sea- A historical review. Cambridge University Press and King Abdul Aziz City for Science and Technology, 181p.
- Atkinson, G. M. and Boore, D. M., 1995.** Ground motion relations for eastern North America. *Bull. Seism. Soc. Am.*, Vol. 85, pp.17-30.
- Barazangi, M., 1981.** Evaluation of Seismic Risk along the western part of the Arabian plate: Discussion and Recommendations, *Bull. Fac. Earth. Sci., K.A.U.*, pp 77-87.
- Boore, D. M. and Atkinson, G. M., 1987.** Stochastic prediction of ground motion and spectral response parameters at hard-rock sites in eastern North America. *Bull. Seism. Soc. Am.*, Vol. 77, pp. 440-467.
- Boore, D. M., 1983.** Stochastic simulation of high frequency ground motions based on seismological models of the radiated spectra. *Bull. Seism. Soc. Am.*, Vol. 73, pp. 1865-1894.
- Boore, D. M., 1996.** SMSIM- Fortran programs for simulating OFR 96-80-A, USGS, Open-File Report 00-509, 55p.
- Boore, D. M., 2002.** SMSIM: Stochastic Method Simulation of ground motion from earthquakes, in: *International Handbook of earthquake and engineering seismology*, (edited by W.H.K. Lee, H. Kanamori, P. C. Jennings, and D.C. Kisslinger), Chapter 85.13, Academic press.
- Boore, D. M., 2003.** Simulation of ground motion using the stochastic method. *Pure and Applied Geophysics* (in press).
- Brown, G. F., Jackson, R. O., Bogue, R. G., and Maclean, W. H., 1963.** Geologic map of the Southern Hijaz quadrangle, Kingdom of Saudi Arabia: U.S. Geol. Survey Misc. Geol. Inv. Map I-210A, scale 1:500,000.

- Drake, C. L. and Girdler, R. W., 1964.** A geophysical study of the Red Sea. Royal Astron. Soc. Geophys. Jourl, 8, 473-495.
- El-Difrawy, M.F. I., 1996.** Earthquake ground motion amplification in the greater Cairo area, Bull. Fac. Sci. Cairo Univ. Vol. 63, pp. 105-132.
- El-Isa, Z. and Al- Shanti, A., 1989.** Seismicity and tectonics of the Red Sea and Western Arabia. Geophysical Journal Royal Astronomical Society 97, pp. 449-457.
- Fairhead, J. D., 1968.** The seismicity of East African rift system 1955-1968, MSc Dissertation, University of Newcastle upon Tyne.
- Fairhead, J. D. and Girdler, R., 1970.** The seismicity of the Red Sea, Gulf of Aden and Afar triangle, Phis. Trans. R. Soc. Lond. A, 267, pp. 49-74.
- Fairhead, J. D. and Girdler, R., 1972.** The seismicity of East African rift system, Tectonophysics, 15, pp.115- 122.
- Gutenberg G.B., and Richter, C., 1965.** The Seismicity of the Earth and Associated Phenomena. Hafner Publishing Co., New York and London, 310p.
- Hanks, T.C., 1982.** f_{max} . Bull. Seism. Soc. Am., Vol. 72, pp. 1867-1879.
- Hanks, T. C. and McGuire, R.K., 1981.** The character of high frequency strong ground motion. Bull. Seism. Soc. Am., Vol. 71, pp. 2071-2095.
- Hatzdimitrio, P., Papadimitio, E., Mountrakis, D. & Papazachos, B., 1985.** The seismic parameter b of the frequency-magnitude relation and its association with the geological zones in the area of Greece, Tectonophysics, 120, 141-151.
- Isacks, B. and Oliver, J., 1964.** Seismic waves with frequencies from 1 to 100 cycles per second recorded in a deep mine in northern New Jersey. Bull. Seismol. Soc. Am., 54, 1941-1979.
- Karnik, V., 1969.** Seismicity of the European area. D. Reidel, Dordrecht, 364pp, Part I.
- Langer C. J., Bollinger G. A., and Merghelani H. M., 1987.** Aftershocks of the 13 December 1982 North Yemen Earthquake: Conjugate normal faulting in an extensional setting, Bulletin of the Seismological Society of America, Vol. 77, No. 6, pp. 2038-2055.
- Makris, J., Berendsen, D and Denecke, C., 1986.** Sonne cruise no. 29 in the central Red Sea. Tech. Rept., Project No. R 341, IfG Hamgurg, 34 p.
- Makris, J., Bobsien, M., Meier, K. and Rihm, R., 1989.** Sonne cruise no. 53 in the southern Red Sea. Tech. Rept., Project No. R 383 B6, IfG Hamburg, 83 p.
- McKenze, D.; Davis D. and Molnar, P., 1970.** Plate tectonics of the Red Sea and east Africa. Nature vol. 226, pp. 243-248.
- Midorikawa, S., 1987.** Prediction of isoseismal map in the Kanto plain due to hypothetical earthquake, Journal of structural engineering, Vol. 33, pp. 43-48.
- Mogi, K., 1962.** Study of the elastic shocks caused by the fracture of heterogeneous materials and its relations to earthquake phenomena, Bull. Earth. Res. Inst., 40, 125-173.
- Mountrakis, D., Sapountzis, E., Kiliass, A., Elefteriadis, G. and Christophides, G., 1983.** Paleogeographic conditions in the western Pelagonian margin in Greece during the intial rifting of the continental area. Can. J. Earth. Sci., Vol. 20, pp. 1673-1681.
- Nuttl, O. and Herrmann R., 1984.** Ground motion of Mississippi Valley earthquakes. Tech. J. Topics in Civil Engineering, Vol. 110, pp. 54-69.
- Papazachos, B.C., 1980.** Seismicity rates and long-term earthquake prediction in the Aegean area. Quaterniones Geodaesiae, Vol.3, pp. 171-90.
- Papazachos, B.C., Kiratzi, A.A., Hatzidimitriou, P.M. and Rocca, A. Ch., 1984.** Seismic faults in the Aegean area. Tectonophysics, Vol. 106, pp. 71-85.
- Papazachos, B. C., Scordilis, E. M., Papagiopoulou, D. G., Papazachos, C. B. and Karakaisis, G. F., 2004.** Global relations between seismic fault parameters and moment magnitude of earthquakes, Bull. Geol. Soc. of Greece, XXXVI, 1482-1489.
- Poirier, J.P. and Taher, M.A., 1980.** Historical Seismicity in the Near and Middle East, North Africa and Spain from Arabic Documents (VIIth-Xviith century).Bull. Seism. Soc. Amer. Vol. 70, No. 6, pp. 2185-2201.
- Powers, R., Ramierez, L., Redmond, C.& Elberg, E., 1966.** Geology of the Arabian Peninsula: Sedimentary geology of Saudi Arabia, US Geol. Surv. Prof. Paper, 560-D, 147 pp.
- Reiter, L., 1991.** Earthquakes hazard analysis, Colombia Univ. Press, New York.
- Thenhaus, P. C. 1983.** Summary of workshop concerning regional seismic zones of parts of the United States, by the U.S. Geological Survey, 865, 36p.
- Thenhaus, P.C.; Algermissen, S.; Perkins, D.; Hansen, S. and Diment, W., 1986.** Probabilistic estimates of the seismic ground-motion hazards in western Saudi Arabia, U.S. Geological Surv. Bull. No. 1968, 40 p.

STABILITY OF THE HIGH DAM BODY AND SURROUNDING AREAS DERIVED FROM LEVELING AND GPS MEASUREMENTS, ASWAN, EGYPT

A.S. Mohamed

National Research Institute of Astronomy and Geophysics, Helwan, Cairo, Egypt

ثبات جسم السد العالي والمناطق المحيطة مشتق من قياسات GPS والميزانية الدقيقة ، أسوان ، جمهورية مصر العربية

الخلاصة: لمراقبة معدلات الهبوط والتغيرات الرأسية على طول جسم السد العالي تم إنشاء ثمانية خطوط ميزانية دقيقة على مستويات مختلفة لقياس التغيرات الرأسية. وتجرى قياسات الميزانية الدقيقة شهريا على هذه الخطوط بواسطة شعبة الجيوديسيا التابعة للهيئة العامة للسد العالي وخزان أسوان منذ عام ١٩٧٠ وحتى الآن. يركز هذا البحث على تحليل بيانات الميزانية الدقيقة على خطوط الميزانية الثمانية خلال فترة الرصد من عام ٢٠٠٠ إلى ٢٠٠٦. لوحظ من تحليل البيانات المتكررة وجود إختلاف في معدلات الهبوط على طول جسم السد العالي خلال فترات الرصد المختلفة حيث أن معدل الهبوط عند معظم النقاط يتراوح ما بين ١-٢ مم في السنة. بمقارنة هذه النتائج بالنتائج السابقة لوحظ أن جسم السد العالي أكثر ثباتا عما كان عليه وقت إنشائه، وبمقارنة هذه المعدلات خلال فترات الرصد المختلفة مع التغيرات في مستوى سطح الماء في البحيرة لوحظ أنه لا توجد علاقة مباشرة حيث أن معدلات الهبوط تعتبر في المعدلات المسموح به ولا تتأثر بزيادة أو نقصان المياه في البحيرة.

ولمراقبة معدلات التغيرات في الحركات الأفقية والرأسية للمناطق المحيطة بالسد العالي ، تم خلال عام ٢٠٠٠ إنشاء شبكة جيوديسية تتكون من ٩ نقاط جيوديسية (محطات) وخط الميزانية الدقيقة الذي يربط ما بين جسم السد العالي وخزان أسوان. وأجريت القياسات الجيوديسية خلال الفترة ما بين عام ٢٠٠٢ إلى ٢٠٠٦ بواقع ٧ رصدات GPS على الشبكة الجيوديسية و٤ رصدات على خط الميزانية الدقيقة. بحساب معدلات الإزاحات الأفقية والرأسية لتلك الأرصاء و كذلك حساب معدلات التشوهات الحديثة للقشرة الأرضية لوحظ أن معدل الإزاحات الأفقية والرأسية تتراوح ما بين ١-٢ مم في السنة و تعتبر هذه القيم صغيرة نسبيا و ليس لها تأثير مباشر على جسم السد العالي وهو ما يتبين منه أن منطقة السد العالي و ما حولها تتميز بدرجة ثبات عالية .

ABSTRACT: For monitoring the height changes along the High Dam body, eight leveling lines were established at different elevations during its construction. The leveling measurements were carried out monthly by the Geodetic Branch of the High Dam and Aswan Dam Authority (HADA) since 1970 till now.

The present work focuses on the data analysis from leveling along eight lines crossing the High Dam body during the period from 2000 to 2006. The analysis reveals to different tendencies of the High Dam body. Rates of the subsidence at most benchmarks of the leveling lines range between 1-2 mm/yr. Rates of the setting of the High Dam body is trending to be stable. The correlation between these rates and water level changes at the up- and down-stream sides is absent during the observed period.

For monitoring the horizontal and vertical movements in the High Dam area, a local GPS network consisting of 9 geodetic stations and one leveling line joining the High Dam and Aswan Dam, were established in 2000. The measurements were carried out during the period from 2002 to 2006. Seven campaigns of GPS and four leveling measurements were carried out in the study area. The measurements are correlated to the water level changes in the lake, as well as to the seismic activity in the area. The displacements for each epoch of observations were calculated and the deformation analysis was performed. The horizontal and vertical displacements vary between 1 to 2 and 0.1 to 1 mm/yr, respectively. The vertical and horizontal rates and strain accumulations are small, which reflect the stable situation, and demonstrates a new information about the present state of the High Dam body and surrounding areas.

INTRODUCTION

Aswan region is located within the stable platform of Northern Africa. The Nile follows the contact between surface exposure of the granite of the Eastern Desert to the East, and the sedimentary cover of the Nubian sandstone to the West. Nubian plain covers most of the area southwest of Aswan city and borders of the reservoir from the West (Issawi, 1969, 1978). Nubian plain is relatively flat, and the surface has an average elevation of 200 m above the mean Sea-level. The structural pattern of Aswan region is governed mainly by faulting. The faults crossing the region are classified into E-W and N-S faults (Fig. 1). The N-S faults are well represented in the vicinity of the reservoir and affect the sandstone beds of the Nubian plain.

The High Dam is located above the first cataract of the Nile, 15 km south of Aswan city. The dam was chosen to be a rock fill dam provided with an impervious core in its main part. Fig. (2) represents the cross-section of the High Dam. The dam bottom elevation is 85 m and its crest elevation is 196 m. The maximum height of the dam is 111 m. The dam length at the crest is 3830 m. The dam width at the base is 980 m and its width at its crest is 40 m. At the eastern bank, a long diversion canal of 1950 m length, provided with six tunnels, had been excavated for releasing the water discharge.

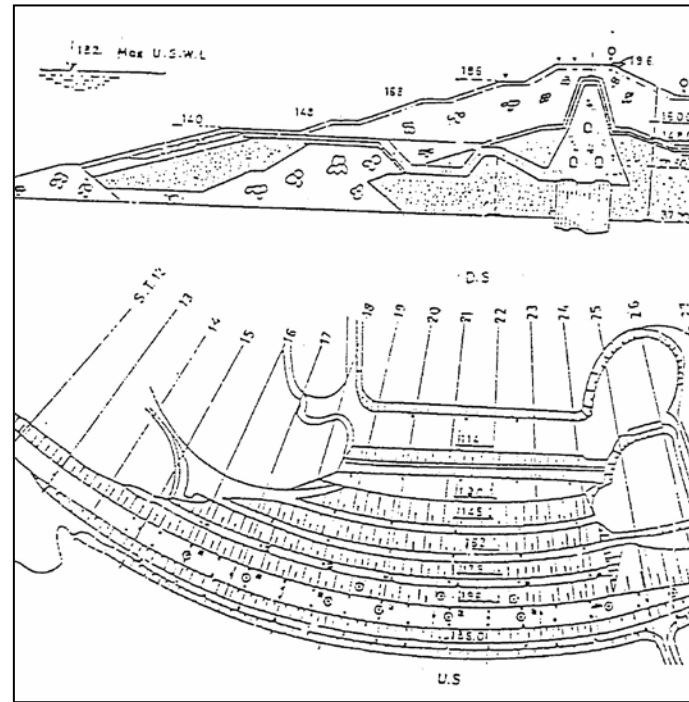


Fig. 2 Cross section of the High Dam and

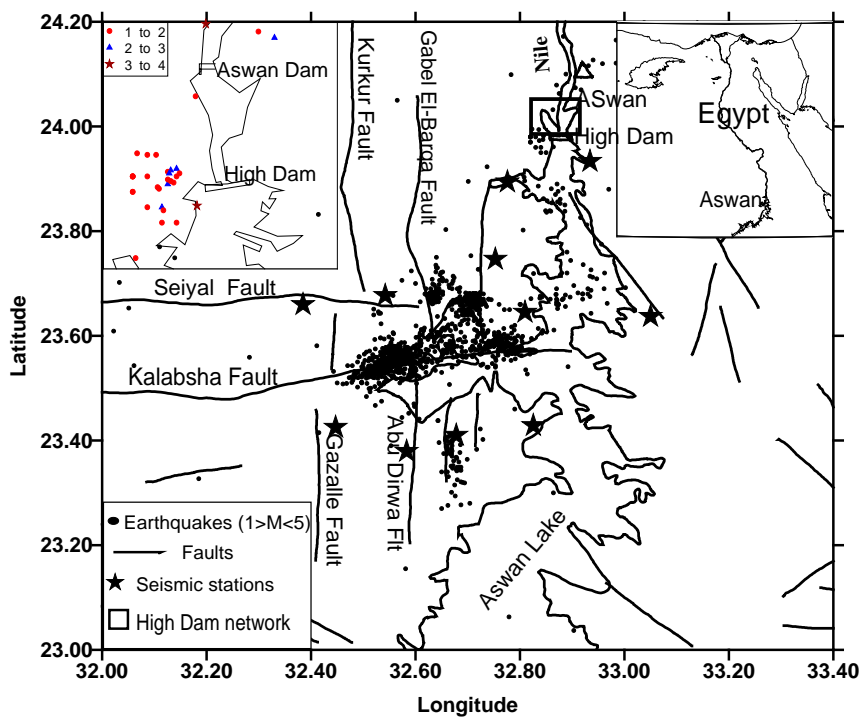


Fig. 1: Structural pattern and seismic activity (1981 - 2006) in Aswan region with focusing to the seismicity in the High Dam area (2000 - 2006).

Each tunnel has two branches at the outlet. Over each of them a turbine was erected for generating electricity. The eastern part of the High Dam is mainly a concrete type structure.

The dam impounds the second largest man-made reservoir in the world. The reservoir began to fill in 1964 and the level rose gradually, with annual irrigation cycles, until it reached a maximum water level of 183 m in November 1999 with a capacity of 160 km³. Fig. (3) shows the water level changes in the lake and number of earthquakes that occurred in the area during the period from 2000 to 2006. Water level fluctuates two times a year as the cycles inflow and discharge.

The historical earthquake activity in Aswan region was rare as revealed by long recorded history (WCC, 1985; Kebeasy et al., 1987; Kebeasy, 1990; Abdel-Monem & Dahy, 1999). The 14 November 1981 earthquake of magnitude 5.3 occurred along the Kalabsha fault 60 km southwest of the High Dam in recent historical time. The micro earthquakes characterize that area till now. The seismicity is recorded by a telemetric network and is concentrated in the area enclosed by latitudes (23.40N, 23.80N) and longitudes (32.40E, 33.00E). It occurs at the intersection between the E-W and N-S fault trends (Mahmoud, 1994 & 2000; Mahmoud et al., 1996; Abdel-Monem, 1997).

Investigation of the vertical movements

The changes in height of a given point relative to the sea level are considered as absolute vertical movements. While the relative movement is a change in height between two points relative to each other. The

velocities can be determined either absolute velocities V_{abs} , or relative ones ΔV in mm/yr.

The heights were determined after adjustment for each epoch of repetition. In general, results of separate adjustment can be given by the following formula:

$$dH = H_i - H_0 \quad (1)$$

where H_i is the height of benchmark derived from repeated leveling, H_0 is the height determined in initial epoch. The difference dH at each benchmark is affected not only by the identical configuration of adjusted network, but also by the time homogeneity. The reduction to common epoch does not satisfy requirements for reliability in determination of time scale. A more correct approach is the adjustment of annual height changes of height differences between benchmarks, which can be determined by the following formulas (Vyskočil, 1969a)

$$dh = dH_i - dH_0 \quad (2)$$

where dh is the difference of height differences dH_0 and dH_i measured in initial epoch (time T_0) or i -epoch (time T_i), respectively. The time T_0 and T_i at each leveling line is known, and the time difference can be determined exactly for each dh .

$$dT = T_i - T_0 \quad (3)$$

The annual velocity of height change ΔV is generally deduced as follows:

$$\Delta V = \frac{\partial H_i - \partial H_0}{\partial T_i - \partial T_0} = \frac{\partial h}{\partial T} \quad (mm/yr) \quad (4)$$

The condition in leveling loop(s) is theoretically correct (under the assumption of linear trend of vertical movement *within* (dT)). After adjustment of the network for repeated levelings, the annual velocities of single benchmark can be computed relatively to chosen initial benchmark (reference surface as mean sea level). The measured values of dh (Eq.(2)), or ΔV (Eq.(4)) can be analyzed usually in graphical form along leveling line. These graphs can be used for choice of benchmarks, proper for vertical movement studies. Moreover, these graphs can serve for determination of "measured" horizontal gradients at each leveling line indicating a possible presence of fault zone etc.

In this work, the precise automatic level Kern GK-2A and invar rods in metallic cover of 3m length and heavy footplates (4.5 kg) were used in the measurements. All instruments and leveling invar rods were tested before and after each measurement. The measurements of difference in heights were performed twice, forward and backward. The leveling observations were corrected to exclude the air temperature and pressure effects. In addition, the gravity measurements were performed on the leveling line at each leveling

benchmarks to take into account effect of the gravity field on the leveling measurements.

The measurements at all stations were carried out continuously without interruptions forward and backward. Accuracy of the measured elevation difference is primary related to the accuracy of the observed elevation difference at each successive leveling section. Corrections for rod scale and/or outer effects are introduced in the measured height differences. The mean square error (m_L) is given by the formula:

$$m_L = \frac{1}{2} \sqrt{\frac{1}{n} \sum \frac{\rho^2}{R}} \quad (5)$$

where m_L is the mean square error; ρ (in mm) is the difference between forward and backward measurements; n is the number of sections used and R is the length of section (km). The reliability of height difference (ΔH) obtained from precise height measurement is generally:

$$\mu_{\Delta H} < \pm 1 \text{ mm} / \sqrt{km} \quad (6)$$

Accuracy of the measurements was tested by means of the usual procedure, using the differences between (forward) and (backward) leveling.

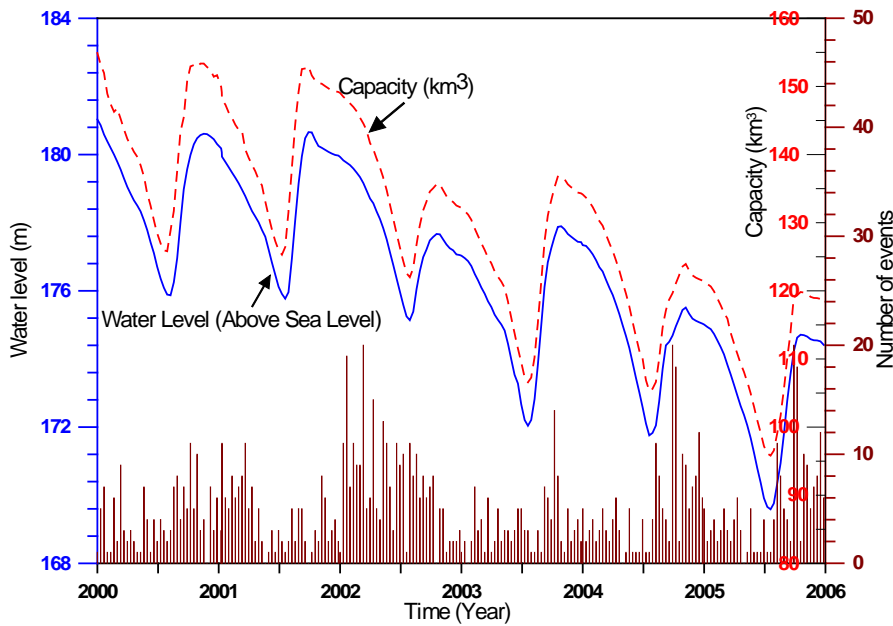
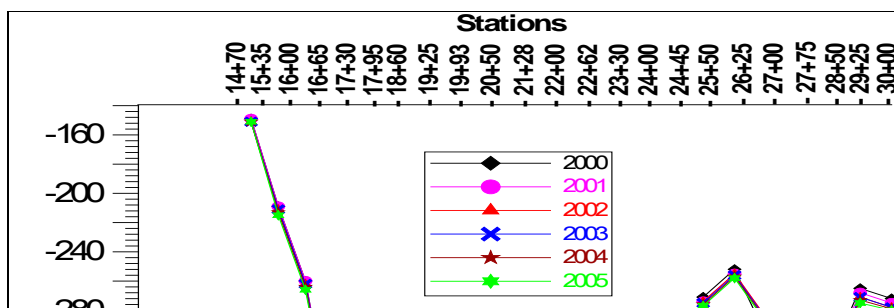


Fig. 3: Water level and the capacity in the reservoir and number of earthquakes within the considered area during the period from 2000 to 2006.



Estimation of the strain parameters

Strain parameters such as dilatations (Δ), shear strains (γ), principal strains (ε_1 & ε_2) and their directions (ω) are usually used to interpret regional and local deformations. The basic principles of strain analysis, as developed in the theory of elasticity, are applicable if the area covered by the network can be considered as a continuum deforming under stress. Thus the deformation is continuous by definition. The theory of infinitesimal strain in three dimensions has been applied in the strain analysis.

The deformations are generally small in comparison with size of the network. So, they may be modeled by a differential relationship. The displacement vector is represented by (Schneider, 1982):

$$\underline{d} = A\underline{r} + T \quad (7)$$

where \underline{d} is the vector of displacements (u, v, w), \underline{r} is the vector of coordinates (x, y, z), T is the vector of translation (T_x, T_y, T_z).

$$A = \varepsilon + \omega$$

where (u, v, w) are the three components of the displacements vectors in (x, y, z) direction, respectively. (ε) is the strain and (ω) is the rotation.

To estimate the crustal strains in GPS data for the period (2002–2006), horizontal components of the displacement vectors are used in the present case. The annual rate of the maximum shear strain (γ) and dilatation (Δ) are estimated within the observation periods using the equations (8) and (9), respectively. The deformation parameters are related to the center of a single triangle within the network.

$$\gamma = \sqrt{\gamma_1^2 + \gamma_2^2} \quad (8)$$

$$\text{where } \gamma_1 = \varepsilon_{xx} - \varepsilon_{yy} \quad \text{and} \quad \gamma_2 = 2\varepsilon_{xy}$$

$$\Delta = \varepsilon_{xx} + \varepsilon_{yy} \quad (9)$$

Data analysis

Leveling lines crossing the High Dam body

Since 1970 leveling measurements were performed along eight lines which were distributed on the up-stream berm (186 m), the up- and down-stream parapets (196 m) and the down-stream berm (179, 162, 145, 130 and 114 m) of the High Dam body (Fig. 2). The benchmarks along the leveling lines were established during the sequential process of the construction of the High Dam body. The measurements were carried out each month since 1970 till now by HADA. Tealeb (1991) and Mohamed et al., (2003) have demonstrated levelling measurements from 1970 to 2000.

The length of each leveling line along the up-stream berm (186 m) and the up- and down-stream parapets (196 m) is about 3300 m. Along each line 36 leveling points were established. These points are extended from the western bank of the High Dam to the rock fill part, the concrete part above the tunnels and eastern bank. The reference benchmark lies on the eastern bank of the High Dam and it is established on basement rocks. The other leveling lines along the down-stream berm lie above the fill part of the High Dam, with relatively short lengths and few leveling points. The measurements were performed to the whole leveling lines since 1976.

Annual height changes along the lines on the up-stream berm (186 m) and the up- and down-stream parapets (196 m) are presented in Figs. (4, 5 and 6), respectively. Amplitudes of height changes during the whole period of measurements (1970–2000) along these profiles are of about 491, 803 and 288 mm recorded in the rock fill part of the High Dam. The annual height changes (setting) are larger along the rock fill part than along the western and eastern banks of the High Dam, as well as the concrete part above the tunnels (Mohamed et al., 2003).

During the period from 2000–2006, the total height changes were about 15, 22 and 18 mm as recorded along the leveling lines on the up-stream berm (186 m) and the up- and down-stream (196 m), respectively. These values are small in comparison with the height changes in the same areal zone during the whole period of measurements (1970–2000). The behavior of different structural units of the High Dam is clear from the height changes, especially during the first decade of measurements (1970–1980), Mohamed et al., (2003) more pointed out the same conclusions. Annual height changes along the lines (2000 to 2006) indicate that, the rates of setting are variable but decrease with time for each part.

Annual height changes along the lines on the down-stream berms (179, 162, 145, 130 and 114 m), which lie mostly above the rock fill part of the High Dam, are presented in Figs. (7–11). These figures reveal that the annual height changes from 2000–2006 decreased with time. Amplitude of the height changes during the whole period of measurements (1970–2000) along these profiles was of about 147, 125, 868, 468 and 118 mm, respectively. During the period from 2000–2006 the total height changes of about 8, 12, 2, 5 and 6 mm were recorded along the leveling lines on the down-stream berms (179, 162, 145, 130 and 114 m), respectively.

Leveling line joins the High Dam and Aswan Dam

Measurements of the leveling line joining the two dams were repeated four times (i.e., February 2002, January 2003, February 2004 and February 2006). Configuration of the leveling line is shown in Fig. (12).

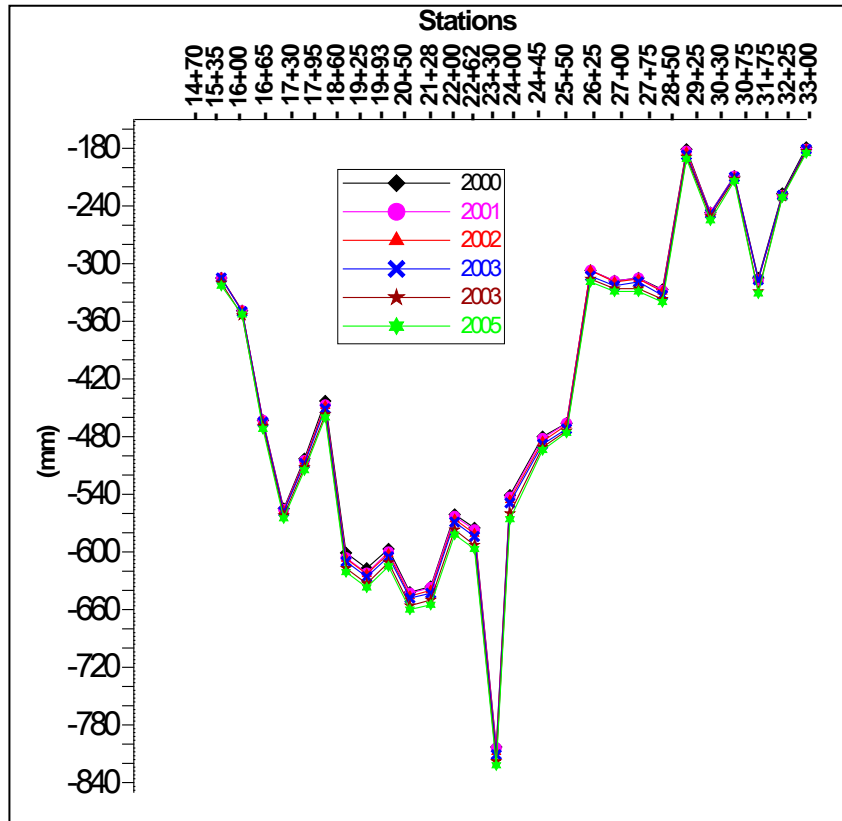


Fig. 5: Annual height changes along the leveling line on the up-stream parapet (196 m) of the High Dam during the period from 2000-2006.

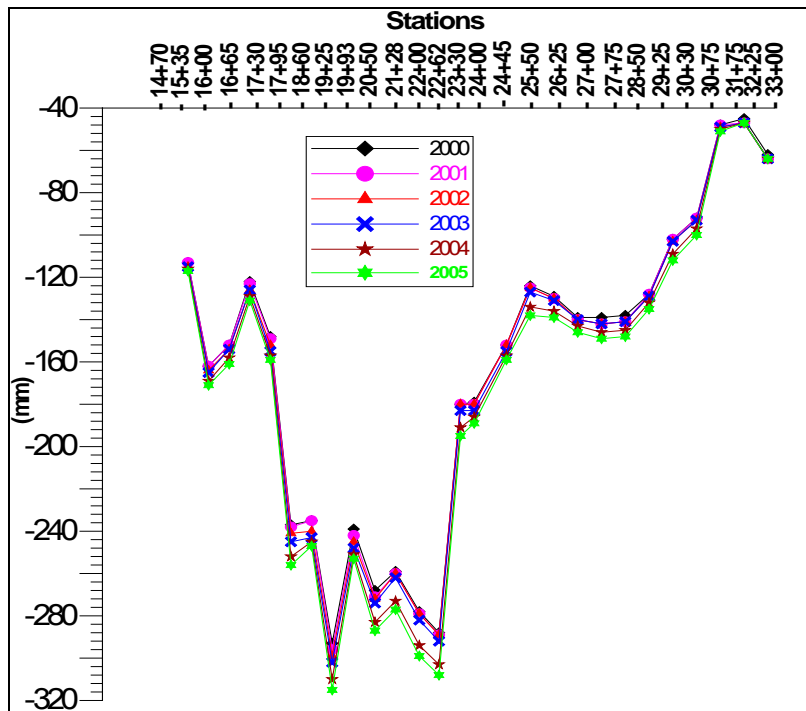


Fig. 6: Annual height changes along the leveling line on the down-stream parapet (196 m) of the High Dam during the period from 2000-2006.

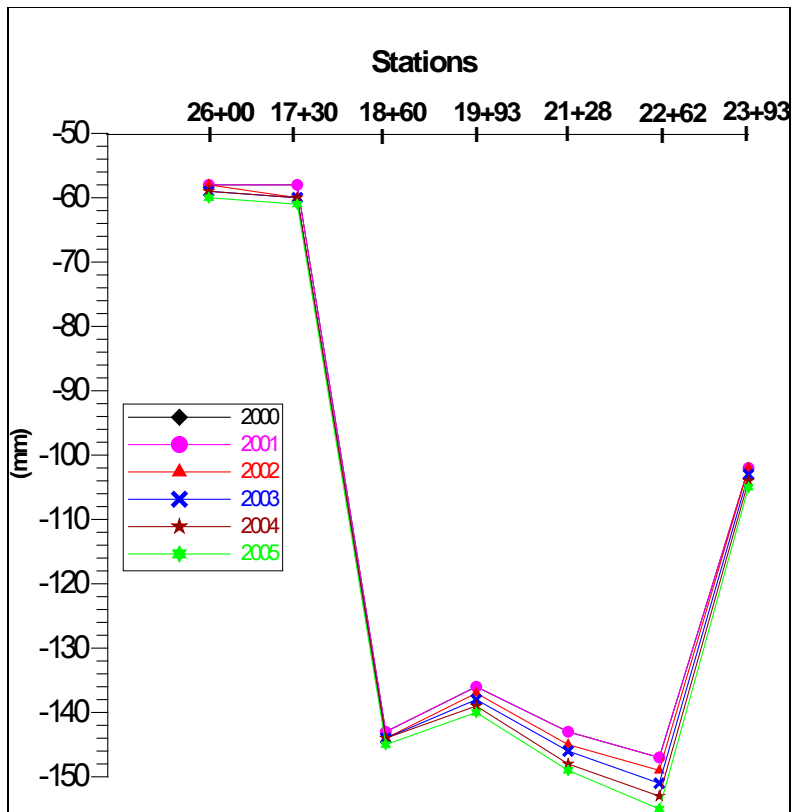


Fig. 7: Annual height changes along the leveling line on the down-stream berm (179 m) of the High Dam during the period from 2000-2006.

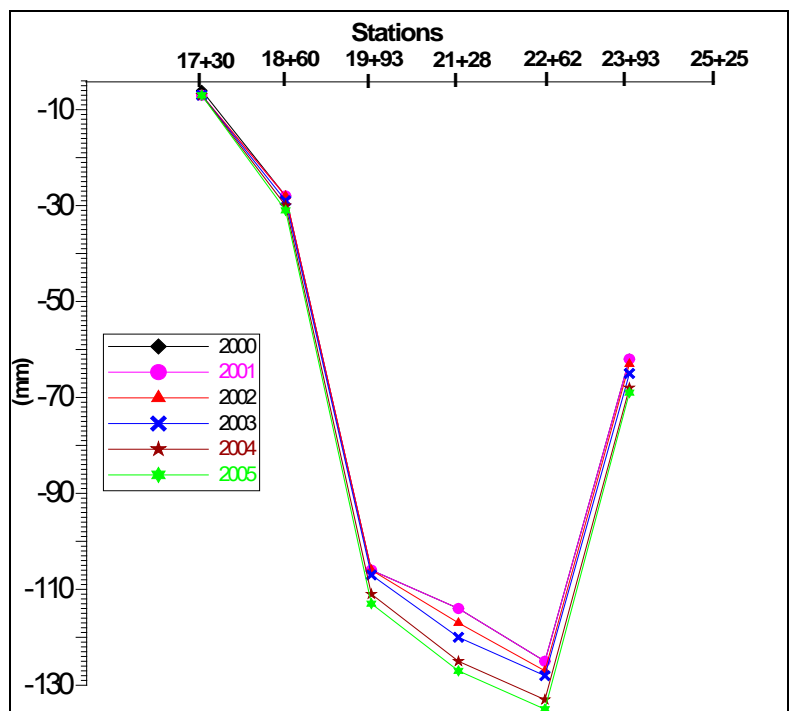


Fig. 8: Annual height changes along the leveling line on the down-stream berm (162 m) of the High Dam during the period from 2000-2006.

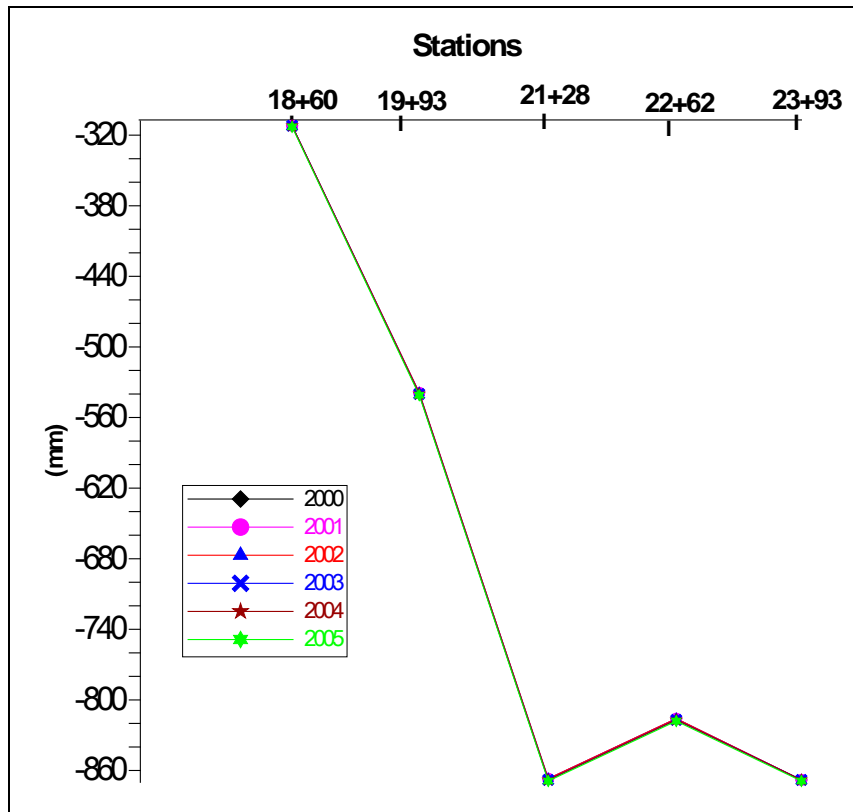


Fig. 9: Annual height changes along the leveling line on the down-stream berm (145 m) of the High Dam during the period from 2000-2006.

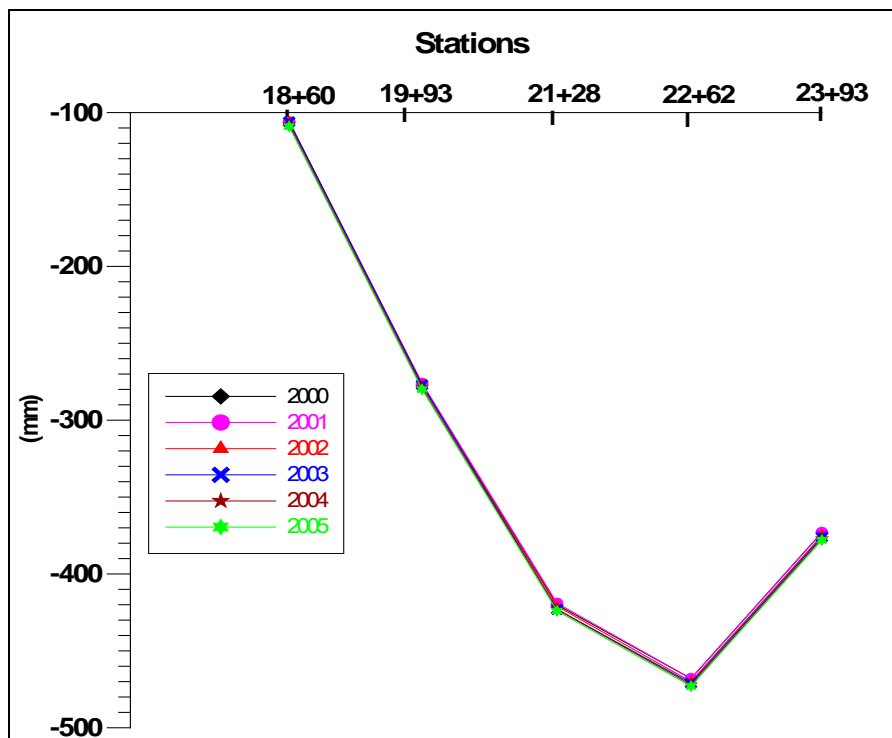


Fig. 10: Annual height changes along the leveling line on the down-stream berm (130 m) of the High Dam during the period from 2000-2006.

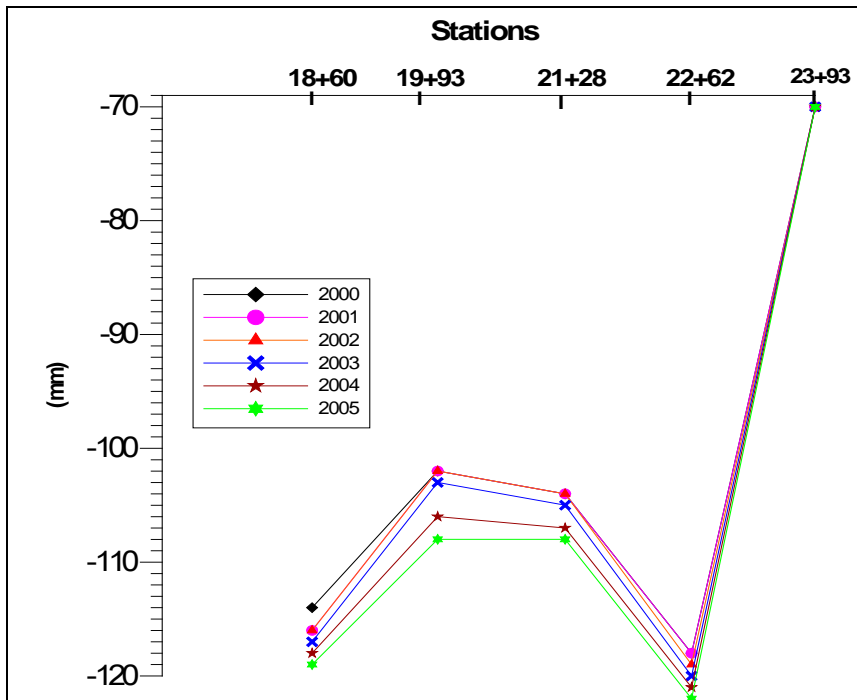


Fig. 11: Annual height changes along the leveling line on the down-stream berm (114m) of the High Dam during the period from 2000-2006.

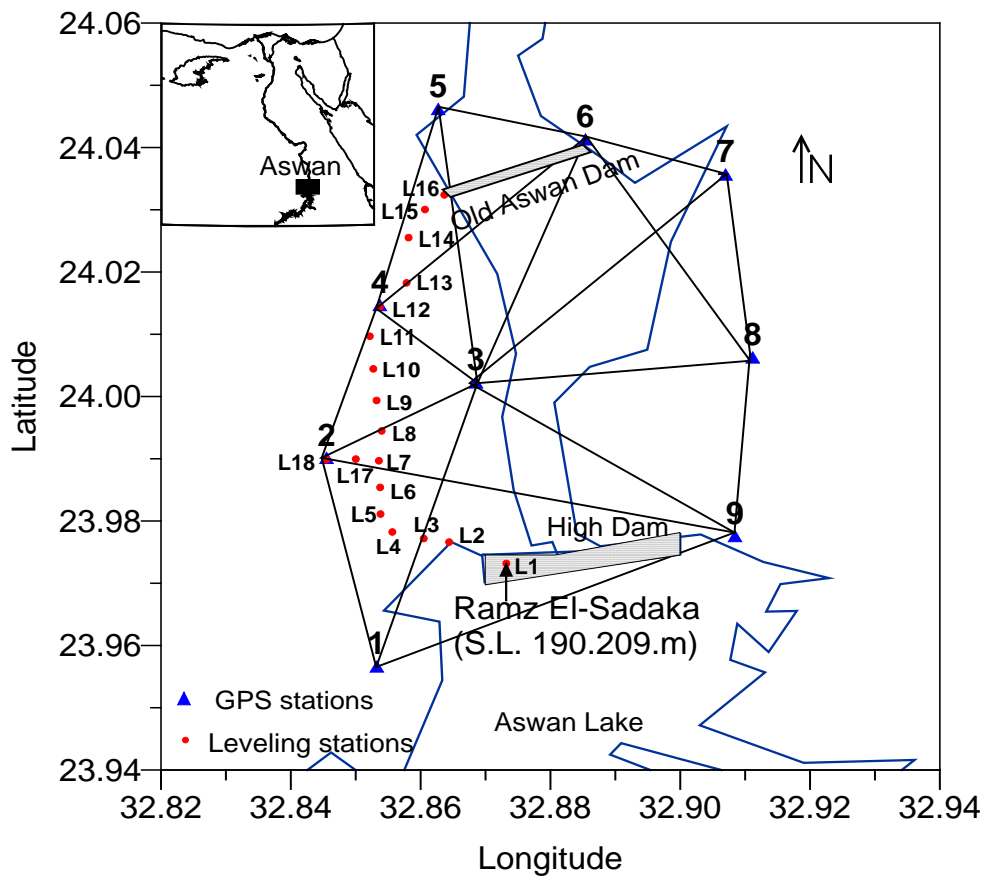


Fig. 12: Configuration of the High Dam GPS network and leveling line.

Adjustment and analysis of the leveling line measurements were carried out and tied to initial benchmark, which located at Ramz El-Sadaka as shown in Fig.(12). The leveling data were arranged in three time intervals: Interval I from 2002 to 2003; interval II from 2003 to 2004 and interval III from 2004 to 2006. The best fit of the leveling data, parameters of heights and rates of vertical movement were estimated by the least squared method (Table 1). The rates of the vertical movements through above three time intervals are charted in Fig. (13), which might gives more details of the pattern of the vertical movements in this important area. The variations of the rates of vertical movements are small and not stable during the intervals of measurements.

The High Dam GPS network

A geodetic network of 9 arrays was established in 2000 around the High Dam and old Aswan dam. The first campaign was performed in December 2001 and repeated in November 2002, April 2003, October 2003, April 2004, October 2004 and January 2006 using GPS receiver's type Trimble 4000SSI. The sampling interval and elevation were fixed throughout the survey at 30 second and 15°, respectively. The GPS observations of every campaign were carried out during 48 hours simultaneously. Processing of baselines analyses were performed using Geomatics (V. 1.5) software packages (Trimble, 2003) and other software for adjustment and calculations of the deformations parameters (Fuji, 1997; Bányai, 2006).

Table 1: Relative vertical height changes and standard deviation for the three intervals

Station	Coordinates		2002 - 2003		2003 - 2004		2004 - 2006	
	X	Y	dh (mm)	m _L (mm)	dh (mm)	m _L (mm)	dh (mm)	m _L (mm)
L1	2651002.676	486592.562	Ramz El-Sadaka (Base station as reference)					
L2	2651643.788	486204.498	-0.025	0.135	-0.23	0.119	-0.6	0.038
L3	2651708.034	485806.768	-0.022	0.063	0.285	0.064	0.015	0.02
L4	2651824.455	485314.704	0.095	0.095	-0.005	0.084	-0.1	0.026
L6	2652618.649	485117.711	-0.163	0.076	-0.145	0.038	-0.145	0.042
L7	2653093.671	485105.343	0.171	0.102	-0.8	0.09	-0.8	0.029
L8	2653622.487	485149.367	-0.496	0.109	-0.935	0.096	-1.2	0.03
L10	2654726.356	485019.516	-0.1	0.236	0.79	0.208	1.1	0.011
L12	2655828.450	485121.014	-0.41	0.179	0.12	0.158	-1.0	0.008
L13	2656254.930	485542.261	0.225	0.109	0.831	0.105	0.531	0.034
L14	2657059.834	485574.536	0.096	0.129	0.34	0.113	0.8	0.036
L15	2657559.729	485831.643	-0.225	0.117	-0.4	0.103	-1.2	0.033
L16	2657819.431	486135.603	0.26	0.078	0.39	0.069	0.1	0.022
L17	2653121.895	484743.880	-	-	-0.35	0.067	-0.025	0.022
L18	2653111.843	484283.664	-	-	-0.92	0.088	0.1	0.022

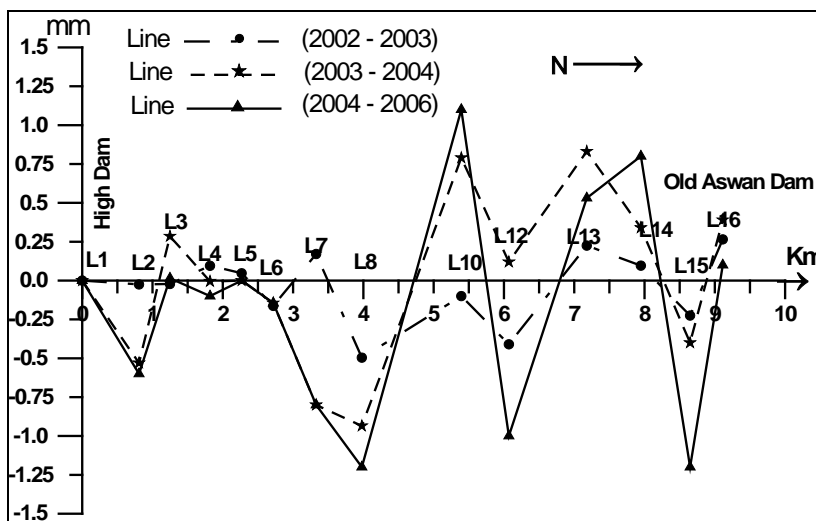


Fig. 13: Vertical movement along the leveling line for the specified intervals (in mm).

The IGS precise ephemeris is applied. The annual rates of the displacement vectors at each GPS station were determined under an assumption of free network adjustment. Horizontal components at each station were computed from the difference of adjusted coordinates of the stations from the last to first epoch. The displacement vectors of each epoch of the observations were calculated, according to WGS-84, from the coordinate changes. Considering the confidence limit, most of these displacement vectors represent the movements within the study area. The horizontal components of the displacement vectors with 95% confidence error ellipses are shown in Fig.(14). The error ellipses represent the standard error in all direction around the observed site. The horizontal displacement vectors are of small magnitude and in the range of 1-2 mm/yr. Some stations of the network indicate significant changes while other stations illustrate negligible changes through the period of observations.

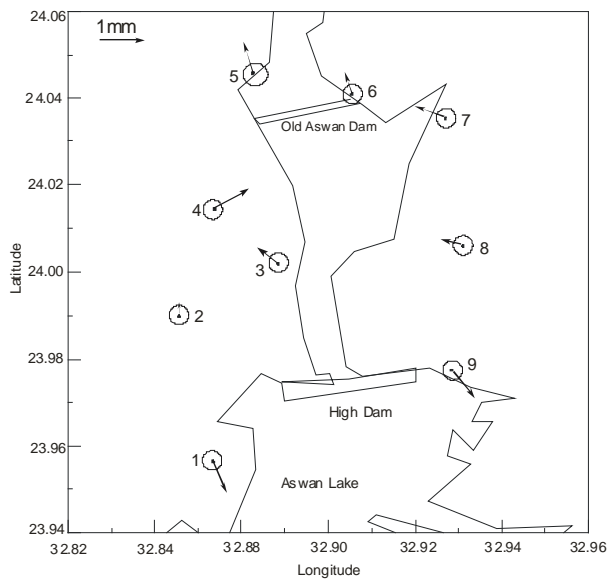


Fig. 14: Rate of horizontal displacement vectors in the studied region for the period from 2001 to 2006.

The horizontal components of the velocity vectors are used to estimate the stress and strain field in the area. Figs.(15&16) show the estimated dilatational and maximum shear strains, respectively. These values are relatively small and sometimes are non-significant an initial look on the crustal deformation, they might well portray characteristics of the crustal deformation around the High Dam area. The low strain rates is consistent with low level of earthquake activity. This indicates that the rate of the deformation in this area is small.

The dilatational strains shown in Fig. (15) shows a patch of compressions strains in the middle part of the Western Bank between the two dams. On the other hand, the Eastern Bank is characterized by an extensive strains. The total amount of maximum shear strain accumulation

during the study interval is relatively small (Fig. 16). The maximum shear strains increases in the middle part of the Western Bank between the two dams. The high rates of the maximum shear strains in the middle area may not relate to any co-seismic and/or post-seismic movements.

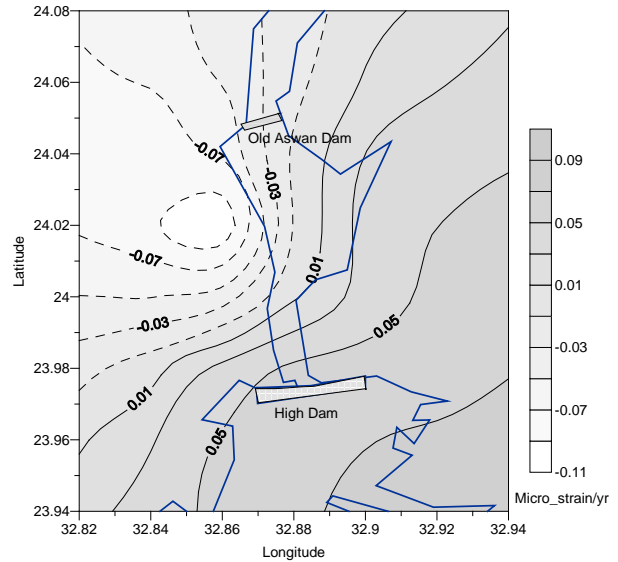


Fig. 15: Rate of dilatation in the studied area for the period from 2001 to 2006.

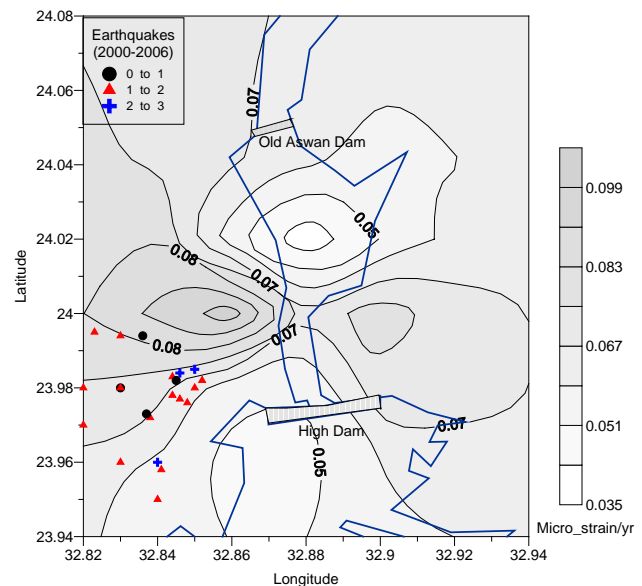


Fig. 16: Distribution of maximum shear strain rates in the studied area with seismic location for the period from 2001 to 2006.

CONCLUSION

The main objective of the current research is the collecting and analysis of the vertical and horizontal data of the considered area. They have been done for better understanding the dynamic characteristics of the High Dam body and its area. The results are summarized as follows:

1. Different rates of settlement were recorded at different structural parts of the High Dam body during the period from 2000 to 2006. Height changes indicate that the High Dam body is stable against the seasonal water level changes. In general, rate of the height changes along all the levelling lines decrease with time and almost reaches a state of stability.
2. Analysis was performed for leveling and GPS data obtained during 2001 to 2006. Although the period of leveling and GPS observations is relatively short, the obtained results might well portray characteristics of the vertical and horizontal movements in this important area. The results indicated that the rate of both vertical and horizontal movements is small and changes from time to time.
3. Rate of the accumulated strains is small and classified into the lowest class of the category of the strain classifications.

ACKNOWLEDGMENTS

The author is very grateful to the staff members of Crustal Movement Laboratory in the National Research Institute of Astronomy and Geophysics for their participation during the leveling and GPS data collection. He thanks engineers of the Geodetic Branch of the High Dam and Aswan Dam Authority for providing the levelling data.

REFERENCES

- Abdel-Monem S.M., (1997):** Recent Crustal Movements and Seismicity Studies Around Active Faults, Aswan, Egypt. *Acta Geod. Geoph. Hungary*, Vol. 32 (1-2), pp. 43-52.
- Abdel-Monem S.M. and Dahy S. A., (1999):** Determination of Earthquake Energy Release and b-Value in the Aswan region, Egypt. *NRIAG Bulletin, Geophysics (B)*, pp. 19-38.
- Bányai L., (2006):** Free network concept of local deformation investigations using precise leveling and GPS measurements in the practice of the Geodetic and Geophysical Research Institute. Study trip between 18-25 April 2006, An advanced lectures at NRIAG, Helwan, Cairo, Egypt.
- Fuji Y., (1997):** Estimation of continuous distribution of Earth's strain in the Kanto-Tokai district, Central Japan, with the aid of least squares collocation. An advanced lectures on geodesy and seismology in Egypt August, 1996-July, 1997. *Bulletin of NRIAG (Special Issue)*. pp. 97- 126.
- Issawi B., (1978):** Geology of Nubia west area, western desert, *Annals of the Geological Survey of Egypt*.
- Issawi B., (1982):** Geology of the southwestern desert of Egypt, *Annals of the Geological Survey of Egypt*.
- Kebeasy R. M., (1990):** Seismicity. In the *Geology of Egypt*. Baklema, Rotterdam, pp.51-59.
- Kebeasy R.M. and Gharib A.A., (1991):** Active Fault and Water Loading are Important Factors in Triggering Earthquake Activity Around Aswan Lake. *J. Geodynamics*, Vol. 14, No.1-4, pp. 73-83.
- Kebeasy R.M.; Maamoun M. and Ibrahim I.M., (1982):** Aswan Lake Induced Earthquake. *Bull. Internal. Inst. Seismol. Earthq. Eng.*, No. 19, pp. 155-160.
- Kebeasy R.M.; Maamoun M.; Ibrahim I.M.; Megahed A.; Simpson D.W. and Leath W.S., (1987):** Earthquake Studies at Aswan Reservoir. *J. Geodynamics*, Vol. 7, pp. 173-193.
- Mahmoud S.M., (1994):** Geodetic and seismotectonic deformation near Aswan reservoir, Egypt. *Bulletin of CRCM No.41*. Praha, Czech Republic. Pp.5-30.
- Mahmoud S.M., (2000):** Recent crustal movements and seismic activity studies in the Aswan region, Egypt. In: *Proceeding of the Ninth Int. Symp. On Recent Crustal Movements*, held in Cairo in 1998, Egypt, pp. 127-143.
- Mahmoud S.M.; Bhattacharya, S.N.; Yunga, S. and Srivastava, H.N., (1996):** Seismicity pattern near Aswan reservoir, Egypt. *Bulletin of the Indian Society of Earthquake Technology*, paper No. 355, Vol. 33, No. 1, pp. 161 – 180.
- Mohamed A.S., Mahmoud S.M., Tealeb A., Sakr K., Zahran K.H. and Abdel Latif M., (2003):** Monitoring of the height changes on leveling lines along the High Dam body, Aswan, Egypt. *NRIAG Journal of Geophysics*, Vol. 2, No. 1, pp. 1-26.
- Schneider D. (1982):** Complex Crustal Strain Approximation. University of New Brunswick, Fredericton, N.B. and Institute of Geodesy and Photogrammetry, Swiss Federal, Institute of Technology, Zürich.
- Tealeb A., (1991):** Analysis of Levelling Measurement along the High Dam, Aswan, Egypt. *J. Geodynamics*, Vol.14, No.1-4, pp. 189-219.

Trimble N.L., (2003), “Geomatics Software’s User Manual”, Trimble Navigation Limited, Sunnyvale, U.S.A.

Vyskočil P., (1969a): A comparison of preliminary maps of annual velocities of vertical crustal movements on the territory of German Democratic Republic, of the Polish Peoples's Republic and of the Czechoslovak Socialist Republic. In: Problems of recent crustal movements. Proceedings of the Third International Symposium of CRCM. AN SSSR, Moscow, Leningrad 1968, pp. 93-100.

Woodward-Cycle Cosultants (WCC) (1985): Evaluation of fault in the Aswan area and along the Nile valley.

CONSTRAINING THE CRUSTAL DEFORMATION AROUND THE NORTHERN PART OF LAKE NASSER USING GPS TECHNIQUES AND SEISMOLOGICAL DATA

S.M. Mahmoud*, A.M. Radwan *, A.A. Tealeb*, A.A. Omran**,
R.A. Fathel-Bary* and A. Rayan *

* National Research Institute of Astronomy and Geophysics, Helwan.

** Geology Department, Faculty of Science, Assiut University.

دراسة تشوهات القشرة الأرضية حول الجزء الشمالي لبحيرة ناصر باستخدام بيانات النظام العالمي للأحداثيات GPS والبيانات الزلزالية

الخلاصة: في ١٤ نوفمبر ١٩٨١ حدث زلزال بقوة ٥.٣ بمقياس ريختر في منطقة كلابشة التي تبعد ٦٠ كم جنوب غرب مدينة أسوان بمصر. ونظراً لأهمية السد العالي بالنسبة لمصر شارك المعهد القومي للبحوث الفلكية والجيوفيزيقية بطلوان مع هيئة السد العالي وخران أسوان في برنامج طويل المدى لمراقبة تحركات القشرة الأرضية والزلزال التي تحدث بهذه المنطقة الحيوية من مصر.

ومن دراسة ميكانيكية التصدع لبؤر الزلازل للنطاقات الخمسة الموجودة بمنطقة الدراسة تبين أن اتجاه الشد في منطقة الدراسة يتفق مع وجود الفوالق العادية التي تأخذ إتجاه شرق - غرب مثل فالق كلابشة.

لمراقبة تحركات القشرة الأرضية التي تحدث بهذه المنطقة ولإيجاد علاقتها بالنشاط الزلزالي تم إنشاء شبكة جيوديسية تتكون ١١ نقطة جيوديسية في عام ١٩٩٧ حول الجزء الشمالي من بحيرة ناصر. وقد تم رصد هذه الشبكة ثمانى مرات في الفترة من عام ١٩٩٧ إلى عام ٢٠٠٤ وذلك بنظام الرصد الدقيق المعروف بالنظام العالمي للأحداثيات GPS علي فترات زمنية متتالية وتم تحليل هذه البيانات وحساب معدلات الحركة للنقاط الجيوديسية المنشأة ومقارنة هذه النتائج بتسجيلات الزلازل الأرضية التي تحدث بالمنطقة.

وقد وجد أن متوسط معدل الحركة حول الجزء الشمالي لبحيرة ناصر ٢ مم في السنة في إتجاه شمال شرق ، وهو ما يدل علي التوافق الجيد لإتجاهات القوي المؤثرة علي المنطقة والتي تم إستخلاصها من دراسات سابقة تم فيها تحليل بؤر وميكانيكية الزلازل . وهذا الإتجاه متفق أيضاً مع إتجاه حركة اللوح الأفريقي .من نتائج الاجهاد المستخلصة لحقب الأرصاء من سنة ١٩٩٧ حتي سنة ٢٠٠٤ أمكن تقسيم منطقة الدراسة إلي ثلاثة أجزاء رئيسية : الجزء الشمالي ويعاني من إجهاد تضاعطي عالي يأخذ إتجاه شمال شرق - جنوب غرب ، وقد بلغ المتوسط السنوي للإجهاد في هذا الجزء حوالي ٠,١ جزء من الإجهاد وأما الجزء الجنوبي من منطقة الدراسة فيعاني من إجهاد تمددي (إجهاد شد) عالي، وقد وجد أن أعلى معدل سنوي للإجهاد يساوي ٠,١ جزء من وحدة الإجهاد ويأخذ أيضاً إتجاه شمال شرق - جنوب غرب ، أما الجزء الثالث من منطقة الدراسة والمتمثل في الجزء المتوسط ويشمل منطقة كلابشة فإنه يعاني من إجهاد ضعيف يتبين منه أن طاقة الإجهاد المتجمعة يتم تحريرها في منطقة فالق كلابشة من خلال الزلازل التي تحدث في هذه المنطقة.

ABSTRACT: On November 14, 1981 an earthquake with magnitude $M_s = 5.3$ occurred along Kalabsha fault, 60 km southwest of Aswan City, Egypt. As the High Dam is the single dam which controls the whole country, a program for monitoring recent crustal movements in Kalabsha area has been started in cooperation between the National Research Institute of Astronomy and Geophysics (NRIAG) and the High Dam Authority.

Analysis of the composite focal mechanism solution of the studied five different seismic zones in Aswan region showed that the focal mechanism is almost strike-slip faulting.

To monitor the crustal deformation around this area and to find its association with the seismic activity , a geodetic network consisting of 11 points was established early in 1997 on both sides of the northern part of Lake Nasser. This network was observed eight times in different campaigns during the period 1997 – 2004. The observed data was analyzed using Bernese 4.2 software to derive velocity vectors along both sides of Lake Nasser and to calculate the principal axes of strains.

The mean velocity for each year was nearly 2 mm/yr in direction nearly NE which is almost consistent with the direction of the African plate. These values of deformations are relatively small. Therefore, the area does not suffer from remarkable deformation except some areas around Kalabsha and Seiyal faults.

From the strain results, the northern part of Lake Nasser may be divided into three main parts: The northern part suffers from high compressional strains in northeast-southwest direction of about 0.1 $\mu\text{s/yr}$; the southern part of Lake Nasser has high extensional strains in the same direction of about 0.1 $\mu\text{s/yr}$; and the middle part of the study area including Kalabsha area has both low compressional and extensional strains in east – west direction and this may due to the energy released through the faults in this area.

INTRODUCTION

Although Egypt is not a major seismic zone, earthquakes may represent a significant seismic hazard.

Seismic zones of moderate seismic activity may affect the economic, strategic and civilized areas of the country.

According to the distribution of the earthquakes occurrences in Egypt, The National Research Institute of Astronomy and Geophysics (NRIAG) has started a program of monitoring recent crustal movements by means of geodetic space techniques since 1997 as shown in figure (1). Also, NRIAG has established a thirteen Telemetric Network around the study area to monitor the occurrence of earthquakes as shown in figure 2. This program includes establishing, measuring and analyzing of the data from the different geodetic networks.

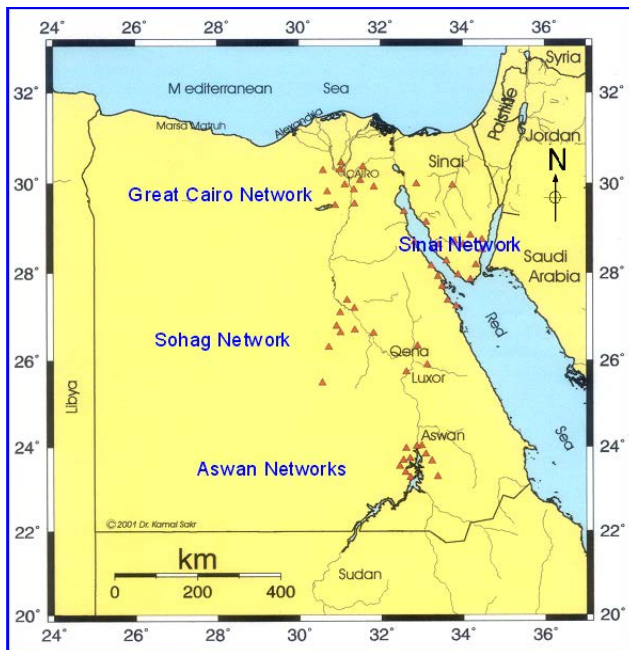


Figure 1: Distribution of the GPS networks in Egypt. (After Saker et al., 2002)

Structural and Tectonic Setting of the Study Area

Said (1990), divided Egypt into four major geological provinces; the Nubian-Arabian shield; stable shelf; unstable shelf, and Gulf of Suez-Red Sea graben. The Nubian-Arabian shield is extended over large parts of Egypt: the Eastern Desert; the southern Sinai Peninsula; and the extreme southern part of the Western Desert at Owienat area. The stable shelf is located north and west of the Nubian-Arabian shield and exhibits gentle tectonic deformation. However, the unstable shelf is situated north of the stable shelf with a transition zone between them

following a line that approximately runs from Siwa Oasis through Cairo-Suez into central Sinai.

As a result of the establishment of the High Dam, the area has been subjected to numerous geological investigations. The geologic studies covered many topics such as the structural settings and geomorphologic conditions of the study area (El-Shazly, 1966 and Issawi, 1978). On the other hand, the geophysical investigations covered the fields of gravity (Tealeb and Radwan, 1991) and geodesy (Mahmoud, 1988).

The structural pattern of Aswan area is characterized by regional basement rock uplift and regional faulting (Issawi, 1968). Local faults are supreme passed on essentially fault-lying structure of the Nubian plain and Sinn El-Kaddab plateau of Lake Nasser, (Issawi, 1968), as well as to the east of the Lake Nasser on Aswan hills as shown in figure 2. East of the River Nile, folds and faults are typically trending northwest having an acute angle to the primary structural upward. The northwest-trending faults are generally less than 50 km long, although some approach 100 km. Faults in the study area are subdivided into two systems depending on their trending direction as shown in figure 3.

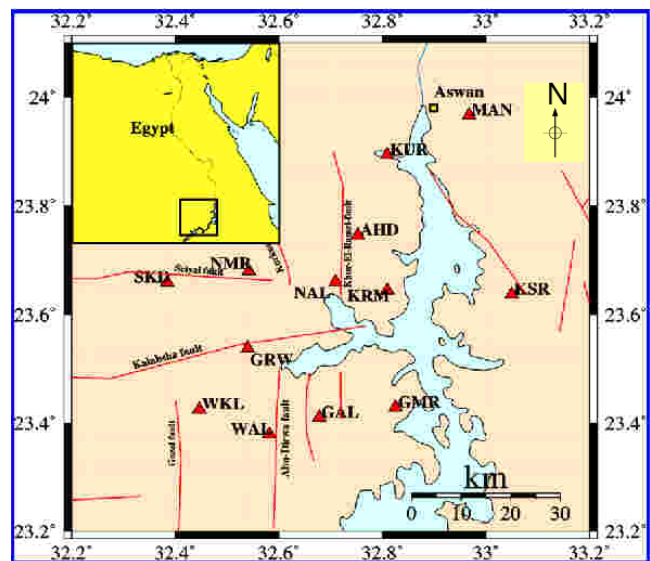


Figure 2: Seismic stations of the Local Seismic Network in Aswan (Egyptian National Seismic Network -ENSN- Bulletin)

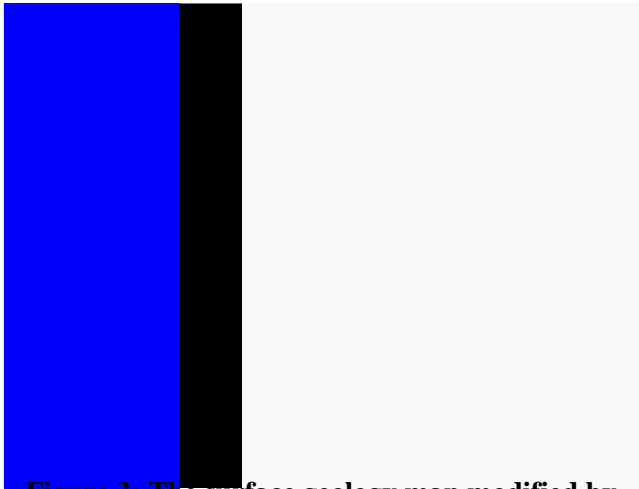


Figure 3: The surface geology map modified by Woodward - Clyde Consultants (WCC), 1985

where: 1- Latest Cretaceous sandstones and shale of Nubian Formation. 2- Precambrian metamorphic and plutonic rocks. 3- Latest Cretaceous rocks, mainly shale of the Dakhla Formation. 4- Paleocene to Eocene-age marine limestone. 5- Undivided Quaternary deposits.

Seismicity of the Study Area

The largest of Aswan earthquakes occurred on 14 November 1981 as shown in figure 4. This earthquake had a magnitude of $M_b=5.6$ (Kebeasy et al., 1982) and it was significant because of its possible association with Lake Nasser. This earthquake is located in Kalabsha area about 60 km south Aswan High Dam site, and it was strongly felt in Aswan and in areas to the north up to Assiut and to the south up to Khartoum. The intensity near the epicenter is between VII and VIII. This earthquake occurred in the Nubian Desert in the immediate vicinity of Lake Nasser at Aswan. Within an area of about 40 km radius from the epicenter, a few rubble masonry houses were badly damaged, and a few more were heavily cracked, but with no casualties. Tension features and ground cracks of doubtful tectonic origin were observed on the west side of the Lake in the Aeolian sands of the desert, running in an E-W direction for more than 10 km as shown in figure 5a. This zone of cracking is close and parallel to the Kalabsha Fault as shown in figure 5b, but the mechanism of the event determined teleseismically shows strike-slip faulting. Rockfalls and ground cracks were also found in the higher ground of the eastern bank of the Nile.

A catalogue for the period from June 1982 to 2004 was used for constructing the seismicity map of the Kalabsha area as shown in figure 6. The space distribution of the earthquakes constructing the seismicity map of Aswan area shows that the seismicity is concentrated in five main cluster zones (Fat-Helbary, 1995):

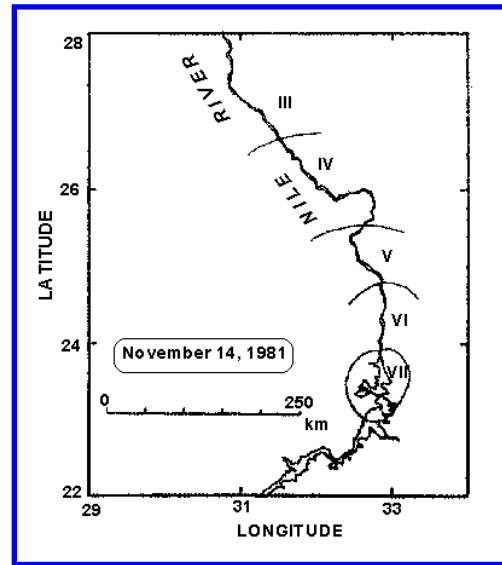
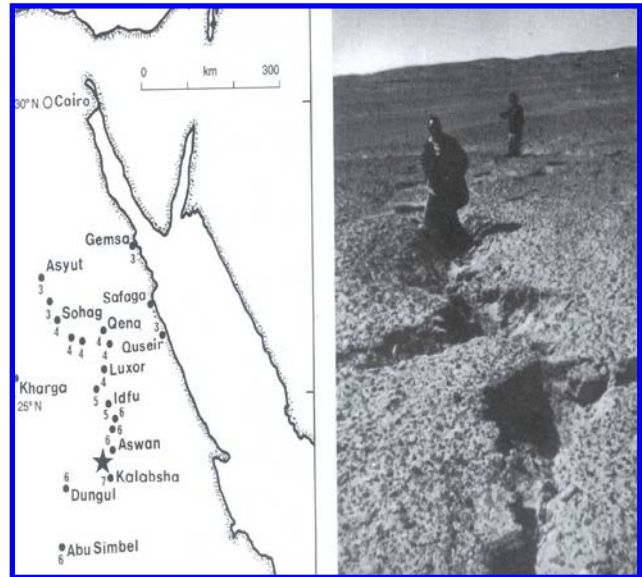


Figure 4: Intensity map of November 14, 1981 Earthquake (After Kebeasy et al., 1988)



5a

5b

Figure 5 (a&b): Cracking occurred due to 14 November, 1981 earthquake at Aswan area and location of Kalabsha fault (After Ambraseys et al., 1994)

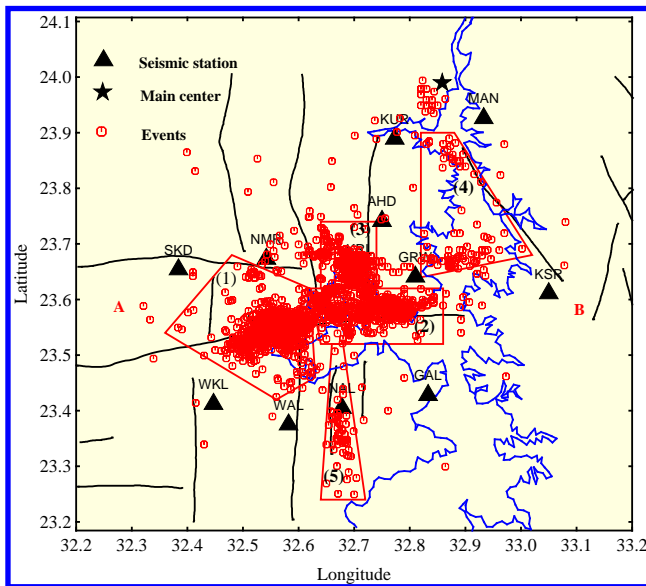


Figure 6: Seismicity zones of Aswan area (After Fat-Helbary, 1995)

Earthquake Focal Mechanism Solution

The focal mechanism studies deal with the mechanism of the resulted faults during earthquakes, where most earthquake occurrences are due to sudden rupture which takes place along faults in the Earth. It tells us about two possible faulting planes. The geological trends and the linear aspects of the earthquake aftershock distributions help to select more proper plane of faulting and determine stress orientations related to the earthquake activity of the geological structures, possibly observed on the surface.

In the present study, the focal mechanism was determined using the P-wave first motion. The first motion data are taken from records of observed stations, for which the true polarity must be known. The polarity of the first P-wave pulse from earthquakes takes either two opposite senses or compressions (up or pushed) or dilatational (down or pulled) depending on whether it is away from or towards the hypocenter. The polarity of P-wave varies, systematically, with azimuth and distance from the hypocenter.

In this study, the composite focal mechanism solution is applied on the classified seismic zones in Aswan area. This method is used when the number of stations is not enough to cover the focal sphere with data from a single earthquake.

Composite Focal Mechanism of Gabel Marawa Zone

Twenty-seven well-located events were used to determining the focal mechanism solution for this zone, with magnitude ranges between 1.8 and 3.1. From these earthquakes, 176 P-wave phases were used in this composite focal mechanism. Thirty-one well-located events, beneath Gabel Marawa, were used for composite fault plane projection, 153 phases of them are accepted for plotting solution (87% from the total phases). The reason of 13% failure for plotting may be related to errors in reading phases, instrument errors, or site noisy effect on the phase's direction and weight.

Figure 7 shows the composite fault plane solution determined in Gebel Marawa zone. The mechanism is characterized by strike-slip fault with normal component faulting, where the two nodal planes are nearly vertical with dip 84° and 87° from the horizontal plane. The nodal planes are 77° and 347° from the north and they are corresponding to the lineation segments which can be seen in the spatial earthquake epicenters distribution in Gebel Marawa zone.

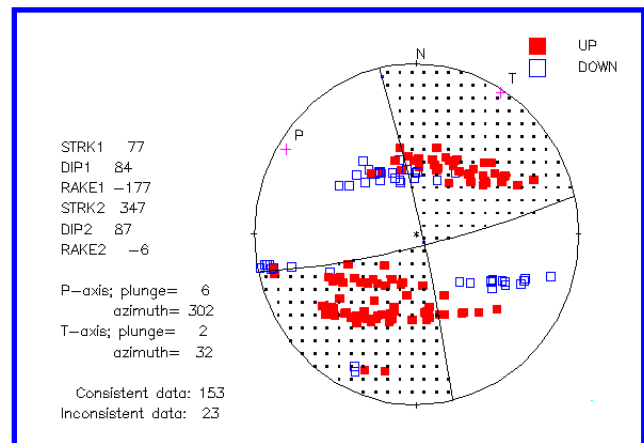


Figure 7: Composite focal mechanism for some events in Gabel Marawa zone (P and T are the inferred axes of maximum compression and tension respectively and double arrows indicate the sense of shear displacement on the plane that was chosen as a fault plane (for location, see fig.6).

Composite Focal Mechanism of East Gabel Marawa Zone

Twenty-five well-located events were used in East Gabel Marawa zone for focal mechanism solution. Their magnitude ranges between 2.4 and 3.4. The used total

number of the first motion polarities is 216. The consistent polarities with the obtained mechanism solution represent 92% from the total phases. The mechanism of this zone is characterized by strike-slip fault with right lateral motion as shown in figure 8. The nodal plane is striking 85° and dipping 85° , and it is considered to be a fault plane because it fits the N-W trend of the earthquakes distribution.

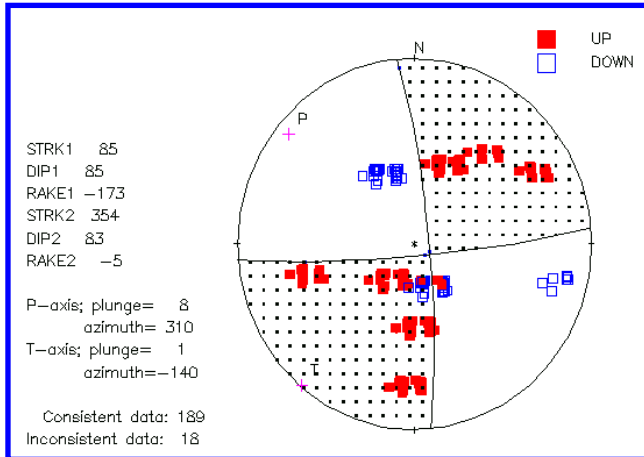


Figure 8: Composite focal mechanism for some events in East Gabel Marawa zone (for location, see fig. 6).

Composite Focal Mechanism of Khor El-Ramla Zone

Twenty well-located events were used to determining the focal mechanism of this zone, their magnitude ranges between 2.5 and 4.0. The used total number of the first motion polarities is 207 P-wave phases, and 87% of them succeeded for plotting the obtained composite fault plane solution. The mechanism of this zone is characterized by strike-slip fault with left-lateral motion as shown in figure 9. The nodal plane strikes 149° and has dip 85° and has left- lateral motion. This nodal plane is considered to be the fault plane. The direction of Khor El-Ramla zone fits well with the linear distribution of earthquake epicenters and approximately coincides, geologically, with the observed fault segment.

Composite Focal Mechanism of Abu Derwa zone

The activity of this zone has an N-S trend, south of Kalabsha fault. 11 well-located events were used to determining the focal mechanism of this zone, their magnitude ranges from 2.0 to 3.1. The used total number of the first motion polarities is 148 P-wave phases, 93% of them succeeded for plotting the obtained characterized by left-lateral strike-slip fault as shown in figure 10. The

nodal plane that has strikes 356° and dips 86° is considered to be the fault plane, corresponding to the lineation segment of the earthquake distribution in this zone and approximately coincides, geologically, with the observed fault segment.

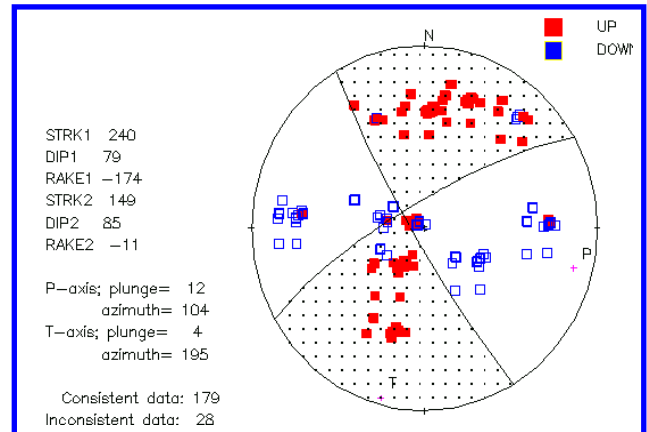


Figure 9: Composite focal mechanism for some events in Khor El Ramla zone (for location, see fig. 6).

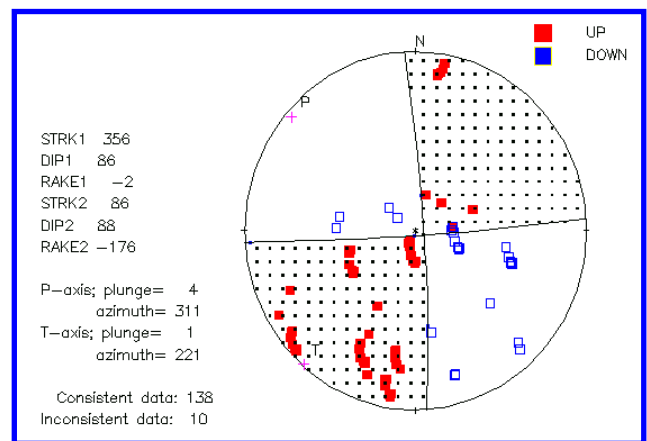


Figure 10: Composite focal mechanism for some events in Abu Derwa zone (for location, see fig. 6).

Composite Focal Mechanism of Old Stream zone

Eleven well-located events in the Nile River were used to determining the focal mechanism of this zone, their magnitude ranges from 1.6 to 3.2. From these earthquakes, 108 P-wave phases were used in this composite focal mechanism where 100 phases of them are accepted for plotting solution (92.5% of total phases). The mechanism of this zone is characterized by left-lateral strike-slip fault as shown in figure 11. The nodal plane of strike 331° and

dips 86° is considered a fault plane because this direction coincides nearly with that defined from the earthquakes clustering.

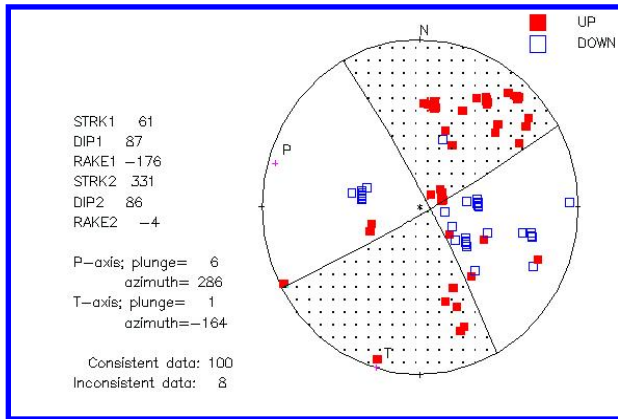


Figure 11: Composite focal mechanism for some events in Old Stream zone (for location, see fig. 6).

The careful analysis of the composite focal mechanism solution of the studied five different seismic zones in Aswan region shows the following remarks:

- ❖ All of the studied composite focal mechanism is almost strike-slip faulting on nearly vertical fault plane.
- ❖ There are two types of motion along these zones; right-lateral motions along the NEE-SWW fault system, and left-lateral motion along the NNW-SSE faults.

The segments are striking in a direction close to that seen in the strike of the fault plane solution and epicenter patterns.

GPS Measurements

GPS network consisting of 11 observation stations was established early in 1997 to detect the postseismic crustal deformation of the 1981 earthquake and to monitor the relative plate motions that surround the Northern part of Lake Nasser.

The initial measurements of this network were carried out in December 1997 using GPS Trimble 4000 SSI receivers. These measurements were repeated on May 1998, December 1998, April 1999, November 1999, 2000, 2002, and 2004 using the same receivers. The Elevation angle varied from 100 to 150 and sampling rate interval 30 seconds. GPS surveying differs essentially from classical surveying, because it is weather independent and there is no need for inter-visibility between the sites. Due to these differences, GPS surveys require different planning,

execution, and processing techniques. The optimum planning of GPS surveying has to consider several parameters such as site or satellite configurations, the number and the type of receivers to be used.

RESULT AND DISCUSSION

Velocity Results

Bernese software v4.2 including ADDNEQ2 was used to compute the common sets of the coordinates and velocities in the ITRF2000 for epochs from 1997 to 2004. The output of horizontal site velocities of the Northern part of Lake Nasser for all each epoch was represented on figures and we have seven tables and figures. But we develop just two examples to preview the results obtained. Table 1 and Figure 12 represent the output of the epoch from December 1997 to May 1998.

Table 1: Station velocities (V_x , V_y , V) in mm/yr and its direction (θ) of Aswan Regional Network in ITRF 2000 reference frame for the epoch from December 1997 to May 1998

Station Name and ID.	Velocity V_x (mm/yr)	Velocity V_y (mm/yr)	Total Velocity V (mm/yr)	θ
University (UNIV)	3.08	1.83	3.58	59.3
Rawraw (RARO)	3.07	1.83	3.58	59.2
Rest (REST)	3.08	1.84	3.59	59.15
North Marawa (NMAR)	3.08	1.84	3.59	59.16
Kalabsha 82 (KL82)	3.06	1.82	3.57	59.26
Gabel Alis (ALIS)	3.06	1.82	3.57	59.28
Garf Hussien (GARF)	3.07	1.82	3.56	59.39
Manam (MANA)	3.07	1.82	3.57	59.35
Dahmeet (DAHM)	3.06	1.82	3.56	59.35
Beer Om Hebal (BEER)	3.07	1.82	3.57	59.35
Wadi Al-Alaki (ALAK)	3.06	1.8	3.55	59.55

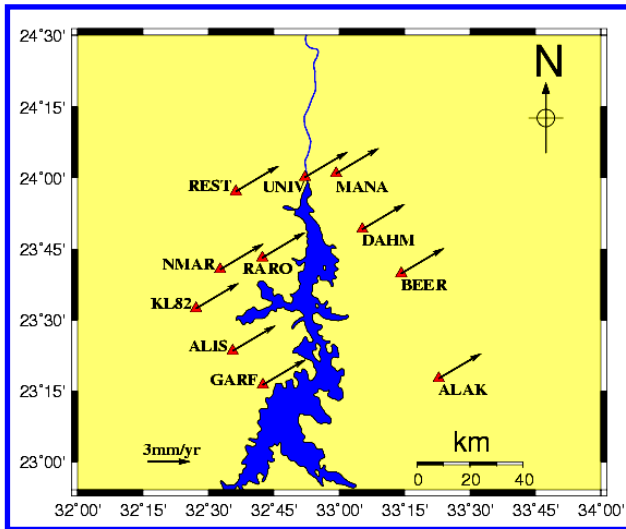


Figure 12: The horizontal velocities of Aswan Regional Network relative to IGS permanent stations from December 1997 to May 1998

Table 2: Station velocities (V_x , V_y , V) in mm/yr and its direction (θ) of Aswan Regional Network in ITRF 2000 reference frame for the epoch from December 1997 to 2004

Station Name and ID.	V_x (mm/yr)	V_y (mm/yr)	Total Velocity V (mm/yr)	θ
University (UNIV)	13.58	7.75	15.64	56.08
Rawraw (RARO)	12.93	8.36	15.40	57.14
Rest (REST)	12.94	8.71	15.60	56.08
North Marawa (NMAR)	12.78	8.76	15.49	55.60
Kalabsha 82 (KL82)	13.5	7.72	15.55	60.27
Gabel Alis (ALIS)	13.1	7.65	15.17	59.75
Garf Hussien (GARF)	11.85	9.11	14.95	52.47
Manam (MANA)	12.33	7.11	14.23	60.06
Dahmeet (DAHM)	14.29	10.71	17.86	53.18
Beer Om Hebal (BEER)	13.59	7.64	15.59	60.69
Wadi Al-Alaki (ALAK)	13.83	7.8	15.88	60.61

Also table 2 and figure 13 represent the output of horizontal site velocities of the Northern part of Lake Nasser of all the period from 1997 to 2004. As shown in table 1 and figure 12, the movement rate in the period from December 1997 to May 1998 around all stations is nearly equal. The mean velocity of this epoch is 3.57 mm/yr in NE direction.

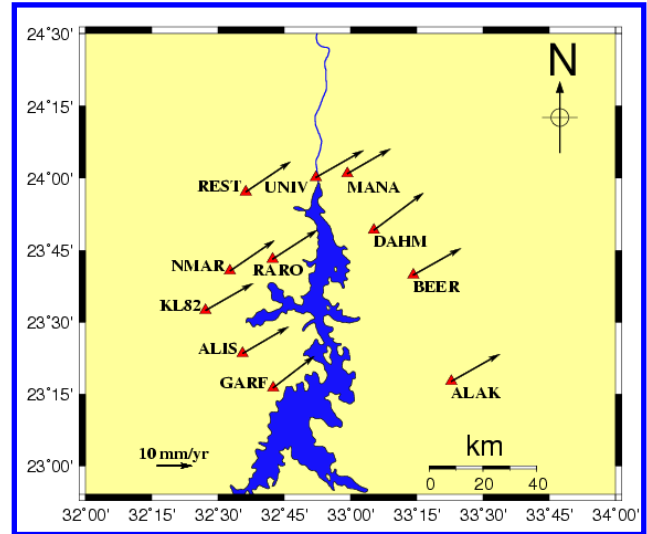


Figure 13: The horizontal velocities of Aswan Regional Network relative to IGS permanent stations from December 1997 to 2004

Also, the combined solutions of all epochs from 1997 to 2004 are outlined in table 2 and figure 13. The maximum velocity was 17.86 mm in eight years at Dahmeet (DAHM) station in NE direction while the minimum velocity was 14.95 mm in eight years at Garf Hussien station (GARF) in NE direction. Last, GPS measurements collected in campaign mode during 1997-2004 have been analyzed to derive velocity vectors around the northern part of Nasser Lake and average of the velocity was 16.02 mm/yr.

Strain Results

The principal axis of strains in the Northern part of Lake Nasser was calculated using strain tensor program (Mahmoud, 2001). The output of this program was shown on several tables and figures but we also choose two examples to preview the results obtained.

As given in table 3 and figure 14 for the epoch from December 1997 to May 1998, the maximum extension strain was 0.13 $\mu\text{s/yr}$ at Wadi Al-Alaki (ALAK) station in the NNE direction while the minimum extension was 0.04 $\mu\text{s/yr}$ at Kalabsha 82 (KL82) station in the EW direction nearly.

Table 3: The strain components of Aswan Regional Network for the epoch from December 1997 to May 1998

Station Name and ID.	Velocity ϵ_1 ($\mu\text{s/yr}$)	ϵ_2 ($\mu\text{s/yr}$)	Direction of ϵ_1 (Azimuth)
University (UNIV)	0.049	- 0.144	40.12
Rawraw (RARO)	0.06	- 0.04	6.55
Rest (REST)	0.064	- 0.168	29.12
North Marawa (NMAR)	0.051	- 0.042	1.32
Kalabsha 82 (KL82)	0.04	- 0.024	0.8
Gabel Alis (ALIS)	0.11	- 0.004	-16.19
Garf Hussien (GARF)	0.091	- 0.05	- 27.95
Manam (MANA)	0.0702	- 0.122	37.5
Dahmeet (DAHM)	0.0413	- 0.109	35.9
Beer Om Hebal (BEER)	0.106	- 0.04	-47.9
Wadi Al-Alaki (ALAK)	0.13	- 0.043	-37.01

Table 4: The strain components of Aswan Regional Network for the epoch from 2002 to 2004

Station Name and ID.	Velocity ϵ_1 ($\mu\text{s/yr}$)	ϵ_2 ($\mu\text{s/yr}$)	Direction of ϵ_1 (Azimuth)
University (UNIV)	0.025	- 0.079	39.19
Rawraw (RARO)	0.04	- 0.026	16.63
Rest (REST)	0.036	- 0.069	27.8
North Marawa (NMAR)	0.046	- 0.051	13.25
Kalabsha 82 (KL82)	0.039	- 0.024	8.29
Gabel Alis (ALIS)	0.077	- 0.036	- 16.18
Garf Hussien (GARF)	0.071	- 0.042	- 17.95
Manam (MANA)	0.039	- 0.088	15.35
Dahmeet (DAHM)	0.035	- 0.099	19.22
Beer Om Hebal (BEER)	0.087	- 0.031	- 27.8
Wadi Al-Alaki (ALAK)	0.086	- 0.043	- 35.8

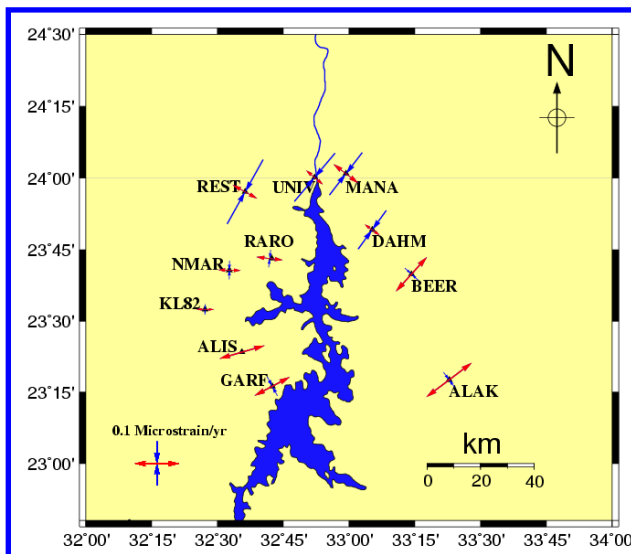


Figure 14: The principal axes of strain of Aswan Regional Network from December 1997 to May 1998.

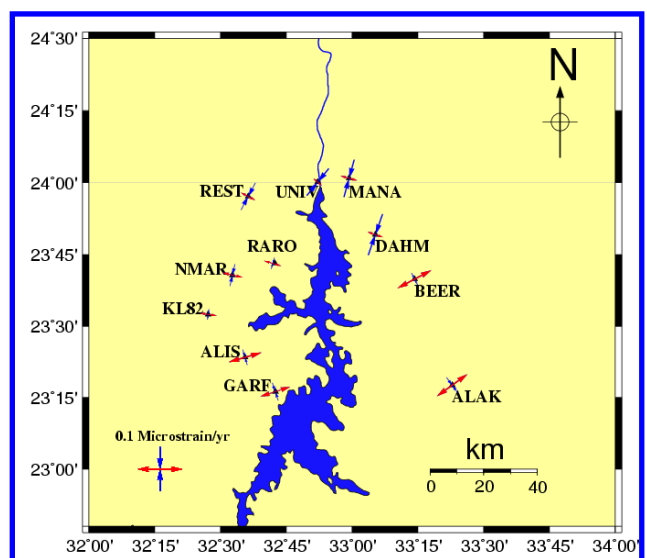


Figure 15: The principal axes of strain of Aswan Regional Network from 2002 to 2004

On the other hand, the maximum compression strain which is perpendicular to the extensional direction was 0.168 $\mu\text{s}/\text{yr}$ at Rest (REST) station in NNE direction while the minimum compression strain was 0.024 $\mu\text{s}/\text{yr}$ at Kalabsha 82 (KL82) station in the EW direction.

For the epoch, from 2002 to 2004, the maximum extension strain was 0.087 $\mu\text{s}/\text{yr}$ in the NNE direction at Beer (BEER) station while the minimum extension strain was 0.025 $\mu\text{s}/\text{yr}$ in the NNE direction at University (UNIV) station. With respect to the compression strain, the maximum compression strain was 0.099 $\mu\text{s}/\text{yr}$ in NNE direction at Dahmeet (DAHM) station while the minimum compression strain was 0.024 $\mu\text{s}/\text{yr}$ in NNE direction at Kalabsha 82 (KL82) station as shown in table 4 and figure 15.

CONCLUSIONS

According to the fact that crustal deformation processes could occur during the accumulation of the energy within the Earth's crust as well as its release producing earthquakes of certain magnitudes. Therefore, monitoring the rates of crustal deformations is valuable information about the seismic activity. This information is important for the seismic hazard assessment and minimizing the losses due to earthquake damage. The difference in magnitude and direction of the horizontal movements in the studied area is deduced from the difference of tectonic patterns.

The careful analysis of the composite focal mechanism solution of the studied five different seismic zones in Aswan region showed that all of the studied composite focal mechanism is almost strike-slip faulting on nearly vertical fault plane and there are two types of motion along these zones; right-lateral motions along the NEE-SWW fault system, and left-lateral motion along the NNW-SSE faults.

The analysis of GPS data using Bernese software showed that the mean horizontal velocity for every year is of about 2 mm/yr in NE direction and the average of the horizontal velocity from 1997 to 2004 is 16.02 mm/8yr in NE direction in general and this has given us an impression that this area of Egypt is nearly seismic stable and does not suffer from any deformations except in areas around Kalabsha fault.

Estimated displacement vectors were used to reconstruct the strains using strain tensor software and the results showed that we can divide the area under study into three parts: the northern parts suffers from high compressional strain of about 0.098 $\mu\text{s}/\text{yr}$ in NE-SW direction; the southern part suffers from high extensional

strain of about 0.096 $\mu\text{s}/\text{yr}$ in the same direction of the previous part; and the middle part of this area has low strain in general and this is owing to release of the energy through Kalabsha fault.

REFERENCES

- Ambraseys, N.N.; Melville, C.P.; and Adams, R.D., (1994):** The Seismicity of Egypt, Arabia, and the Red Sea. Cambridge Press, P. 181.
- El-Shazly, E.M., (1966):** Structural development of Egypt, U.A.R., Geol. Soc. Egypt, Fourth Annu. Meeting, Programme and Abstracts, PP. 31-38.
- Fat-Helbary, R.E., (1995):** Assessment of seismic hazard and risk in Aswan area, Egypt. Ph.D. Thesis. Architectural Engineering Department. Tokyo Univ., Japan. P. 182.
- Issawi, B., (1968):** The Geology of Kurkur-Dungul area, southwestern Desert, Egypt. Ann.Geol.Survey. Egypt: 102.
- Issawi, B., (1978):** The Geology of Nubia, west area, Western Desert. Ann.Geol.Survey. Egypt, Vol. 8, PP. 237-253.
- Kebeasy, R.M.; Maamoun, M.M.; and Ibrahim, E.M., (1982):** Aswan Lake Induced Earthquakes; Bull. of the Int. Instit. of Seismology and Earthquake Engineering, Japan, Vol. 19, PP. 155-160.
- Kebeasy, R.M.; Tealeb, A.; Gharib, A.; and Mahmoud, S.M., (1988):** Water loading is an effective factor in inducing seismicity around Aswan Lake. Proc. 6th annual Meeting of the EGS, Cairo, March, 1988.
- Mahmoud, S.M., (1988):** Crustal deformation measurement in the southwestern part of Lake Nasser based on observation from local seismic and geodetic networks. M.Sc. thesis, Ain Shams University, Cairo, Egypt.
- Mahmoud, S.M., 2001.** Strain Analysis deduced from the results of GPS measurements in Sinai Peninsula and around the Gulf of Suez, Egypt. Bull. of NRIAG, Cairo, Egypt. pp. 265-282.
- Said, R., (1990):** The Geology of Egypt. Balkema, Rotterdam, Book Field, P. 734.
- Sakr, K.; Tealeb, A.; Mohamed, A.S.; and Mahmoud, S.M., (2002):** Monitoring of crustal deformation using Geodetic Technique: case study in Egypt. NRIAG Journal of Geophs. Vol. 1, No. 1, PP. 131-153.

Tealeb, A., and Radwan, A.H., (1991): Gravity map of Seiyal area, northwest of Aswan Lake and its subsurface structural setting. *J. of Geodynamics*, Vol. 14, PP. 137-146.

Woodward - Clyde Consultants, WCC (1985): Earthquake activity and Dam stability evaluations for the Aswan High Dam, Egypt: Report for the High and Aswan Dams Authority, Ministry of Irrigation, A.R. Egypt, (internal report), Egypt, Contract No. 263-0102-C-00-HADA-00 USAID Project No. 263-0042.

ABEL INVERSION FOR DERIVING REFRACTIVITY PROFILE FROM DOWN LOOKING GPS RADIO OCCULTATION: SIMULATION ANALYSIS

A. MOUSA

National Research Institute of Astronomy and Geophysics, Helwan, Cairo, Egypt,
E-Mail : ashrafkm@yahoo.com

استنباط التوزيع الرأسى لمعامل الانكسار فى الغلاف الجوى باستخدام طريقة أبل العكسية وبيانات النظام العالمى للإحداثيات GPS
القادمة من أسفل والمستترة فى الغلاف الجوى

الخلاصة: تستخدم موجات الـ GPS القادمة من أسفل والمستترة فى الغلاف الجوى فى حساب التوزيع الرأسى لمعامل الانكسار فى الغلاف الجوى. وتعتبر زاوية انحناء الأمواج كدالة فى معامل التأثر هي الأرصاد الرئيسية لهذا الاستخدام. توفر موجات الـ GPS القادمة من أسفل كل من الأرصاد ذات زوايا الأرتفاع الموجبة والسالبة. ولحساب التوزيع الرأسى لمعامل الانكسار فى الغلاف الجوى يمكن استخدام طريقة أبل العكسية. وتطلب طريقة أبل شرط التماثل الكرى. و لذلك يتم حساب فرق زوايا انحناء الأمواج ذات زوايا الأرتفاع الموجبة و السالبة مما يعنى التخلص من تأثير طبقة الأيونوسفير. يقيم البحث الحالي طريقة أبل لحساب التوزيع الرأسى لمعامل الانكسار فى الغلاف الجوى باستخدام نماذج المحاكاة التى تستعين ببيانات النماذج الرياضية للغلاف الجوى و كذلك أرصاد البالونات. و قد تم عمل تحليل البيانات باعتبار الغلاف الجوى فى حالتيه الجافة و الرطبة. و قد أظهرت النتائج أنه يمكن استخدام طريقة أبل لحساب التوزيع الرأسى لمعامل الانكسار بدقة عالية. و كانت قيمة الخطأ النسبى المئوية فى حدود ٠,٢%.

ABSTRACT: Down Looking (DL) GPS radio occultation can produce an estimate of the atmospheric refractivity profile. The main observations are the bending angle as a function of the impact parameter. DL Provides both negative as well as positive elevation angle measurements. Abel inversion can be operated on a profile of partial bending angle found by subtracting the positive elevation measurement from the negative one with the same impact parameter. Abel inversion requires the spherical symmetrical assumption. Basically, partial bending calculation removes the ionospheric bending and hence it is possible to use a single frequency GPS receiver.

The current paper introduces a simulation data for the case of a receiver on Mountain top. The simulation uses model refractivity from MSISE-90 Model as well as radiosonde data. Random noises are added to the bending angle profile before inversion. The result shows that it is possible to produce accurate vertical refractivity profile below the receiver altitude. The calculation of the water vapor profile is also made using temperature profile information from the MSISE-90 Model as well as radiosonde. The relative errors in the retrieved refractivity profile are always less than 0.2%.

INTRODUCTION

When electromagnetic signal passes through the atmosphere, it is refracted. The magnitude of the refraction depends on the gradient of refractivity normal to the path, which depends on the gradients of density and water vapor. Thus measurements of refraction will contain information on the density (and hence temperature) and the water vapor along the path. The effect is more pronounced when the signal traverses a long atmospheric limb path. A series of such a path at different tangent heights yields measurements containing information on the vertical profile of refractivity (fig. 1). Refractivity can be converted to a profile of temperature and/or water vapor. At radio frequencies, it is not possible to make direct and accurate measurements of the refracted angle. However, if the transmitter and receiver are in relative motion, the refraction introduces a change in the Doppler shift of the received signal, and this can be related to the refracted angle [Eyre, 1994; Larsen et al, 2004].

There were early proposals for remote sensing of the earth's atmosphere using such "radio occultation" or "refractometry" techniques [Fishbach, 1965; Lusignan et al, 1969]. However, due to technical limitations, till recently they have only been applied successfully to studies of the planetary atmosphere [e.g. Kliore et al, 1965]. With the advent of Global Positioning System (GPS), together with the possibility of GPS receiver aboard a Low Earth Orbiter (LEO), it is now used for accurately sensing the earth's atmosphere.

The high accuracy of the radio occultation measurements using GPS at wavelengths 19 and 24 cm was demonstrated [Melbourne et al., 1994; Ware et al., 1996; Kursinski et al., 1996, 1997; Rocken et al, 1997; Feng and Herman, 1999; Schreiner et al., 1999]. First experiments in other frequency bands have been conducted in 1989-1998 years at wavelengths 2 and 32 cm as described by Yakovlev et al. [1995] and Yakovlev [1998].

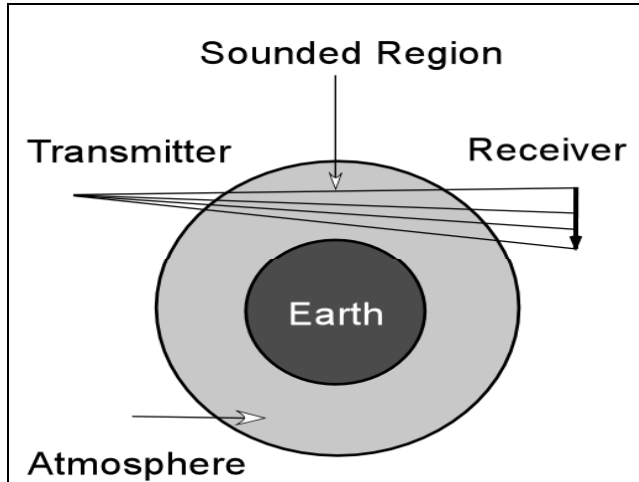


Fig. 1. Concept of refractivity profiling using Radio Occultation Technique

While GPS-LEO occultation data have the advantage of being global (One receiver in LEO provides about 500 globally distributed occultations per day), the sampling in any region is relatively sparse without a large number of orbiting receivers [e.g. Kursinski et al, 1997]. By contrast, a receiver located inside the earth's atmosphere (such as on a mountain top, or an airplane) can be used to provide data over specific areas of interest for the purpose of regional weather and climate studies [Cinzia et al, 1999].

A mountain-based or airborne receiver would track any GPS satellite as it sets or rises behind the earth's limb. Therefore data can be collected at both negative and positive elevation angles relative to the receiver local horizon (fig. 2). The Viewing geometry of a down-looking GPS receiver located inside the atmosphere can be considered as a hybrid between the space and the ground based geometry. It combines the high vertical profiling capabilities of space data (at least for heights below the receiver) with the benefit of routinely obtaining a relatively large number of daily profiles in region of interest. Every occultation will produce a profile of refractivity below the height of the receiver, with a diffraction-limited, vertical resolution of 150-250m.

One receiver with a full 360^0 field of view will observe nearly 96 occultations per day scattered within 200 km radius of the receiver. If the topography allows the use of several receivers, separated by distance of 50-200 km, hundreds of daily occultation can be obtained over that region. Such profiles when integrated with the accumulated water vapor distribution derived from ground based receivers, and possibly moisture information from any other accurate observations, is extremely useful for

regional weather monitoring as well as hydrological research.

For LEO occultation, Abel inversion is used to obtain the refractivity profile. Although fundamentally DL measurements are similar to the LEO measurements, it was originally thought that the limits of integration used in the Abel transform prevented its implementation when the receiver is inside the atmosphere [Zuffada et al. 1999]. In fact, it is possible to use an Abel inversion for the DL case. The measurement geometry is similar to the one considered by Bruton and Kattawar [1997] when inverting solar occultation data.

The current paper introduces down looking GPS occultation concept. The paper is organized as follows: section 2 introduces the GPS occultation technique and the Abel inversion to drive the refractivity profile from the observation. Section two ends with the procedure used to calculate the temperature and/ or vapor from the obtained refractivity. The simulation is carried out for a 3.8 km high Mountain. The simulation analysis and the results are introduced in section 3. The analysis indicates that GPS receiver inside the atmosphere can be used to retrieve accurately the refractivity profile with high resolution.

GPS OCCULTATION TECHNIQUE

For each occultation event, the GPS occultation data analysis chain from the measured phase delay to the derivation of the neutral atmospheric parameters and can be divided into three main steps [e.g. Mousa and Tsuda, 2001]:

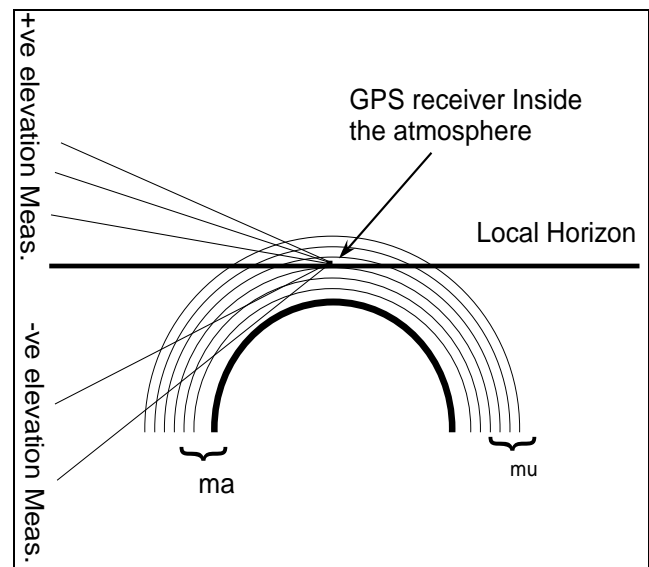


Fig. 2. A pictorial view of GPS down looking scheme. Atmospheric layers below the receiver

location are denoted by μ and those above the receiver by μ .

1. Calculation of the atmospheric bending angle profile from the observed L1/L2 excess phase path time series (L1 and L2 are the phases of the two GPS carrier frequency).
2. Retrieval of the refractivity profile from the atmospheric bending angle
3. Calculation of the density, pressure and temperature or water vapor profiles based on the retrieved refractivity profile.

BENDING ANGLE CALCULATION

In the geometric optics approximation, a ray passing through the atmosphere behaves according to Fermat's principle of least time. The ray travel along a curve defined by:

$$n \times r \sin(\varphi) = \text{constant} \equiv a \tag{1}$$

Where r is the distance from the origin of symmetry to a point on the ray path, φ is the angle between the direction of r and the tangent to the ray path, and n is the refractive index at r (fig. 3). Equation (1) corresponds to Snell's law in polar coordinates for a spherically symmetric medium, and known as Bouguer's formula. On this basis, a signal travelling in a spherically symmetric medium will bend by an angle (α) [Born and Wolf, 1980]:

$$\alpha = -2a \int_{a \sqrt{(n^2 r^2 - a^2)}}^{\infty} \frac{1}{n \sqrt{(n^2 r^2 - a^2)}} \frac{dn}{dr} dr \tag{2}$$

Where a is the impact parameter of the ray.

The basic GPS data from which the bending angle (α) is derived are the L1 and L2 phase delay. From knowledge of the position of the transmitter (r_t) and the receiver (r_r) and their clocks (fig. 3), the extra delay due to the atmosphere can be isolated [e.g., Hajj et al., 1996].

From knowledge of the atmospheric extra delay as a function of time the extra atmospheric Doppler can be derived. This extra atmospheric Doppler is related to the bending of the signal via the equation:

$$\Delta f = -f/c (V_r^r \cos \Phi_r + V_r^\theta \sin \Phi_r + V_t^r \cos \Phi_t - V_t^\theta \sin \Phi_t) \tag{3}$$

Where f is the GPS transmitter frequency, c is the speed of light, V_r and V_t are the receiver and transmitter velocity vectors. The superscript r and θ indicate the radial and tangential component of the velocity vector, respectively. Φ_r and Φ_t are the angles between the ray bath and the direction of r as before, but for both the receiver and the transmitter respectively.

From equation (3) and the following equation, that is implied by Bouguer's formula,

$$r_t n_t \sin(\psi_t + \delta_t) = r_r n_r \sin(\psi_r + \delta_r) = a \tag{4}$$

(Angles are defined in figure 3) we can drive the total bending of the ray ($\alpha = \delta_t + \delta_r$) as a function of the impact parameter (a). This bending angle (α), as a function of the impact parameter (a), is the fundamental function to be inverted.

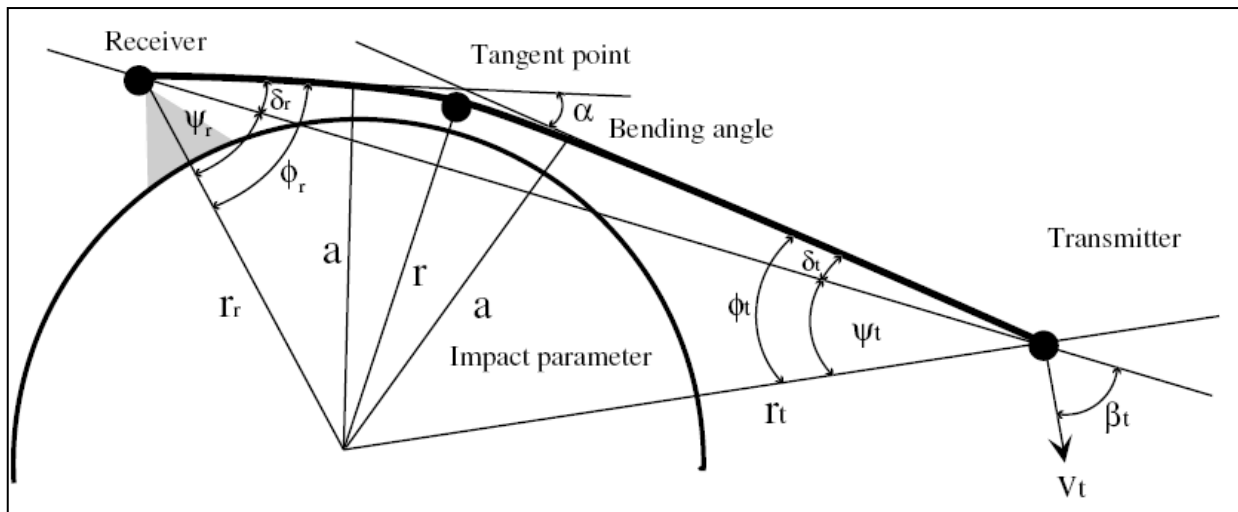


Fig.3. A schematic diagram defining the geometrical variables for a GPS transmitter/receiver link.

INVERSION SCHEME

The Abel inversion has been used extensively in seismic and astronomical inversions, as well as planetary and Earth occultation data [e.g. Fjeldbo et al. 1971; Kursinski et al. 1997]. Starting with the bending angle determined from the GPS Doppler shift, equation (2) is inverted with Abel inversion to give the refractive index [e.g. Tricomi, 1977]:

$$n(x) = \exp\left(\frac{1}{\pi} \int_a^\infty \frac{\alpha(a)}{\sqrt{(a^2 - x^2)}} da\right) \quad (5)$$

Where $x = nr$ is the refractive radius.

Unlike the LEO case, in DL occultations there may be significant ray bending along sections of the path above the receiver position, so the bending will not be equal on both sides of the tangent point. However Bruton and Kattawar [1997] noted that when the receiver is within the atmosphere, it is possible to observe rays at both positive and negative elevations. These refer to rays that intersect the receiver from above and below the local tangent. They also pointed out that, assuming spherical symmetry, for every negative elevation ray with bending angle α_{neg} there is a corresponding positive elevation value α_{p} with the same impact parameter value. Subtracting α_{p} from α_{neg} gives the partial bending angle α' (a)

$$\alpha'(a) = \alpha_{\text{neg}}(a) - \alpha_{\text{p}}(a), \quad (6)$$

Where α' (a) is the bending that occurs along the section of path below the receiver. By definition, as the tangent point approaches the receiver distance, r_r , the partial bending approaches zero.

The partial bending angle α' (a) can be written as:

$$\alpha'(a) = -2a \int_a^{n(r_r)r_r} \frac{d \ln(n)/dx}{\sqrt{(x^2 - a^2)}} dx \quad (7)$$

Where $x = nr$, $n(r_r)$ is the refractive index at the receiver position and r_r is the receiver position. Equation (7) can be inverted with,

$$n(x) = n(r_r) \exp\left(\frac{1}{\pi} \int_x^{x(r_r)} \frac{\alpha'(a)}{\sqrt{(a^2 - x^2)}} da\right) \quad (8)$$

Where $x(r_r)$ is the refractive radius at the receiver position.

CALCULATION OF ATMOSPHERIC PARAMETERS

In the third step of the data analysis, the atmospheric parameters density (ρ), pressure (P), temperature (T) and /or water vapor (e) are derived from the refractivity profile

using the dependence of refractivity on these parameters [e.g. Steiner et al., 1998]. Neutral refractivity (N) is given as [Smith and Weintraub, 1953]:

$$N = 77.6 P/T + 3.73 \times 10^5 e/T^2 \quad (9)$$

In regions where the atmosphere is drier than a volume-mixing ratio of 10^{-4} , the atmospheric parameters ρ , P, T can be derived directly from equation (9) (as the vapor pressure e is zero in that case). However, in a warmer tropical region, the contribution of the water vapor to refractivity is significant and cannot be ignored. In such a case, there is ambiguity between the temperature and water vapor. One can only solve for either the water vapor or the temperature using a priori meteorological and observation data.

An iteration process is proposed by Gorbunov and Sokolovskiy[1993] to solve for the water vapor, starting with temperature knowledge and assuming dry air and then derive the pressure using the hydrostatic equation. After that, the pressure and temperature is used (via equation (9)) to calculate a first estimate water vapor and so on. The procedure converges after two iterations.

SIMULATION ANALYSIS

In order to validate the algorithm's ability to retrieve refractivity (as well as temperature and /or water vapor) when a receiver is inside the atmosphere, we constructed three sets of simulated measurements; dry case, wet case and wet case based on Radiosonde observations. The receiver is fixed at 3.8 km altitude tracking GPS signals at both positive and negative elevations.

When the receiver is outside the atmosphere, bending measurements are smoothed over the time it takes the tangent height of the ray to descend the diameter of the first Fresnel zone [Kursinski et al., 1997]. In the geometric optics framework these smoothed measurements are approximately independent. Layer boundaries are then introduced between the tangent point of each of the measurements. The radius of the tangent point corresponding to a certain (α) measurement is estimated by solving the relation ($a = r \cdot n(r)$) where $n(r)$, the index of refraction at r , is obtained from the a priori model used as a first guess.

For a receiver inside the atmosphere, the bending measurements α_i are grouped into a set of m_a 'negative elevation' measurements and a set of m_p 'positive elevation' measurements. The typical behavior of the bending $\alpha(a)$ is given in figure (4). This figure shows that, for a fixed receiver, the transition between negative and positive elevation data correspond to the maximum (a) of the (α) vs. (a) curve. This property is used to separate the negative observation from the positive one.

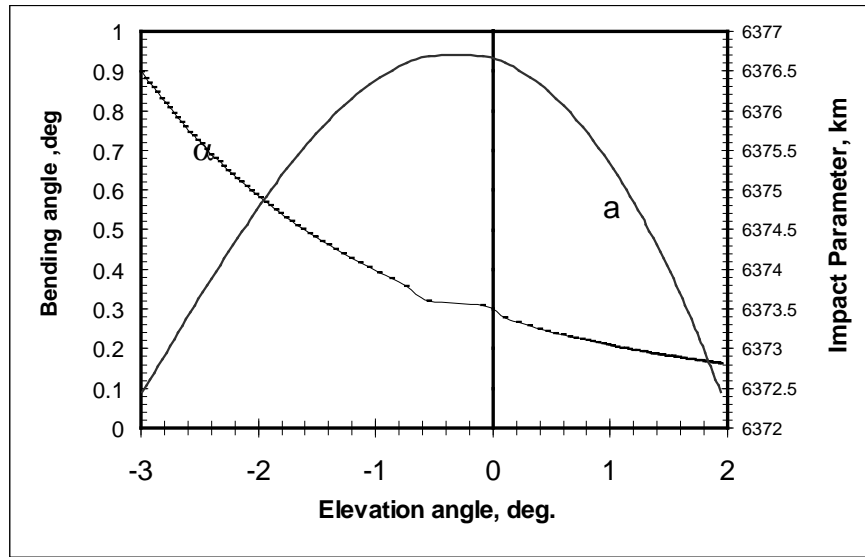
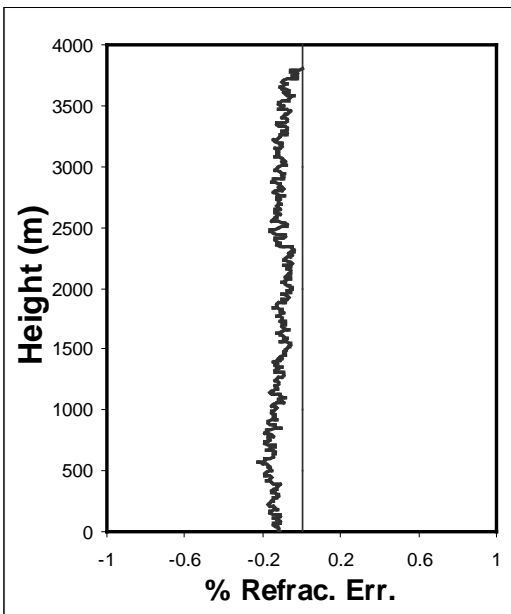
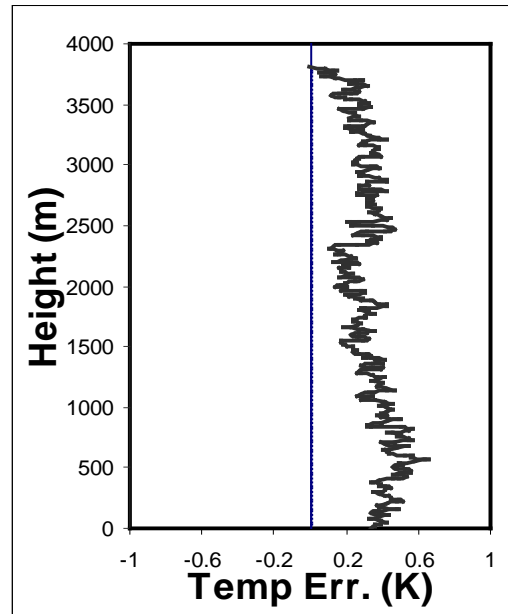


Fig. 4. bending (α) and impact parameter (a) as a function of elevation angle for a receiver at 3.8 km altitude.



a



b

Fig. 5. Dry atmospheric case. (a) Fractional error in retrieved refractivity as a function of height; (b) error in retrieved temperature as a function of height.

In all cases, starting with a model refractivity to be the truth, a set of rays linking the transmitter to the receiver were constructed with specified tangent heights, ranging from the earth's surface to the receiver's height. In a similar fashion, a set of rays linking the GPS satellite to the receiver was constructed to represent positive elevation angles above the receiver horizon. The positive measurements have impact parameter given by equation (1), where r is the radius of the receiver and φ is between 90° (0° elevation) and 180° (zenith). Noise was added to the simulated bending measurements assuming the standard deviation of the bending angle to be (σ) ($\sigma = 0.01 + 10^{-5}$ (radian)). This value accounts for the spherical approximation as well as to the receiver noise.

Dry case

The MSISE-90 [hedin, 1991] model is used here to represent the model refractivity from which the synthetic bending data were generated. The retrieved refractivity (after inversion) is compared to the model one to check the accuracy of the solution. The percentage of the fractional errors of the retrieved refractivity is introduced in figure (5-a). It is obvious from figure (5-a) that the errors are usually less than .2% up to the receiver height.

For this dry case, the temperature was driven using the hydrostatic equation following the procedure described before in section (2-3). From figure (5-b) we easily deduce that the error of the temperature retrieval is always less than 1 K. The temperature errors are gradually reduced from the earth's surface (about 0.6 K) to the receiver location (about 0.2 K).

WET CASE

Similar to the dry case, the MSISE-90 model is used here to represent the dry part of the model refractivity. The wet part is added by assuming water vapor pressure to follow an exponential model with scale height equal to 2.5 km. A weighting function is used to insure that the water vapor goes to zero at the height of 10 km. The total refractivity (dry + wet) is used as the model to derive synthetic bending data. The percentage of the fractional errors of the retrieved refractivity is shown in figure (6-a). Figure (6-a) shows that the errors are usually less than 0.2% up the receiver height.

For that wet case, water vapor was driven using the iterative procedure described earlier in section (2-3). The temperature is assumed known and taken from the MSISE-90 model. From figure (6-b) it is seen that the error of the water vapor retrieval is always less than 0.1 mbar.

RADIOSONDE BASED CASE

In this case the radiosonde observation is used to calculate the dry and wet refractivity model. The total refractivity (dry + wet) is used as the model to derive synthetic bending data. The percentage of the fractional errors of the retrieved refractivity is shown in figure (7-a). Figure (7-a) shows that the errors are usually less than 0.2%.

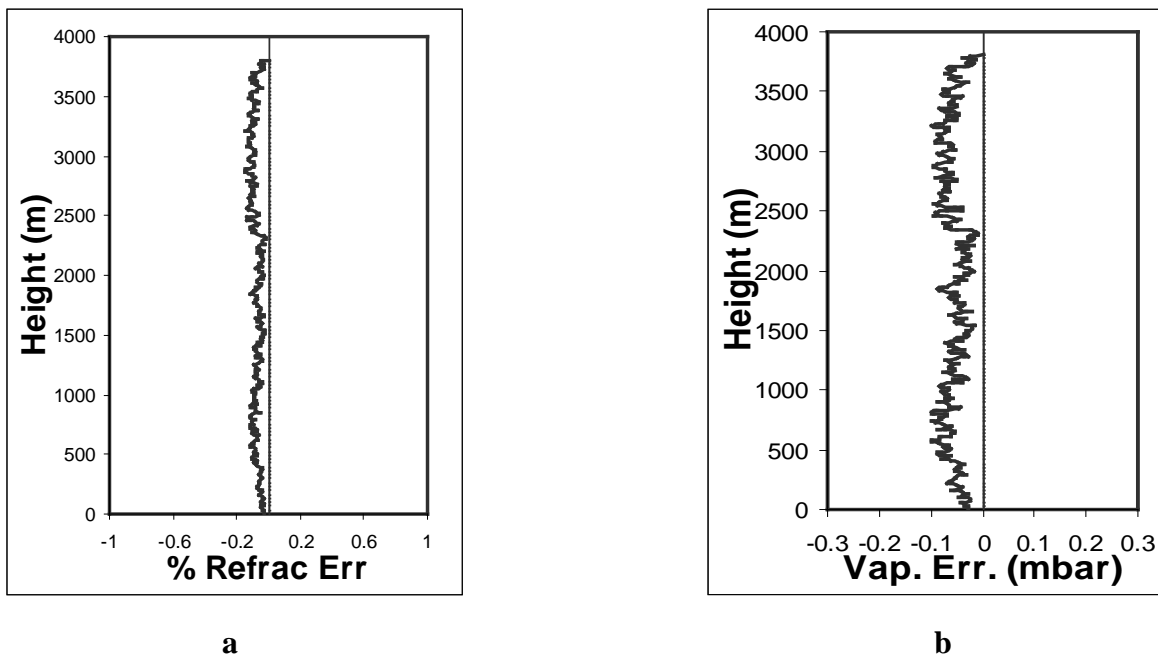


Fig. 6. Same as figure 5; but for the wet case. Both dry and wet part of the refractivity follow an exponential law; (b) water vapor retrieval errors.

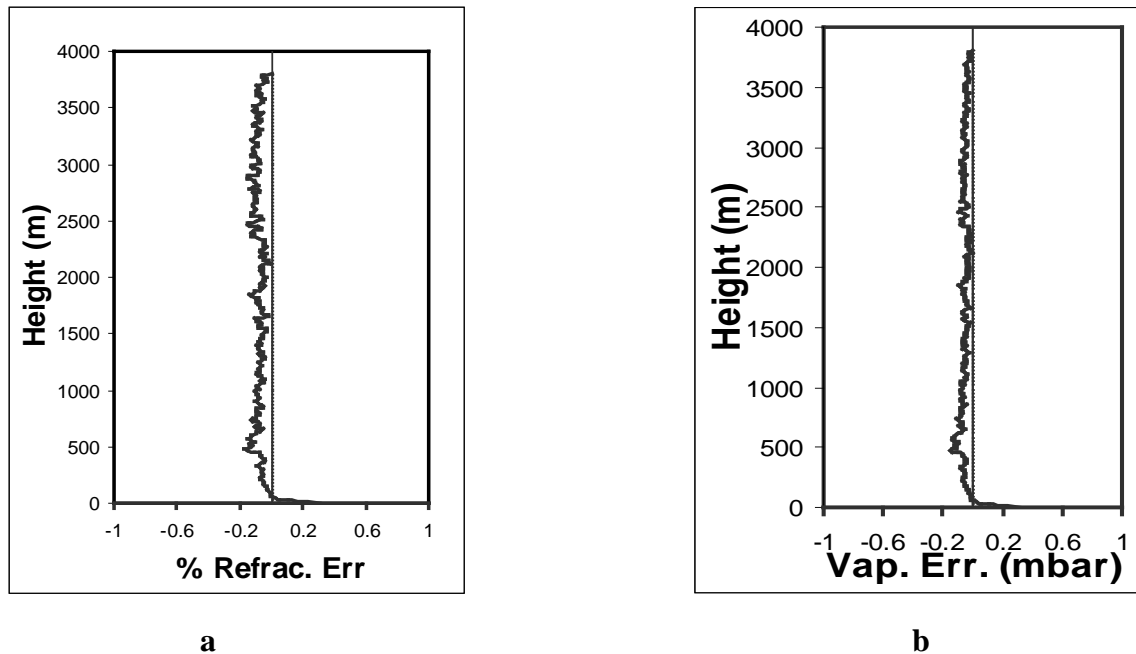


Fig. 7. Same as figure 6; but the wet part of the refractivity is driven from radio sonde data.

Water vapor again was driven using the iterative procedure described earlier in section (2-3). The temperature is assumed known and taken from the radiosonde observation. From figure (7-b) it is seen that the error of the water vapor retrieval is generally very small and always less than 0.1 mbar.

CONCLUSIONS

The paper describes and introduces the analysis of GPS occultation data for a receiver inside the atmosphere. The inversion technique can be used as a part of the data assimilation into numerical weather prediction system. The inversion technique is validated using data from MSISE-90 model as well as actual radiosonde observation. An exponential atmosphere was used for the validation, but the technique is general enough to be applied to any one dimensional atmospheric model.

Results of the simulation show that the bending angle measurements can retrieve the refractivity profile below the receiver altitude. The errors in the retrieved refractivity are always less than .2%. The results also show that, it is possible to derive the water vapor with errors less than .1 mbar. These results can improve the tropospheric models which in turn can help to improve the GPS position accuracy.

REFERENCES

- Born ,M., and E. Wolf. (1980)** "Principles of Optics", 6th ed., Pergamon, New York.
- Bruton W.D., G.W. Kattawar. (1997)** "Unique temperature profiles for the atmosphere below an observer from sunset images" *Appl. Opt* 36, 27, 6957-6961 pp.
- Cinzia, Z., G.A. Hajj, and E.R. Kursinski. (1999)** "A Novel approach to atmospheric profiling with a mountain-based or airborne GPS receiver" *J. Geophys., Res.*, 104, No. D20, 24435-24447 pp.
- Eyre, J.R. (1994)** "Assimilation of radio occultation measurements into a numerical weather prediction system" *Tech. Memo 199*, Eur. Cent. for Medium-Range Weather Forecasts, Reading, England.
- Feng, D.D., and B.M. Herman. (1999)** "Remotely Sensing the Earth's atmosphere using Global Positioning Syetem (GPS) – the GPS/MET data analysis" *J. Atmosphric and Oceanic Technology*, 16, 989-1002 pp.
- Fishbach, F.F. (1965)** "A satellite method for temperature and pressure below 24 km" *Bull. Amer. Meteorol. Soc.*, 9, 528-532 pp.

- Fjeldbo G, A.J. Kliore, V. Eshleman. (1971)** “The neutral atmosphere of venus studied with the mariner V radio occultation experiments” *Astron. J.*, 76, 2, 123-140 pp.
- Gorbunov, M.E., and S.V. Sokolovskiy. (1993)** “Remote sensing of refractivity from space for global observations of atmospheric parameters” rep. 119, Max-Planck-Institute for Meteorology, Hamburg.
- Hajj, G. A., E.R. Kursinski, W. I. Bertiger, S.S. Leroy, T. Meehan, L. J. Romans, and J.T. Schofield. (1996)** “Initial results of GPS-LEO occultation measurements of Earth’s atmosphere obtained with GPS/MET experiment” *Proc. Symp. On GPS Trends in Precise Terrestrial, Airborne, and Spaceborne Applications*, Springer-verlag, New York.
- Hedin, A.E. (1991)** “Extension of the MSIS Thermospheric Model into the Middle and Lower Atmosphere” *J. Geophys. Res.* 96, 1159-1991 pp.
- Kliore, A., D.L. Cain, G.S. Levy, V.R. Eshleman, G. Fjeldbo and F.D. Drake. (1965)** “Occultation experiment: results of the first direct measurement of Mars’ atmosphere and ionosphere” *Science*, 149, 1243-1248 pp.
- Kursinski, E.R., G.A. Hajj, W.I. Bertiger, S.S. Leroy, T.K. Meehan, L.J. Romans, J.T. Schofield, D.J. McCleese, W.G. Melbourne, C.L. Thornton, T.P. Yunck, J.R. Eyre, and N. Nagatani (1996)** “Initial results of radio occultation observations of Earth’s atmosphere using the Global Positioning System” *Science*, 271, 1107-1110 pp.
- Kursinski, E.R., G.A. Hajj, K.R. Hardy, J.T. Schofield, and R. Linfield. (1997)** “Observing Earth’s atmosphere with radio occultation measurement using the Global Positioning System” *J. Geophys., Res.*, 102, 23429-23465 pp.
- Larsen, G.B., K.B. Lauristen, F. Rubek and M.B. Sorensen. (2004)** “GRAS-SAF Radio Occultation Data from EPS/Metop” In *Occultations for Probing Atmosphere and Climate*, edited by G. Kirchengast, U. Foelsche and A. K. Steiner, pp 111-118, Springer, Germany.
- Lusignan, B., G. Modrell, A. Morrison, J. Pomalaza, and S.G. Ungar. (1969)** “Sensing the Earth’s atmosphere with occultation satellites” *Proc. IEEE*, 4, 458-467 pp.
- Melbourne, W.G., E.S. Davis, C.B. Duncan, G.A. Hajj, K.R. Hardy, E.R. Kursinski, T.K. Meehan, L.E. Young, and T.P. Yunck. (1994)** “The application of spaceborne GPS to atmospheric limb sounding and global change monitoring” *JPL Publication 94-18*, 147 pp., Jet Propulsion Lab, Pasadena, CA.
- Mousa, A.K., T. Tsuda. (2001)** “Retrieval of Key Climate Variables Using Occultation Geometry of a Mountain top GPS Receiver” *ION GPS 2001 proceedings*, 1117-1126 pp.
- Rocken, C., R. Anthes, M. Exner, D. Hunt, S. Sokolovskiy, R. Ware, M. Gorbunov, W. Schreiner, D. Feng, B., Herman, Y.-H. Kuo, and X. Zou. (1997)** “Analysis and validation of GPS/MET data in the neutral atmosphere” *J. Geophys., Res.*, 102, 29849-29866 pp.
- Schreiner, W.S., S.V. Sokolovskiy, C. Rocken, and D.C. Hunt. (1999)** “Analysis and validation of GPS/MET radio occultation data in the ionosphere” *Radio Sci.*, vol. 34, No. 4, 949-966 pp.
- Smith, E.K., and S. Weintraub. (1953)** “The constants in the equation for atmospheric refractive index at radio frequencies” *Proc. Of the I. R. E.*, 41, 1035-1037 pp.
- Steiner, A.K., G. Kirchengast, H.P., ladreiter. (1998)** “Inversion, error analysis, and validation of GPS/MET occultation data” *Ann. Geophysicae*, 17, 122-138 pp.
- Tricomi, F.G. (1977)** “Integral Equations” Dover, Mineola, New York.
- Ware, R., M. Exner, D. Feng, M. Gorbunov, K. Hardy, B. Herman, Y. Kuo, T. Meehan, W. Melbourne, C. Rocken, W. Schreiner, S. Sokolovskiy, F. Solheim, X. Zou, R. Anthes, S. Businger, and K. Trenberth. (1996)** “GPS sounding of the atmosphere from Low Earth Orbit: preliminary results” *Bull. Am. Meteorol. Soc.*, vol. 77, No 1, 19-40 pp.
- Yakovlev, O.I., S.S. Matyugov, and I.A. Vilkov. (1995)** “Attenuation and scintillation of radio waves in the Earth’s atmosphere from radio occultation experiments on satellite-to-satellite links” *Radio Sci.*, vol. 30, No. 3, 591-602 pp.
- Yakovlev, O.I. (1998)** “Space Radio Physics” Edited by Russian Fund of Fundamental Researches (RFBR), 478 PP., Moscow.

LOCAL MAGNITUDE (M_L) ESTIMATION OF THE KUWAIT NATIONAL SEISMIC NETWORK, NORTHEASTERN ARABIAN PENINSULA

N.S.N. Al-Arifi

Department of Geology, King Saud University, P. O. Box 2455, Saudi Arabia, 11451
E-mail: nalarifi@ksu.edu.sa

تقدير القوة الزلزالية المحلية لشبكة الرصد الزلزالي الكويتية في الجزء الشمالي الشرقي لشبه الجزيرة العربية

الخلاصة: تم تطوير معادلة خاصة بالقوة الزلزالية لشبكة الرصد الزلزالي الوطنية الكويتية (KNSN) من معلومات الزلازل التي تم إنشاء هذه الشبكة لغرض مراقبة النشاط الخاص بها. بواسطة هذه المعادلة الخاصة بالقوة الزلزالية (المحلي) و التي تم استخلاصها بواسطة الاستنتاج كما في المعادلة التالية:
 $ML = \log(A) + 1.43 \log(\Delta) + 1.0 + Di$
تم أستخراج معادلة القوة الزلزالية كنتيجة لتقنية الانحسار الخطي الهندسي المتعدد للمعلومات الخاصة بالسعة الموجية (A) و المتوفرة من ست محطات رصد زلزالي ضمن الشبكة الوطنية الكويتية لرصد الهزات الأرضية (KNSN).
لضمان إمكانية تطبيق هذه المعادلة (القوة الزلزالية المحلية) على الشبكة تم حساب التصحيح الخاص بكل محطة رصد زلزالي ضمن المعادلة (Di). تم تقييم التصحيح الخاص بكل محطة رصد زلزالي من خلال الفوارق بالقيم بين المحسوبة بواسطة المعادلة والتي تم الحصول عليها من كل محطة رصد زلزالي.

ABSTRACT: A magnitude formula is preliminarily developed from Kuwait National Seismic Network (KNSN) data which is proposed and intended for application by the network in its seismic monitoring activities. This is an adapted local magnitude scale of measurement which is empirically determined and expressed as:

$$ML = \log(A) + 1.43\log(\Delta) + 1.0 + Di .$$

The magnitude formula is a result of applying multiple regression techniques to the data which is the amplitude, A, that is availed from 6 stations of the network. To ensure applicability of the magnitude equation for the network, stations corrections were determined which are indicated by the Di for the ith station. The station corrections are evaluated from the average of the difference values between the proposed magnitude formulas to respective magnitude equations obtained from each seismic station.

INTRODUCTION

Magnitude is a measure of an earthquake size. It is one of the contributing factors that are reckoned with when considering the degree of destructiveness of a seismic event. A reliable and standardized measure of the size of an earthquake is an essential and important need for consideration in the concept of seismic disaster mitigation and minimization of earthquake losses. Hence, it becomes imperative for a seismic network to develop and establish its own formulas and methods in determining and defining the seismic parameters of local earthquake events that are related to the level of destructiveness. It is advisable and desirable that a seismic network can react immediately and promptly provides information regarding the occurrence of an earthquake of concern independently from other seismological agencies. An appropriate timely reaction to an earthquake emergency may mitigate disaster and minimize seismic losses. Time delay in responding to an earthquake emergency may contribute further disaster from potential contributory secondary effects such as fire and strong aftershocks generated by the main seismic event. A seismic network needs to be prepared and ready to meet satisfactorily the national and local demands and requirements in seismic disaster preparedness.

The concept of a magnitude scale for an earthquake is introduced by Richter (1935) for earthquake in California, U. S. A. This is known as the local magnitude

scale developed in terms of the records of Wood-Anderson torsion seismograph. The amplitude- distance relation was derived for California and is not applicable to other regions. Although the definition of the local magnitude is quite arbitrary, this became a basis for further development of the magnitude concept. Gutenberg (1945) introduced the body-wave magnitude (Mb) based on P-waves depth phases from shallow earthquakes, and later developed it further to include earthquakes of any focal depth. The amplitude-distance correction was determined by combination of theory and observation and included effects due to geometrical spreading and anelastic absorption.

In 1958, Bisztricsany found a linear relation between magnitude of teleseismic events and the logarithm of the surface-wave trace duration. This concept was applied to local earthquakes with the seismic signal trace duration defined as the total length of the trace instead of the surface-wave (Solov'ev 1965, Tsumura 1967, Crosson 1972, Lee et al 1972, Real & Teng 1973, Hermann 1975, Bakun & Lindh 1977, Suteau & Whitcomb 1979).

Regional and local peculiarities require that each local seismic network should fundamentally developed their own methods, tools, and formulas for classifying and defining seismic events within their area of responsibility and region of concern. Particularly, a

seismic parameter of interest in this paper is the measurement of the magnitude of an earthquake event. This parameter is related to the release seismic energy due to an earthquake occurrence and therefore an important number of characteristic in the evaluation of earthquake hazards are generated. It is apparent that to develop a system of reliable magnitude measurement becomes one of the fundamental contributions to earthquake disaster mitigation. The system paves the way for immediate assessment of the level of destruction when other physical factors such as soil properties, focal depth, and elements at risk are as well taken into consideration.

Substantially, the empirical magnitude formulas that are developed from regional and local considerations are more appropriately applicable and reliable for a local seismic network. These are based from data that reflect the regional and local characteristics of geometric spreading and anelastic absorption that influence and affect the behavior of calibrating functions. Hence, it is for this purpose, an attempt to develop preliminary magnitude formula from the Kuwait National Seismic Network (KNSN) was carried out. KNSN stations data are undertaken, for contribution and proposed application in the determination of the strength of recorded local and regional seismic events. This study may also encompass the intention of promoting and cultivating regional cooperation among neighboring seismological networks.

DATA SOURCE

There are two main sources of seismic data that are referred in this study for magnitude formula development. These are the seismic bulletins from the KNSN from the year 1998-2003 and the preliminary determination of epicenters (PDE) of the United States Geological Survey (USGS) corresponding to these years. The seismic data that were taken from KNSN earthquake bulletins are the amplitude values from its short period seismic stations: QRN, RDF, NAY, RST, MIB, and UMR. The location of these seismic stations and the study area is shown in figure 1.

The corresponding body-wave magnitude (Mb) values and epicenters are availed from the PDE of USGS. The values of these seismic parameters were referred to and assumed as standard measurements in reference to the preliminary development of the magnitude formulas.

The numbers of amplitude values utilized in each seismic station are tabulated as follow:

Station code	QRN	RDF	NAY	RST	MIB	UMR
No. of Amplitude	68	73	85	58	70	73

The data from the KNSN and USGS are used as initial hypotheses in the fulfillment of the objectives of this paper.

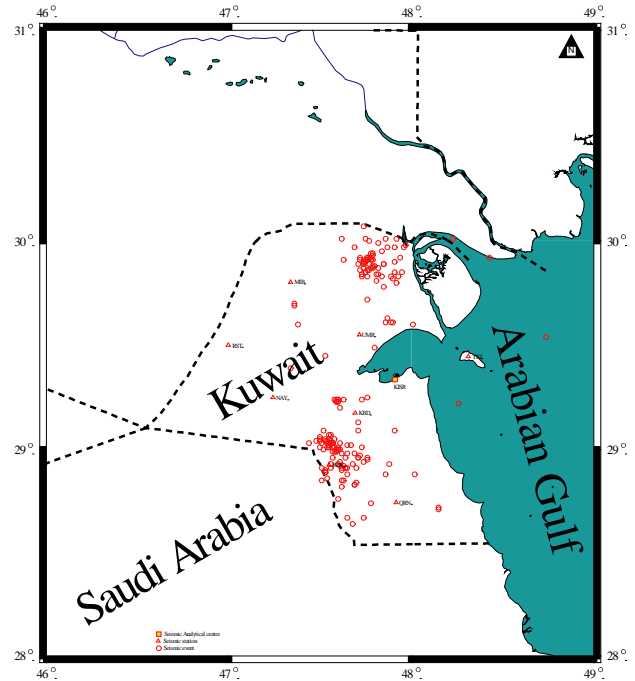


Fig. (1): Location map of the Kuwait National Seismic Network stations and the analytical center.

METHODOLOGY

A magnitude formula was envisioned to be developed from the KNSN data. This is the magnitude based on the extremal amplitude of seismic signal. The generally applied method in the preliminary development of the magnitude formulas when sufficient data is available is by means of statistical procedures. The amplitude with the associated epicentral distance data are regressed against corresponding values of a standard and internationally accepted magnitude scale to determine the calibrating function.

Local Magnitude Scale

Two procedural steps are conducted in the preliminary development of this type of magnitude based from the collected and compiled data. These are the calibration of the duration magnitude scale for each seismic station and the other is the development of a single formula for all the considered stations. Comparative analysis of the two approaches will generate correction for each seismic station, thereby facilitating the application of a single formula for the whole network for this type of magnitude.

The local magnitude scale for earthquakes is developed by Richter in 1935. The scale considers the maximum trace amplitude from Wood-Anderson seismometer. No period is taken into account and no conversion to ground amplitude is made. The local magnitude scale (MI) is given as

$$Ml = \log A - \log A_0 \tag{1}$$

Where $\text{Log}A$ and $\text{Log}A_0$ are the decadic logarithm of the maximum trace amplitude (A) at epicentral distance (Δ) and A_0 is the amplitude of the zero magnitude at 100 km respectively. $\text{Log}A_0$ is the calibrating function given as

$$-\log A_0 = a \log \Delta + b \quad (2)$$

That compensates for the value of A when brought to a 100 km distance, and a and b are constants. Substitution of equation (2) in (1) gives for the local magnitude scale the relation

$$M_l = \text{Log}A + a \log \Delta + b \quad (3)$$

or

$$M_l - \log A = a \log \Delta + b \quad (3a)$$

The local magnitude scale developed by Richter is based on a particular type of seismic instrument and geological condition. Different types of seismic instrument and ground properties may generate a calibrating function whose characteristic and properties may vary significantly from Richter's results. An inaccurate magnitude determination may underrate the level of seismicity of an area and the evaluation of the earthquake hazards that are generated when seismic events occur. Hence, there is an essential need to develop a local magnitude scale that conforms to the type of seismic instrumentation and geological units within the location of a specific seismic network. The adapted local magnitude scale will be similar in literal form with equations (3), but may be numerically different with respect to the coefficient and constant (Kim 1998, Bakun & Lindh 1977).

To determine the local magnitude scale for the KNSN, a set of standard magnitude values (M_b) is substituted in place of M_l . The body-wave magnitude is developed by Gutenberg in 1945 for the determination of magnitude values of earthquake events occurring at variable focal depths and being recorded by different types of seismic instruments. In a sense, the M_b values are appropriate for substitution.

From the set of collected and compiled data (M_b , A , Δ) from the KNSN seismic stations, where the unit of the amplitude (A , 0.5* peak to peak) is in millimicrometer or nanometer and Δ is in degrees, regression techniques is applied in equation (3a) for the determination of the appropriate magnitude scale for the network. The local magnitude scale is determined for each seismic station having sufficient data. Secondly, the seismic data for all the stations having almost the same attenuating characteristics are combined for the determination of a single formula. Thirdly, station corrections are evaluated by taking the average of the difference values between the proposed single local magnitude formula and representative local magnitude equation for each seismic station as indicated similarly in relation (1).

Incidentally, the evaluation of the single formula for the adapted local magnitude requires three equations to be determined due to the preliminary results from each station. A respective single formula for each of the

two groups that show closely related calibrating function. The third is when all the seismic data is considered. The graphical presentation for the single formula for the proposed local magnitude scale for the KNSN are shown in figures (2a, 2b, and 2c).

The results of the statistical analyses are shown in table 1, and the graphical representation for the estimation of the adapted local magnitude scale for the six seismic stations of KNSN is shown in figure (3). Table 1 is composed of six columns. The first column is for the seismic station. The second and third are for the regression constants, and the fourth, fifth, and sixth are for respective station correction from the 3 single formulas (Tot 1, Tot 2, and Tot 3). The number of rows is 9. The seventh rows is for the single formula (Tot 1) for the seismic stations QRN, RDF, RST, the eight row is for seismic stations NAY, MIB, UMR, and the last row is for the 6 seismic stations.

DISCUSSION AND CONCLUSION

The KNSN seismic stations are distributed in strategic locations, but relatively near each other. However, it is possible that each seismic station can respond differently to seismic signals due to the influence of some physical factors. These factors could be due to geological and environmental conditions at each station site that could affect the response of the seismic instruments. These possibilities prompted separate analysis of the seismic data which is the amplitudes that are gathered and compiled at each KNSN station. The assumptions seemed to be supported and validated by the results as shown in table 1.

The restrictions of the local magnitude scale developed by Richter require the determination of an adapted local magnitude that is appropriate for particular local networks. The formula can be developed in the same mathematical form, but having different values with respect to the constant and coefficient that reflect the geological condition, instrument type and response, and hypocentral location of seismic events.

As shown in table 1, the calibrating function for each of the considered seismic stations indicates varying coefficients and constants. Four seismic stations (NAY, RST, MIB, and UMR) give close coefficient values, while the other stations (QRN, RDF) indicate relative similarities considering possible statistical data errors that need correction. The seismic stations (NAY, RST, MIB, UMR) signify relatively higher attenuating function that reflects better instrument response than the other 2 stations (QRN, RDF) when ground amplitude is considered.

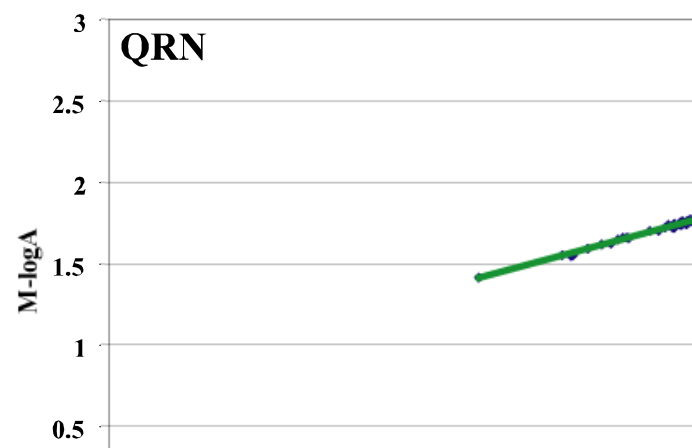


Fig. (2a): Plots of the data points between the difference of magnitude (M) and the logarithm of the amplitude (A) against logarithm of distance.

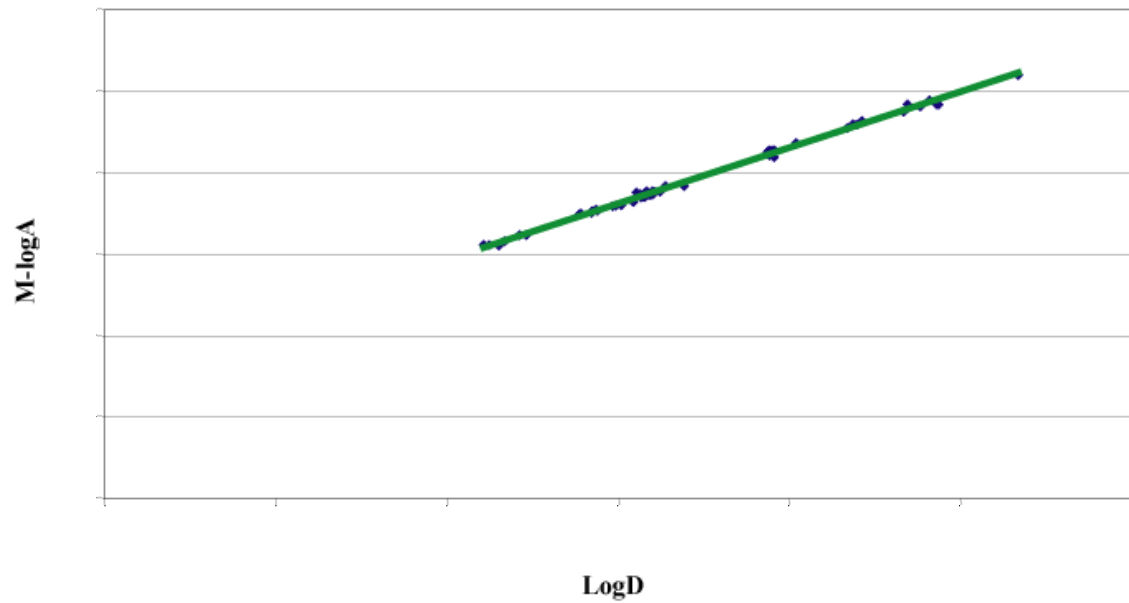
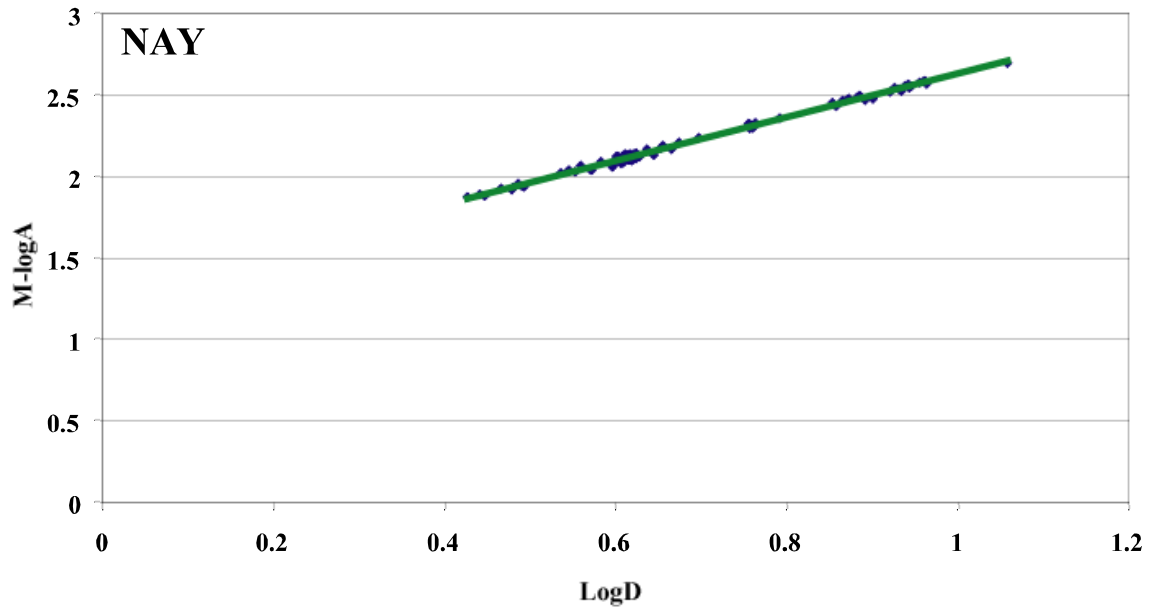


Fig. (2b): Plots of the data points between the difference of magnitude (M) and the logarithm of the amplitude (A) against logarithm of distance.

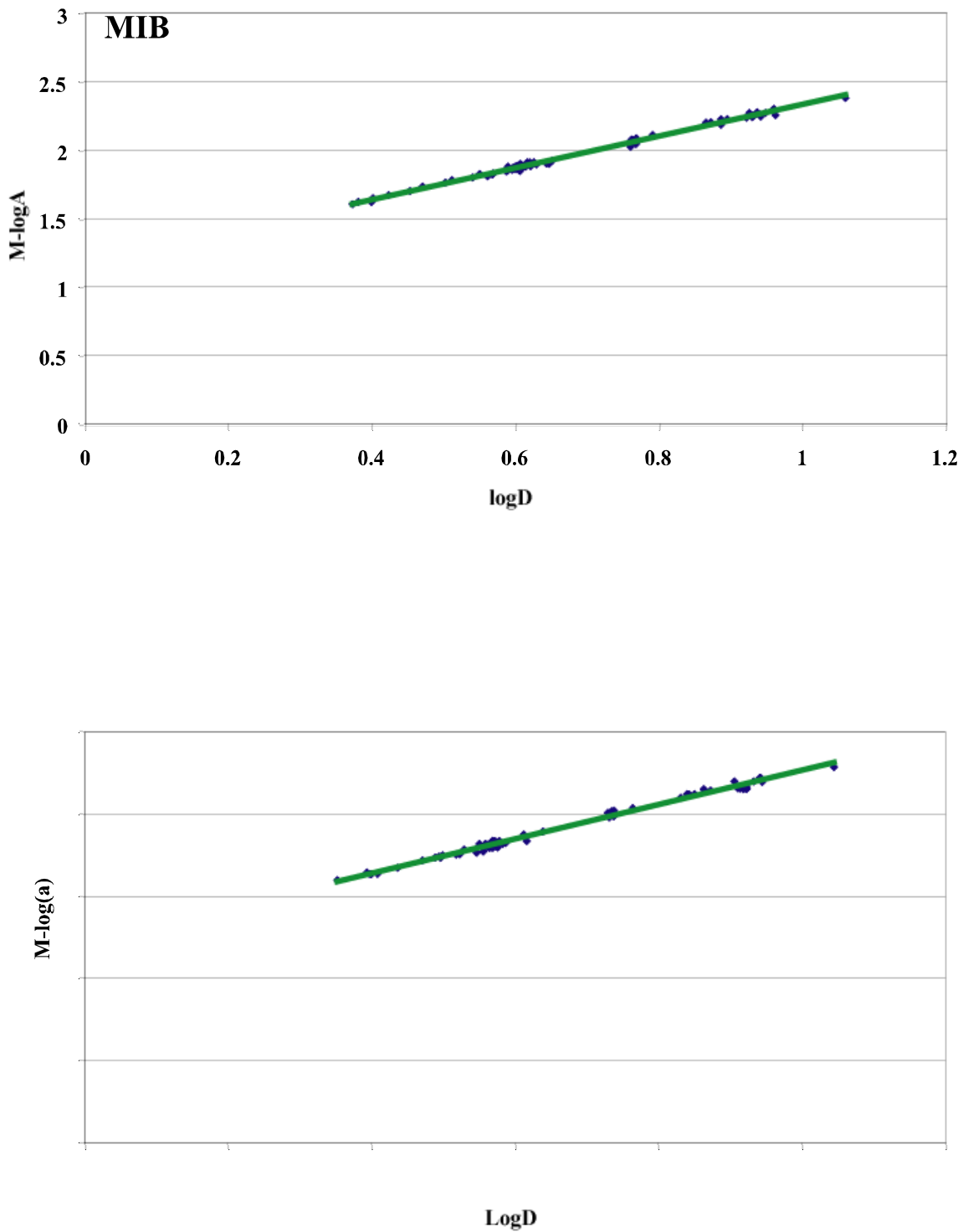


Fig. (2c): Plots of the data points between the difference of magnitude (M) and the logarithm of the amplitude (A) against logarithm of distance.

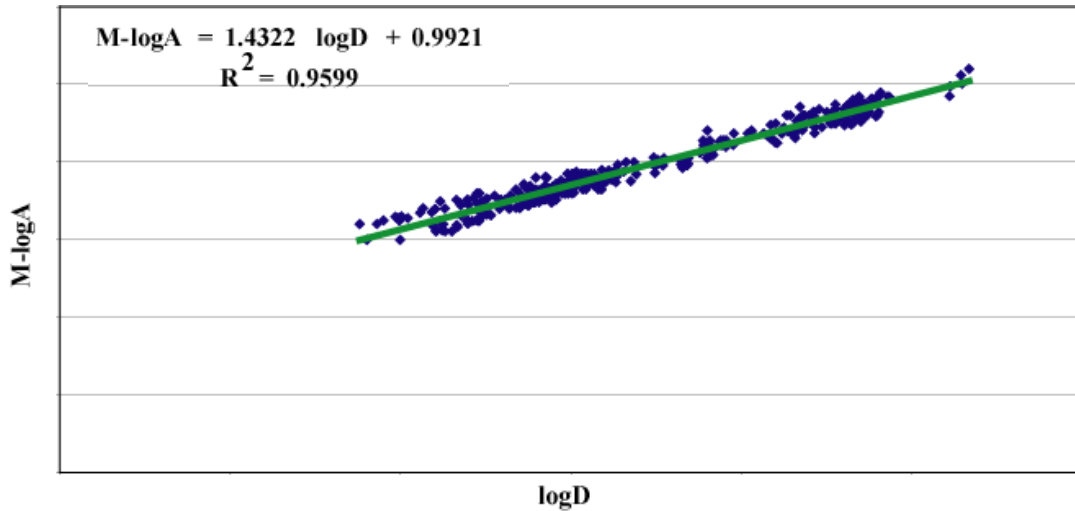


Fig.(3) Plots of the single magnitude formula for local magnitude scale that are proposed for application by the KNSN in its seismic monitoring activities.

The varying results in the development of the adapted local magnitude scale indicate the necessity of determining three preliminary single formulas for the network. One is for the seismic stations (QRN, RDF), the other for stations (NAY, RST, MIB, UMR), and the other is when the total data is considered. Hence, three formulas were determined which are not necessarily in conflict since seismic trace and not ground amplitude is reckoned. The appropriateness of the three formulas was afterward tested from the whole seismic data. The test is based on the results of station corrections when each of the three single formulas is applied separately to respective station magnitude relation and data. The formula that gives the least station correction for each station was assumed and taken to be the appropriate equation that is applicable for the seismic network. Among the three single formulas for the local magnitude scale, it would seem that the empirical equation that is obtained from the whole data is the most appropriate for application.

The result of the validity test in table 1, show that five seismic stations can be utilized in local magnitude determination. These are QRN, RDF, RST, MIB, and UMR. Except for seismic stations RDF and NAY, the other stations give relatively accurate magnitude value using amplitude. Station RDF seems to be fitted better for local magnitude estimation.

The development of the empirical formula for the adapted local magnitude scale is based mainly within the hypothesis of the initial seismic data taken from the KNSN seismic stations. Hence, the magnitude equations are affected by the reliability and accuracy of the utilized seismic data. Comparison of preliminary determination of seismic parameters such as location and magnitude of seismic events from KNSN and USGS indicates some discrepancies. In case of discrepancies, preference is given to the USGS determinations, for the reason that this agency relies from more seismic stations and application of statistical procedures to the utilized seismic reports.

It is also observable from the KNSN seismic data some unintentional errors of recordings for the amplitude value when based from the corresponding magnitude and distance of earthquake events. The occurring errors could be due to malfunctioning in the system of response of the instruments. These errors were considered for correction in relation to the general trend of the graphs and corresponding values from the other seismic stations. It is therefore advisable that automated evaluation of the required data be counter-checked for the realistic assessment of magnitude.

Table (1). Adapted local magnitude formula for the KNSN as evaluated and obtained from the compiled seismic data in each six station.

Station Code	Regression Constants		Station Correction		
	a	b	Tot1	Tot2	Tot3
QRN	1.7	0.8	-0.03	0.09	0.017
RDF	1.68	0.74	0.043	0.16	0.091
NAY	1.34	1.29	-0.27	-0.157	-0.22
RST	1.71	0.79	-0.026	0.092	0.02
MIB	1.16	1.17	-0.035	0.084	0.012
UMR	1.04	1.22	-0.004	0.115	0.043
Tot 1	1.7	0.77			
Tot 2	1.24	1.34			
Tot 3	1.43	1			

Hence, magnitude estimates from the preliminarily developed equations can be considered as conservative values due to encountered constraining factors. The level of accuracy is within the limits of the utilized seismic data and assumptions that were taken regarding similarities in the calibrating functions. Although the station corrections imply the significance and relative accuracy of the proposed formulas, the level of validity can be improved from application for further verification.

REFERENCES

- Bakun W. and Lindh A. 1977.** Local magnitudes, seismic moment and coda duration for earthquakes near Oroville, California, Bull. Seism. Soc. Am., 67, pp. 615-629.
- Crosson R. 1972.** Small earthquakes, structure, and tectonics of the Puget Sound region Bull. Seism. Soc. Am., 62, pp. 1133-1177.
- Gutenberg B. 1945.** Amplitudes of P, PP, and S and magnitudes of shallow earthquakes, Bull. Seism. Soc. Am., 35, pp. 57-69.
- Kim W. 1998.** The Ml scale in eastern North America", Bull. Seism. Soc. Am., Vol. 88, pp. 935-951.
- Lee W, Bennet R., and Meahger K. 1972.** A method of estimating magnitude of local earthquakes from signal duration, USGS Open File Rept., 28.
- Real C. and Teng T. 1973.** Local Richter magnitude and total signal duration in southern California, Bull. Seism. Soc. Am., 63, 1809-1827.
- Richter C. 1935.** An instrumental earthquake scale, Bull. Seism. Soc. Am., 25, pp. 1-32.
- Solov'ev S. 1965.** Seismicity of Sakhalin", Bull. Earthq. Res. Inst., Tokyo Univ., 43, 95-102.

DURATION MAGNITUDE (M_D) ESTIMATION OF THE KUWAIT NATIONAL SEISMIC NETWORK, NORTHEASTERN ARABIAN PENINSULA

N.S.N. Al-Arifi

Department of Geology, King Saud University, P. O. Box 2455, Saudi Arabia, 11451
E-mail: nalarifi@ksu.edu.sa

حساب القوة الزلزالية الزمنية لشبكة الرصد الزلزالي الكويتية لشمال شرق شبه الجزيرة العربية

الخلاصة: تم تطوير معادلة خاصة بالقدر الزلزالي لشبكة الرصد الزلزالي الوطنية الكويتية (KNSN) من معلومات الزلازل التي تم إنشاء هذه الشبكة لغرض مراقبة النشاط الخاص بها. بواسطة هذه المعادلة الخاصة بالقدر الزلزالي (الخاص بالاستمرارية) و التي تم استخراجها بواسطة الاستنتاج كما في المعادلة التالية:

$$MD = 2.66 \log(\tau) + 0.036\Delta - 1.97 + C_i$$

تم استخراج معادلة القدر الزلزالي كنتيجة لتقنية الانحسار الخطي الهندسي المتعدد للمعلومات الخاصة باستمرارية الإشارة الزلزالية (τ) و المتوفرة من ست محطات رصد زلزالي ضمن الشبكة الوطنية الكويتية لرصد الهزات الأرضية (KNSN).

لضمان إمكانية تطبيق هذه المعادلة (القدر الزلزالي الخاص بالاستمرارية للإشارة الزلزالية) على الشبكة تم حساب التصحيح الخاص بكل محطة رصد زلزالي ضمن المعادلة (C_i). تم تقييم التصحيح الخاص بكل محطة رصد زلزالي من خلال الفوارق بالقيم بين المحسوبة بواسطة المعادلة و التي تم الحصول عليها من كل محطة رصد زلزالي.

ABSTRACT : One type of magnitude formula are preliminarily developed from Kuwait National Seismic Network (KNSN) data which is proposed and intended for application by the network in its seismic monitoring activities. This is the duration magnitude scale of measurement which are empirically determined and expressed as:

$$M_D = 2.66 \log(\tau) + 0.036\Delta - 1.97 + C_i$$

The magnitude formula is the result from applying multiple regression techniques to the data which have the seismic signal duration, τ , that are available from 6 stations of the network. To ensure applicability of the magnitude equation for the network, stations corrections were determined which are indicated by the C_i for the i th station. The station corrections are evaluated from the average of the difference values between the proposed magnitude formulas to respective magnitude equations obtained from each seismic station.

INTRODUCTION

Magnitude is a measure of an earthquake size. It is one of the contributing factors that are reckoned with when it is considering the degree of destructiveness of a seismic event. A reliable and standardized measure of the size of an earthquake is an essential and important need for consideration in the concept of seismic disaster mitigation and minimization of earthquake losses. Hence, it becomes imperative for a seismic network to develop and established its own formulas and methods in determining and defining the seismic parameters of local earthquake events that are related to the level of destructiveness. It is advisable and desirable that a seismic network can react immediately and promptly provides information regarding the occurrence of an earthquake of concern independently from other seismological agencies. An appropriate timely reaction to an earthquake emergency may mitigate disaster and minimize seismic losses. Time delay in responding to an earthquake emergency may contribute further disaster from potential contributory secondary effects such as fire and strong aftershocks generated by the main seismic event. A seismic network needs to be prepared and ready to meet satisfactorily the national and local demands and requirements in seismic disaster preparedness.

The concept of a magnitude scale for an earthquake is introduced by Richter (1935) for earthquake in California, U. S. A. This is known as the local magnitude scale developed in terms of the records of Wood-Anderson torsion seismograph. The amplitude- distance relation was derived for California and is not applicable to other regions. Although the definition of the local magnitude is quite arbitrary, this became a basis for further development of the magnitude concept. Gutenberg (1945) introduced the body-wave magnitude (M_b) based on P-waves depth phases from shallow earthquakes, and later developed it further to include earthquakes of any focal depth. The amplitude-distance correction was determined by combination of theory and observation and included effects due to geometrical spreading and anelastic absorption.

In 1958, Bisztricsany found a linear relation between magnitude of teleseismic events and the logarithm of the surface-wave trace duration. This concept was applied to local earthquakes with the seismic signal trace duration defined as the total length of the trace instead of the surface-wave (Solov'ev, 1965; Tsumura, 1967; Crosson, 1972; Lee et al, 1972; Real & Teng, 1973; and Bakun & Lindh, 1977).

Regional and local peculiarities require that each local seismic network should fundamentally developed their own methods, tools, and formulas for classifying and defining seismic events within their area of responsibility and region of concern. Particularly, a seismic parameter of interest in this paper is the measurement of the magnitude of an earthquake event. This parameter is related to the release seismic energy in an earthquake occurrence and therefore an important number characteristic in the evaluation of earthquake hazards that are generated. It is apparent that to develop a system of reliable magnitude measurement becomes one of the fundamental contributions to earthquake disaster mitigation. The system paves the way for immediate assessment of the level of destruction when other physical factors such as soil properties, focal depth, and elements at risk are as well taken into consideration.

Substantially, the empirical magnitude formulas that are developed from regional and local considerations are more appropriately applicable and reliable for a local seismic network. These are based on data that reflect the regional and local characteristics of geometric spreading and anelastic absorption that influence and affect the behavior of calibrating functions. Hence, it is for this purpose that an attempt to develop preliminary magnitude formula from the Kuwait National Seismic Network (KNSN). KNSN stations data is undertaken, for contribution and proposed application in the determination of the strength of recorded local and regional seismic events. This study may also encompass the intention of promoting and cultivating regional cooperation among neighboring seismological networks.

DATA SOURCE

There are two main sources of seismic data that are referred in this study of magnitude formula development. These are the seismic bulletins from the KNSN in the period from 1998 to 2003 and the preliminary determination of epicenters (PDE) of the United States Geological Survey (USGS) corresponding to these years. The seismic data that were taken from KNSN earthquake bulletins are the duration values from its short period seismic stations: QRN, RDF, NAY, RST, MIB, and UMR. The location of these seismic stations and the study area is shown in figure (1).

The corresponding body-wave magnitude (Mb) values and epicenters are availed from the PDE of USGS. The values of these seismic parameters were referred to and assumed as standard measurements in reference to the preliminary development of the magnitude formulas.

The numbers of duration and amplitude values utilized in each seismic station are tabulated as follow:

Station code	QRN	RDF	NAY	RST	MIB	UMR
No. of Duration	21	30	43	29	38	40

The data from the KNSN and USGS are used as initial hypotheses in the fulfillment of the objectives of this paper.

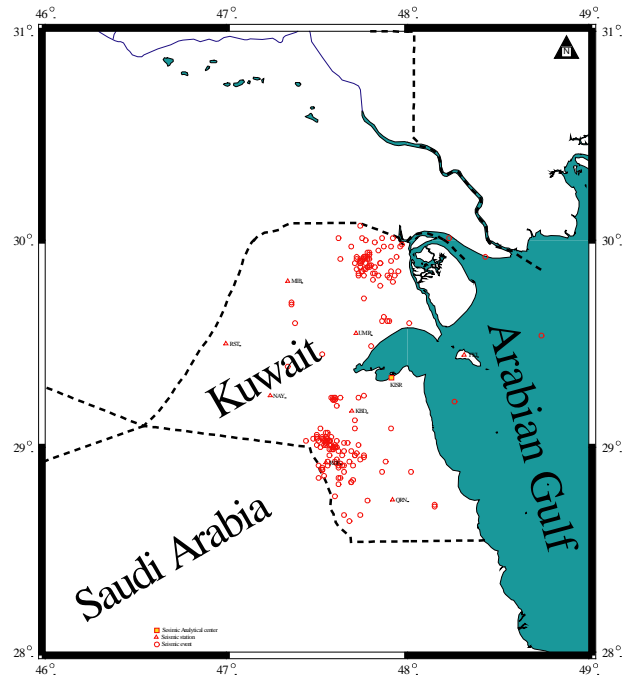


Fig. (1): Location map of the Kuwait National Seismic Network stations and the analytical center.

METHODOLOGY

One type of magnitude formula was envisioned to be developed from the KNSN data. This is the magnitude based on the duration of seismic signal. The generally applied method in the preliminary development of the magnitude formulas when sufficient data is available is by means of statistical procedures. The amplitude and duration with the associated epicentral distance data are regressed against corresponding values of a standard and internationally accepted magnitude scale to determine the calibrating function.

Duration Magnitude

Two procedural steps are conducted in the preliminary development of this type of magnitude based from the collected and compiled data. These are the calibration of the duration magnitude scale for each seismic station and the other is the development of a single formula for all the considered stations. Comparative analysis of the two approaches will generate correction for each seismic station, thereby facilitating the application of a single formula for the whole network for this type of magnitude.

The relation of the magnitude of an earthquake to seismic trace duration is known (Lee et al 1972, Real & Teng 1973, Tsumura 1967, Bakun & Lindh 1977) to be expressed by the equation

$$M_D = a \log \tau + b \Delta + c \quad (1)$$

where M_D is the duration magnitude that is referred from the body-wave magnitude which is taken as the standard magnitude value in this paper, $\log \tau$ is the decadic logarithm of the seismic signal trace duration (τ) in seconds which is measured from the initial onset of the seismic signal up to the time when the signal is twice the normal trace as defined by KNSN, Δ is the epicentral distance in degrees, a , b , c are constants. The determination of equation (1) can be performed in two steps. The first step is conducted without considering the distance, that is,

$$M_D = a \log \tau + k \quad (2)$$

Where k is a constant and the other variables are as defined previously. The second step is to consider the contribution or correction due to the influence of the distance to equation (2) which is

$$M_D - a \log \tau = b \Delta + c \quad (3)$$

for each seismic station for equations (2 & 3). Another approach is a direct consideration of equation (1) which is applied in preference in this paper since the distances are relatively larger compared to local events. Then by applying the usual method of least square approximation, the regression constants a , b , c can be determined for each seismic station. The graphical presentation of the steps for the six stations of KNSN is shown in figures (2a, b, and c).

The determination of the single formula from the seismic data of the network follows the same procedures and regression of equations (2 & 3) or (1) by considering all the utilized data from each seismic station. The development of the single formula is represented as

$$M_D - d \log \tau = e \Delta + f \quad (4)$$

or

$$M_D = d \log \tau + e \Delta + f \quad (4a)$$

for purposes of discussion. The parameters M_D , τ , and Δ are as defined in equation (1), and d , e , f are regression constants to be determined by multiple regression analysis from the total data of the considered seismic stations. The graphical presentation for this type is shown in figure (3).

Station corrections for equation (4a) are determined as follows. Equation (4a) is applied separately to each considered seismic station data to evaluate the magnitude values. Likewise, the representative magnitude equation (1) for each seismic station is also applied to respective data for evaluation. The average of the corresponding magnitude differences is then determined and this is taken and assumed as the station correction. The procedure can be expressed as

$$M_{corr.} = [(d-ai) \log \tau + (e-bi) \Delta + (f-ci)] / N_i \quad (5)$$

where $M_{corr.}$ is the magnitude correction, N_i is the number of data considered for the i th seismic station,

with the coefficients and constants as defined previously. Eventually, equation (4) becomes

$$M_{Di} = d \log \tau_i + e_i \Delta_i + f_i M_{corr. i} \quad (6)$$

for the i th seismic station when reckoned.

The results of the statistical analyses are shown in table 1. The table is composed of five columns. The first column is for the seismic stations. The second is for the regression constants. The third is for respective station correction.

DISCUSSION AND CONCLUSION

The KNSN seismic stations are distributed in strategic locations, but relatively near each other. However, it is possible that each seismic station can respond differently to seismic signals due to the influence of some physical factors. These factors could be due to geological and environmental conditions at each station site that could affect the response of the seismic instruments. These possibilities prompted separate analysis of the seismic data which are the seismic trace duration that are gathered and compiled at each KNSN station. The assumptions seemed to be supported and validated by the results as shown in table (1).

The results for the preliminary determination of the duration magnitude formula for the KNSN show close values for the coefficient of $\log \tau$ as shown in Table 1. However, this conformity is not shown in the consideration and correction due to distance. Two seismic stations which are RDF and RST behave differently from the other seismic stations QRN, NAY, MIB, and UMR. The duration magnitude formula for each of the two seismic stations (RDF and RST) seems to indicate increasing seismic signal trace duration with distance. Initially, the characteristics of the respective equations reflect that the station sites are suitable for the generation and recordings of surface waves and possibly some signal noise. However, the initial guess for the explanation of the different behavior need further study and investigation for validation. Nevertheless, when the seismic data from the other stations (QRN, NAY, MIB, and UMR) are included with RDF and RST data for the determination of the single duration magnitude formula gives an appropriate result as indicated by the station corrections. The treatment for the whole data seemed to be appropriate since the results from equation (2) give relatively close values for each seismic station. These considerations including the nearness of the seismic stations reflect that the single duration magnitude is recommendable and advisable to apply for the KNSN with the inclusion of respective station correction.

The result of the validity test in table 1 indicates that five seismic stations using the single duration magnitude formula can be used. These are QRN, NAY, RST, MIB, and UMR. Station NAY seems to be fitted better for duration magnitude determination.

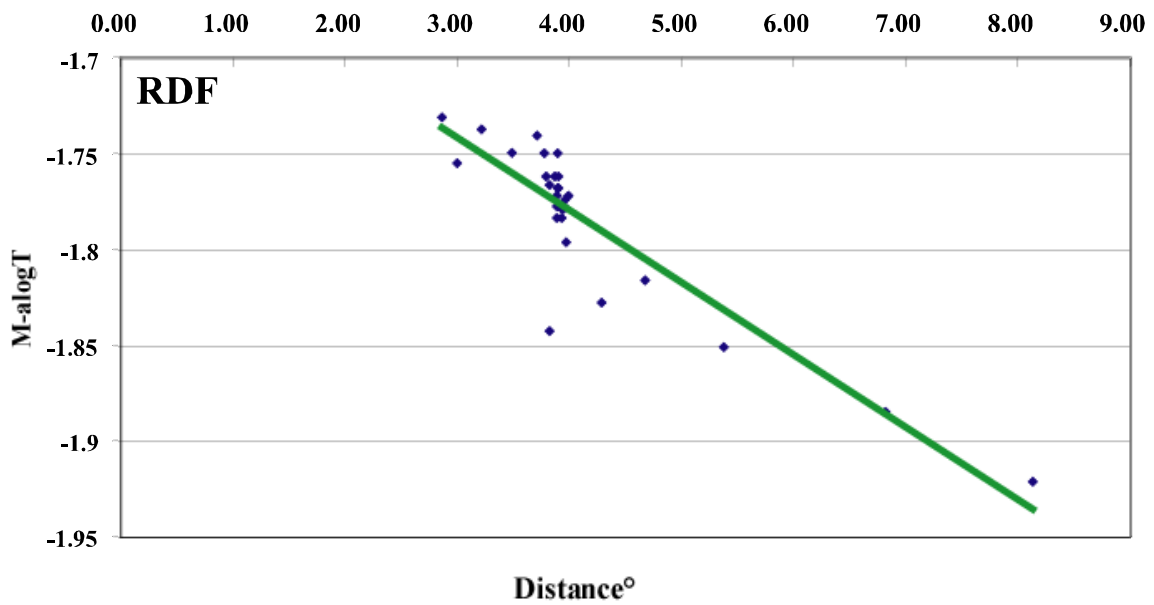
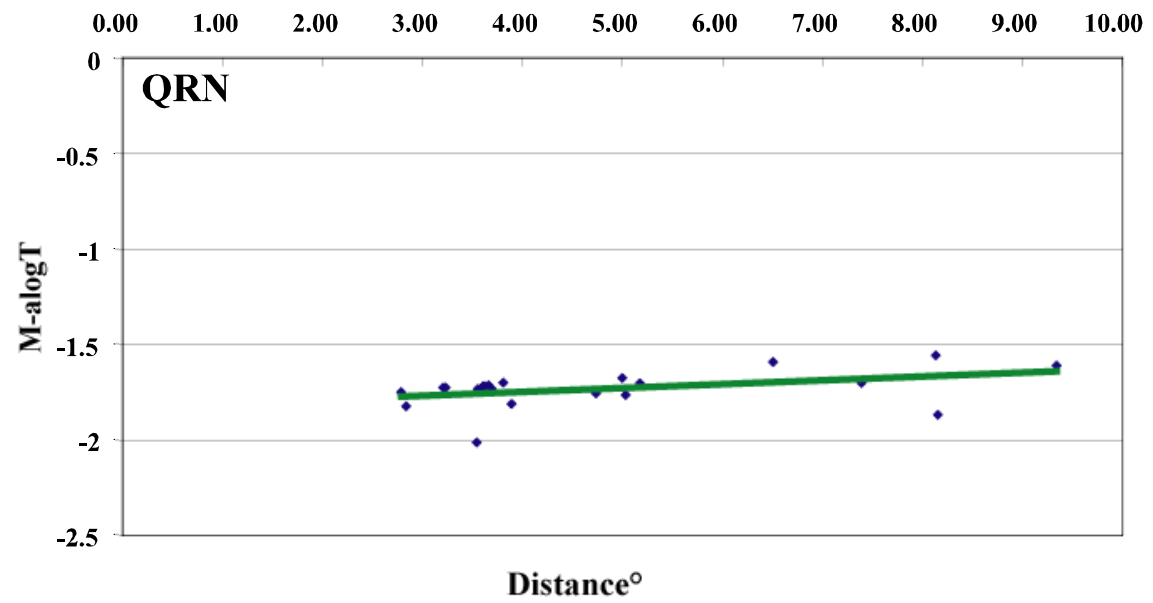


Fig. (2a): Plots of the data points between the difference of magnitude (M) and product of the coefficient (a) and logarithm of the seismic signal duration (T) against distance for the QRN and RDF seismic stations of RNSN.

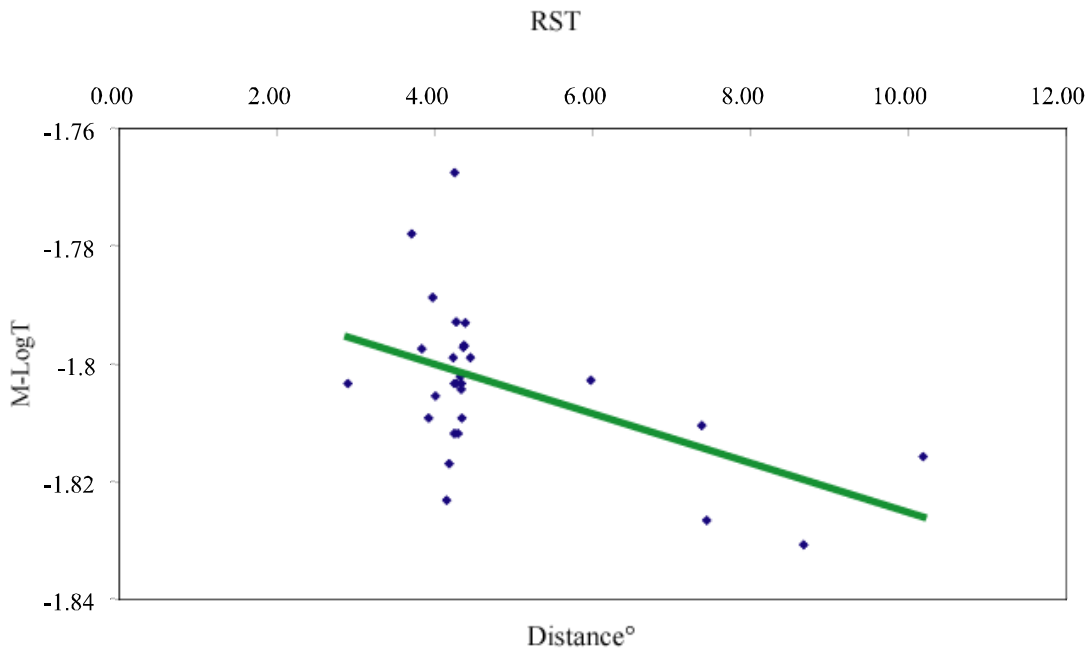
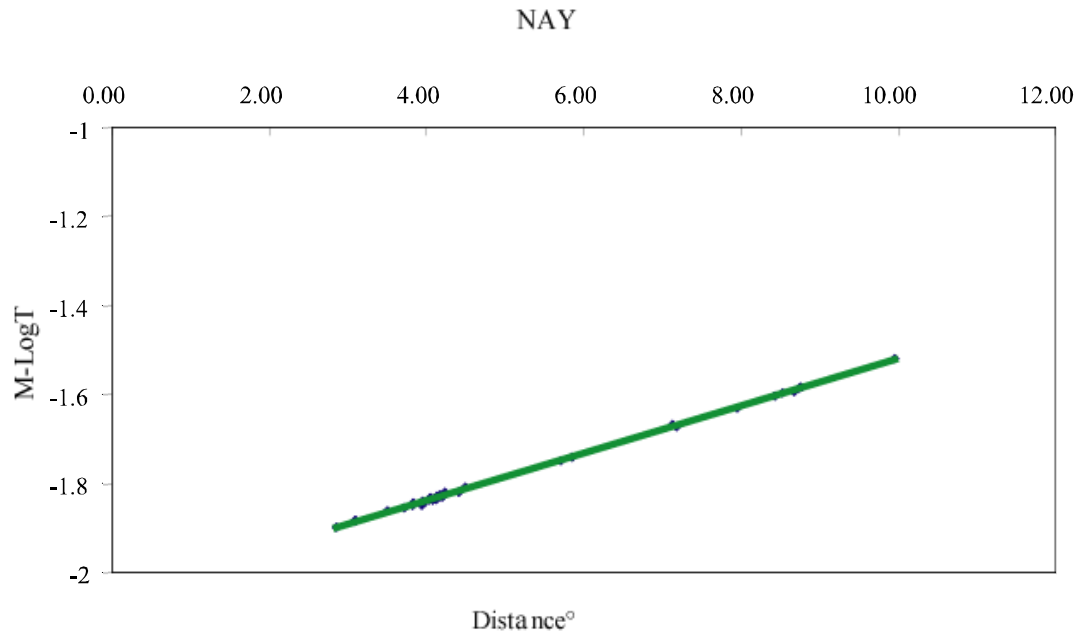


Fig. (2b): Plots of the data points between the difference of magnitude (M) and product of the coefficient (a) and logarithm of the seismic signal duration (T) against distance^o for the NAY and RST seismic stations of KNSN.

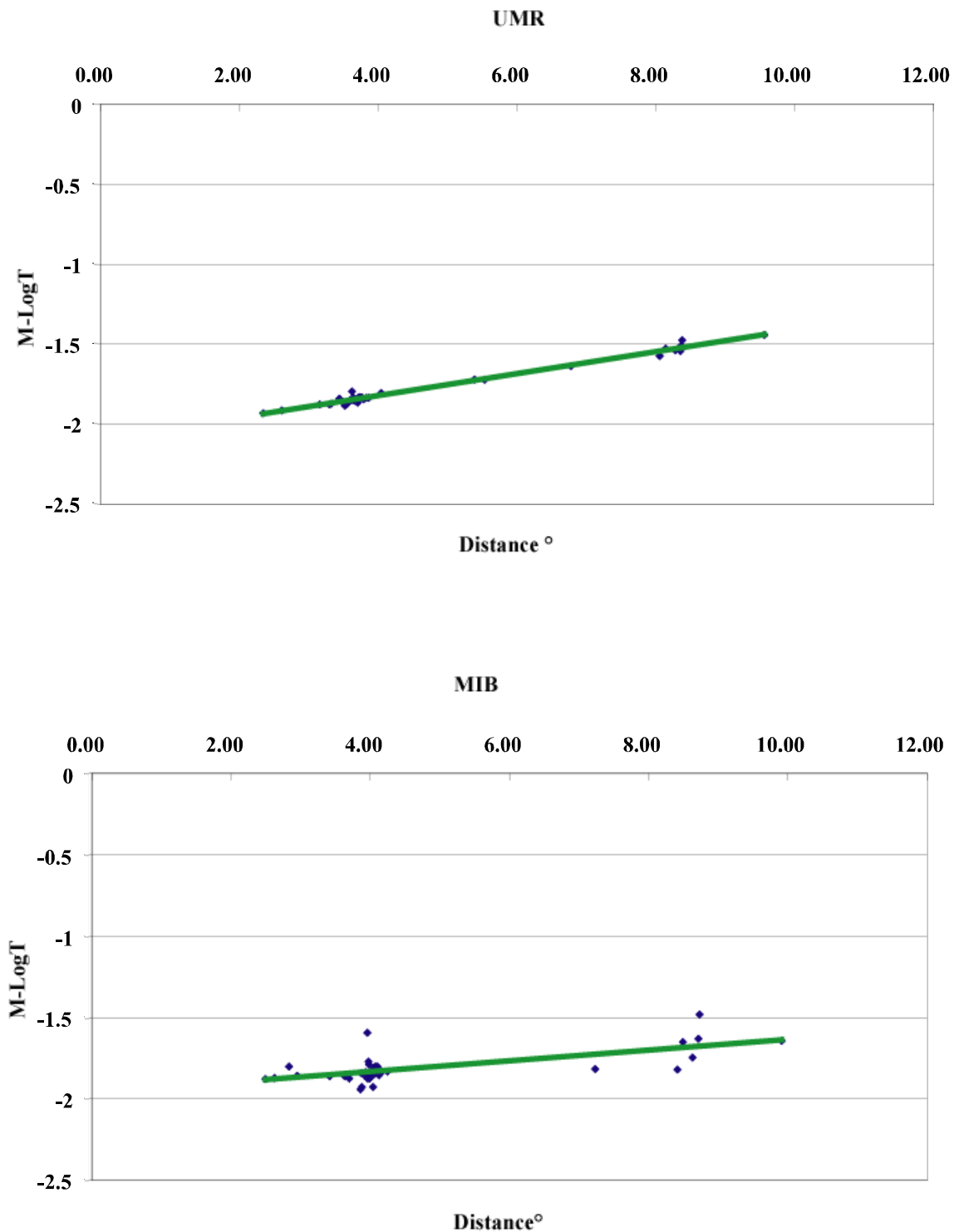


Fig. (2c): Plots of the data points between the difference of magnitude (M) and product of the coefficient (a) and logarithm of the seismic signal duration (T) against distance for the UMR and MIB seismic stations of KNSN.

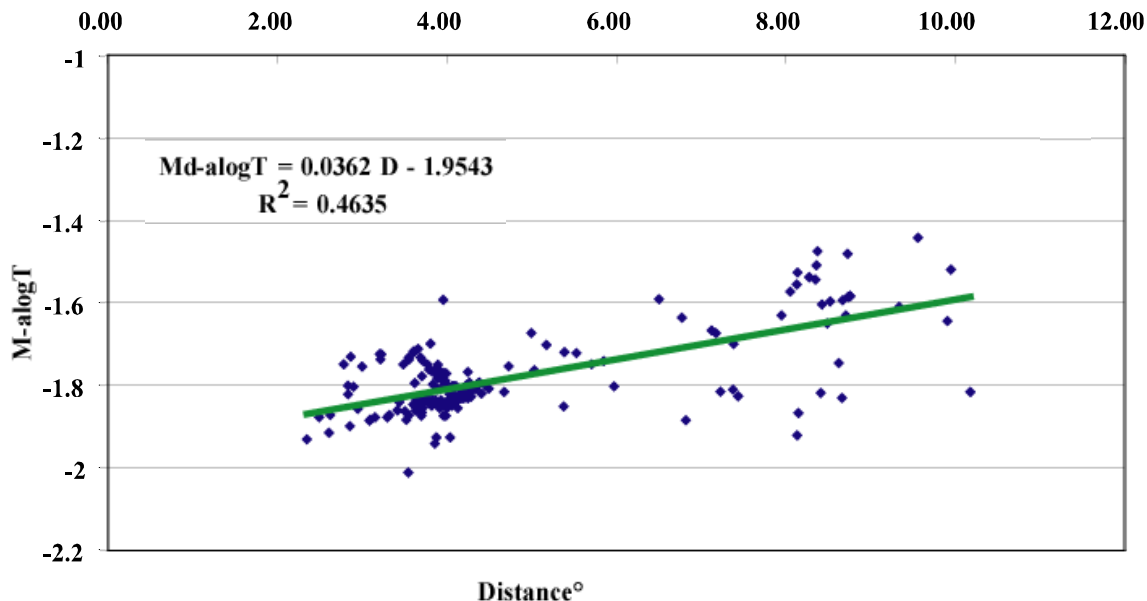


Fig. (3): Plots of the single magnitude formulas for duration magnitude scale that are proposed for application by the KNSN in its seismic monitoring activities.

Table (1): Duration magnitude formula for each KNSN seismic station as indicated and for a single representative equation for the considered stations of the network. Each seismic station correction is evaluated from the single formula (total).

Station Code	Regression Constants			Station Correction
	a/d	b/e	c/f	
QRN	2.25	0.036	-0.91	-0.026
RDF	2.54	- 0.035	-1.36	0.35
NAY	2.66	0.053	-2.06	-0.069
RST	2.73	-0.0053	-1.94	0.18
MIB	3.2	0.015	-3.14	0.00
UMR	2.76	0.067	-2.3	-0.017
Total	2.66	0.036	-1.97	

The development of the empirical formula for the duration magnitude scale is mainly based within the hypothesis of the initial seismic data taken from the KNSN seismic stations. Hence, the magnitude equations are affected by the reliability and accuracy of the utilized seismic data. Comparison of preliminary determination of seismic parameters such as location and magnitude of seismic events from KNSN and USGS indicates some discrepancies. In case of discrepancies, preference is given to the USGS determinations, for the reason that this agency relies from more seismic stations and application of statistical procedures to the utilized seismic reports. It is also observable from the KNSN seismic data some unintentional errors of recordings for the duration values when based from the corresponding magnitude and distance of earthquake events. The occurring errors could be due to malfunctioning in the system of response of the instruments.

These errors were considered for correction in relation to the general trend of the graphs and corresponding values from the other seismic stations. It is therefore advisable that automated evaluation of the required data be counter-checked for the realistic assessment of magnitude.

Hence, magnitude estimates from the preliminarily developed equations can be considered as conservative values due to encountered constraining factors. The level of accuracy is within the limits of the utilized seismic data and assumptions that were taken regarding similarities in the calibrating functions. Although the station corrections imply the significance and relative accuracy of the proposed formulas, the level of validity can be improved from application for further verification.

REFERENCES

Bakun W. and Lindh A., 1977. Local magnitudes, seismic moment and coda duration for earthquakes near Oroville, California, Bull. Seism. Soc. Am., Vol. 67, pp. 615-629.

Crosson R., 1972. Small earthquakes, structure, and tectonics of the Puget Sound region Bull. Seism. Soc. Am., Vol. 62 , pp.1133-1177.

Gutenberg B., 1945. Amplitudes of P, PP, and S and magnitudes of shallow earthquakes, Bull. Seism. Soc. Am., Vol. 35, pp. 57-69.

Kim W., 1998. The Ml scale in eastern North America”, Bull. Seism. Soc. Am., Vol. 88, pp. 935-951.

Lee W, Bennet R., and Meahger K., 1972. A method of estimating magnitude of local earthquakes from signal duration, USGS Open File Rept., 28.

- Real C. and Teng T., 1973.** Local Richter magnitude and total signal duration in southern California, Bull. Seism. Soc. Am., Vol. 63, pp. 1809-1827.
- Richter C., 1935.** An instrumental earthquake scale, Bull. Seism. Soc. Am., Vol. 25. pp. 1-32.
- Solov'ev S., 1965.** Seismicity of Sakhalin", Bull. Earthq. Res. Inst., Tokyo Univ., Vol. 43, pp. 95-102
- Tsumura K., 1967.** Determination of earthquake magnitude from total duration of oscillation, Bull. Earthq. Res. Inst., Vol. 15,pp. 7-18.

DELINEATION OF SUBSURFACE FEATURES USING SHALLOW GEOPHYSICAL SURVEYS AT NEW CAIRO CITY

H.H. El-Kadi*, M.A.H., Abdel Aziz ** and A.M. Saad*

* Geology Department, Faculty of Science, Al-Azhar University

** Atomic Energy Authority

استنباط الخصائص التحتسطحية لمدينة القاهرة الجديدة باستخدام المسح الجيوفيزيقي الضحل

الخلاصة: يلعب الوضع الجيولوجي العام وكذلك الخصائص الفيزيائية والديناميكية لطبقات الأساس دوراً فعالاً في استقرار المنشآت وخاصة في حالة تعرض المنشآت لقوة ديناميكية مصاحبة لحدوث الزلازل ويتعلق هذا البحث بتطبيق الطرق الجيوفيزيائية الضحلة واستخدامها في استنباط الخصائص الفيزيائية والديناميكية للطبقات الضحلة وذلك لتحديد طبقة الأساس. وقد استخدمت طريقة المقاومة النوعية الكهربية لتحديد المقاومة الحقيقية للطبقات الضحلة وكذلك أسماك تلك الطبقات وأعماق المياه الجوفية. ومن ناحية أخرى فقد استخدمت طريقة المسح السيزمي الانكساري لتقسيم القطاع الضحل إلى طبقات ذات سرعات سيزمية محددة والتي استخدمت في تحديد معاملات المرونة لطبقات الأساس.

وقد استخلص من الدراسة أنه قد أمكن تقسيم القطاع الضحل لمدينة القاهرة الجديدة إلى أربع طبقات ذات خصائص صخرية وفيزيائية مختلفة وتتراوح قيمة المقاومة النوعية للطبقة الأولى من ١٥ إلى ١٠٠ أوم متر، كما يتراوح سمكها من ٠,٦ إلى ٣٦ متراً. بينما تتراوح قيمة المقاومة النوعية للطبقة الثانية من ١٠٠ إلى ٥٠٠ أوم متر، وسمكها يتراوح من ٠,٧ إلى ٣٧ متراً. وتتميز الطبقة الثالثة بمقاومة نوعية أقل من ١٥ أوم متر وسمك يتراوح من ٠,٧ إلى ٢٥ متراً. بالنسبة للطبقة الرابعة فتصل مقاومتها النوعية إلى أكثر من ٥٠٠ أوم متر. كما بينت الدراسة أن سعة التحميل القصوى للطبقة الثانية تتراوح من ٨٩٨ إلى ١٦١٤ جرام/سم^٢ بينما تتراوح سعة التحميل المسموح بها من ٢٩٩ إلى ٥٣٨ جرام/سم^٢.

ABSTRACT: The geologic setting and physical and dynamic properties of foundation beds are playing a crucial role in the stability of building, especially in case of the subjection of building to dynamic forces associated with the earthquake occurrence. The present work is concerned with the application of shallow geophysical investigations to delineate the shallow subsurface geologic characteristics and determine the physical and dynamic properties of foundation beds in New Cairo city. The electric resistivity survey was applied by using Schlumberger array to identify the resistivity and thickness of the different shallow layers. The shallow seismic refraction technique was also used to evaluate the foundation rock properties in the area by recording the time arrivals of seismic waves and their interpretation in terms of subsurface geoseismic layers and their physical and dynamic properties.

The shallow section of New Cairo city, could be divided into four types of lithologic units; sandy soil (a resistivity from 15 to 100 Ohm-m and thickness from 0.6 to 36m), gravely soil (sand and gravel with a resistivity from 100 to 500 Ohm-m and thickness from 0.7 to 37m), clayey soil (silty clay of less than 15 Ohm-m and thickness is varying from 0.7 to 25m) and rocky soil (sandstone, sandy limestone and weathered basalt of more than 500 Ohm-m). The ultimate bearing capacity in the second layer is ranging from 898.72 to 1614.07 gm/cm², the allowable bearing capacity in the second layer is between 299.57 and 538.02 gm/cm² and hence the factor of safety is equal to 3.

INTRODUCTION

The New Cairo city is located at the eastern part of Cairo. It is bounded by Cairo Suez desert road from the North, El-Qattamiya-Ain El-Sokhna road from the South, Ring road from the West and Gebel El-Anqaabiya from the East Fig.(1). The study area lies between latitudes 29°55' and 30°05' N and longitudes 31°20' and 31°40' E. The New Cairo city is characterized by an arid climate, very low rainfall, high temperature and high evaporation rate. Geomorphologically, the New Cairo area has a moderate relief. The elevation ranges from 50 to 460 m above sea level. There are three main geomorphologic units; the lime plateau, cuestas hills and rolling palm unit.

Both the resistivity and seismic refraction surveys are broadly used in the civil engineering projects. Electrical survey is used to determine the depth of bedrock, weathered zone thickness, depth to

groundwater and clay extension. On the other hand, the seismic refraction survey is generally utilized to divide the shallow section into layers, delineate the geologic structure intersects the continuity of the encountered layers and deduce the physical and dynamic properties of the foundation beds.

Geologic Setting

In the area of study, the exposed stratigraphic units exposed are all sedimentary rocks. The general stratigraphic successions are belonging to (1) Eocene deposits: These deposits are exposed in this area and can be classified into two units: a-) Middle Eocene deposits: which are subdivided into three Formations: the Observatory, Qurn and Wadi Garawi. The Observatory Formations composed of yellowish white fossiliferous chalky limestone and hard dolomitic limestone. While

the Qurn Formation is mainly represented by chalky, marly limestone and limestone alternating with sandy marl. The Wadi Garawi Formation is composed of limestone, marl and sandy shale. b) Late Eocene deposits representing Wadi Hof Formation. They are composed of shale and sandstone with a basal limestone bed. The Wadi Hof Formation overlies conformably the Wadi Garawi Formation and underlies unconformably the Oligocene sediments. (2) Oligocene deposits: represented mainly by the Cairo Facies (Gebel Ahmer Formation), which is composed of sand with gravels and sedimentary quartzites with silicified wood. Basaltic flows are recorded at the top of the Oligocene sediments in this Facies. (3) Miocene deposits: which can be classified into two units: a) Marine Miocene (Homth Formation): The marine Miocene section occurs as patchy, isolated outcrops along the Cairo –Suez road, but eastward it covers larger areas. It is made up of sparsely fossiliferous calcareous sandstone and arenaceous limestone. b) Non-marine Miocene (Hagul Formation): which covers most of north eastern part of the study area. It is composed of white to grayish sand. It intercalated by gravels beds. (4) Pliocene deposits: which are found on the top of the non-marine Miocene at gebel El-Nassuri and El- Anqabiya. They consist of cross bedded sand with some clay, conglomerate and white hard and very dense limestone.

INSTRUMENTATION AND PROFILES LAYOUT

For that reason, 22 Schlumberger vertical electrical soundings (Fig. 2) were conducted with a maximum electrode spacing of 200 m. These vertical electrical soundings have been carried out by the Swedish apparatus. ABEM-terrameter SAS 300 C. On the other hand, 24 channels S2-echo seismograph, manufactured by Sintrex was employed during field survey. Ten profiles were surveyed in the studied area. Each profile has 48 m long with 4m geophones spacing. Each profile has two shots located at the ends of the profile as shown in Fig. 2.

DATA PROCESSING AND INTERPRETATION

(A) Resistivity Data:

The resistivity interpretation was carried out using the method developed by Van der Velpen (1988) in which, the values of $AB/2$ and ρ_a were used in fast iterative procedure to give a multilayer model reflecting the inferred true depths and resistivities. The initial model proposed to the Resist-program is taken to determine the parameters of the bedrock. The geoelectric parameters (resistivity and thickness of the different geoelectric layers) obtained from the interpretation of each VES are given in Table 1. Also, a number of geoelectric cross sections have been established along a number of the executed profiles to define the lithological

succession in the shallow section and determine the depth to water table.

Geo-electric Cross-Sections

The interpreted resistivity data have been utilized to construct a number of cross sections that reflect the shallow section underneath the studied area. They show that the shallow section consists mainly of four geoelectrical layers as shown in Fig.3. The first layer exhibits electrical resistivity values varying from 15 to 100 Ohm.m corresponding lithologically to sandy soil. Its thickness varies from 0.6 to 36m. The second layer has resistivity values ranging from 100 to 500 Ohm.m corresponding to gravel. Its thickness ranges between 0.7 to 37m. The third layer has a relatively low resistivity values less than 15 Ohm.m and its thickness varies from 0.7 to 25m, and corresponds lithologically to clayey silt. The fourth layer has resistivity values more than 500 Ohm.m with a thickness varying from 0.3 to 32m, and correspond, to rocky soil.

(B) Shallow Seismic Data

Seismic refraction data have been interpreted using RF software developed by OYO company giving the depth not only at the two ends of the profile but at each geophone. So, It reflects the undulations and irregularities in the strata. The processing and interpretation of the data cited from the apparent velocities, distances between shot points and geophones and depths were carried out using Haigwara method. Table 2 shows the variation of the seismic wave velocities along ten profiles executed in the studied area.

Subsurface Cross Sections:

A number of cross sections reflecting the nature and continuity of the geo-seismic layers in the shallow section underneath the studied area (Fig.4). The shallow section could be divided into two geo-seismic layers with S-wave velocities ranging from 141m/sec to 647 m/sec and P-wave velocities from 240 m/sec to 1100 m/sec for the first layer. Also, seismic wave velocities have been calculated for the second layer to range from 317 m/sec to 3700 m/sec (table 2). The large variation in seismic wave velocities reflect the variation in the rock type occupied the shallow section in the area.

Dynamic Properties of Foundation Bed

The measured P- and S- wave velocities have been used to calculate the dynamic properties of the foundation bed including the Poisson's ratio, standard penetration test, bulk modulus, shear modulus, rigidity modulus, allowable and ultimate bearing capacity using a number of empirical relationships. These relationships were developed by many authors like Gardner et al., 1974, Imai et al., 1976.

Table 1: Resistivity (R) and corresponding thickness (H) of different geoelectrical layers.

VES No.	Layer No.	I		II		III		IV		V
	R ₁	H ₁	R ₂	H ₂	R ₃	H ₃	R ₄	H ₄	R ₅	
1	2752	4	207	38.2	876	--	--	--	--	
2	62	3.6	288	6.7	30	29.4	100	--	--	
3	34	0.6	296	4.3	14	15.3	127	--	--	
4	80	1.6	134	3.3	42	8.6	78	--	--	
5	58	1.6	135	41.6	34	--	--	--	--	
6	161	1.5	89	5.1	4	10.7	134	34	8	
7	13	2.6	26	13.5	103	--	--	--	--	
8	29	0.5	199	12.7	348	--	--	--	--	
9	39	2	60	36	20	--	--	--	--	
10	107	1.9	111	45.9	134	--	--	--	--	
11	62	1.1	292	15.6	55	31	660	--	--	
12	167	0.7	277	15.5	12	--	--	--	--	
13	111	2.9	136	12.7	100	--	--	--	--	
14	114	0.7	1950	1.6	330	37.4	202	--	--	
15	482	1	276	1.2	2238	4.4	2	98	233	
16	2662	1.3	3639	7	8	25	172	--	--	
17	2480	1.2	917	8.9	2	13.2	74	--	--	
18	317	1.3	198	6.9	2	9	10	--	--	
19	836	0.7	66	24.9	10502	--	--	--	--	
20	16382	0.3	117	2.9	920	32.8	7	--	--	
21	27	0.6	748	10.7	495	17	105	--	--	
22	27	13	186	4.7	34	12.8	244	--	--	

Table 2: Distribution of seismic wave velocities along the profiles at New Cairo city.

Profile No.	Velocity (m/sec) 1st layer		Velocity (m/sec) 2nd layer		Expected type of lithology
	P-wave	S-wave	P-wave	S-wave	
1	240	141	850	500	Fill and compacted sandstone.
2	1100	647	1900	1117	Weathered calcareous sandstone and compacted sandstone intercalated compacted clay.
3	760	447	3200	1882	Weathered sandstone and compacted sand with gravels.
4	510	300	800	470	Sand with gravel and compacted sandstone.
5	370	217	3700	2176	Sand with gravel and sandy limestone.
6	560	329	700	411	Loose sand with gravel and compacted sandstone.
7	650	382	750	441	Weathered sandstone and sand with gravel.
8	500	294	750	441	Weathered and graded sand.
9	510	300	550	323	Weathered and graded sand
10	490	288	540	317	Weathered sand and graded sand.

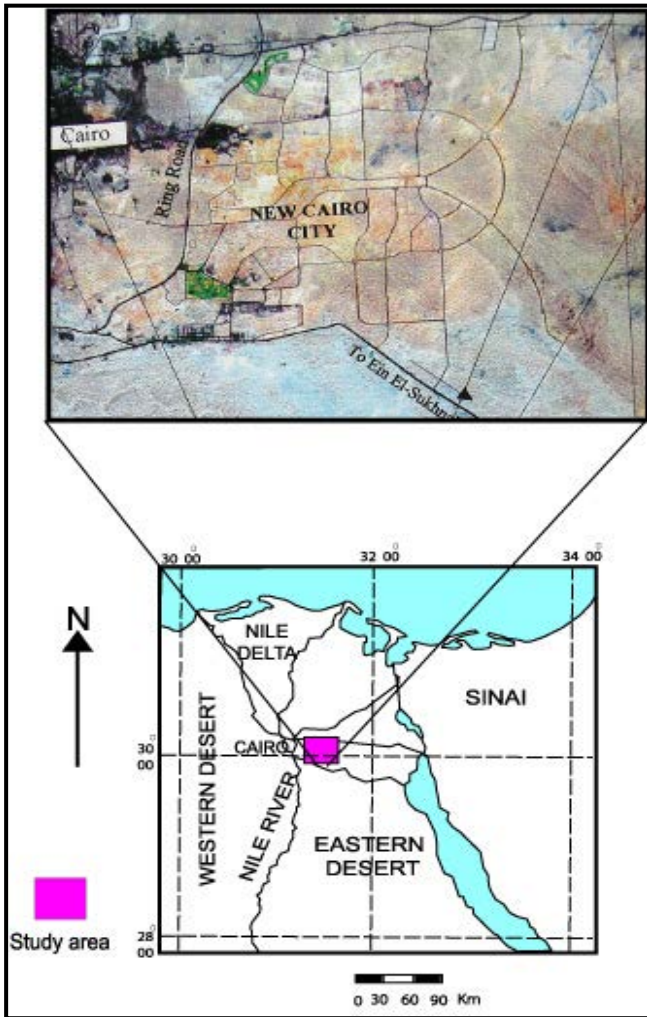
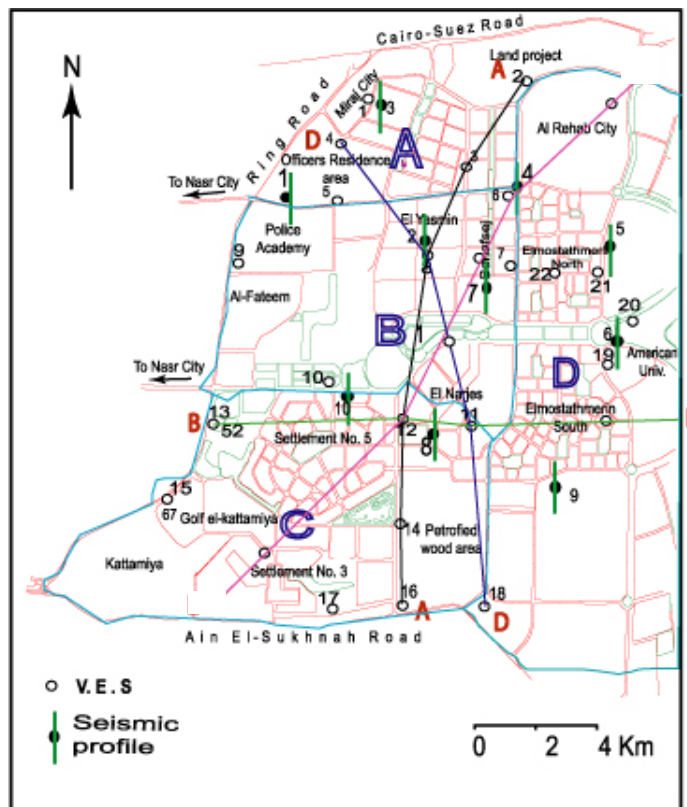


Fig. (1): Location map of New Cairo City modified after. EGSMA, 1983.

Fig. (2): Location map of VESes and seismic profiles, New Cairo City



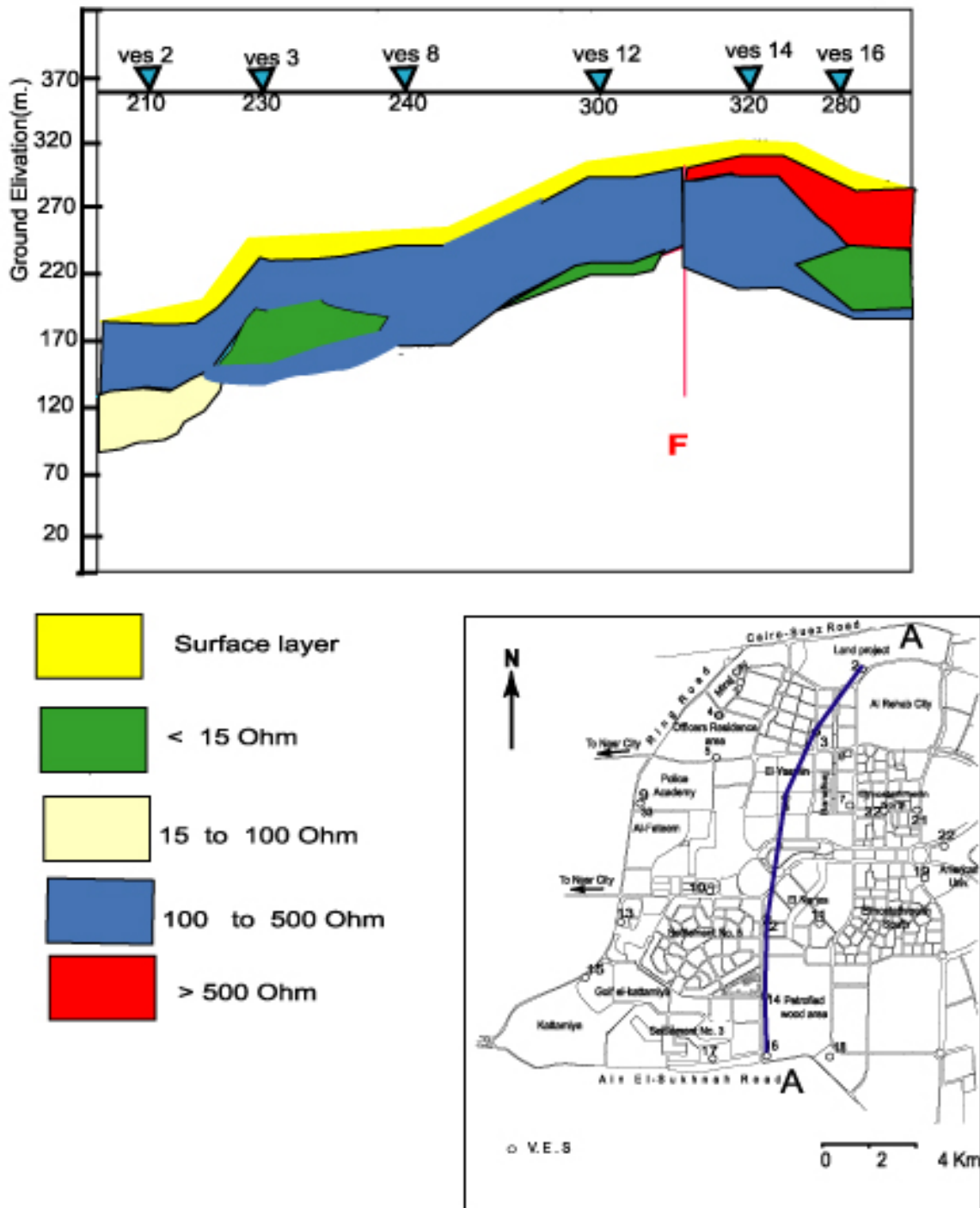


Fig. 3. Geo-electric cross section along profile A-A'

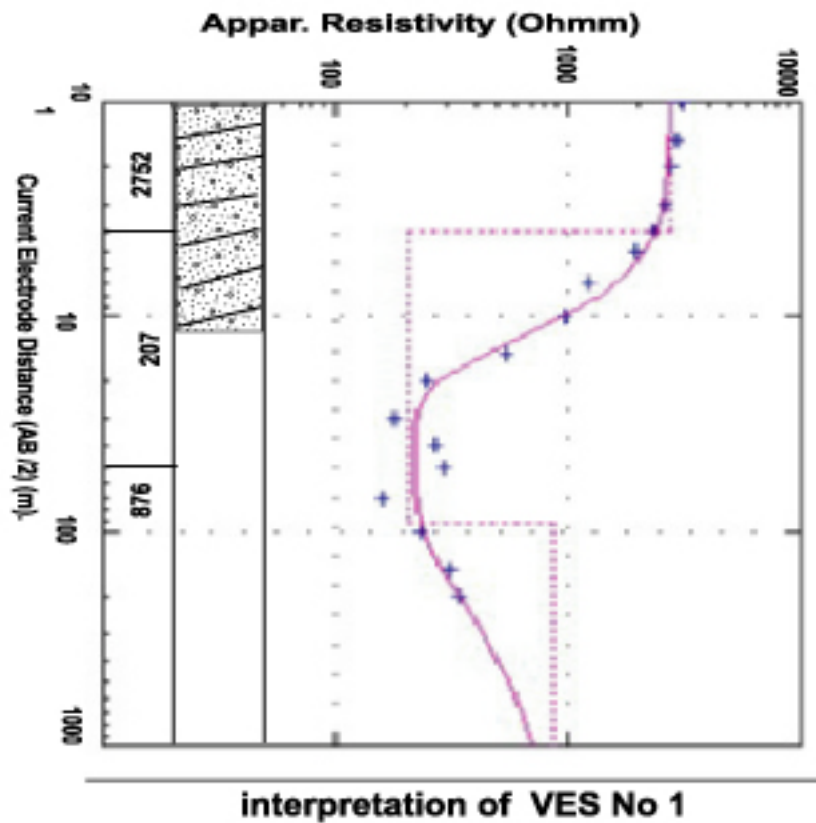
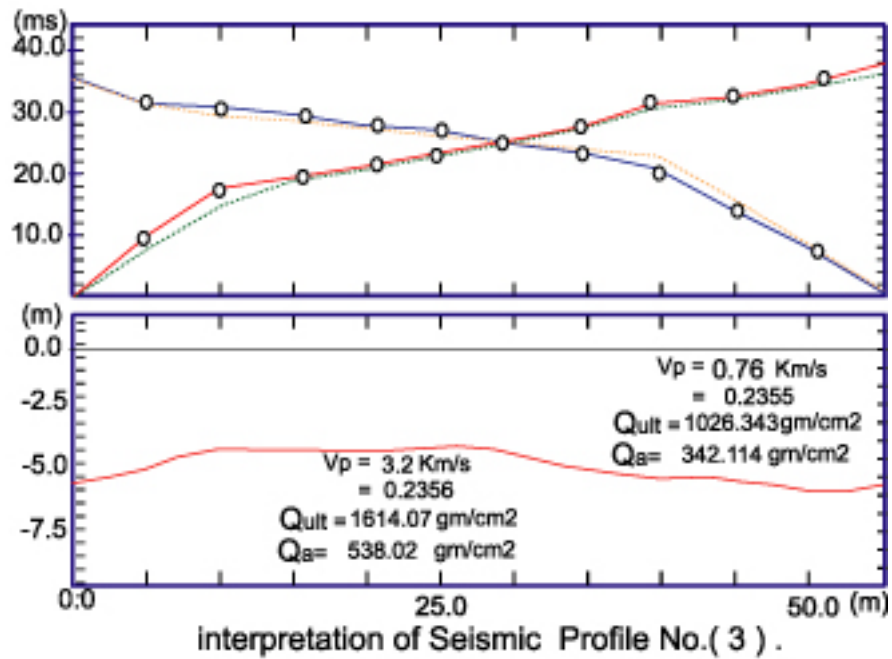


Fig. 4. Travel-time curve and its corresponding geo-sismic cross section

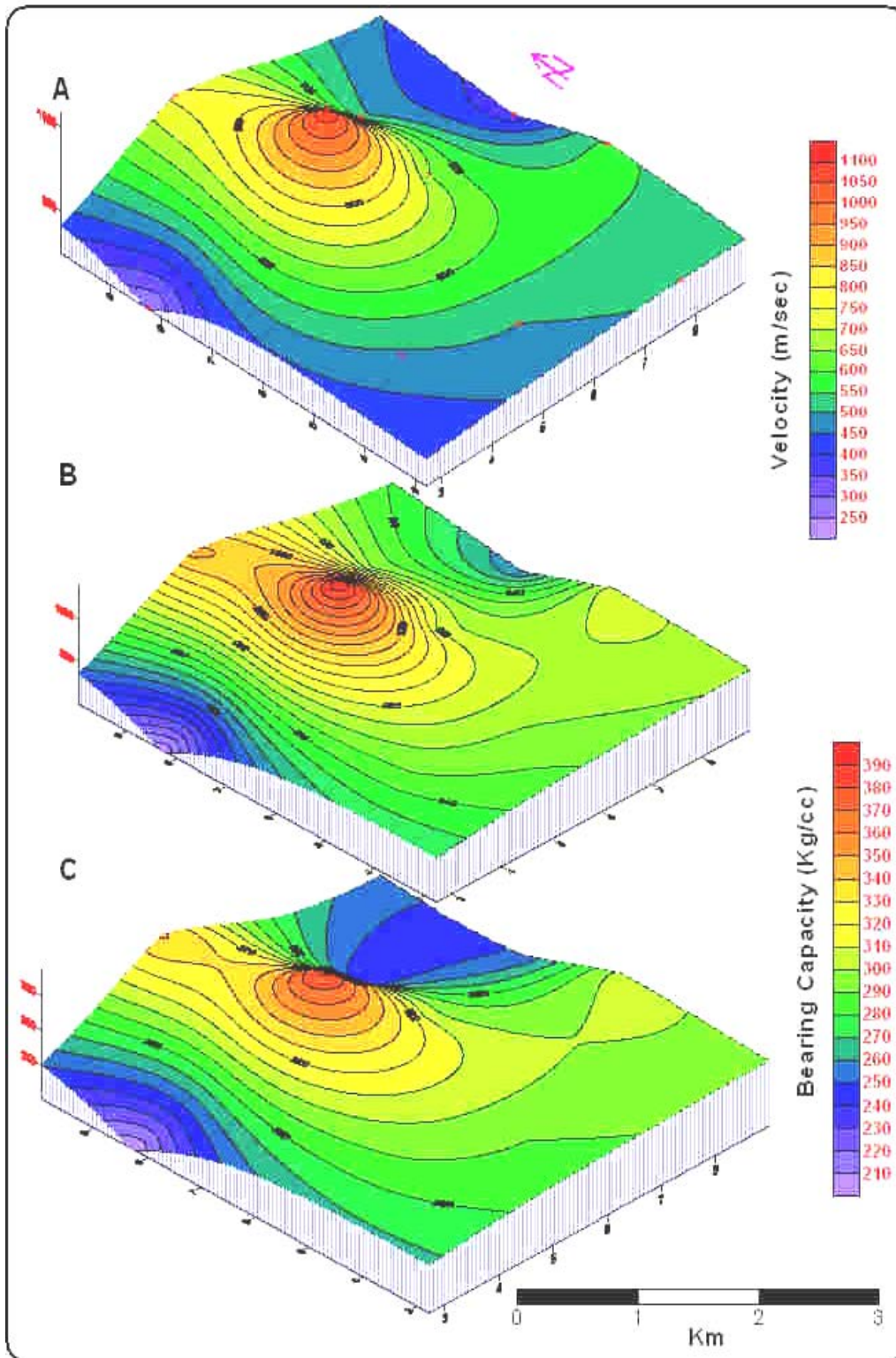


Fig. 5: Compressional wave velocity, ultimate bearing and allowable bearing capacity of the first layer.

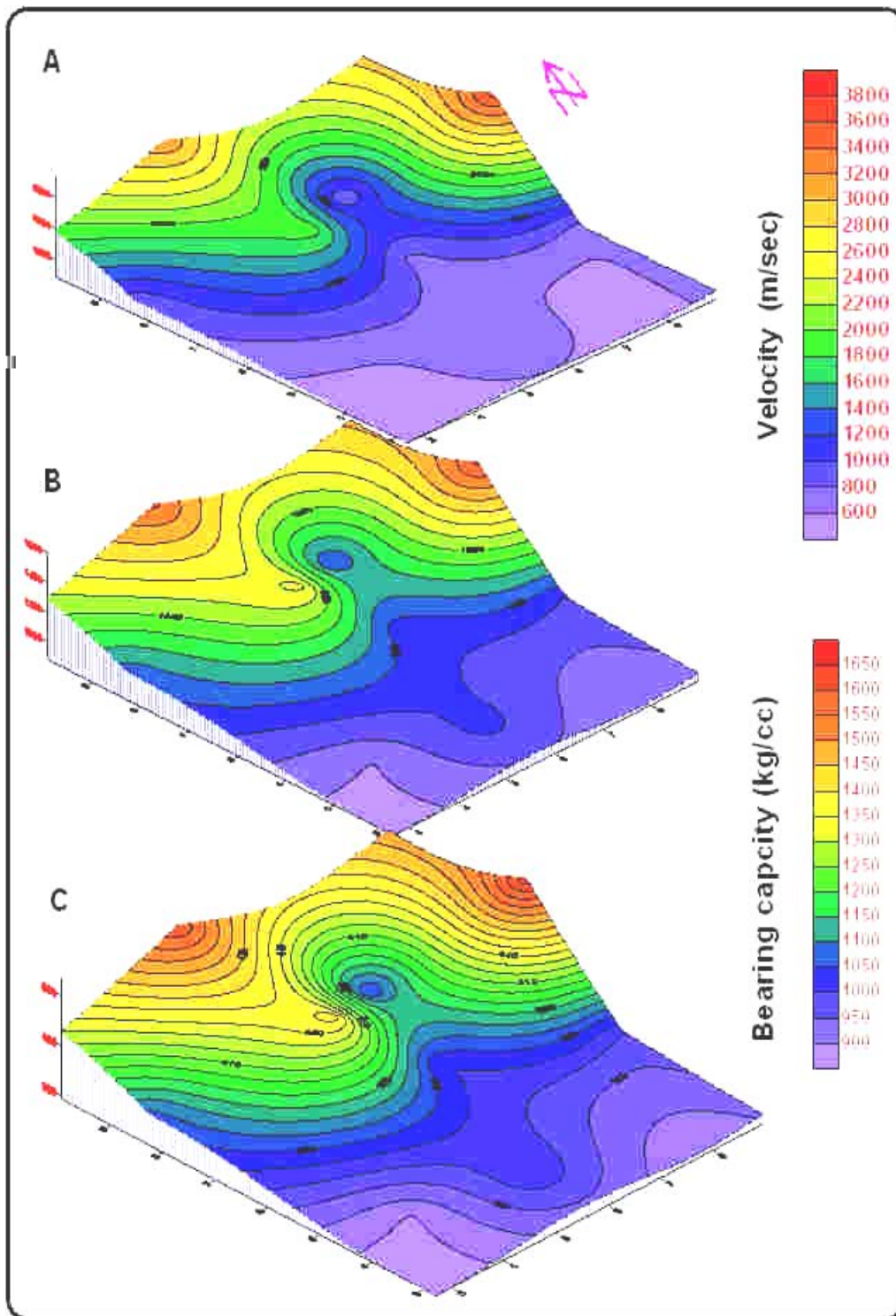


Fig. 5: Compressive wave velocity, ultimate bearing and allowable bearing capacity of the second layer.

Figs (5) and (6) show the distribution of the ultimate and allowable bearing of the first and second layers as an example of one of the dynamic properties. The ultimate bearing capacity of the first layer is characterized by values ranging from 597 gm/cm² to 1163 gm/cm². In the second layer, the values range between 898 gm/cm² to 1614 gm/cm².

CONCLUSION

Processing and interpretation of acquired shallow geophysical data in New Cairo city proved that, the shallow section is divided into four types of lithological units: sandy soil, gravely soil (sand with gravels), clayey soil (silty clay) and rocky soil (sandstone, sandy limestone and weathered basalt). The first type has a resistivity value ranging from 15 to 100 Ohm-m and thickness varying from 0.6 to 36m. The second type has a resistivity value ranging from 100 to 500 Ohm-m and a thickness from 0.7 to 37m. The third type has a relatively low resistivity value (less than 15 Ohm-m) and its thickness varies from 0.7 to 25. The fourth type has a resistivity value more than 500 Ohm-m and its thickness varies from 0.3 to 32 m.

The first and second layers of soil are considered good foundation beds having good allowable bearing capacity but the second layer has an increase in its competence capabilities compared with the first layer. The two types are classified as coarse grained soils with good load bearing capacities and good drainage qualities, and their strength and volume change characteristics are not significantly affected by the change in moisture content.

REFERENCES

- Abd El-Rahman, M.M. (1991):** Rock material competence assessed by seismic measurements with emphasis on soil competence scales and their applications in some urban areas in Yemen ; EGS. Proc. 9th Ann. Meeting; p. 206-228.
- Gardner, L.W. (1974):** An areal plan of mapping subsurface structure by refraction shooting ; Geophysics, V.4 pp. 247-259.
- Imai, T.; Fumoto, H. and Yokota, K. (1976):** P- and S-wave velocities in subsurface layers of ground in Japan : Urawa Research Institute, Tokyo.
- Parry, R.H.G. (1977) :** Estimating bearing capacity of sand from SPT values. JGED, ASCE, 103 : GT. Vol. 9 pp. 1014-1043.
- Saad, A.M.(2000):** Geophysical, sedimentological and engineering studies of El-Sherouq city, East of Cairo, Egypt. M.Sc. Thesis, Faculty of Science, El-Azhar Univ. 188p.
- Swedan, A.H. (1991):** A note on the geology of Greater Cairo area. Annals of the geological survey of Egypt, V. X. VII, PP. 239-251.
- Telford, W.M.; Geldast, L.P.; Sheriff, R.E. and Keys, D.A. (1976):** Applied geophysics, Cambridge Univ. Press, 860 pp.
- Van-der-Velpen, B.P.A. (1988) :** Resist, Version 1.0, a package for the processing of the resistivity sounding data. M.Sc. Research Project, Netherlands.
- Zohdy, A.A.R. (1975):** Automatic interpretation of Schlumberger sounding curves using modified Dar. Zarrouk functions, Bull. 1313-E, U.S.; Geological Survey, pp. 39.

MAGNETOTELLURIC AND AEROMAGNETIC INTERPRETATION AT FAYOUM-CAIRO DISTRICT, NORTHERN WESTERN DESERT, EGYPT

M. Mekkawi *, A. Khalil*, M. Elbohoty*, T. RabeH*,
A. Saleh*, R. Abuel ezz** and A. Khalaf*

* National Research Institute of Astronomy and Geophysics (NRIAG), Helwan, Cairo, Egypt.

** Al-Azhar University, Faculty of Engineering, Cairo, Egypt.

E-mail: mekkawi05@yahoo.com

تأويلات تيارات المغناطيسية الأرضية وخرائط المغناطيسية الجوية بطريق القاهرة – الفيوم، شمال الصحراء الغربية، مصر

الخلاصة: تقع منطقة إقليم الفيوم-القاهرة في الجزء الجنوب الغربي من مدينة القاهرة، التي تأثرت بالعديد من الزلازل. طبقا لتصريحات الشبكة القومية للزلازل التابعة للمعهد القومي للبحوث الفلكية والجيوفيزيقية، قد حدث زلزال في ٣١ يوليو سنة ٢٠٠٥ في منطقة الدراسة قوته ٤.٢ بمقياس ريختر. طريقة التيارات المغناطيسية الأرضية تعطى افضل الطرق للبحث عن السوائل الموجودة في الفوالق التي تؤدي الى الشاذات الجيدة التوصيل للتيار الكهربي. الاهداف المرجوه من هذه القياسات متنوعة. ايجاد مواقع الفوالق النشطة بالنسبة للنشاط الزلزلي بمنطقة الفيوم-القاهرة وعلاقتها بالتراكيب الجيولوجية ذات المقاومات الكهربية بواسطة التيارات المغناطيسية الأرضية. وقد اخذ قطاع من التيارات المغناطيسية الأرضية يمر بمنطقة الدراسة لتوضيح التراكيب الجيولوجية البعيدة ذات المقاومات الكهربية. وايضا خريطة الشاذة المغناطيسية الجوية استخدمت لتبيين التراكيب الجولوجية الضحلة.

ABSTRACT: The Fayoum–Cairo district lies in the south western part of Cairo, which is affected by several earthquakes. According to the Egyptian Network Seismology of National Research Institute of Astronomy and Geophysics (NRIAG), the last one occurred in the 31st July, 2005 (Magnitude = 4.2 in Richter scale). Magnetotelluric (MT) method can offer good opportunity to detect crustal fluids along faults due to their high electrical conductivity anomalies. The targets of these measurements are various. Its always desired to determine the location(s) of active fault(s) to study the connection of the Fayoum–Cairo seismicity and MT resistivity structure. A single MT profile was carried out across the area in order to investigate the deep resistivity structures. Beside RTP aeromagnetic anomaly map was used to delineate the shallow structures.

INTRODUCTION

The area under study is located in the northern part of Egypt between latitudes 29° 40' N & 29° 55' N and longitudes 30° 55' E & 31° 20' E, occupying a total surface area of about 1225 km² (Fig. 1). The earthquake activity in Egypt is moderate ($M \leq 6$); but some events caused extremely severe damage to recent and historical constructions (Fig. 2b). The MT survey was conducted along eight stations on a northeast-southwest trending profile, selected perpendicular to the regional geologic structures and extremely for about 20 km of the study area (Fig. 2a).

The Magnetotelluric method (MT) is an electromagnetic (EM) technique that is used to determine the electrical resistivity structure of the earth by measuring natural magnetic and electric fields at the surface. Two dimensional (2-D) inversions were applied to (MT) data. The reduced to the pole (RTP) aeromagnetic map compiled by the Western Digital Company (1983) has been used for determination of subsurface structures. Filtering, power spectrum and 2D-magnetic modeling were applied to the RTP aeromagnetic data.

Recent MT studies on active areas (Soyer and Unsworth, 2006; Unsworth et al. and the INDEPTH-MT team, 2005; Mekkawi et al., 2005; Mekkawi, 2003; Bedrosain et al., 2002 and Unsworth et al., 2000) showed that the MT method could be used to delineate the electrical resistivity structures (anomalies) along the fault zones. The low electrical resistivity is attributed to high porosity and fluids present in the highly fractured zone.

Meshref et al. (1980) analyzed the magnetic trends in the northern part of Egypt and stated that the basement rocks in the Western Desert have been affected by two fault systems having large vertical and horizontal displacements. The oldest E-W and ENE faults are intersected by the youngest NW and NNW ones. Abuel ata (1990) based on seismic and gravity data, outlined three structural highs and two lows included in the study area:

- The Abu Roash high that strikes in the NNE-SSW and then ENE-WSW directions.
- Elsagha high which is oriented NW-SE directions.

- The Elfaras-Elfayoum high, which is oriented in ENE-WSW and NNW-SSW directions. Ghazala, 2001 concluded that four significant tectonic zones characterize the area of study:

- 1- Nile Valley graben
- 2- East Nile Valley uplift
- 3- Ginidi basin and
- 4- Kattaniya uplift.

The main aim of this study is to analyze the magnetotelluric and magnetic data and correlate them with the geological information, in order to define the significant fault patterns, which are responsible for the structural development of its geological units. To achieve this goal, various methods and techniques of analysis were applied to interpret the magnetotelluric and magnetic data of the study area.

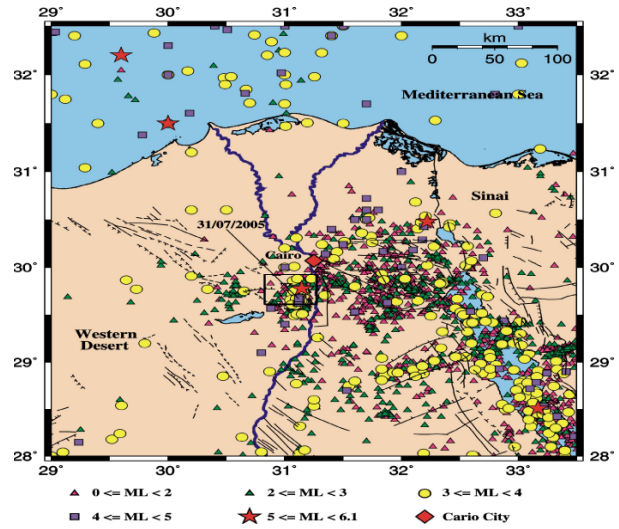


Fig. (1). Location map of the studied area and seismicity map from 1900 to 2005, a part of Northern Egypt (Awad et al., 2006).

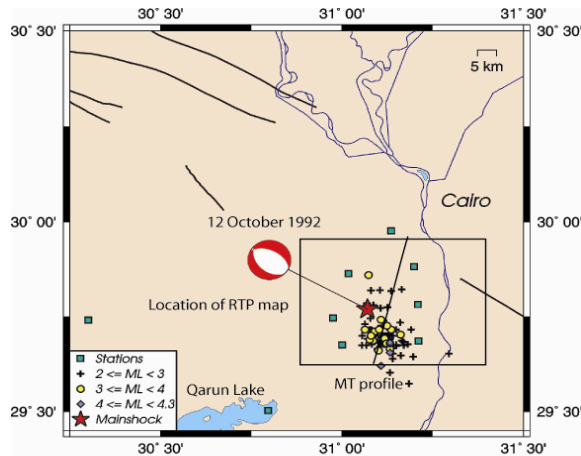


Fig. (2a). Location map of RTP aeromagnetic & MT profile with focal mechanism of the 12th October, 1992, earthquake (M=5.9), Fayoum-Cairo District, Egypt (Awad et al., 2006).

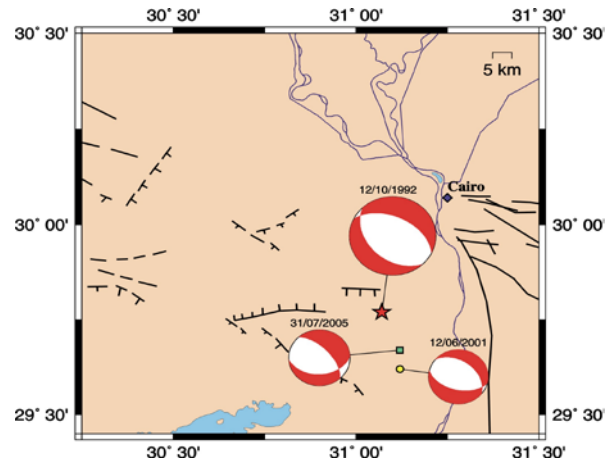


Fig. (2a). Location map of RTP aeromagnetic & MT profile with focal mechanism of the 12th October, 1992, earthquake (M=5.9), Fayoum-Cairo District, Egypt (Awad et al., 2006).

Available Geologic Information

From the geological point of view, the area extends from the southwest of Cairo to Gabal Qatrani at to east and northeast of the Qarun Lake. This lake covers an area of about 200 km²; it has a length reaching about 40 km along its east-west axis, while its maximum width is less than 15 km in the north-south direction (Fig. 2a). It is at an average elevation of about 45 m below sea level. The desert borders the lake from the north and partly eastward, while

cultivated land encircles it from the southwest and southeast. The lake receives most of the drainage of the cultivated lands, coming through El-wadi drains (Sweidan, 1986). Recent deep drilling in the study area (Fig. 6 and Table 1) has shown that a simple geologic structure affects the relatively thick cover of younger sediments. An intricate geologic structure made up of a large number of swells and basins conceals beneath it. The geological units of the study area started from Middle Eocene, to Recent Nile sediments (Naeim et al., 1993).

Fayoum-Cairo province became tectonically active after the active earthquake, which stroked the area in 12th October 1992 of M=5.9 (Awad et al., 2006). The recent suffered earthquake (Fig. 2b) occurred 30 km southwest of Cairo on the 31st July 2005 with medium magnitude (M = 4.4) took our attention to carry magnetotelluric measurements (MT) in the area. The structure of the study area is dominated by faults, many of which can be identified from seismic and well data. The majority is steep normal faults, and most of them have a long history of growth. Some of the normal faults suffered strike-slip movements during a part of their history. Strike-slip movements seem to have affected the orientation of many of the old fold axes. The strike-slip movements were probably related to the lateral movements which the Africa plate underwent during Jurassic and Late Cretaceous (Said, 1990).

Magnetotelluric Data

Magnetotelluric technique (MT) provides information about the electrical resistivity distribution of the earth's subsurface. It is based on the relationship between transient electric and magnetic fields, which are measured at the earth's surface. The main source of the fields is the natural fluctuations of the earth's magnetic field, which occur over a wide spectrum of frequencies. The magnetic field diffuses into the earth and induces electric currents, the so called telluric currents, which in turn cause secondary magnetic fields. The recordings are processed into frequency-dependant responses and then used for the interpretation of the earth's resistivity (Schneegg, 1998).

A good MT site must be protected against weather effects, like wind and direct heat from the sun. It must be setup at least 300 m away from a road, since trucks would generate noticeable variations in the magnetic field at shorter distances. Choosing a convenient site to perform MT sounding requires some experience. Inhabited areas and power lines must be kept at least 4-5 km away. Distance to railway lines should be even larger, particularly for DC trains. The magnetotelluric measurements carried out along eight stations on a single northeast-southwest profile that is perpendicular to earthquakes activity, along 20 km. MT instruments developed at Geompex-Poland for long period measurements were used. The fluxgate magnetometer and telluric amplifiers allow to record field variations in the period range from 1 to 10000 seconds. In the telluric lines of about 100 m length, unpolarised electrodes were used. The average recording for each station was about four days. For more detail about field measurements and instruments used to collect MT data (Elbohoty and Mekkawi, 2005).

Processing of MT Data

For natural source fields, in the frequency domain, the horizontal electric ($E_{x,y}$) and the horizontal magnetic ($H_{x,y}$) are connected via a linear relationship (Yungul, 1996):

$$\begin{aligned} E_x(\omega) &= Z_{xx}(\omega)H_x(\omega) + Z_{xy}(\omega)H_y(\omega) \\ E_y(\omega) &= Z_{yx}(\omega)H_x(\omega) + Z_{yy}(\omega)H_y(\omega) \end{aligned} \quad (1)$$

or in a matrix form

$$\begin{bmatrix} E_x \\ E_y \end{bmatrix} = \begin{bmatrix} Z_{xx} & Z_{xy} \\ Z_{yx} & Z_{yy} \end{bmatrix} \begin{bmatrix} H_x \\ H_y \end{bmatrix} \quad (2)$$

Usually, the components of the impedance (Z) are used to calculate the apparent resistivity functions ρ_{xy} and ρ_{yx} and phase functions ϕ_{xy} and ϕ_{yx}

$$\rho_a(\omega) = \frac{1}{\omega\mu_0} |Z(\omega)|^2 \quad (3)$$

$$\rho_a(\omega) = \frac{1}{\omega\mu_0} |Z(\omega)|^2 \quad (4)$$

$$\phi_{ij}(\omega) = \arg(Z_{ij}(\omega)) = \tan^{-1} \{ \text{Im} Z_{ij}(\omega) / \text{Re} Z_{ij}(\omega) \} \quad (5)$$

where ω is the angular frequency and μ_0 is the magnetic permeability of the vacuum. The impedance tensor and its random errors are estimated using least square method (Pedersen, 1989).

A similar relation exists between the vertical magnetic field intensity (H_z) and the horizontal components magnetic field ($H_{x,y}$) (Schneegg 1998):

$$H_z(\omega) = AH_x(\omega) + BH_y(\omega) \quad (6)$$

$$\text{a length: } T(\text{Re}) = \sqrt{\text{Re}(A)^2 + \text{Re}(B)^2} \quad \text{and}$$

$$\text{an angle: } \mathcal{G}(\text{Re}) = \arctan \frac{\text{Re}(B)}{\text{Re}(A)} \quad (7)$$

$$\text{a length: } T(\text{Im}) = \sqrt{\text{Im}(A)^2 + \text{Im}(B)^2}$$

$$\text{and an angle: } \mathcal{G}(\text{Im}) = \arctan \frac{\text{Im}(B)}{\text{Im}(A)} \quad (8)$$

where T (Re,Im) and θ (Re,Im) are tipper or induction arrows (TP) with length and angle. In the 2D case the real component of induction arrow points away from regions which are good conductors.

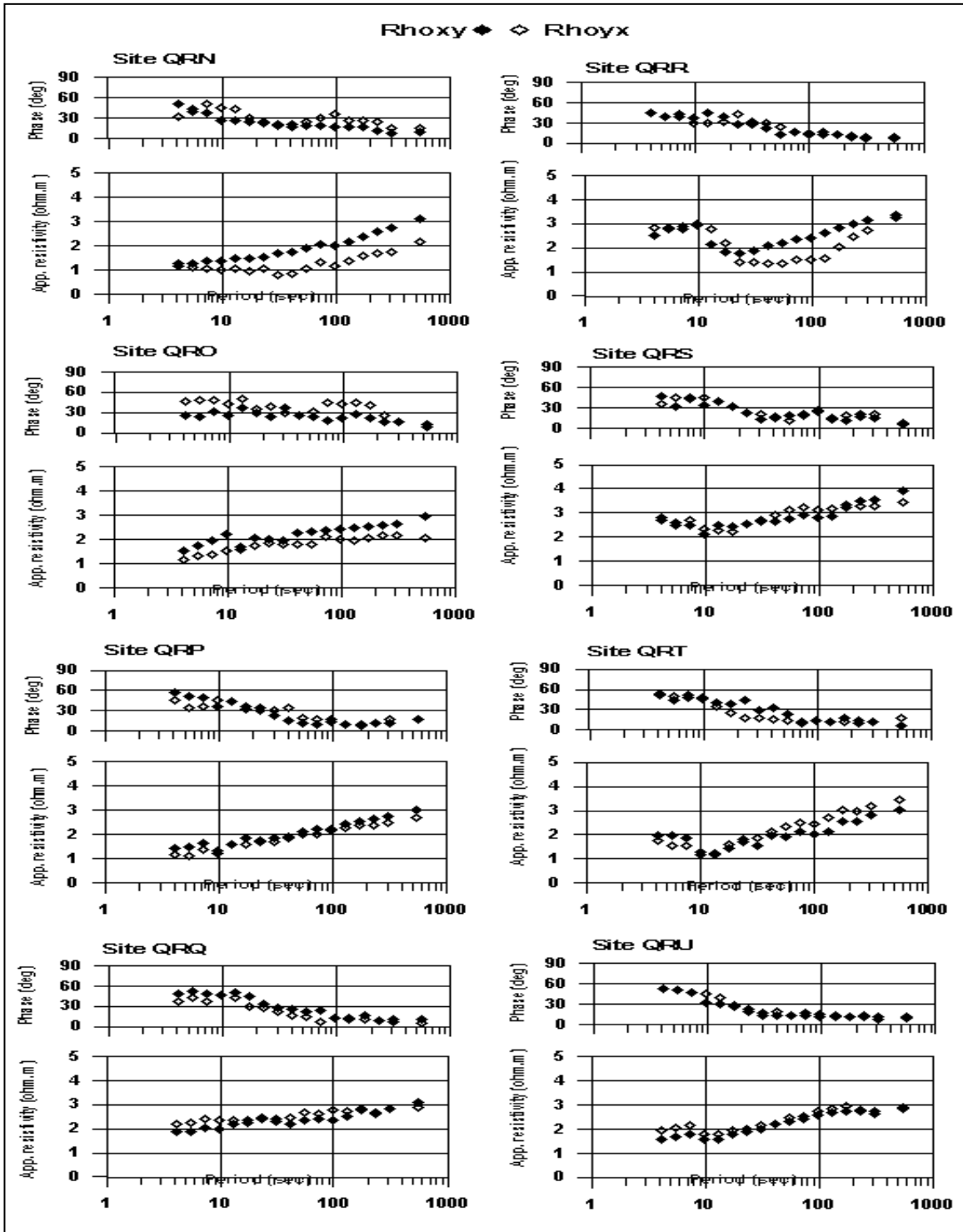


Fig. (3). Apparent resistivity and phase computed for the impedance tensor Z_{xy} (TE) and Z_{yx} (TM), Fayoum-Cairo District, Egypt.

Fig. 3 shows the apparent resistivity (phase (degree) computed for two polarizations Z_{xy} (TE) and Z_{yx} (TM) at the sites QRN to QRU. The MT curves are very similar from site to site along the whole profile. The apparent resistivity modes Z_{xy} diverge above a period of 1 sec., indicating 2D geometry. The two modes steadily increase from values of hundreds of second) to thousands of second) profile is never far away from the high-resistive rocks (granite). Z_{xy} curves are gently increasing between 1,000-10,000 at a deep conducting body (fault or dyke?) embedded into a resistive matrix.

In the induction arrows diagram (Fig. 4), it is noticed that between the stations QRQ and QRR (induction arrows directed in opposite direction) the presence of a good conductor and a similar case between stations QRT and QRU, indicating two faults in the studied area.

Two-Dimensional Modeling and Interpretation of MT Data

Simultaneous inversion of transverse electric (TE), transverse magnetic (TM) modes and tipper (real induction arrows only) was carried out using REBOCC inversion program (Siripunvaraporn and Egbert 2000). The static shift distortion parameters were set free, so that the program could automatically adjust the values. The results of the inversion are shown in (Fig.5) after 12 iterations, the inversion finds a model with R.M.S. misfit of 1.5. The 2D model shows a region of a good-conductive material, that is located in the depth between 0.1 and 5 km. In the central part, there is a zone of high resistive rocks (granite).

Aeromagnetic Data

The qualitative interpretation for the constructed magnetic maps, aims to get a clear view of the subsurface structures, estimate of the relative depth of magnetic anomalies sources. It deals with the description of anomalies, especially their symmetry, strike, extension, width, amplitude and gradients (Nettelton, 1976).

The quantitative interpretation has been used to determine the depth of shallow subsurface structures (faults and dykes), basaltic intrusions as well as the basement complex of the studied area. The method of interpretations includes radially averaged power spectrum and 2D magnetic modeling. The analysis and processing were done by specialized computer program (Geosoft V.4.3, 1993).

The clear investigation of the RTP aeromagnetic map (Fig. 6) compiled by the Western Digital Company (1983),

revealed that the magnetic field increases up in the area with a maximum relief of about 110 nT in the eastern part and decreases to a minimum of about 170 nT in the southern part. It includes several local anomalies in the central, southwestern and northeastern parts of the studied area. These anomalies have different reliefs, polarities and shapes. The general magnetic trends of these regions are almost NW-SE, NE-SW and E-W.

Several zones of high and low magnetic values are present. The magnetic highs are separated from magnetic lows by steep gradients. The elongations of magnetic contour lines and their gradients in the central part of the study area indicate that it is structurally-controlled by faults having major axes in NW-SE and E-W directions. The high magnetic anomalies in the northwestern side can be attributed to the occurrence of subsurface basic intrusions of high magnetic contents. Fault axes as well as the directions of magnetic anomalies are trend in the NW-SE and NE-SW in the northwestern, central and the southern parts of the study area.

Processing of Aeromagnetic Data

Frequency filtering represents a major component of magnetic data processing. As a rule, digital filters are used for signal enhancement, that is to remove unwanted noises, and enhance the desired signals. The nature of "noises" and "signals" varies from case to case or even from a stage of processing to another according to its target. In this study, 2D filtering was applied to the RTP aeromagnetic map. The wavelength linear filtering of the RTP magnetic data is carried out utilizing three types of filtering, these are:

- a- Low-pass filter: It is defined as the filters which passes the long wavelengths and reject all wavelengths smaller than the cut-off wavelength.
- b- High-pass filter: It emphasizes short wavelengths and eliminates wavelengths larger than the cut-off wavelength.
- c- Band-pass filter: It passes wavelengths within a certain range (Peter and John, 1970).

In the present study, filtering technique was performed using a cut-off frequency that ranges between 0.08 cycle/ unit data and 2.0 cycle/ unit data. The high-pass filtered map (Fig. 7) elucidates high-frequency and short-wavelength spot-like magnetic anomalies, which are inferred as residual components. The majority of these local magnetic anomalies are located in the central and southern parts of the study area. These anomalies are distributed with two defined trends (NW-SE and NE-SW).

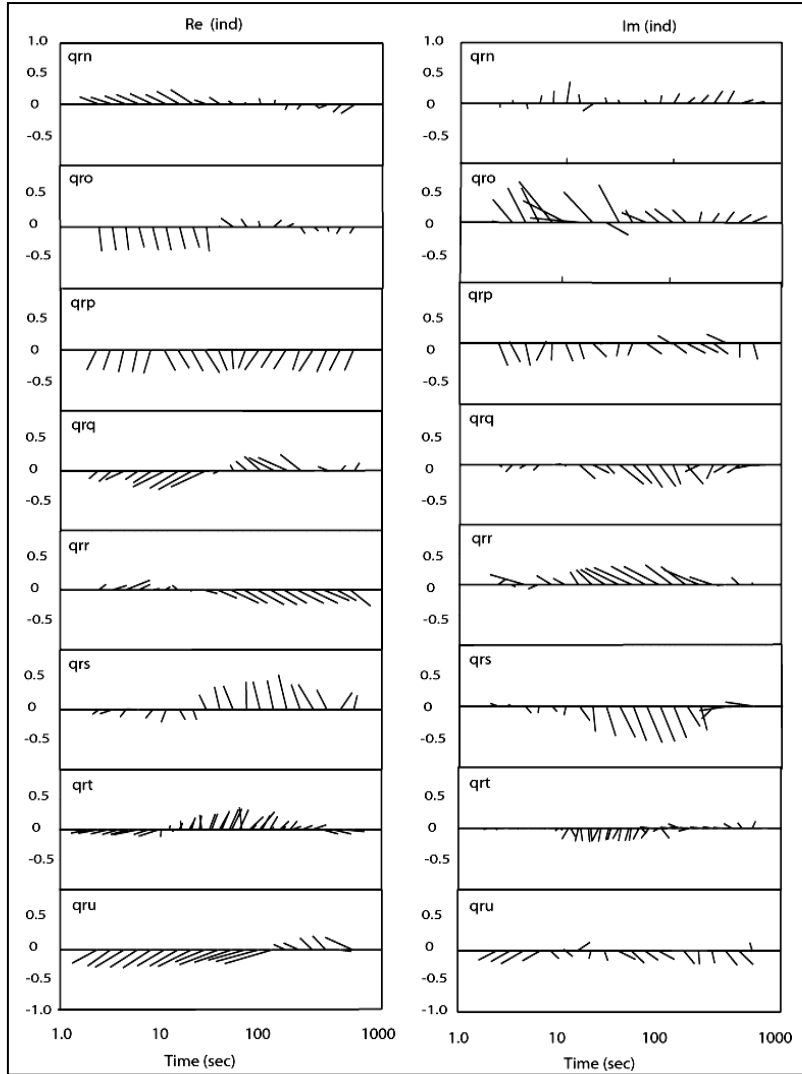
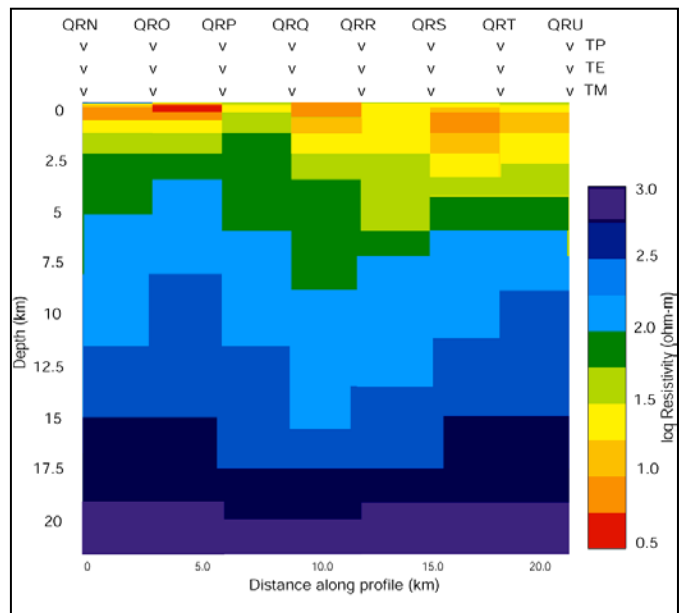


Fig. (4). Real and imaginary induction arrows (Tipper), Fayoum-Cairo District, Egypt.

Fig. (5). Final 2-D model based on MT data along a Profile crossing Fayoum-Cairo District. The location of active faults in Dahshour (between stations QRQ and QRR) in NE-SW direction and the symbols above the model identify the MT sites.



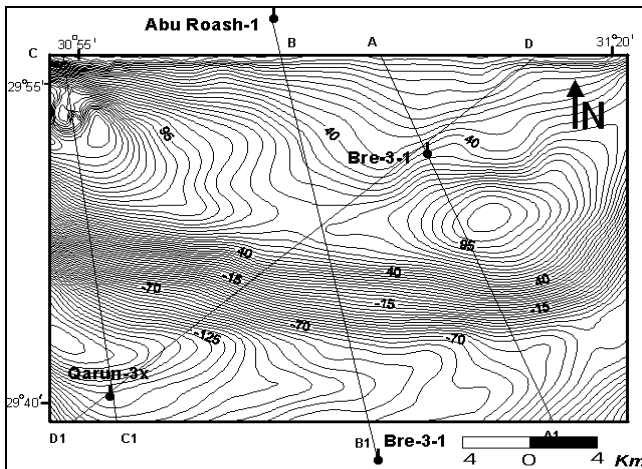


Fig. (6). RTP aeromagnetic anomaly map of the studied area (compiled by the Western Digital Company, 1983), showing the locations of 2-D modeling profiles (A-A1, B-B1, C-C1 and D-D1) and boreholes data, Fayoum-Cairo District, Egypt.

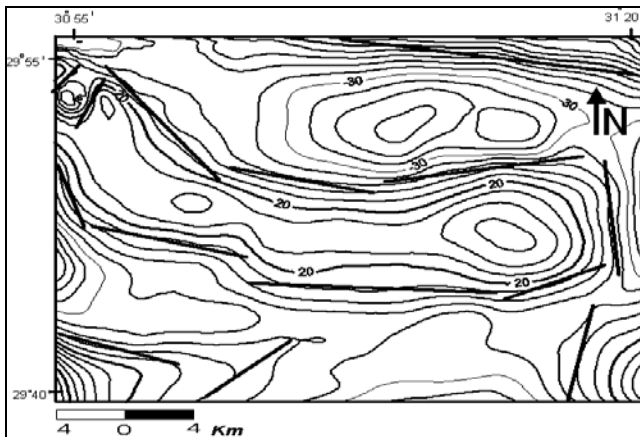


Fig. (7). High-Pass Filter of the RTP aeromagnetic map, Fayoum-Cairo District, Egypt.

However, the prominent NW-SE anomalies lie the northeastern and central parts of the study area. Meanwhile, the NE-SW trending anomalies lie in the northern and southeastern corner of the study area. They are retained but with shorter wavelength than in the original filtered ones. This indicates that the prominent fault trends on the RTP aeromagnetic map extend in the subsurface up to shallow depths. Moreover, the random orientation of small-scale anomalies reflecting that the shallow subsurface has been affected by different stress regimes of the neo-tectonics that may have not affected deep-seated rocks.

The band-pass magnetic filtered anomaly map (Fig. 8) shows that the well-defined trends of anomalies on the RTP aeromagnetic map still persist. However, some smooth regional anomalies that appear not be related to a subsurface structures are most probably a result of regional variations in the magnetization or magnetic susceptibility of the rocks at medieval depths.

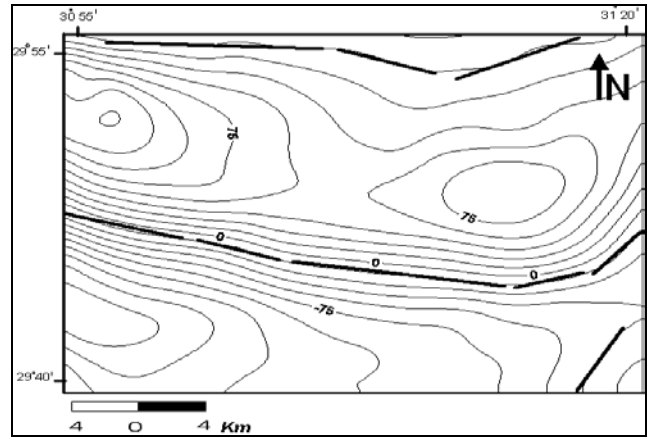


Fig. (8). Band-Pass Filter of the RTP aeromagnetic map, Fayoum-Cairo District, Egypt.

The low-pass magnetic filtered anomaly map (Fig. 9) shows a pattern of gradual rotation of magnetic trends from NE-SW and NW-SE to a E-W trend. As the low-pass filtered anomalies give view about the subsurface deep depths, then the gradual rotation of trends implies that the two suggested stress regimes (NE-SW and NE-SW) were contained to the shallow depths where the E-W one dominated only in the deepest part. The deep-seated zone seems to be affected by an E-W stress trend.

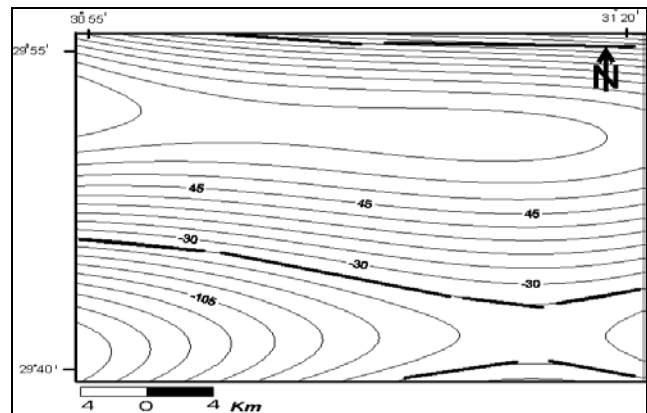


Fig. (9). Low -Pass Filter of the RTP aeromagnetic map, Fayoum-Cairo District, Egypt.

Depth Estimation

The depth to the top of causative magnetic bodies is a useful tool for finding the configuration of the sedimentary basins, and sometimes for locating major structures in basement rocks. Calculation of the depth to the top of the source or the depth to the bottom of the source can be made from the shape of the anomalies, or the shape of the power spectrum computed from potential field data. In this study, Spectral frequency analysis method was used to calculate the depths of the causative bodies utilizing the magnetic data.

Radially average power spectrum method is used to determine the depths of volcanic intrusions, depths of the basement complex and the subsurface geological structures. Several authors, such as Bhattacharyya (1966), and Spector and Grant (1970), Garcia and Ness (1994), Maurizio et al. (1998), explained the spectral analysis technique. It depends on the analysis of the magnetic data using the Fourier Transform of the spectral, map and its complex conjugate. It is a function of wavelengths in both the X and Y directions. In the present study, the Fast Fourier Transform (FFT) was applied on the RTP aeromagnetic data (Fig. 10) to calculate the energy spectrum. As a result, a two-dimensional power spectrum curve was obtained on which three main average levels (interfaces) at depth 0.55 km, 1.35 and 3.95 km below the measuring level were revealed for the deep seated, intermediate level and near surface magnetic components respectively.

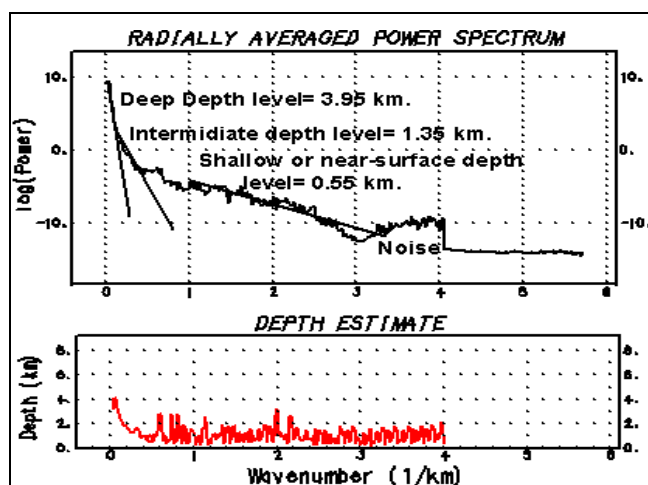


Fig. (10). Radially averaged power spectrum (upper) and the resultant depth estimates (lower), RTP aeromagnetic anomaly map, Fayoum-Cairo District, Egypt.

Two Dimensional (2-D) Modeling of Aeromagnetic Data

Such models assume the earth as two dimensional, i.e., it changes with depth (the Z-direction) and in the direction of the magnetic profile (i.e. the X-direction, perpendicular to the strike), while the strike length of the body (i.e. the Y-direction) is considered to be infinite. The magnetic modeling involves four separate parameters: top surface, bottom surface, magnetic susceptibility contrast, and the observed magnetic anomaly. If three of these parameters are known or assumed, the fourth may be calculated. The forward modeling specifies the first three items and calculates the anomaly.

To confirm the interpreted magnetic basement structural framework of the studied area, four regional magnetic profiles (Fig. 6) were modeled using the 2D-forward modeling technique and available well information in the study area (Table 1). The selected profiles were taken from RTP aeromagnetic map and denoted as A-A1, B-B1, C-C1 and D-D1 (Fig. 6). The magnetic susceptibility contrast values for the sedimentary rocks and basement rocks along the four structural cross-sections were assumed. The magnetic field was calculated iteratively for these geological models, until a good fit was reached between the observed (dots) and calculated (line) profiles. The four models are shown on Figures 11, 12, 13 and 14. On these four figures, the horizontal x-axis represents the horizontal distance in km along the profiles, while the vertical axis is the magnetic field scale in nT and the lower part represents the depth scale in km. The magnetic susceptibility of the basement rocks ranges between 0.003 to 0.004 S.I. units. The magnetic field responses computed for the geological models used magnetic declination of 2.0° east and magnetic field inclination 42°. The regional magnetic field intensity utilized was 42700 nT.

Table 1. Available well information that were used in 2D magnetic modeling (see Fig. 6), Fayoum-Cairo District, Egypt.

Name of well	Formation at end of drill	Total depth (m)
Abu Roash1	Basement	1916
Bre-3-1	Albian (Late Cret.)	3293
Bre-6-1	Basement	2268
Qarun-3x	Late Eocene	3840

From the investigation of the two-dimensional magnetic model A-A1 (Fig. 11), it can be noticed the eastern and western part is deeper than the central part. This mean that the depth is increasing from the central toward the eastern and western side of the model the basement is uplifted in the central part with a depth of 2.5

km, while the depth in the deepest part of the model is 3.5 km. The profile B-B1 (Fig. 12), lies in the central part of the area and directed NW-SE. The basement is uplifted in the northern and central parts with a depth of 1.25 km, and deepening in the southern part with a depth of 2.95 km.

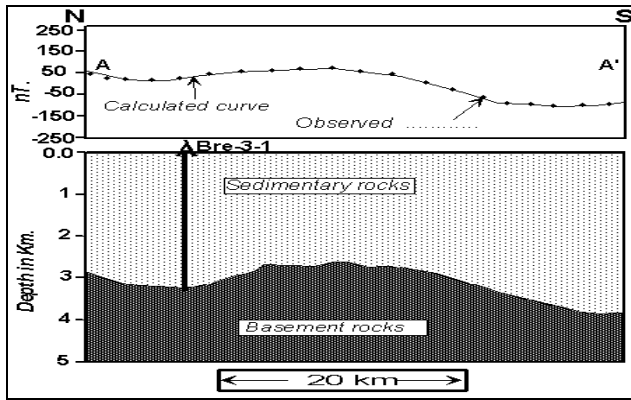


Fig. (11). Two-dimensional magnetic mode along profile A-A1 of the aeromagnetic map, Fayoum-Cairo District, Egypt.

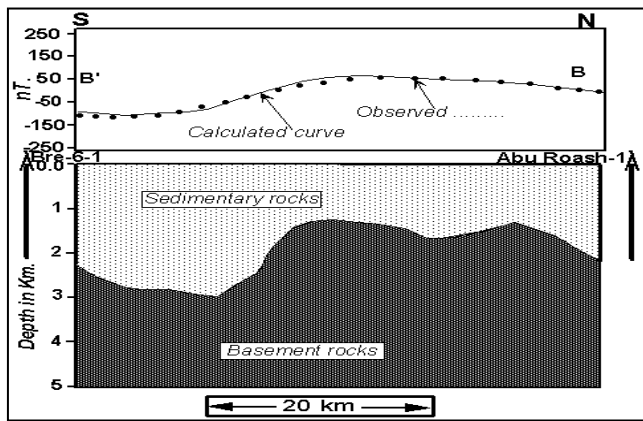


Fig. (12). Two-dimensional magnetic mode along profile B-B1 of the aeromagnetic map, Fayoum-Cairo District, Egypt.

Two dimensional magnetic models along the profile C-C1 (Fig. 13) lies in the western part of the area and directed nearly N-S. The basement is uplifted in the northern part of the profile with a depth of 1.8 km and deepening toward the southern part of the profile with the depth of 4.1 km. The profile D-D1 (Fig.14) lies in the northeastern and southwestern part of the area. The basement is uplifted near the northern part of the model, with a mean depth about 3.8 km, and the general deepening toward the central part, with a basement depth of 4.1 km.

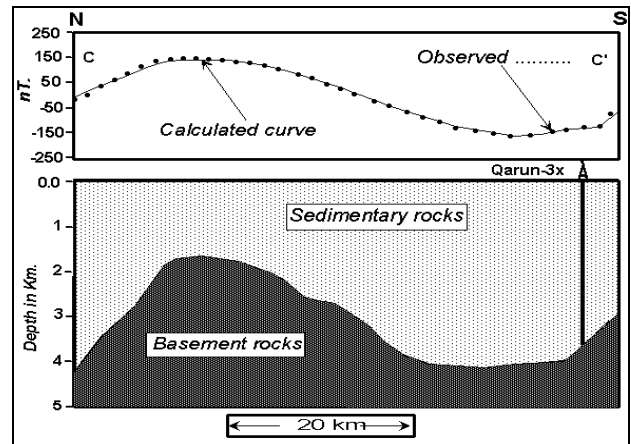


Fig. (13). Two-dimensional magnetic mode along profile C-C1 of the aeromagnetic map, Fayoum-Cairo District, Egypt.

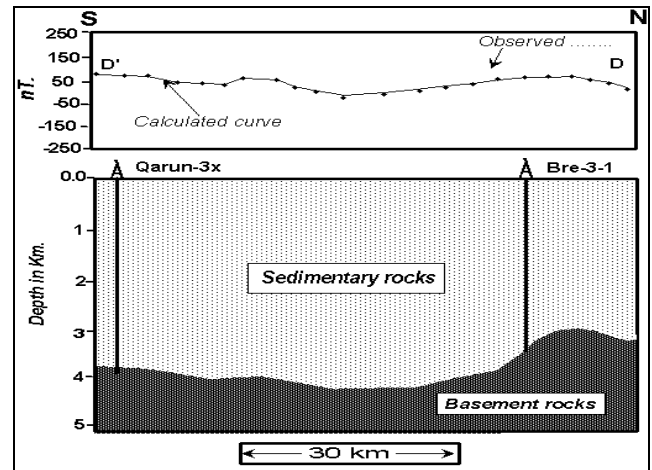


Fig. (14). Two-dimensional magnetic mode along profile D-D1 of the aeromagnetic map, Fayoum-Cairo District, Egypt.

CONCLUSION

The present study is devoted for the transformation and interpretation of the magnetotelluric and RTP aeromagnetic data through the integration of some geophysical techniques in order to detect of subsurface major structural elements affecting both the sedimentary section and the underlying basement complex. Close examination of the different anomalies through the RTP aeromagnetic map reveals that, the study area is characterized by intensive positive magnetic anomalies with different amplitudes. These anomalies may be attributed to the occurrence of subsurface basic intrusions of high magnetic content at different depths. Besides, it can be noticed that, the elongated magnetic anomaly zones in the northern part of the study with steep gradients could

indicated the occurrence of subsurface faulting trending principally in the NW-SE and NE-SW directions. These faults may be responsible of the recent earthquakes in the study area.

The results obtained from the induction arrows (tipper) and the two-dimensional magnetotelluric inversion model yielded a clear imaging of deep active faults that affect and could be responsible of earthquake activity in the studied area. These faults may be activated by the presence of fluids along fractured zones. Most probably increasing stresses could reduce the porosity of the fractured zones then reactivated these faults after certain time.

REFERENCES

- Abuel ata A. S. (1990).** The role of seismic-tectonics in establishing the structural foundation and saturation conditions of Elginidi basin, western Desert, Egypt. (Egyptian Geophysical Society) EGS. Proc., of the 8th Ann. Meet, pp. 150-189.
- Awad H., Mekkawi M., Saleh A., Saleh S., Fergany E., Hassib G., (2006).** Seismicity application of the Empirical Green Function (EGF) method and subsurface structure study in the Nile delta area, Egypt. Egyptian Society of Applied Petrophysics (ESAP), J. appl. Geophys, vol. 5, No. 2, pp. 70-84.
- Bedrosian, P.A., Unsworth, M.J. and Egbert, G.D., 2002.** Magnetotelluric imaging of the creeping segment of the San Andreas Fault near Hollister. Geophys. Res. Lett., vol. 29, No. 11, pp. 1506-1511.
- Bhattacharyya, B. K. (1966).** Two-dimensional harmonic analysis as a tool for magnetic interpretation. Geophysics, vol. 30, pp. 829-857.
- Elbohoty M. and Mekkawi M., 2005.** Shallow and deep structures at Gabal Qatamia, Cairo-Suez Road, as deduced from magnetotelluric and magnetic data. Egyptian Society of Applied Petrophysics (ESAP), J. applied Geophysics, vol 4, No. 2, pp. 110-124.
- Garcia. J. G., and Ness, G.E., 1994.** Inversion of the power spectrum from magnetic anomalies. Geophysics, vol. 59, pp. 391-400.
- Geosoft, V.4.3 (1993).** Geosoft Software for the Earth Science, Geosoft Inc., Toronto, Canada.
- Ghazala, H., (2001).** Tectonic setting of the area between Cairo and Fayoum provinces, Western Desert, Egypt: Implications of gravity models. Proc. 2nd the Intern. Symp. of Geophys. Tanta University, Egypt, pp. 101-110.
- Maurizio. F., Tatina. Q., and Angelo.S., 1998.** Exploration of a lignite bearing in Northern Ireland, using ground magnetic. Geophysics, vol.62, No. 4, pp. 1143- 1150.
- Mekkawi, M. 2003.** Magnetotelluric and seismicity studies along active fault zones, Ph. D. Thesis, Institute of geology, University of Neuchatel, Switzerland, 119 p.
- Mekkawi M., Schnegg, P.-A., Arafa-Hamed, T., Elathy, E., 2005.** Electrical structure of the tectonically active Kalabsha Fault, Aswan, Egypt. Earth Planet. Science. Letter, vol. 240, pp. 764-773.
- Meshref W., Abdel baki S., Abdel hady H.,and Soliman, S. (1980).** Magnetic trend analysis in the northern Arabian Nubian Shield and its tectonic implications. Ann. Geol. Surv. Egypt, vol. 10, pp. 939-953.
- Naeim, G., Hussein, A., El-Hakim, B., and Sewidan, A., (1993).** A preliminary Report on the Dahshour earthquake, 12 October 1992. Egyptian Geological Survey, Intern report, pp. 1-55.
- Nettelton, L., 1976.** Gravity and magnetics in oil prospecting. McGraw Hill Book Company, New Yourk, London and Paris.
- Peter, L. J. and John, F. D., (1970):** Direct design of two-dimensional digital wave number filters. Geophysics, vol. 35, No. 6, pp. 1073 -1078.
- Said, R. (1990):** The geology of Egypt. Elsevier Publishing Co., Amsterdam- NewYork.
- Schnegg, P.-A., 1998:** The magnetotelluric survey of the Penninic Alps of Valais, Bern, Swiss Geophysical Commission, 76 pp.
- Siripunvaraporn, W., and Egbert, G. (2000).** An efficient data-subspace inversion method for 2-D magnetotelluric data. Geophysics, vol. 65: pp. 791-803.
- Soyer, W. and Unsworth, M., 2006.** Deep electrical structure of the northern Cascadia subduction zone (British Columbia, Canada): implications for the role of fluids. *Geology*, 34, 53-56.15
- Spector, A. and Grant, F. S. (1970):** Statistical models for interpreting aeromagnetic data. Geophysics, vol. 35, pp. 293-302.

Sweidan, A. H., (1986). Contribution to the geology of Fayoum area. Ph.D. Thesis submitted to the degree of doctor of philo. Faculty of science, Cairo Univ. Egypt, 1986.

Unsworth, M., Bedrosian, P., Eisel, M., Egbert G.D., and Siripunvaraporn, W. (2000). Along strike variations in the electrical structure of the San Andreas fault at Parkfield, California. *Geophys. Res. Lett.*, vol. 200, pp. 3021-3024.

Unsworth, M.J., A.G. Jones, W. Wei, G. Marquis, S. Gokarn, J.E. Spratt, and the INDEPTH-MT team, 2005. Crustal rheology of the Himalaya and Southern Tibet inferred from magnetotelluric data. *Nature*, vol, 438, pp. 78-81.

Western Digital Company (1983): Reduced to the Pole (RTP) aeromagnetic map of Fayoum-Cairodistrict, Northern Western Desert, Egypt, (Scale 1: 100000).

Yungul, E. H., 1996: Electrical methods in geophysical exploration of deep sedimentary basins. Printed in Great Britain by Edmundsbury Press, 207 p.

EVALUATION OF THE TRANSIENT ELECTROMAGNETIC METHOD AS APPLIED IN WADI-FILL DEPOSITS, SOUTH SINAI, EGYPT

A.K. Mohamed*, M. Metwaly**, M. Khalil**, E. Al Sayed**

* Geology Department, Faculty of Science, Mansoura University, Egypt

** National research Institute of Astronomy and Geophysics, Helwan, Egypt

تقييم لطريقة الحث الكهرومغناطيسي كتطبيق في رسوبيات الأودية جنوب سيناء - مصر

الخلاصة: يعتبر وادي فيران من المصادر الرئيسية للمياه الجوفية في جنوب سيناء . نظرا لتعدد التركيب الطبقي لمثل هذه الأودية وعدم تجانس المكونات الصخرية وكذلك لوجود تتابعات من الطبقات الكهربية العاليه والمنخفضة المقاومه، فإن هذا الوضع الطبقي يعطى صوره غير واضحه للتراكيب التحت سطحيه والمياه الجوفيه عند استخدام طرق المقاومه الكهربية التقليديه. ولذلك تم استخدام طريقة الحث الكهرومغناطيسي في المدى الزمني كطريقه حديثه لا تتأثر بعدم التجانس القريب من السطح . تم قياس عدد ٢٣ محطه كهرومغناطيسييه وعدد ٢ جسه كهربييه متعامده بترتيب أشلمبرجيوذلك حول ٧ آبار مياه جوفيه متواجده في المنطقه . أعطت النتائج صوره واضحه للتتابع الطبقي وخزان المياه الجوفى بالمنطقه وكانت بمثابة تقييم جيد لأستخدام طريقة الحث الكهرومغناطيسي في المدى الزمني مع الأخذ في الاعتبار أن عمل نموذج ثلاثي الأبعاد يعطى تفاصيل أدق في مثل هذه البيئات الوديانيه.

ABSTRACT : Wadi Feiran is considered one of the main sources for groundwater in Southern Sinai, Egypt. The stratigraphic make-up of such wadi is complex with the presence of near surface inhomogeneties and alternations of resistive and conductive layers. This could produce undesirable results in subsurface imaging using DC resistivity method. Therefore, TEM as an alternative tool which is less affected by distortion from near surface anisotropy has been evaluated and assessed for lithological identification, aquifer characterization and direct removal of static shift in DC sounding curves in such wadi. Twenty three single loop TEM and two Schlumberger VES soundings have been carried out around seven boreholes in the area of study. The output results have shown the effectiveness of the proposed TEM method in handling of such wadies. However, it is recommended to use a contiguous transient electromagnetic profiling and 3D modeling for obtaining highly resolved mapping in such environments.

INTRODUCTION

Transient electromagnetic (TEM) method is an inductive method that utilizes strong current which is passed through a rectangular loop commonly laid on the surface of the ground. The flow of this current in the surface loop creates a magnetic field that spreads out into the ground in the form of a primary magnetic field and induces eddy currents in the subsurface.

Recently, transient electromagnetic (TEM) method is widely used for hydrogeological, engineering, and environmental applications (e.g. Kafri and Goldman, 2005, Rubin and Hubbard, 2005). This is attributed to its ability for penetrating thick conductive overburden overlying resistive bedrock targets (Meju et al., 1999). TEM method has shown its efficiency as an integrated method with Vertical Electrical Sounding (VES) and Audio-Magnetotelluric (AMT) methods in the semiarid areas (c.f. Mohamed et al., 2002). On the other hand, TEM has been used to correct the DC and MT data for the so called static shift since it is less affected by near surface inhomogeneties .

In this study, transient electromagnetic method has been carried out in typical wadi fill deposits of Wadi Feiran, which is considered one of the main sources for groundwater in southern Sinai, Egypt (Fig.1). Sedimentations in such Wadi are complex and consist of poorly sorted flash-flood deposits and normal alluvial deposits originated from local lacustrine or swampy

conditions (Issar and Eckstein 196). However, in spite of the possible presence of a complex stratigraphic sequence and near-surface inhomogeneities, discrete direct current resistivity soundings are commonly made in such Wadis (e.g. El-Gamili et al., 1994; Shendi, 2001) at widely spaced stations and which could produce undesirable results in subsurface imaging. Therefore the TEM method has been evaluated in this study as a cost effective rather than the DC resistivity method, which sometimes gives unreliable results and when even applied needs massive effort to carry out in this complex lithology of thick resistive overburden overlying alterations of conductive and resistive layers (Fig.2). Twenty three single loop TEM and two Schlumberger VES soundings were conducted for lithological identification, aquifer characterization and direct removal of static shift in DC sounding curves at the outlet of Wadi Feiran.

Acquisition and Processing of TEM and DC resistivity data

The TEM data have been collected in Oct. 2005 by Sirotem equipment, an Australian built field system. It consists of a transmitter and a receiver components housed together and powered by two 12 volt batteries.

Fig.1: Location map of the area of study showing the locations of TEM-VES and boreholes

Single-loop TEM data were acquired at these sites using 50 m-sided transmitter loops and the spacing interval was 150m. The time window bands applied were composite, high resolution and early time series. Composite time series was mainly selected in processing to get at large extent a greater depth of investigation. The recording number of windows selected varied depending on the quality of data. IP effect has been reported as negative response over some range of the measurement at late time which has not been accounted for. In the mean time, two vertical electrical soundings have been done at two sites (Fig.1) using Schlumberger array with maximum AB/2 equal to 500m. The equipment used is Syscal/R2 resistivity meter.

The TEM voltage measured has been converted into its late stage apparent resistivities (Kaufman, 1983).

The late time apparent resistivities calculated were plotted versus time. A simple approximate scheme for TEM data sets (Meju et al. 1999) have been evaluated and assessed to see whether it can be applied in these heterogeneous conditions for obtaining an initial model especially if there is no previous information. Therefore, TEM apparent resistivity data have been converted before modeling into effective subsurface resistivity at depth yielding a continuous picture of the resistivity-depth distribution of the subsurface (Fig. 3). 1-D modeling was then used for forward and automatic inversion approaches of the TEM data set (Meju, 1994). This program takes the turnoff time effect into account. The inverse modeling was done on the preliminary model and ridge regression method was used to adjust iteratively the parameters of the starting model until obtaining a model that best fits the data.

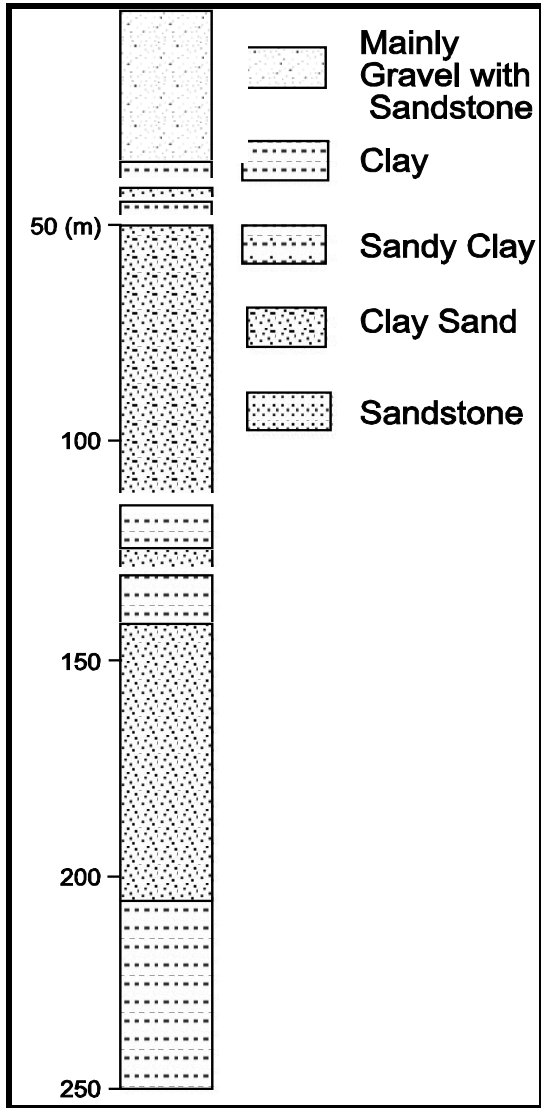


Fig. 2: Lithostratigraphic column borehole site Wf16.

1-D Synthetic response

VES and transient electromagnetic (TEM) 1D response were calculated for the known subsurface resistivity distributions at site WF11 and WF13, which have complex lithology and alternations of conductive and resistive layers. The TEM data for various transient times are plotted at their equivalent AB/2 spacing using an approximate scaling relation (Meju et al., 1999). Synthetic response shows that The TEM responses generally proved to be better for defining the conductive units (Fig. 4). The contrast between the geoelectric layers is clearly shown in the TEM synthetic data. These TEM depth soundings can be efficiently conducted in geometrically restricted areas of Wadi Feiran where it is difficult to expand the current electrodes of DC resistivity method beyond 500 m to reach the potential aquifer which is at depths greater than 170 m in such wadi.

Static shift correction

Electric and electromagnetic methods are still affected differently by the presence of small-sized three-dimensional (3D) bodies in the near-surface. It is still an unresolved problem in geoelectrical exploration (e.g. Barker 1981; Groom and Bailey 1989). Essentially, TEM method is less affected by near surface inhomogeneity than the DC resistivity method which might be vertically shifted on sounding curves (Meju et al, 1999). Therefore, the main tenet of collecting DC resistivity data is to see whether TEM method can be applied in heterogeneous geological media, enabling accurate identification and removal of static shift in DC resistivity sounding curves. Subsequently electrical and EM depth-sounding techniques can be combined to yield more complete profiling of the resistivity of the subsurface. Joint DC and TEM soundings were executed at two sites then simple approximate schemes (Meju et al, 1999) for DC and TEM data sets, have been applied in these heterogeneous conditions.

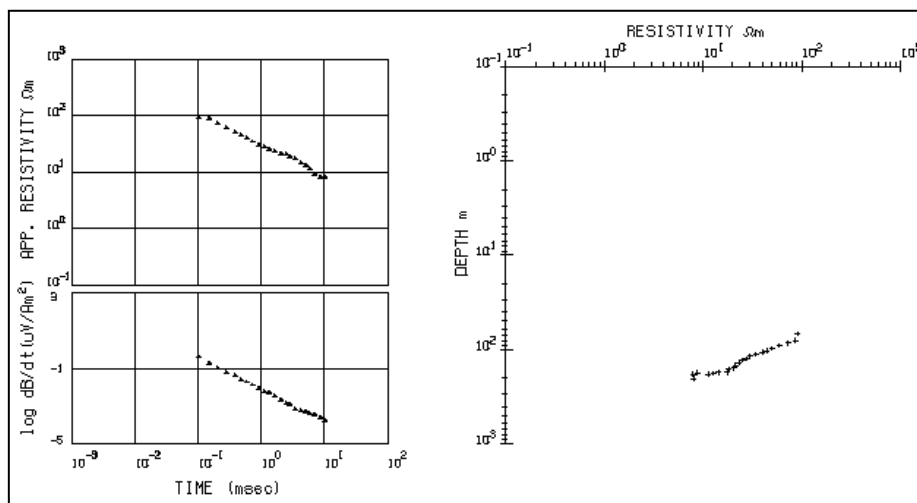


Fig 3: An example of TEM resistivity-depth transformation at sit W23.

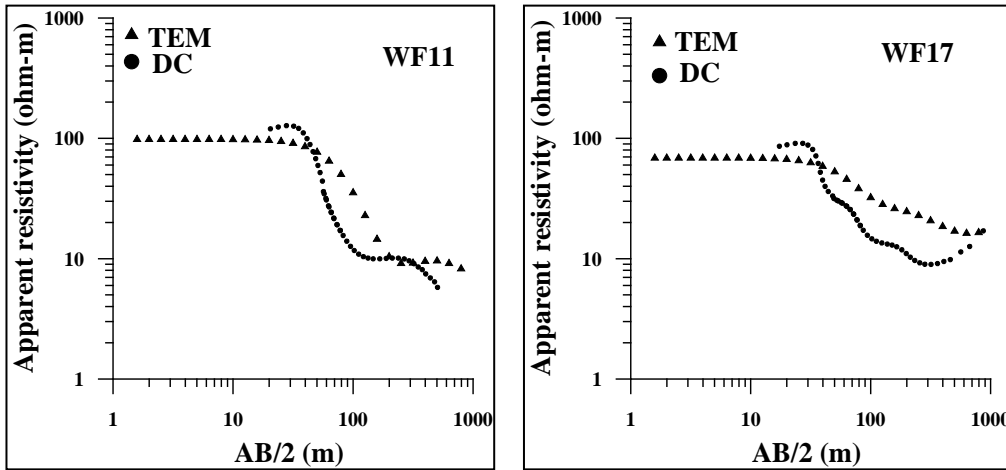


Fig. 4: Synthetic response of broadband TEM and VES 1D apparent resistivities calculated for two borehole sites (WF11 and WF17) using the average values of the resistivities recorded in the boreholes.

Selective example is given in (Fig. 5a). Note the good correlation between resistivity data and TEM data after the removal of static shift effect (Fig. 5b) and the ranges of resistivity values get closer to those recorded by resistivity log (not shown here) at the same location.

TEM modeling and the effect of a priori information

The resistivity-depth transformation and 1-D forward and inverse modeling results have been conducted to the collected TEM data. The initial model was designed from resistivity logs of the boreholes after doing environmental corrections. Figure (6) shows the forward modeling at site w8. The initial model was selected at the nearest borehole (WF14) beside the site taking any guidance from TEM resistivity-depth transformation. As shown, the fit between observed and calculated data is generally good. Note the agreement between the resistivities of layer boundaries with the changes of resistivity-depth transformation.

However, inverse modeling was carried out to get the best fit and through it the thickness of the third resistive layer has become thinner than realism. Generally, most of TEM data set collected at the borehole illustrate that the forward response from the initial model was plausible with the observed data. Selective examples of 1-D inverse modeling results are given at sites W7, W9, W13, and W2 beside boreholes WF13, WF12, WF11, and WF16, respectively (Figs. 7, 8, 9, 10). These figures demonstrate that the initial models have been deduced from the recorded resistivity logs taking into consideration depth to water. In these models, the thick resistive and conductive zones are clearly defined and their boundaries are concordant with the alterations of resistivity-depth transformation which could be very useful for getting a starting model if there is no previous information. The distinction between the clay layer and the water bearing formation could be delineated. This is attributed to the high sensitivity of the TEM method for detecting conductive zones.

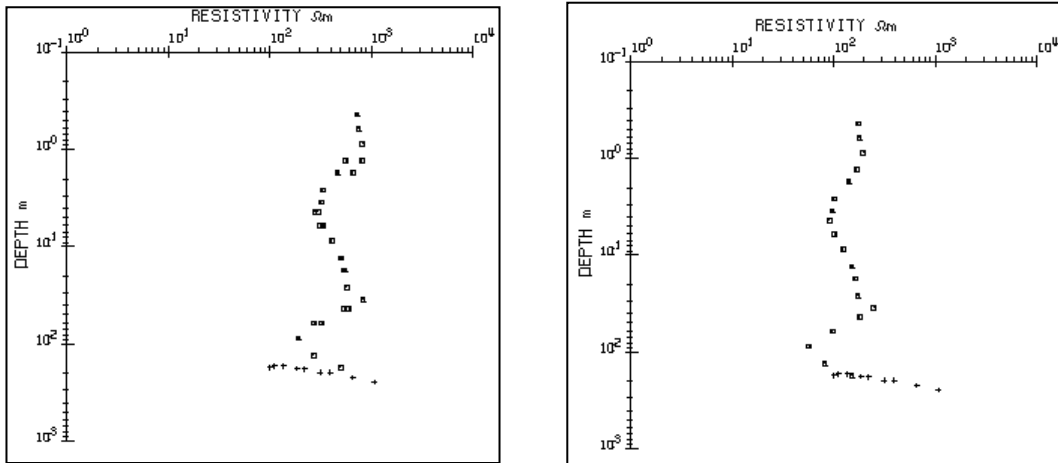
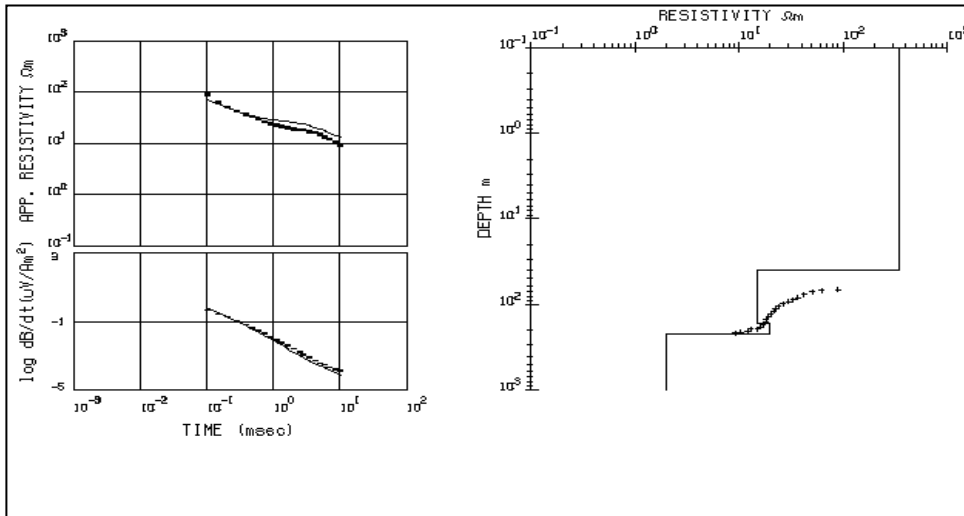


Fig.5: DC resistivity data before and after the removal of static shift at sit wf16.

a)



b)

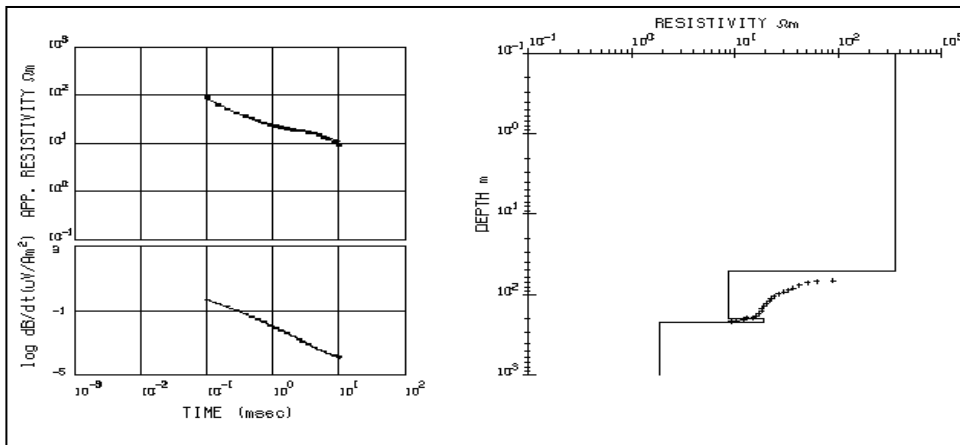


Fig.6:1-D forward and inverse modeling results of TEM data at site W8.

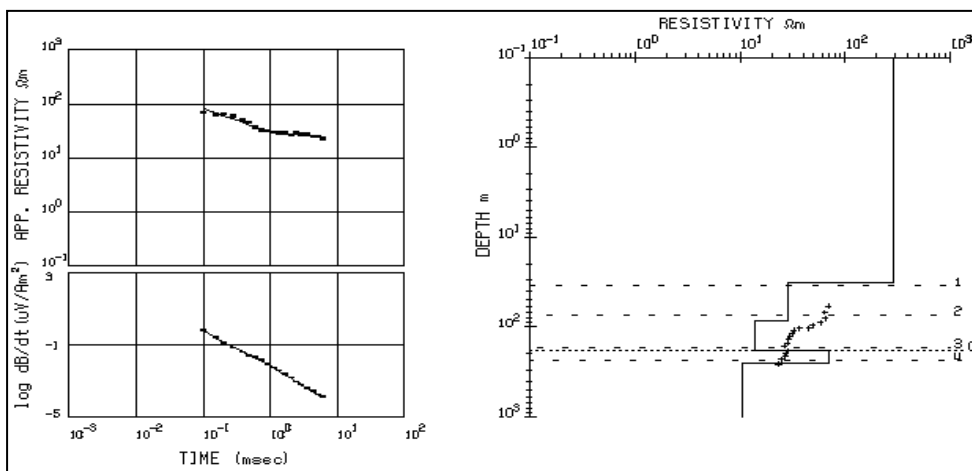


Fig. 7: 1-D inverse modeling of TEM data at site W7 beside the borehole WF13 (the lithological boundaries and depth to water are indicated).

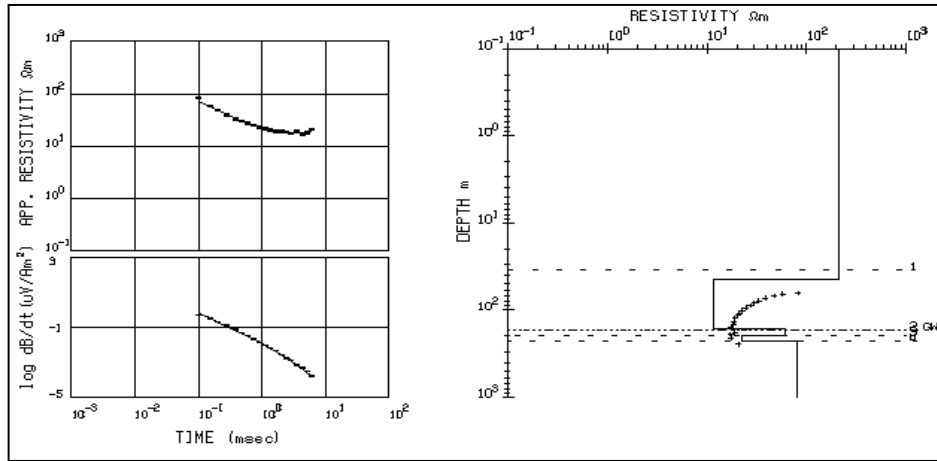


Fig.8: 1-D inverse modeling of TEM data at site W9 beside the borehole WF12.

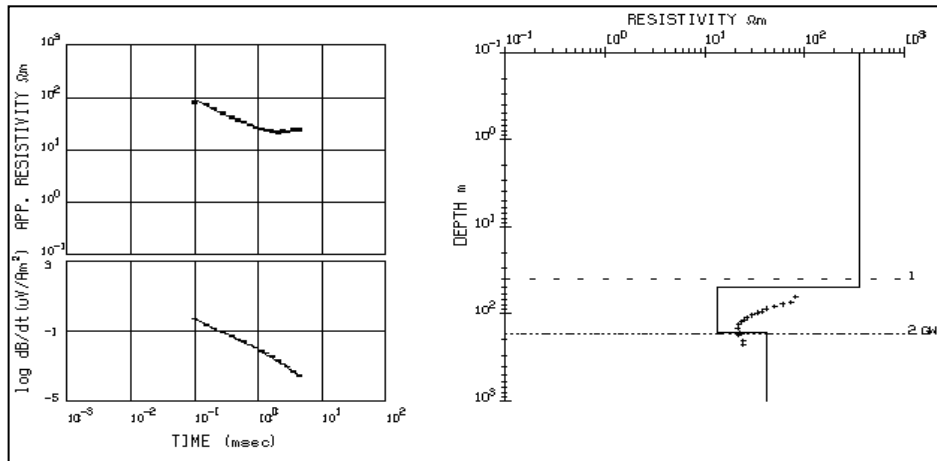


Fig. 9: 1-D inverse modeling of TEM data at site W13 beside the borehole WF11.

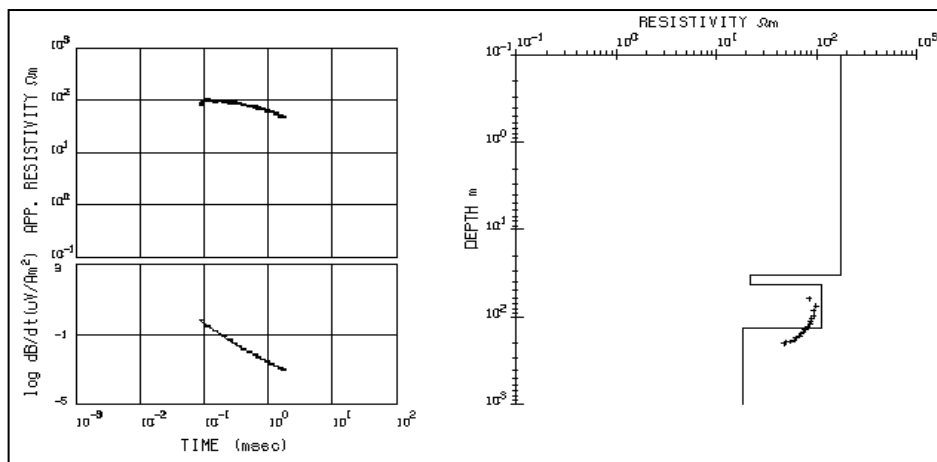


Fig. 10: 1-D inverse modeling of TEM data at site W2 150m away from borehole wF16.

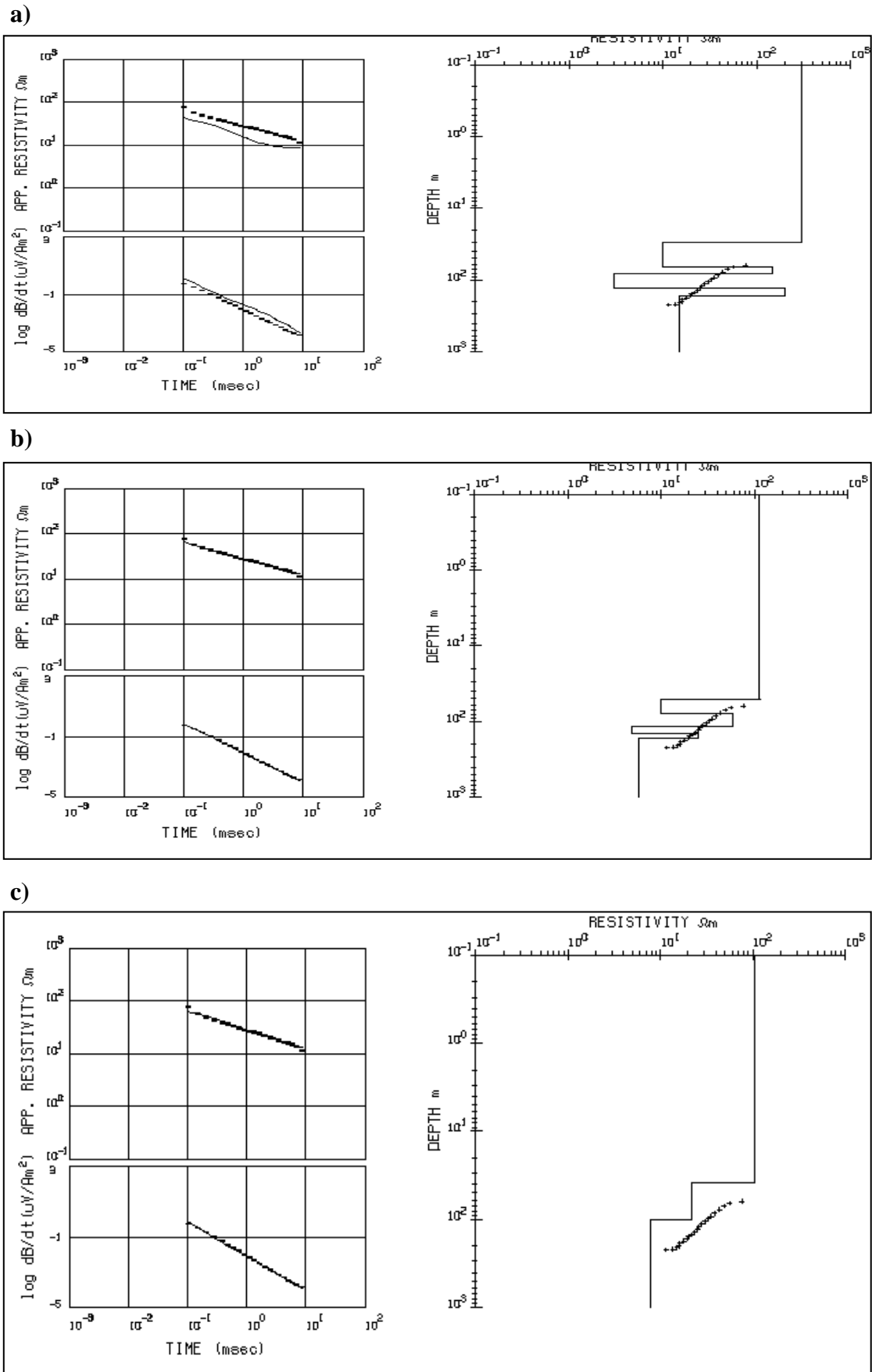


Fig. 11: Forward and inverse modeling results at site w11 beside the borehole site wf17.

Although, TEM has shown its consistency with geological and hydrogeological background, the forward response derived from a priori information represented at site w11 was not reasonable with the observed data (Fig. 11a). The inferred initial model deduced from well logging records at this site displays alterations of resistive and conductive layers. As illustrated, the fitness is actually not sensible enough in this field example. The inverse modeling results has enhanced the fitness, though the thickness-resistivity values of layers had changed (Fig 11b). If we are not guided by geological information, and according to the effect of non-uniqueness, very simple model could produce the same fit and the resistivity-depth transformation might lead defining the preliminary model (Fig 11c). Nevertheless, the data at this site penetrated the top resistive layer and delineated the underlined conductive layers.

One dimensional geoelectric cross-section

The output results of 1-D inverse modeling of TEM data were collated to produce geoelectric cross sections. We have presented some of them along two profiles. The first one (A-A') passes through some of the available boreholes and TEM data beside them were only selected for comparative study with the geological information (Fig12) The other profile includes all the TEM data collected along that profil. In profile A-A', a priori information was used from geological information as input for inverse modeling results.

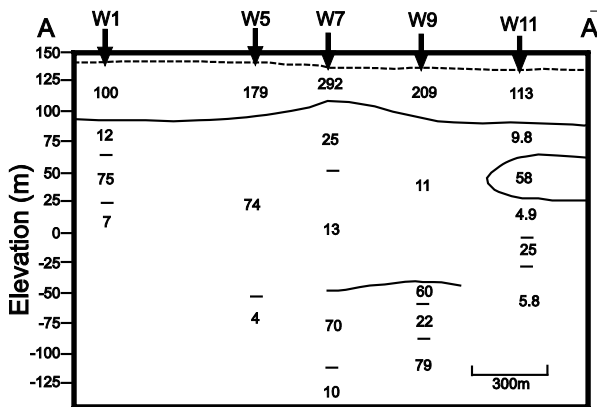


Fig.12: 2-D geoelectric section along profile A-A' using 1-D inversion results

Comparing the output results of TEM data along profile A-A' with the geological cross section along the same profile (Fig. 13), shows a good agreement, where the overlying resistive layer of gravel is well delineated. The underlying thick conductive layers of clay are also defined. However, the thin layers of clay and sandstone cannot be clearly demarked at some sites (e.g. w5) to merge together in one geoelectric layer. The margin between the resistive layer of gravel and the underlying conductive layer is reasonable with an error that does not exceed ~3m at some boundaries. The second profile (B-B') was modeled taking a simplified initial model

(Fig.14). This preliminary model was carried out using the least number of layers from the resistivity-depth transformation of the observed data. Therefore, it portrays three dominant geoelectric layers where the resistive layer of gravel is underlain by two geoelectric layers corresponding mainly to sandy clay and clay. This indicates that TEM data could produce the gross boundaries if it is not constrained by a priori information. The top resistive layer of gravel is also well differentiated from the underlain conductive zones though a simplified initial model.

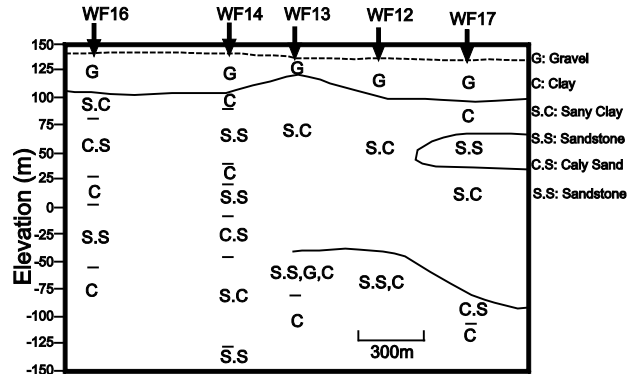


Fig.13: Litho-stratigraphic succession at the borehole sites passing through profile A-A'

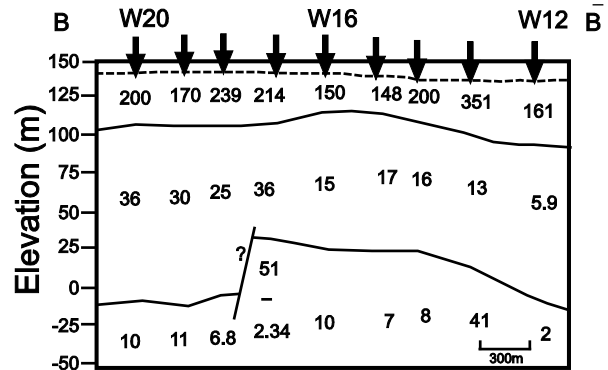


Fig.14: 2-D geoelectric section along profile B-B' using 1-D inversion results

Comparative study between Well log analysis and TEM data

As shown earlier, TEM in most of the data sets is very sensitive to conductive zones. Since we have well log records representing porosity logs (density, neutron, and sonic), shallow and deep resistivity logs, gamma ray, self potential and caliper logs in most wells, these data were first corrected for environmental effects and then analyzed to obtain the most important parameters which might control TEM resistivity values. These are total porosity, volume of shale (clay) and matrix. The output results were presented vertically and compared with TEM resistivity data. A selective example is portrayed in

figure (15). As shown, the resistivity values are generally affected by the above mentioned hydrogeophysical parameters, particularly the volume of clay, which plays an important role in the variation of TEM resistivity values.

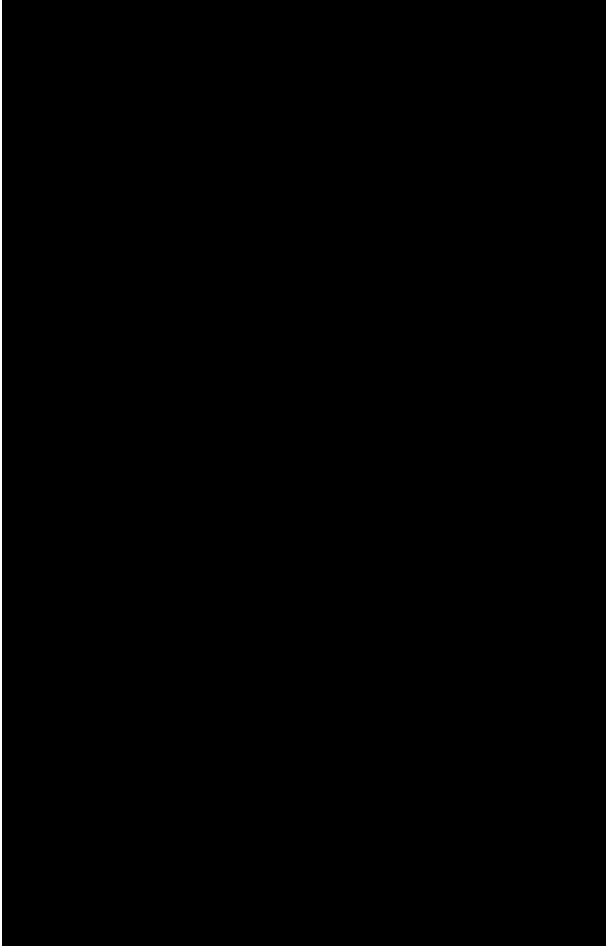


Fig.15: A comparative study between well log analyses and TEM apparent resistivity values at wf 13.

Conclusions and recommendation

The following conclusions may be drawn for this work

- 1) The method enables a good assessment of the resistivity characteristics of the unconsolidated sediments of sandstone and clay that underlie assemblage boulders of gravel with an average thickness of about 35m.
- 2) The transient electromagnetic method was able, in most cases, to recognize systematic changes in resistivities of the heterogeneous alluvium deposits, related mainly to variation of lithology. The clay minerals in particular have shown its effectiveness in controlling the TEM voltages.
- 3) Applications of apparent resistivity-depth transformation to TEM field data for such geological environments show its help for obtaining

a simplified initial model even if there is no a previous information.

- 4) TEM method is well recommended for easy identification of electrical static shift in direct current (DC) sounding curves in such environment.
- 5) The clay layers have been differentiated from the water bearing formation in most TEM soundings.

Although the 1-D interpretation has proved feasible and reliable in many practical cases, significant inaccuracies may occur when true geoelectrical structure is essentially multidimensional. In this case, multidimensional inversion scheme would be more useful. We hope future work will enable us to collect data set (3-D survey) for 3-D modeling scheme.

REFERENCES

- Barker R.D. 1981.** The offset system of electrical resistivity sounding and its use with a multicore cable. *Geophys. Prosp.* 29, 128-143.
- El-Gamili M.M., Shaaban F.F. and El-Morsi O.A. 1994.** Electrical resistivity mapping of the buried stream channel of the Canopic Branch in the Western Nile Delta, Egypt. *Jour. African Earth Sciences* 19, 135-148.
- Groom R.W. and Bailey R.C. 1989.** Decomposition of magnetotelluric impedance tensors in the presence of local three-dimensional galvanic distortion. *Journal of Geophysical Research* 94, 1913-1925.
- Issar A. and Eckstein Y. 1969.** Lacustrine beds of Wadi Feiran, Sinai: their original Significance. *Israel Journal of Earth-Science* 18, 21-27
- Kafri, U. and Goldman, G. 2005.** The use of the time domain electromagnetic method to delineate saline groundwater in granular and carbonate aquifers and to evaluate their porosity, *Journal of applied geophysics*, 57, 167–178
- Kaufman, A.A., and Keller, G.V. 1983.** Frequency and transient sounding: Elsevier Science Publ. Co. Inc.

- Rubin, Y. and Hubbard, S. 2005.** Hydrogeophysics, Springer Publ., pp511.
- Meju, M.A. 1994.** Geophysical data analysis: Understanding inverse problem theory and practice, SEG Course Notes Series, V. 6, 296 p.
- Meju, M.A., Fontes S.L., Oliveira M.F.B., Lima J.P.R., Ulugergerli E.U, Carrasquilla A.A. 1999.** Regional aquifer mapping using combined VESTEM/EMAP methods in the semiarid eastern margin of Parnaiba Basin Brazil. *Geophysics* 64, 337-356.
- Mohamed, A.K. 2004.** Evaluation of borehole geophysical well logging and discrete surface resistivity sounding for stratigraphic mapping in Wadi Feiran, Sinai, Egypt, Proc. 3rd International Symposium on Geophysics, Tanta University, Egypt, 332-345.
- Mohamed, A. K., Meju, M.A., and Fontes, S.L. 2002,** Deep structure of the northeastern Parnaiba Basin, Brazil, from Magnetotelluric, *Geophysical prospecting* 2002, 50,589-602.
- Shendi E.H. 2001.** Geophysical prospecting for groundwater in crystalline basements rocks in arid regions (case study from south Sinai, Egypt). Proc. 7th Meeting of Environmental and Engineering Geophysics Soc. (EEGS), Birmingham University, England, pp. 236-237.